UNIVERSITAT POLITÈCNICA DE CATALUNYA
BARCELONATECH
Departament de Ciència i Enginyeria de Materials

BIOMATERIALS, BIOMECHANICS & TISSUE ENGINEERING

CIEFMA

Surface characterization and cell instructive properties of superficially modified dental zirconia

Doctoral Program of Materials Science and Engineering

Joaquim Minguela Díaz

Carles Mas-Moruno, supervisor

Joan Josep Roa Rovira, supervisor

Thesis as a compendium of publications

Biomaterials, Biomechanics and Tissue Engineering Research Group
Center for Structural Integrity, Reliability and Micromechanics of Materials

Universitat Politècnica de Catalunya - BarcelonaTech

Barcelona, May 2021

Preface

The Ph.D. Thesis is presented as a compendium of three original papers. All the work included in these papers has been carried out at the *Departament de Ciència i Enginyeria de Materials* at the *Universitat Politècnica de Catalunya - BarcelonaTech*, under the supervision of Dr. Carles Mas Moruno and Dr. Joan Josep Roa Rovira. Part of the work, in particular the evaluation of residual stresses and the laser-patterning, were carried out during my research stage conducted at the Chair of Functional Materials (FuWe) group at the Universität des Saarlandes (Saarbrücken, Germany).

This PhD. Thesis has been supported by a Predoctoral fellowship from the *Barcelona Research Center in Multiscale Science and Engineering*.

Joaquim Minguela

Barcelona, 2021

Abstract

Tetragonal polycrystalline zirconia doped with 3 mol% yttria (3Y-TZP) has become one of the most popular dental ceramics. Thanks to its outstanding mechanical properties (including high hardness, toughness and wear resistance), biocompatibility and white color, it is now commonly employed to produce components such as crowns, implants, abutments, bridges or posts and cores.

In the case of dental implants, which are directly screwed into the jawbone, implant's surfaces can be modified through different physical or chemical techniques to ensure a rapid and proper osteointegration. In the first case, surface topography is known to play a critical role in cell-material interactions and to influence several cell functions such as adhesion, proliferation or differentiation. In the second case, specific chemical cues such as integrin-binding peptidic molecules from bone extracellular matrix can affect cell behavior with a high degree of specificity. The combination of both strategies may provide a powerful tool to obtain an improved bone-to-implant contact and ensure long lasting implants.

In this Ph.D. Thesis a dual approach employing surface topographical modification and peptidic biofunctionalization on dental zirconia is explored, with the aim of providing a flexible tool to improve tissue integration of ceramic restorations.

Regarding surface topographical modifications, two different strategies are investigated: *grinding* and *laser-micropatterning*. Both of them can generate not only rough surfaces at the micro- and submicrometric length scale but also other features such as grooves, which may guide cell growth. However, these two techniques are based on different principles. While in *grinding* technique the material is removed by a mechanical process, laser patterning is based on the thermal effects of absorbed photons.

However, these methods are not exempt from introducing a certain degree of surface damage, which can be detrimental for the final application. In addition, 3Y-TZP is susceptible of a spontaneous surface phase transformation from tetragonal (*t*-) to monoclinic (*m*-) phase under two different scenarios. One is known as transformation toughening and it is a stress-assisted mechanism accompanied by a volume increase (~ 4%) activated by the near tip crack stress field, which increase crack propagation resistance. On the other hand, a second scenario exists known as low temperature degradation (LTD). In this case, aging by progressive $t \rightarrow m$ transformation at the surface is triggered by water molecules. In this particular case, this mechanism induces roughening and micro-cracking, which can drastically reduce the mechanical properties and in particular the wear resistance by generating pull-out of 3Y-TZP grains. In this regard, some surface treatments can affect the LTD resistance of the material, or even induce this phase transformation. For these reasons, a particular emphasis is placed on the changes in the surface and subsurface introduced by both methods. Damage, microstructure, phase transformation and residual stresses are characterized, as well as its effects on LTD and mechanical properties.

On the other hand, peptidic biofunctionalization is carried out by using a peptidic platform that incorporates the cell-adhesive RGD and the osteogenic DWIVA motives. This strategy is combined with the best performing topography-modifying treatment. On this surface that integrates the stimuli provided by topography and the peptides, cell adhesion, cell migration and osteogenic properties are characterized in detail.

The results of this Ph.D. Thesis may serve as a further step in the journey of developing zirconia-based ceramic materials to become a reference material in prosthodontics. The dual functionalization presented here is a powerful tool to improve the tissue integration and healing success of 3Y-TZP dental implants. Importantly, both the topography and the peptidic platform can be easily modified and designed to fulfill different requirements (osteogenic, angiogenic, antibacterial, etc.).

Resum

La zircònia policristal·lina tetragonal dopada amb un 3% d'ítria (3Y-TZP) s'ha convertit en una de les ceràmiques dentals més populars. Gràcies a les seves excel·lents propietats mecàniques (inclosa l'alta duresa, tenacitat i resistència al desgast), la biocompatibilitat i el color blanc, ara s'utilitza habitualment per produir components com corones, implants o ponts.

En el cas d'implants dentals, que es cargolen directament a l'os de la mandíbula, les superfícies de l'implant es poden modificar mitjançant diferents tècniques físiques o químiques per garantir una osteointegració ràpida i adequada. En el primer cas, se sap que la topografia superficial té un paper crític en les interaccions cèl·lula-material i que influeix en diverses funcions cel·lulars com ara l'adhesió, la proliferació o la diferenciació. En el segon cas, els estímuls químics específics com els que indueixen les molècules peptídiques de la matriu extracel·lular òssia poden afectar el comportament cel·lular amb un alt grau d'especificitat. La combinació d'ambdues estratègies pot proporcionar una eina poderosa per obtenir una millor interacció entre l'os i l'implant i garantir una vida llarga als implants.

En aquesta tesis doctoral s'explora una estratègia dual que utilitza la modificació superficial de la topografia i la biofuncionalització peptídica sobre zircònia dental, amb l'objectiu de proporcionar una eina flexible per millorar la integració amb els teixits de les restauracions ceràmiques.

Pel que fa a les modificacions superficials de la topografia, s'estudien dues estratègies diferents: rectificat i micro-patrons làser. Tots dos poden generar no només superfícies rugoses a l'escala micro- i submicromètrica, sinó també altres característiques com ara canals/solcs, que poden guiar el creixement cel·lular. Tot i això, aquestes dues tècniques es basen en principis diferents. Mentre que en

la tècnica de rectificat el material s'elimina mitjançant un procés mecànic, el patró làser es basa en els efectes tèrmics dels fotons absorbits.

No obstant això, aquests mètodes no estan exempts d'introduir un cert grau de dany a la superfície, que pot ser perjudicial per a l'aplicació final. A més, la 3Y-TZP és susceptible d'una transformació espontània de fase des de la fase tetragonal (t-) a la monoclínica (m-) sota dos escenaris diferents. Un es coneix com a *augment de tenacitat per transformació de fase* ("transformation toughening", en anglès) i és un mecanisme activat per esforços acompanyat d'un augment de volum (~ 4%). Aquest procés està activat pel camp d'esforços proper a una esquerda, augmentant la resistència a la propagació de les esquerdes. D'altra banda, existeix un segon escenari conegut com degradació a baixa temperatura ("low temperature degradation", en anglès). En aquest cas, la progressiva transformació de t → m a la superfície és provocada per les molècules d'aigua. Aquest mecanisme indueix rugositat i micro-esquerdes a la superfície, que poden reduir dràsticament les propietats mecàniques i, en particular, la resistència al desgast. En aquest sentit, alguns tractaments superficials poden afectar la resistència a la degradació del material o fins i tot induir aquesta transformació de fase. Per aquestes raons, es fa un èmfasi especial en els canvis en la superfície introduïts per tots dos mètodes. Es caracteritzen els danys, la microestructura, la transformació de fase i les tensions residuals, així com els seus efectes sobre les propietats mecàniques i la degradació a baixa temperatura.

D'altra banda, la biofuncionalització peptídica es realitza mitjançant una plataforma peptídica que incorpora el motiu adhesiu RGD i el motiu osteogènic DWIVA. Aquesta estratègia es combina amb el tractament modificador de la topografia amb el millor rendiment (rectificat o micro-patrons làser). En aquesta superfície on s'integren els estímuls proporcionats per la topografia i els pèptids, s'estudia l'adhesió cel·lular, la migració cel·lular i les propietats osteogèniques.

Els resultats d'aquesta tesis doctoral es poden considerar com un pas més en el desenvolupament de materials ceràmics amb base de zircònia per convertir-se

en un material de referència en prostodòncia. La doble funcionalització presentada aquí és una potent eina per millorar la integració del teixit i la capacitat de curació dels implants dentals de 3Y-TZP. És important destacar que tant la topografia com la plataforma peptídica es poden modificar i dissenyar específicament per complir altres requisits (osteogènic, angiogènic, antibacterià, etc.).

Acknowledgements

Now that I am at the end of this journey I can turn my head back and see the long road walked. It's just now, at its very end, that I can judge this unique experience with a smile in my face. Along this adventure many people have contributed to my thesis professionally and personally. I would like to acknowledge the support from all of you:

Carles Mas and **Joan Josep Roa**, my supervisors, who have been my mentors and guided me during these years. Thanks for sharing your knowledge and passion for research with me. Your support, patience and trust have been the foundations of this thesis.

Luis Llanes and **Maria Pau Ginebra**. Thanks for giving me the opportunity of being part of CIEFMA and the BBT. I would like to especially thank your help in the revision of all my articles. I appreciate your experienced comments and thoughts about my work.

To **Sebastian Slawik** and **Daniel Müller**, for your selfless assistance, collaboration and teachings. My work would not have been possible without your valuable contributions. Also to **Frank Mücklich** and **Flavio Soldera**, who made possible my research stage in Saarbrücken and to **Sebastián Suárez**, **Katherine Aristizabal** and **Tobias Fox**, who also contributed to my project. I would like to thank all the people from the *Lehrstuhl für Funktionswerkstoffe* in the *Universität des Saarlandes*, for their warm reception and help. I cannot finish this paragraph without mentioning my dearest friend in Saarbrücken, **Idriss El Azhari.** Thanks for your friendship.

To all my friends, colleagues and professors in the **BBT**, **CIEFMA** and **PROCOMAME** groups. Your kindness, fellowship and support have made this

experience so special. I have enjoyed all the hours we have spent together in the labs, offices… and (mostly) polishing room!! It has been a pleasure knowing all of you. I want to also acknowledge all the **technical staff** of the BBT and CIEFMA groups, whose everyday job made this thesis possible. Also to the technical staff in the Centre de Recerca en Ciència i Enginyeria Multiescala de Barcelona.

To the people that has stayed by my side, in the good and the bad moments. Thanks **Sergio**, **Mona**, **Junhui**, **Johana B.**, **Danielas**, **Harsha**, **Angelica**. I would like to especially thank **Yafeng Zheng**. Thanks for the long afternoons in the office, for the coffees we shared, for the great conversations, for sharing your culture with me, for being a friend when I needed one, for your wise advice, for always giving without expecting anything in return, thanks for being you.

Finally, to all my **family** and especially to **Ana**. Thanks for being my travelling companions. I couldn't have reached the finish line without you.

P.S. I cannot forget the millions of cells and bacteria that gave their life for this thesis. You were lysed, aspired, fixed, stained, frozen and thrown away. Yet, you never complained. Thanks for your sacrifice.

List of publications and other contributions

Publications

I. J. Minguela, S. Slawik, F. Mücklich, M.P. Ginebra, L. Llanes, C. Mas-Moruno, J.J. Roa, *Evolution of microstructure and residual stresses in gradually ground/polished 3Y-TZP*, J. Eur. Ceram. Soc. 40 (2020) 1582–1591.

II. J. Minguela, M.P. Ginebra, L. Llanes, C. Mas-Moruno, J.J. Roa, *Influence of grinding/polishing on the mechanical, phase stability and cell adhesion properties of yttria-stabilized zirconia*, J. Eur. Ceram. Soc. 40 (2020) 4304–4314.

III. J. Minguela, D.W. Müller, F. Mücklich, L. Llanes, M.P. Ginebra, J.J. Roa, C. Mas-Moruno, *Peptidic biofunctionalization of laser patterned dental zirconia: a biochemical-topographical approach*, Mat. Sci. Eng. C 125 (2021) 112096.

Participation at Congresses

- J.Minguela, A.García, L.Llanes, M.P.Ginebra, C.Mas-Moruno, J.J.Roa, *Grinding of biomedical yttria-doped zirconia as a surface finishing technique: microstructural, mechanical and biological characterization.*

Oral presentation at the V Congreso Hispano-Luso de Cerámica y Vidrio. Barcelona, Spain. 8th-10th October 2018.

- J.Minguela, S. Slawik, L.Llanes, M.P.Ginebra, C.Mas-Moruno, J.J.Roa, *Microstructural evaluation and residual stresses in zirconia-based materials after grinding.* Oral presentation at the 10th EEIGM International Conference on Advanced Materials Research. Moscow, Russia. 25th-26th April 2019.

- J.Minguela, S. Slawik, L.Llanes, M.P.Ginebra, F. Mücklich, C.Mas-Moruno, J.J.Roa, *Grinding/polishing of dental yttria-doped zirconia. Fine tuning mechanical, degradation and biological properties via microstructural changes.* Oral presentation at the EUROMAT 2019: European Congress and Exhibition on Advanced Materials and Processes. Stockholm, Sweden. 1st-5th September 2019.

- J.Minguela, S.Suárez, K.Aristizabal, L.Llanes, M.P.Ginebra, F.Mücklich, C.Mas-Moruno, J.J.Roa, *Femtosecond laser interference patterning on dental zirconia.* Poster at the EUROMAT 2019: European Congress and Exhibition on Advanced Materials and Processes. Stockholm, Sweden. 1st-5th September 2019.

- J.Minguela, L.Llanes, M.P.Ginebra, J.J.Roa, C.Mas-Moruno, *Synergizing topographical and chemical modifications for improved zirconia surfaces: laser patterning and peptidic functionalization.* Poster at the 11th World Biomaterials Congress (Virtual). 11th-15th December 2020.

Table of Contents

Preface I
Abstract III
Resum V
Acknowledgements IX
List of publications and other contributions XI
Table of Contents XIII
Glossary of acronyms XV
Introduction 1
1.1 Zirconia: an overview 3
1.1.1 Brief history of zirconia 3
1.1.2 Classification 5
1.1.3 Yttria-stabilized zirconia (Y-TZP) 6
1.1.4 Stabilization mechanism of yttria 9
1.1.5 Transformation toughening mechanism 11
1.1.6 Low-temperature degradation 13
1.2 Zirconia in restorative dentistry 18
1.2.1 Brief history of dental zirconia 18
1.2.2 Applications in dentistry 19
1.3 Implant biointegration 24
1.3.1 The osteointegration process 24
1.3.2 The role of surface in osteointegration 27
1.4 Surface modification of zirconia based ceramics 34
1.4.1 Topographical modifications 34
1.4.2 Chemical modifications - coatings 50
1.5 State of the art of dual surface modification in zirconia 59
Aim and structure of the thesis 61
2.1 Aim of the thesis 63
2.2 Structure of the thesis 65
Summary of the main results 67
3.1 Effects of the topographical modification techniques 69
3.2 Selection of a topographical modification technique 74
3.3 The combined effects of topography and peptidic biofunctionalization ... 75
Paper I 79
Paper II 91
Paper III 105
Main conclusions and relevance of the findings 125
References 131
Annex A Selection of an optimal surface modification technique 149

Glossary of acronyms

3Y-TZP 3 mol% yttria stabilized tetragonal zirconia polycrystal

ALP Alkaline phosphatase

BIC Bone-implant contact

BMP-2 Bone morphogenetic protein 2

BMSC Bone marrow stromal cells

c- Cubic

CAD Computer-aided design

CAM Computer-aided manufacturing

Ce-TZP Ceria stabilized tetragonal zirconia polycrystal

CLSM Confocal laser scanning microscopy

CN Coordination number

DAPI 4′,6-diamidino-2-phenylindole

DLIP Direct laser interference patterning

DNA Deoxyribonucleic acid

DWIVA Asp-Trp-Ile-Val-Ala tetrapeptide

ECM Extracellular matrix

FBR Foreign body response

FIB Focused ion beam

FPD Fixed partial denture

FSZ Fully stabilized zirconia

GAG Glycosaminoglycans

HA Hydroxyapatite

IGF-1 Insulin-like growth factor 1

IR Infrared

L-DOPA L-3,4-dihydroxyphenylalanine

LTD Low temperature degradation

M Multidirectional

m- Monoclinic

m → t Monoclinic to tetragonal phase transformation

MC3T3 Mouse osteoblast-like cells

Mg-PSZ Magnesia doped partially stabilized zirconia

MSC Mesenchymal stem cell

PBS Phosphate-buffered saline

PCL Polycaprolactone

PEG Polyethylene glycol

PFA Paraformaldehyde

PLGA Poly(D,L-lactic-co-glycolic acid)

PMA Polymethacrylic acid

PSZ Partially stabilized zirconia

PVA Poly(vinyl alcohol)

R_a Average roughness

RGD Arg-Gly-Asp tripeptide

S_a Surface average roughness

SaOS-2 Human sarcoma osteogenic cell

SBF Simulated body fluid

SEM Scanning electron microscopy

SOFC Solid oxide fuel cell

t- Tetragonal

t → m Tetragonal to monoclinic phase transformation

TBC Thermal barrier coating

TEM Transmission electron microscopy

TGF-β Transforming growth factor β

THR Total hip replacement

TZP Tetragonal zirconia polycrystal

U Unidirectional

UV Ultraviolet

V_m Monoclinic volume fraction

XRD X-ray diffraction

Y-TZP Yttria stabilized tetragonal zirconia polycrystal

ZTA Zirconia toughened alumina

Chapter 1
Introduction

1 Introduction

1.1 Zirconia: an overview

1.1.1 Brief history of zirconia

Zirconia (ZrO_2) was first extracted in 1787 from jacinth, a variety of zircon ($ZrSiO_4$) used as a gemstone, by the German chemist Martin Heinrich Klaproth (1743 - 1817). During the following 150 years after its discovery, no technological uses were found for ZrO_2, except for certain niche applications, such as the production of bricks for high temperature applications and its employment in glasses of high index of refraction [1]. This apparent lack of technical uses was mainly due to the impossibility of producing solid and dense parts after sintering.

Pure ZrO_2 is a polymorphic material and can be found in three main crystalline arrangements: monoclinic (*m*), tetragonal (*t*) and cubic (*c*), as displayed in **Figure 1** [2]. At room temperature it presents a *m*-structure and transforms into *t*- when heating above 1170°C. If further heated, it transforms into *c*-phase at 2370°C. After the sintering process, the *t*-phase-containing material is cooled down and reversibly transforms again into *m*-phase. Such transformation is of martensitic nature and is accompanied by a 4 % of volume expansion, which cannot be accommodated by the bulk material and leads to extensive cracking.

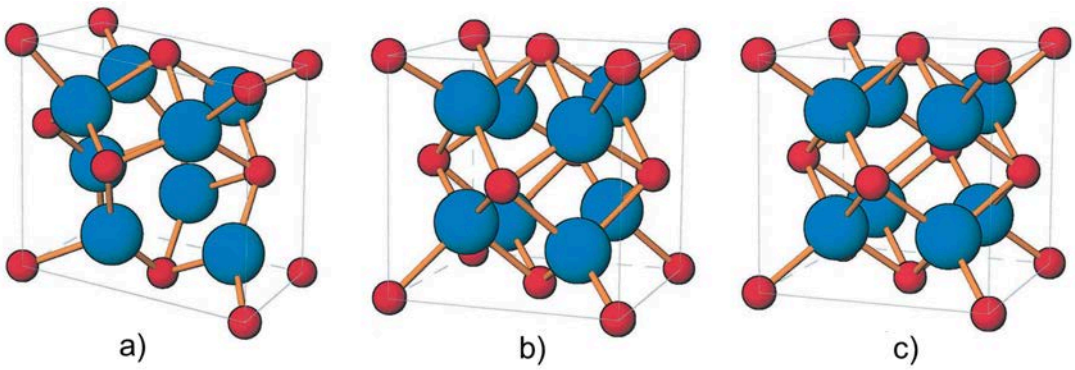

Figure 1 *The three polymorphs of ZrO_2. a) Monoclinic, b) tetragonal and c) cubic. Red atoms correspond to zirconium, while blue atoms correspond to oxygen [2].*

It was not until 1929 that Ruff *et al.* showed that *c*-phase could be stabilized at room temperature by the addition of oxides, such as magnesium oxide (MgO) and calcium oxide (CaO) [3,4], avoiding the detrimental $t \rightarrow m$ phase transformation. Through this method, both *c*- and *t*-phases were retained at room temperature in a metastable form. A material known as partially-stabilized zirconia (PSZ) was produced, consisting on a dispersion of fine *m*-/*t*- precipitates in a *c*-matrix. However, the key discovery for the production of high-strength zirconia was made in 1975 and published in the work *Ceramic steel?* by Garvie *et al.* [5]. Garvie and his coworkers found that the presence of metastable *t*-precipitates in PSZ improved drastically the mechanical properties. It was stated that the increase in strength was mainly due to the energy absorption of the stress-induced $t \rightarrow m$ phase transformation. This mechanism is now known as "transformation toughening" and relies on the phase expansion of the *m*-phase. Stresses at the tip of an advancing crack can destabilize the metastable *t*-phase and trigger the $t \rightarrow m$ phase transformation. The volume change associated to the *m*-phase creates a compressive field that opposes to the opening of the crack, strengthening the material [2], as illustrated in **Figure 2**. In order to take advantage of this mechanism, efforts on the successive years were put on creating fully *t*- phase materials, known as tetragonal zirconia polycrystals (TZP) [6], and first developed by Rieth *et al.* [7] and by Gupta *et al.* [8].

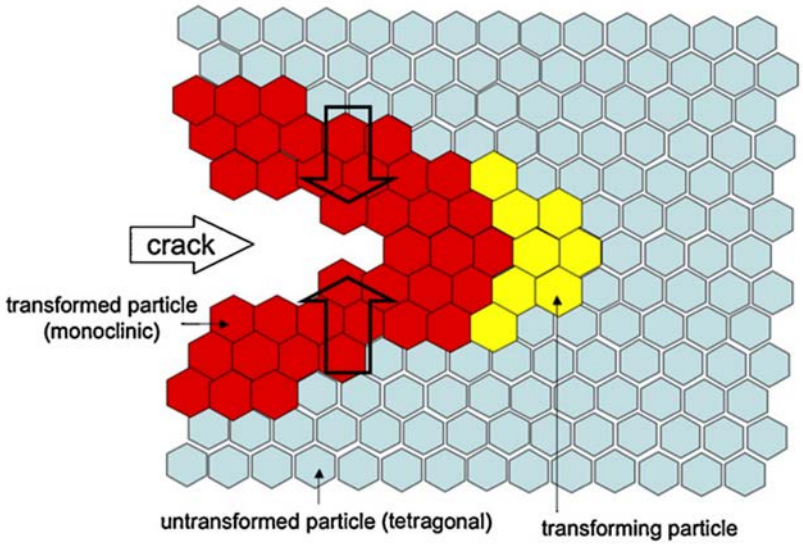

Figure 2 *Transformation toughening mechanism. Stresses at the tip of the crack trigger the t- to m-phase transformation. The volume increase of the transformed material closes the crack, hampering its propagation [9].*

1.1.2 Classification

According to its stabilization degree, several types of microstructures can be obtained:

- **Fully stabilized zirconia (FSZ)**: such materials are constituted by only *c*-zirconia. They are obtained by employing a high concentration of stabilizers. Their applications include, among others, the production of refractory materials, solid oxide fuel cells (SOFCs) or oxygen sensors.
- **Partially stabilized zirconia (PSZ)**: they are constituted by a *c*-matrix with a dispersion of nano-sized *t*-precipitates. They can be obtained by doping with MgO (as shown in **Figure 3a**) or CaO.
- **Tetragonal zirconia polycrystals (TZP)**: they consist in a stabilized *t*-phase material, which can contain a certain amount of *c*-phase, depending on the stabilizer concentration. They possess high strength and toughness. The most common stabilizers to obtain such microstructures are yttrium oxide or yttria (Y_2O_3, see **Figure 3b**) and cerium oxide or ceria (CeO_2).

In addition, combinations with other ceramics are possible, mainly with alumina (Al_2O_3). For example, zirconia toughened alumina (ZTA) consists in an Al_2O_3 matrix embedded with stabilized zirconia particles, as depicted in. **Figure 3c.**

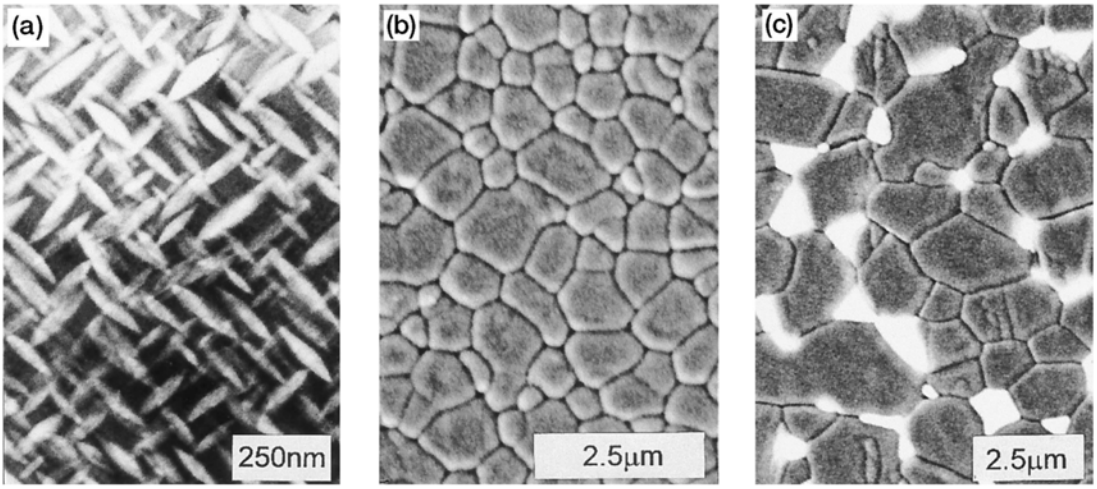

Figure 3 *Microstructures of different zirconia materials. a) Transmission electron microscopy (TEM) micrograph of Mg-PSZ. t-precipitates can be observed. Scanning electron microscopy (SEM) micrographs of b) Y-TZP and c) ZTA. In the latter, ZrO_2 grains appear bright while Al_2O_3 grains are darker.*

1.1.3 Yttria-stabilized zirconia (Y-TZP)

Fully fine-grained *t*-microstructures can be obtained by the addition of Y_2O_3 (Y-TZP), and have become one of the most common zirconia formulations due to its excellent mechanical properties. Among the different stabilizers available (e.g. MgO, CaO, Y_2O_3, CeO_2, etc. [10]), Y-TZP materials present a remarkable combination of strength and fracture toughness (see **Figure 4** and **Table 1**).

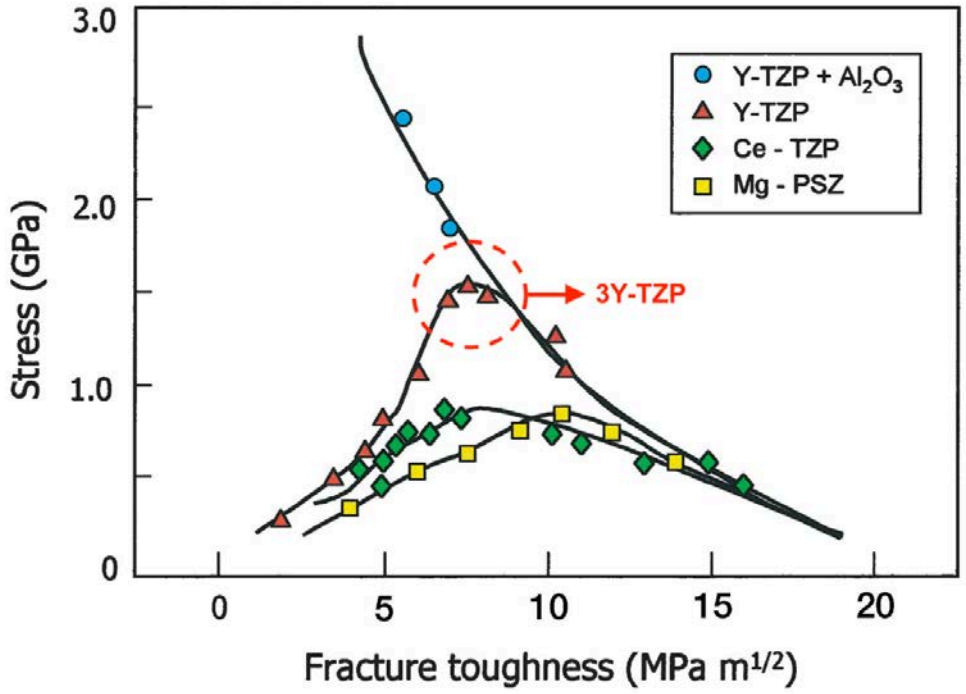

Figure 4 *Strength versus fracture toughness in stabilized TZP and PSZ materials. Among the different TZP ceramics (excluding combinations with Al_2O_3), Y-TZP presents the best combination of properties at Y_2O_3 contents of around 3 mol% (highlighted with a red circle in the plot) [2].*

Table 1 *Mechanical properties of different biomedical ceramics, including different zirconia compositions. The material labeled as "Zirconia" is made from 3Y-TZP. The material labeled as A10Z0Y, corresponds to an alumina matrix with 10 vol% of pure zirconia [11].*

Material	**Toughness (K_{Ic}, MPa·m$^{1/2}$)**	**Strength (MPa)**	**Vickers hardness**
Alumina	4.2	400-600	1800-2000
Zirconia	5.4	1000	1200-1300
A10Z0Y	5.8	700-900	1800
Hydroxyapatite	0.9	50-60	500
Tricalcium phosphate	1.3	50-60	900
Mg-PSZ	8	600	1000
12Ce-TZP	7.8	700	1000-1100
Micro-nano-alumina-zirconia	6	600	1800
Nano-nano-Ce-TZP-alumina	8.4	900	1300

Among its properties, Y-TZP gathers not only high strength and fracture toughness, but also wear resistance, chemical inertness, ionic conductivity at high temperatures, refractoriness as well as specific optical properties in its cubic form. In this regard, Y-TZP zirconia has found a place in several industrial fields and it can be employed to produce [12]:

- **Pumping components** subjected to high stress, wear and corrosion, such as shafts or thrust plates. These pumps are commonly employed as sludge pumps or in the chemical industry. Ceramic elements such as valves or nozzles are also common in the petrochemical industry.
- **Blade edges**. Thanks to its mechanical properties zirconia elements can retain edges for longer times as compared to conventional steel blades. It is employed in the paper or medical industry, as well as for cutting Kevlar fibers.
- **Parts subjected to intense wear** in the mechanical industry, such as dies for metal forming and extrusion and parts for the canning industry as well as nozzles for slurry and metal handling.
- **Prostheses** in the medical industry including ball heads for total hip replacement, knee replacements or dental restorations. Its inertness and low friction make it a good candidate to substitute metallic components.
- **Refractory components** in the form of fibers, panels and powders for ultra-high temperature applications.
- **Thermal barrier coatings** (TBCs) in engine blades, due to its thermal insulation as well as relatively high thermal expansion coefficient. It allows for engines to work at higher temperatures, increasing efficiency.
- **Electrolytes** for solid oxide fuel cells (SOFCs) and oxygen sensors, due to its ionic conductivity at high temperature (above 600°C).
- **Gemstones** can be produced of *c*-ZrO_2, as it presents both a refractive index and dispersion similar to diamond. Colored gemstones can be produced by adding rare earth or transition metal oxides.

Pictures depicting some of the abovementioned applications are displayed in **Figure 5**.

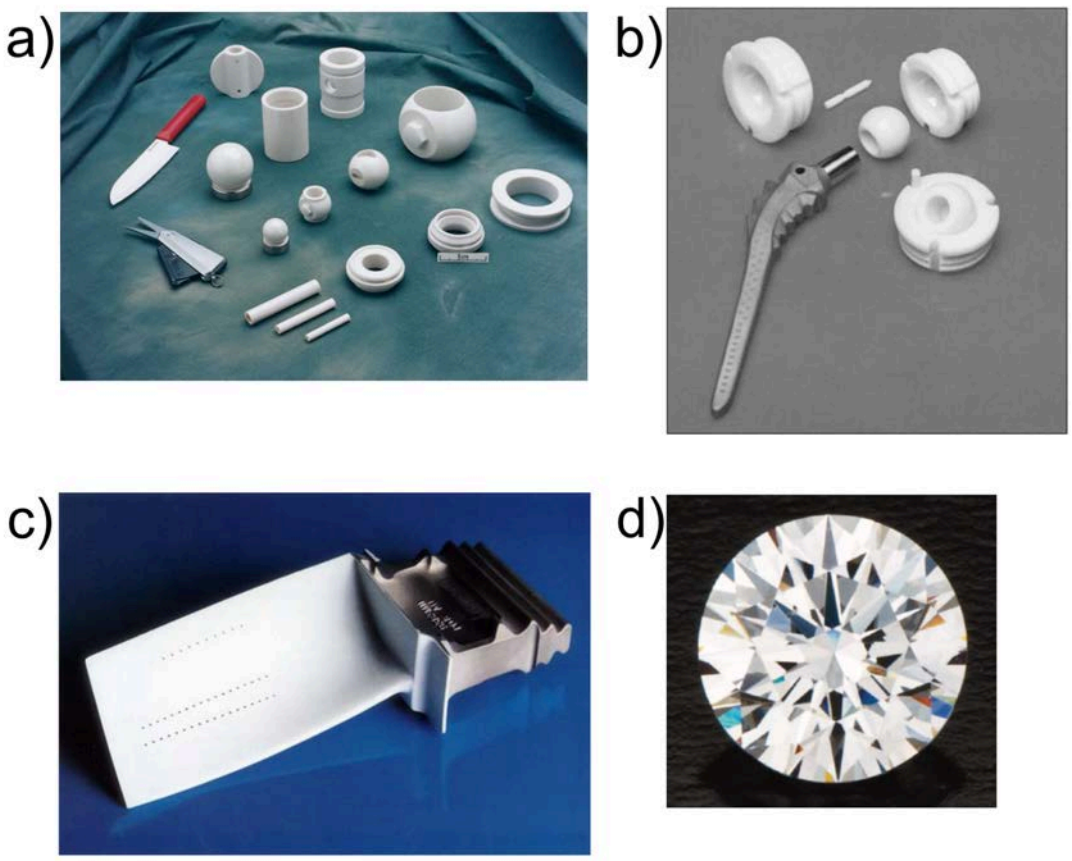

Figure 5 *Zirconia applications. a) Industrial parts such as knives, scissors, valves and other components for the metal processing industry, including rollers for closing metal cans and a wire guide [2]. b) Total hip replacement made of ceramic components [13]. c) TBC on a high pressure engine blade [14]. d) c-zirconia gem [15].*

1.1.4 Stabilization mechanism of yttria

Yttria can stabilize the *t*- as well as the *c*-phases at room temperature through the generation of oxygen vacancies. In brief, the nature of the Zr-O bond favors a coordination number (CN) of 7. Thus, pure zirconia presents a *m*-structure at room temperature. When heated at higher temperatures oxygen ion vacancies are created, lowering the effective CN. In order to keep it as close to 7 as possible, the crystal structure transforms into *t*-phase, with a theoretical CN of 8. Due to the presence of oxygen vacancies, the effective CN decreases, between 7 and 8, and the *t*-phase becomes the most favored crystalline arrangement [16]. The

same effect can be obtained at low temperature through the addition of trivalent cations such as Y^{3+}, which introduce enough vacancies to stabilize the *t*- and the *c*-phases (see **Figure 6**). In this way, fully *t*-phase materials can be obtained with the addition of Y_2O_3. Depending on the stabilizer content, the *t*-, the *c*- or a combination of both phases can be present in the resulting materials in a metastable form, as shown in the zirconia-yttria phase diagram of **Figure 7**.

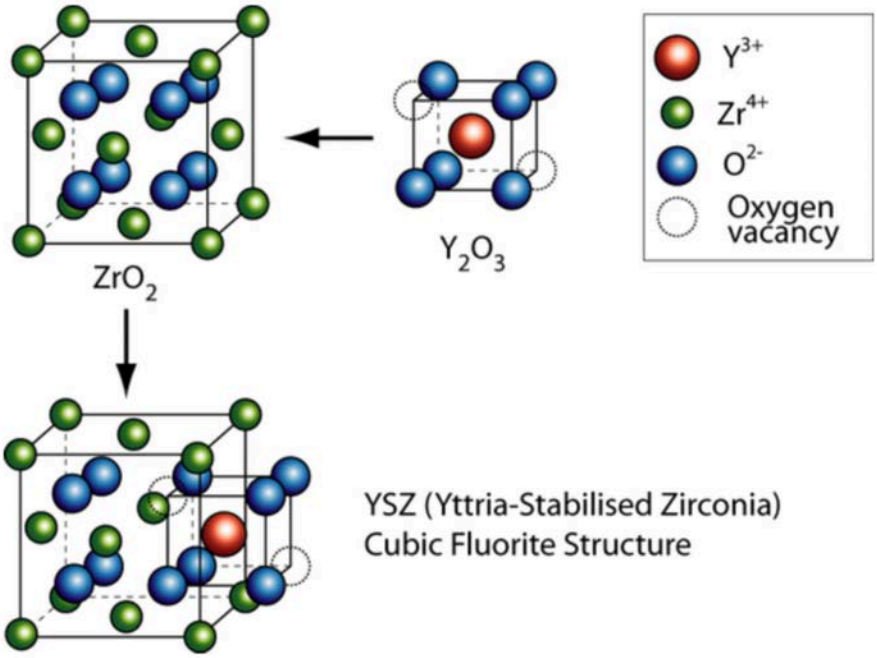

Figure 6 *Formation of oxygen vacancies in the ZrO_2 structure by doping with Y_2O_3 [17].*

One of the most common formulations to optimize mechanical properties is 3 mol% yttria doped zirconia (3Y-TZP). As observed in the diagram (**Figure 7**) and explained in detail by Chevalier *et al.* [18], at sintering temperatures (between 1400 - 1500°C) 3Y-TZP is constituted by a majority of *t*-phase, with small amounts of *c*-phase. At such temperatures diffusion kinetics are slow and after short heat treatments, no yttria partitioning between the *t*- and *c*-phases occur. Thus, and as depicted with a red arrow in the phase diagram (**Figure 7**), after cooling down both constitutive phases retain a similar amount of yttria and remain metastable, below the metastable $T_o(t/m)$ boundary. In such conditions, if higher Y_2O_3 contents were used (in blue), the obtained *t*-phase could fall above

the $T_o(t/m)$ boundary, resulting in a low-transformable *t*-phase, with higher *c*-content. In contrast, if less Y_2O_3 were employed (in purple), the obtained *t*-phase could not be stable enough and transform to *m*-phase during cooling.

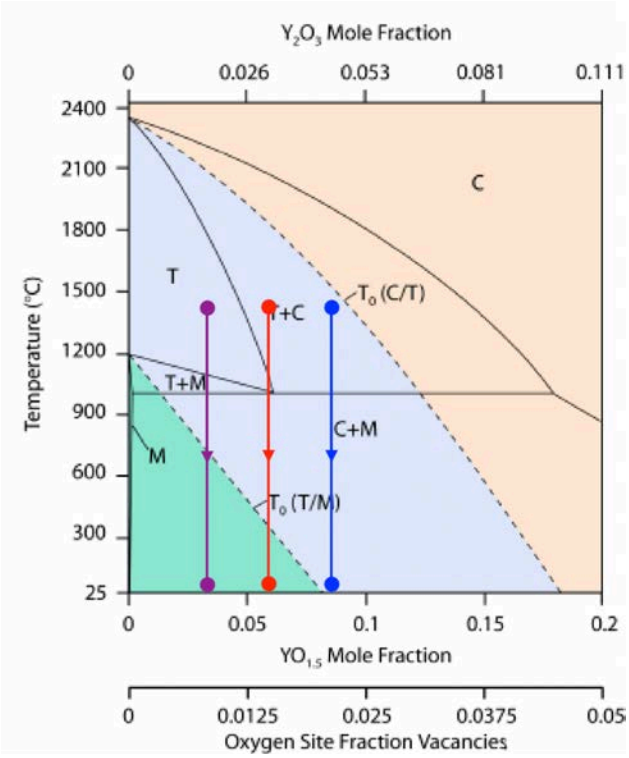

Figure 7 *ZrO_2-Y_2O_3 phase diagram. Note that $T_o(t/m)$ indicates the metastability boundary of the t-phase. In the blue area the t-phase is stable, while in the green zone it is metastable [18].*

1.1.5 Transformation toughening mechanism

As previously mentioned, the metastable nature of the stabilized *t*-phase, combined with the volume change of the $t \rightarrow m$ phase transformation, constitutes the basis of the toughening mechanism. However, it is also responsible for the generation of micro-cracks, which can be deleterious in certain cases. This aspect will be covered with further detail in ***section 1.1.6***.

The $t \rightarrow m$ phase transformation is a martensitic transformation, i.e. a diffusionless process involving a coordinated motion of the atoms in the lattice over a distance less than an atomic diameter, resulting in a macroscopic shape

change. As depicted in **Figure 8** the first step consists in the nucleation of a martensite plate, with a shear component of ~0.16 and a volumetric change of ~0.045 [2]. If constraint in a bulk material (i.e. not in the surface), the stresses derived from the shear component induce the formation of a second variant with an opposed shear strain, cancelling the shear effects of the first variant. This phase transformation process is autocatalytic and proceeds with the formation of twin related variants. The result is a shear component near to zero, and a net volume change around ~0.045.

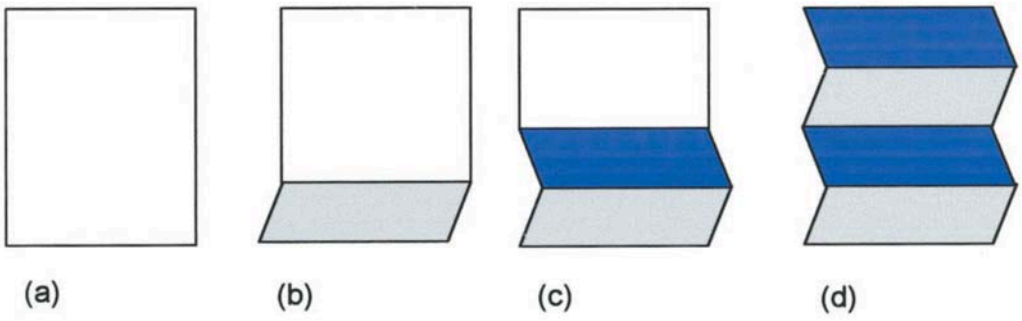

Figure 8 *$t \rightarrow m$ phase transformation process. a) t- material. b) Transformation starts and a m- lath nucleates. c) Stresses originated in the surrounding matrix promote the formation of a second twin-related variant, with an opposed shear component. d) Transformation further proceeds [2].*

As described by Lange [19], from a thermodynamical point of view the condition for transformation can be written as:

$$\Delta G_{t-m} = \Delta G_c + \Delta U_{SE} + \Delta U_S \qquad \textit{Eq. 1}$$

where ΔG_{t-m} is the change in total free energy of the $t \rightarrow m$ phase transformation. When it becomes negative, *t*- particles are unstable and may transform. ΔG_c is the difference in chemical free energy between the *t*- and *m*- phases. Below the $T_o(t/m)$ temperature, $\Delta G_c < 0$ (see **Figure 7**). It depends on both temperature and stabilizer content. Thus, in order to have a *t*- particle $|\Delta G_c| < \Delta U_{SE} + \Delta U_S$. The term ΔU_{SE} is > 0 and corresponds to the elastic strain

energy associated to the phase change of the particle. It depends on the stiffness of the matrix, size and shape of the particle and surrounding stresses. In this sense, hydrostatic tensile stresses reduce the value of this variable, favoring transformation. On the contrary, compressive stresses increase its value, stabilizing the *t*- particle. Finally, ΔU_S is also > 0 and refers to the change in energy associated to the surface of the particle, such as crack generation.

With the above considerations, transformation toughening can be explained, as follows. In the front of an advancing crack, shear and tensile stresses reduce ΔU_{SE} enough so that ΔG_{t-m} becomes negative and *t*- particles become unstable. The $t \rightarrow m$ transformation is triggered and the volume expansion of the material at the crack tip produces a compressive stress field, opposing to crack propagation. This mechanism has been presented in ***section 1.1.1*** and is depicted in **Figure 2**. Thus, transformation toughening is able to reduce the stress intensity factor at the crack tip [18,20], increasing fracture toughness:

$$K_{Itip} = K_I - K_{Ish} \qquad Eq.\ 2$$

where K_I is the stress intensity factor applied by external forces; K_{Ish} is the stress shielding effect due to the transformation toughening mechanism; and K_{Itip} is the real stress intensity factor at the crack tip.

1.1.6 Low-temperature degradation

As explained previously in **section1.1.5**, one of the consequences of the *t*-phase metastability is the transformation toughening mechanism. However, it also constitutes the basis of a deleterious process, known as low-temperature degradation (LTD), ageing or hydrothermal degradation.

This process was first reported in 1981 by Kobayashi [21] and has been described by other authors [22–28]. In humid environments, a progressive and

uncontrolled transformation of the grains in the surface from the *t*- to the *m*-phase is triggered. This transformation is associated to the generation of micro-cracks and can advance inside the material until the catastrophic failure of the specimen. Yoshimura [22] described its main features as:

- The degradation occurs significantly at temperatures between 200 and 300°C in air. However, it must be noted that it can also occur at body temperature after prolonged periods of time, with a special relevance in biomedical implants [29].
- Degradation starts in the surface and progresses to the bulk.
- The volume change associated to the $t \rightarrow m$ phase transformation produces macro- and micro-cracking.
- Water and water vapor accelerate the $t \rightarrow m$ phase transformation.
- By increasing dopant concentration or by reducing grain size, the process can be delayed.

The exact mechanisms by which water molecules can destabilize the *t*-phase are still debated, but there is a consensus about the important role played by oxygen vacancies. In humid environments, water–derived species (OH^-) occupy the oxygen vacancies of the surface, reducing its number and introducing stresses in the lattice [30,31]. Schubert and Frey [32] found a contraction in the lattice after LTD, which introduced tensile stresses of around 300-500 MPa, destabilizing the *t*-phase. According to the authors, the introduction of OH^- was the responsible of this contraction, with oxygen atoms occupying the vacancies and hydrogen atoms located at interstitial sites. However, more recently, Duong *et al.* [33] found that moisture diffusion occurs by parallel but independent H^+ and O^{2-} diffusion. What is clear, is that diffusion of such species can destabilize the *t*-phase on the surface and that this process can continue inside the bulk material. The series of events are as follow (see **Figure 9**):

- First, an *m*-phase lath nucleates at the surface of the most unstable grain (i.e. larger grains, grains with lower Y_2O_3 content, etc.) and it propagates

inside the grain by self-accommodated variants, as described in **Figure 8**. This initial stage is shown in **Figure 9a**.

- Martensite (*m*-) plates reaching the grain boundaries generate micro-cracks as well as stresses at the neighboring grains, favoring the creation of new plates on the surrounding grains (see **Figure 9b**). This is known as autocatalytic propagation [27]. In addition, the net volume increase of the transformed particles generates additional stresses and micro-cracks. Thus, *m*-phase does not appear homogeneously throughout the surface, but nucleates in specific grains and propagate, by a nucleation-and-growth mechanism.
- Water can penetrate through micro-cracks, promoting the degradation of deeper layers in combination with the autocatalytic propagation. Pull-out of superficial grains can be observed. Transformation advances to deeper layers weakening the material, until final failure happens as depicted in **Figure 9c**.

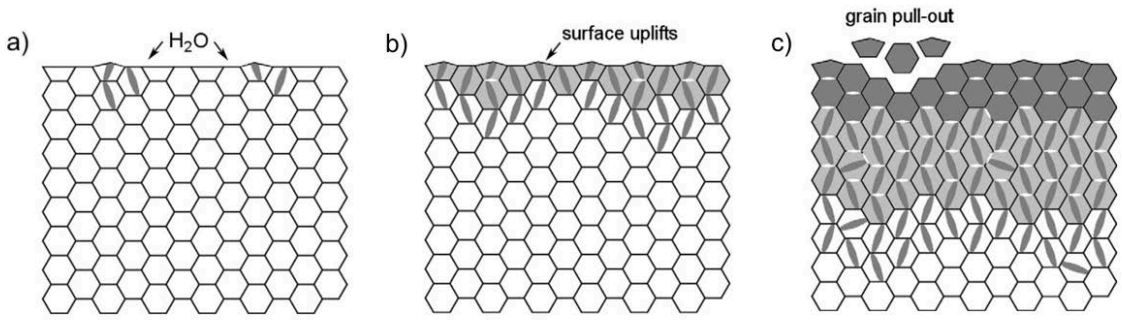

Figure 9 *Schematic representation of the LTD process. a) m-phase nucleates on the surface. b) Once the surface is transformed, the process extends to deeper layers. At this point, micro-cracks and grain uplifts due to volume expansion are observed on the surface. c) Transformation propagates inside the bulk. The surface is totally transformed and extensive grain pull-out can be observed as well as micro-cracking. Water can penetrate inside the material, assisting degradation. Mechanical properties of the surface get severely affected [27].*

The main features of the subsurface damage after LTD have been characterized in detail. Jiménez-Piqué *et al.* [34] studied the network of micro-cracks after degradation. They found that the cracks were mostly parallel to the surface and that they displayed a density gradient from the surface. A 3D focused Ion beam (FIB) tomography reconstruction is displayed in **Figure 10a**, where a small volume of the degraded layer is shown. The crack network (in purple) induced during the LTD process is clearly evident.

In addition, Jiménez-Piqué *et al.* concluded that the decrease in elastic modulus of the degraded layer was not due to the increase in *m*-content, but rather to the presence of the micro-cracks, which can be observed in **Figure 10b**.

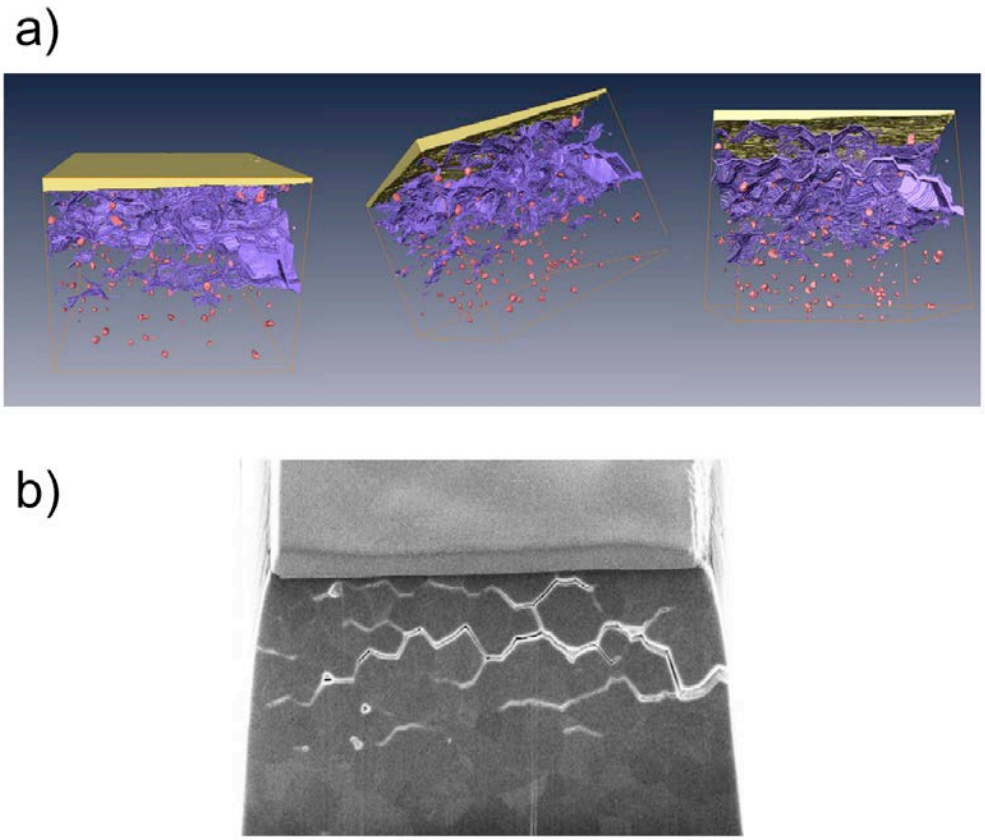

Figure 10 *a) Three perspectives of the reconstructed network of micro-cracks (in purple) under the surface after LTD process. Yellow material corresponds to the protective platinum layer deposited onto the surface. Red dots correspond to pores. b) A FIB cross-section showing the crack network [34].*

LTD is of especial relevance in the biomedical field, where the lifespan of implants can be reduced due to the moisture of the biological environment [29]. In 2001 a series of failures in 3Y-TZP hip replacements (i.e. femoral heads), resulted in drastic decrease in the use of 3Y-TZP for orthopedic applications [24]. Although the failures were mainly related to an increase in porosity due to a change in the sintering process, an increase in the $t \rightarrow m$ phase transformation was identified in the porous regions, playing a secondary role in the deterioration of properties [35]. Since then, efforts have been made to understand, control and avoid LTD. In order to evaluate the behavior of a ceramic component after LTD, accelerated tests can be carried in water steam. In this regard, the degradation process kinetics can be described by the Mehl-Avrami-Johnson equation [36], as follows:

$$f_m = 1 - exp[-(bt)^n] \qquad Eq.\ 3$$

where f_m is the monoclinic volume fraction, t is the degradation time, b is an activation energy term ($b = b_o\ exp\ [-\frac{Q}{RT}]$) and n an exponent related to the nucleation and growth conditions. At higher temperatures, reaction kinetics are faster. Thus, by performing experiments at such temperatures, the relevant parameters can be extracted, and kinetics extrapolated at room temperature. Ageing kinetics of 3Y-TZP are typically determined in water steam at 134°C and 2 bar of pressure, with 1 hour of degradation corresponding to 3-4 years *in vivo*. However, as the particular microstructural features of each material affect the degradation kinetics, for accurate results the correct determination of b and n should be carried out [23,37].

1.2 Zirconia in restorative dentistry

1.2.1 Brief history of dental zirconia

The loss of teeth, particularly anterior teeth, creates not only a functional impairment, but also psychological and social problems, due to its aesthetic role. Before the advent of modern artificial implants, it was common to use natural materials to replace missing teeth, such as teeth from human donors, carved animal teeth, ivory, wood or bone. These solutions were unstable in human oral environment, presenting several disadvantages, including change in color and unpleasant odor. In 1774, the Parisian apothecary Alexis Duchâteau and the dentist Nicholas Dubois de Chémant made the first successful porcelain denture. Since then and during the following two centuries, a continuous improvement was made in ceramic dental materials [38,39].

The first paper regarding a biomedical application for zirconia was published in 1969 by Helmer and Driskell [40], and it was not until 1988 when Christel *et al.* suggested the use of zirconia to produce femoral heads for total hip replacement (THR) [41]. Unfortunately, as noted above, after a LTD-related failure of around 400 zirconia ball heads in 2001, the use of zirconia in the biomedical field suffered a drastic decrease [24]. However, thanks to the developments made in the 90s, the dental community showed a special interest in the material due to its excellent mechanical properties (strength, hardness, wear resistance and fracture toughness), biocompatibility and its good aesthetic appearance. These properties, which make it suitable in dental restorations, depend on: grain size, presence of an intergranulary glassy phase, stability of the *t*-phase, porosity, elastic modulus and thermal expansion mismatch between components. In this sense, Y-TZP was introduced to produce several restorations, including fixed partial dentures (FPD), implants, abutments, post and cores, etc. Thus, during the last twenty years TZP-based ceramics have attracted an increasing attention from the dental community, with several products in the market and an evolving composition and processing techniques to match market needs [42,43] (see **Table 2**).

Table 2 *Listing of some representative TZP formulations in the dental market* [44].

Classification	Generation	Material name	Manufacturer	Composition
Y-TZP	1	Lava Frame	3M ESPE	3Y-TZP
		Zenostar MO	Wieland Dental	3Y-TZP
	2	Lava Plus	3M ESPE	3Y-TZP
		Zenostar T	Wieland Dental	3Y-TZP
	3	Lava Esthetic	3M ESPE	5Y-PSZ
		Zenostar MT	Wieland dental	4Y-PSZ
Y-TZP/ Al_2O_3	-	ZirTough	Kuraray-Noritake	Y-TZP/4 mass% Al_2O_3
Ce-TZP/ Al_2O_3	-	NANOZR	Panasonic	70 vol.% 10Ce-TZP/30 vol.% Al_2O_3

Although most of the commercial products are based on Y-TZP, Ce-TZP/Al_2O_3 composites are also available. During the short live of zirconia in the dental field, three generations of materials in terms of composition and powder processing have been developed. After a first generation of Y-TZP materials (containing 0.25 wt% alumina, as a sintering aid) with excellent mechanical properties, a second generation of zirconia was developed, with lower Al_2O_3 content and higher sintering temperatures in order to improve translucency. A third generation has recently been developed with a higher Y_2O_3 content (4-5 mol%), which improved translucency by increasing its *c*-phase content, at the expense of mechanical properties [43,44]. As the interest in such materials grow, new formulations and processing techniques will arise, with the aim at obtaining high strength, translucent and LTD-resistant materials.

1.2.2 Applications in dentistry

Several dental components are produced nowadays with Y-TZP, including crowns, fixed partial dentures, posts and cores, implants and abutments. The manufacturing process is based on computer-aided design/computer-aided

manufacturing (CAD/CAM) technology, allowing to produce both prefabricated and custom-made components. Regarding the latter type and depending on the component, a personalized computer design can be made based on three dimensional (3D) scans of the patient's defect. Two approaches can be followed on the manufacturing process: hard and soft machining [43,45–47].

- In hard machining, a fully sintered Y-TZP block is milled down to the final shape with diamond tools. Such approach involves high tool wear and costs, is time-consuming and requires robust milling systems.
- On the other hand, soft machining is the most common technique, and is based on the milling of pre-sintered blocks of zirconia with tungsten carbide burs. At this point, binders of the original powders have already been burnt and the Y-TZP block is minimally hardened by the pre-sintering treatment. The machined part is enlarged by a 20-25% relative to its final dimensions, as during the final sintering step it suffers a linear shrinkage, which may involve the need of final shape corrections after the heat treatment.

Regardless of the manufacturing process, the final material must meet some general requirements, which are listed in **Table 3**.

Table 3 *Engineering guides for manufacturing zirconia-based ceramics for dental applications [37].*

Property	**Unit**	**Requirement**
Density	% of theoretical density	> 99%
Stabilizer content: Y_2O_3	mol%	3 < x < 8
Grain size	μm	GS < 0.3
Residual stress	MPa	σ < 300 (tensile)
Monoclinic content	Volume fraction to total zirconia	
Initial		Negligible
After aging test (134°C, 2 bar H_2O, 1 h)		Negligible
Strength in 4-point bending	MPa	
Initial		600
After aging		600

The following paragraphs include a description of the different dental prostheses that can be produced of zirconia-based ceramic materials:

Crowns: crowns are used when teeth present functional or aesthetic defects in size, shape, color or function. They consist on a "cap" that covers the tooth. They can also be placed on the top of an implant-abutment system in order to replace a tooth. As zirconia presents a white color and opacity that does not fully match the natural look of a tooth, they can be stained before sintering and veneered with feldspathic porcelain. In posterior crowns, however, due to the lower aesthetic requirements and the higher loads monolithic crowns can be placed, avoiding the use of veneers, which can suffer from chipping. Surface mechanical pre-treatments such as grinding or sandblasting may be applied to the surfaces in order to improve adhesion of the veneer and/or the adhesion of the crown to the underlying structures. Other alternatives to zirconia are full metallic crowns (with low aesthetics) or porcelain fused to metal.

Fixed partial dentures: fixed partial dentures (FPDs) are meant to replace several missing teeth and are permanently fixed to adjacent teeth or implants. Its structure (see **Figure 11**) is similar to a "bridge" lying over two "pillars". The "pillars" can be the adjacent teeth or dental implants (abutments). The "bridge" consists on the retainers (that unite the bridge to the underlying teeth or abutment), the pontic (the suspended part of the bridge) and the connector (that unites retainer and pontic) [48]. When a force from biting is applied to the pontic, the load is transmitted to the connector, retainer and finally to the abutment and the surrounding bone structure. Similarly to crowns, chipping of the veneering is the major problem that may occur over time [45].

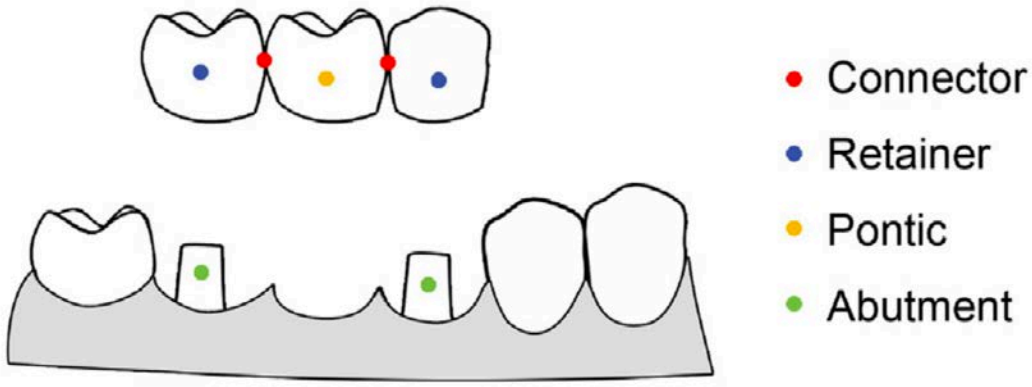

Figure 11 *Representation of a fixed partial denture and its different elements [48].*

Posts and cores: sometimes, when a crown must be placed, the underlying teeth structure is severely damaged and cannot retain the crown. However, the remaining root structure can still provide a substrate to retain the crown by using a post and core. After preparation of the root channel, a post is inserted in it, and the core placed on the top of the post (see **Figure 12a**). The core can then be used as a support for the crown [48].

Implants and abutments: a dental implant is an artificial tooth that is inserted into the jawbone to serve as an anchor for orthodontic prostheses, such as dentures or crowns [49]. They are screwed or plugged into the jawbone and get bond to the surrounding bone. The healing process can take from three to six months, resulting in a stable load-bearing unit. On the top of the implant, the abutment serves as a connecting element to the suprastructure, which may include a crown or a FPD, as shown in **Figure 12b**. The abutment may be included to the implant as a single-piece, or screwed into it. Finally, the suprastructure may be screwed, cemented or bonded to the abutment. Currently, two materials can be chosen for both implants and abutments: titanium and zirconia. Although both of them display excellent survival rates, some disadvantages of titanium include possible accumulation of titanium particles in surrounding tissues [50], cellular sensitization [51], and a

greyish color that can carry aesthetic consequences when visible or covered by a thin layer of soft tissue [52].

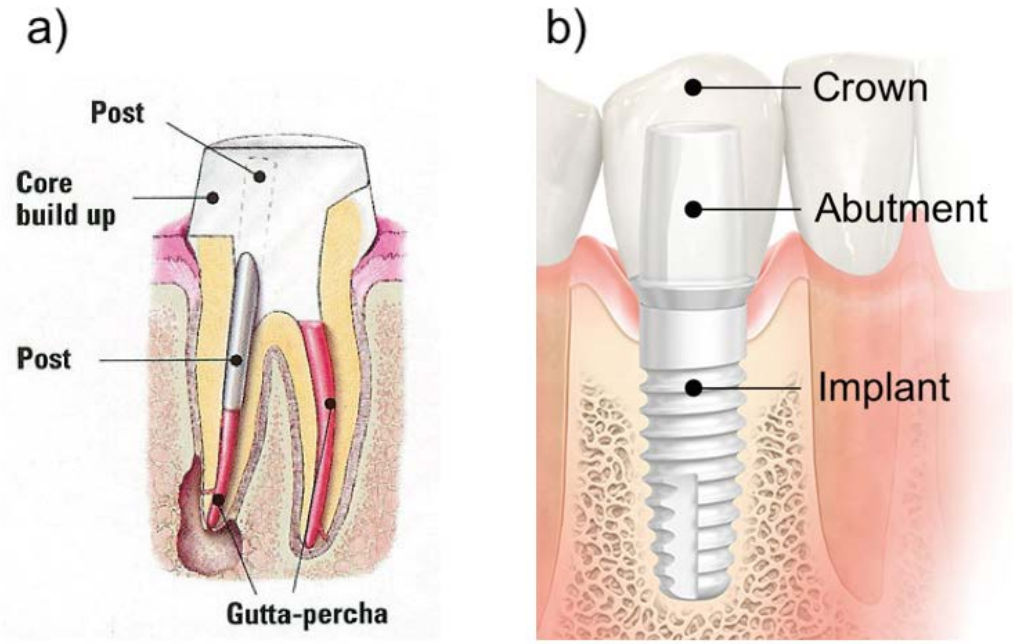

Figure 12 *a) Representation of a post and core restoration. As depicted, the post is inserted in the root channel, which has been previously prepared and sealed (gutta-percha). The core is placed on the top, acting as a support for a crown* [53]*. b) Structure of a zirconia dental implant. Modified from* [54]*.*

1.3 Implant biointegration

1.3.1 The osteointegration process

After an implant is placed, the success of the procedure lies on the subsequent healing process, which dictates the quality of bone anchorage and thus, the load bearing capacity of the implant. A simplified description of the process towards a successful or a failed osteointegration is schematized in **Figure 13.** As reviewed by Gittens *et al.* [55], the first step when the implant is placed (**Figure 13a**) is the adsorption of water molecules, proteins and lipids from blood (**Figure 13b**). The exact composition of this layer depends on the surface chemical properties. In this regard, the first thing that cells "feel" when come in contact with the surface is the layer of adhered proteins. Some of these proteins are involved in cell attachment (e.g. fibronectin or vitronectin) or in the inflammatory response (e.g. fibrinogen).

Next, the blood platelets arriving to the site release their inner content and promote the formation of fibrin clots (**Figure 13c**). This network is used by different cells to reach the surface. Some of the first cells to arrive the site belong to the immune system (e.g. neutrophils and macrophages) and clean the zone from pathogens and necrotic tissue. Another type of cells that reach the surface are mesenchymal stem cells (MSCs) (**Figure 13e**). There, they are exposed to inflammatory cytokines as well as growth factors, which are crucial for the following steps in tissue repair. MSCs have the ability to differentiate into several cell types including osteoblasts, chondrocytes and fibroblasts. The biochemical environment at the injured site, including the growth factors and other cytokines entrapped in the fibrin clot (**Figure 13d**), drive the differentiation of MSCs into osteoblasts (**Figure 13f, left side**).

The newly differentiated osteoblasts start laying down a non-collagenous variety of proteins (**Figure 13g, left side**) that initiate mineralization (**Figure 13h, left side**) and thus, bone formation. Such layer is made from different proteins, such as bone sialoprotein, osteopontin and proteoglycans, and further promotes

osteoblast recruitment and maturation. Further processes are needed for a proper bone formation, including bone remodeling by osteoclasts, which resorb the new bone in order to eliminate micro-cracks and prepare the surface for new bone formation.

Apart from the biochemical stimuli from the environment surrounding the injury, other factors play an important role in the osteodifferentiation of MSCs and in the bone forming process. In particular, the physical, chemical and mechanical properties of the biomaterial surface are key factors for achieving a proper osteointegration.

In this sense, when the properties of the surface are not entirely favorable, cells can form a layer of fibrous tissue surrounding the implant. Briefly, if the differentiation of osteoblasts at the tissue-material interface fails (**Figure 13f, right side**), acute inflammation is followed by chronic inflammation. At this point, monocytes that have migrated to the surface and differentiated into macrophages, try to phagocytize and digest the implant (**Figure 13g, right side**). This process constitutes a mechanism of defense from the body to an invading, non-recognized agent. When the attempt to degrade the material fails, macrophages fuse together into multinucleated giant cells. These giant cells send signals to recruit fibroblasts (**Figure 13h, right side**), which deposit a collagenous layer that encapsulates the implant (**Figure 13I, right side**). In this situation, there is no close contact between bone and the implant's surface. This mechanism constitutes a foreign body response (FBR) [56]. The intermediate collagenous layer formed during this process is responsible for implant micro-motion and is accompanied by inflammation and bone degradation, which finally leads to implant failure.

A correct design of the implant's surface properties can avoid the detrimental effects of the FBR and ensure a proper osteointegration. This aspect is covered in detail in **section 1.3.2**.

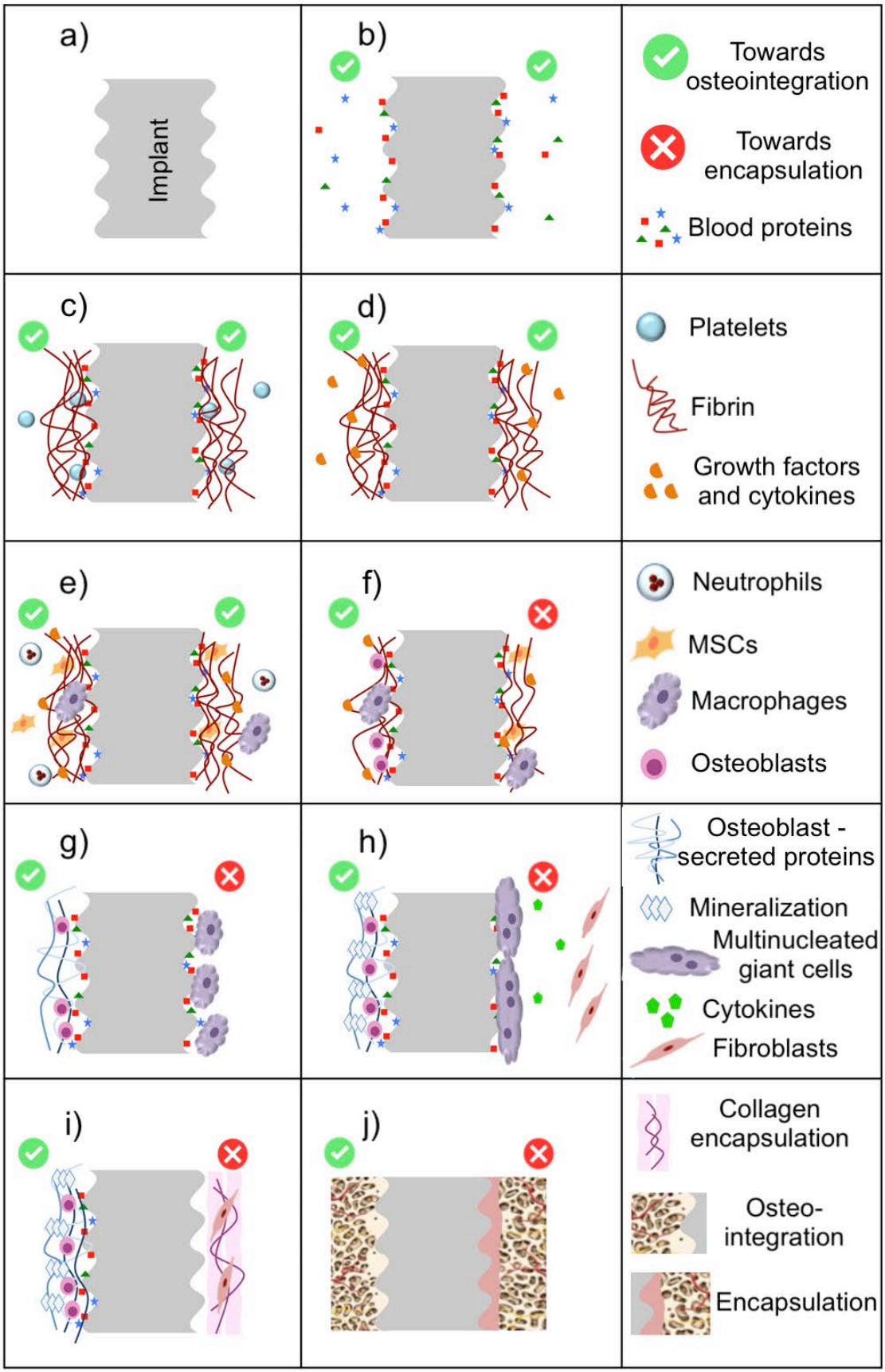
a)
Implant
b)
Towards osteointegration
Towards encapsulation
Blood proteins
c)
d)
Platelets
Fibrin
Growth factors and cytokines
e)
f)
Neutrophils
MSCs
Macrophages
Osteoblasts
g)
h)
Osteoblast - secreted proteins
Mineralization
Multinucleated giant cells
Cytokines
Fibroblasts
i)
j)
Collagen encapsulation
Osteo-integration
Encapsulation

Figure 13 *Body reactions after an implant placement: osteointegration or encapsulation. a) The implant is placed, b) blood proteins adsorb to the surface, c) platelets produce a fibrin clot, d) growth factors and cytokines get entrapped in the fibrin mesh, e) neutrophils and macrophages reach the surface, as well as MSCs. f) Body reaction can be driven to osteointegration (left side) or encapsulation (right side) depending on the surface properties. Left side, MSCs differentiate into osteoblasts. Right side, MSCs do not differentiate or differentiate into other lineages. g) Left side, osteoblasts produce a layer of proteins. Right side, chronic inflammation. Macrophages try to degrade the implant. h) Left side, the layer of osteoblast-secreted proteins gets mineralized. New bone is produced. Right side, macrophages cannot digest the implant and secrete cytokines to recruit fibroblasts. i) Left side, new bone grows at the surface. Right side, fibroblasts produce a collagenous layer encapsulating the implant. j) Left side, direct implant-to-bone contact, osteointegration achieved. Right side, there is a fibrous layer between bone and the implant, osteointegration not achieved. The implant will fail.*

1.3.2 The role of surface in osteointegration

Cells can sense the properties of the surfaces in which they grow. This ability is of special relevance, as the cues provided by the substrate govern to a large extent the correct function and the fate of cells. These properties include both chemical and physical features.

From the **chemical point of view**, properties such as *surface energy, charge, and wettability* can affect cellular behavior *per se* [57,58]. However, the larger influence they have on cells is due to their effect on the layer of adsorbed proteins. As represented in **Figure 14**, when a biomaterial is placed in the body, the surface is immediately coated with proteins present in the biological fluids, and cells initially respond to this layer, rather than to the material itself [59,60].

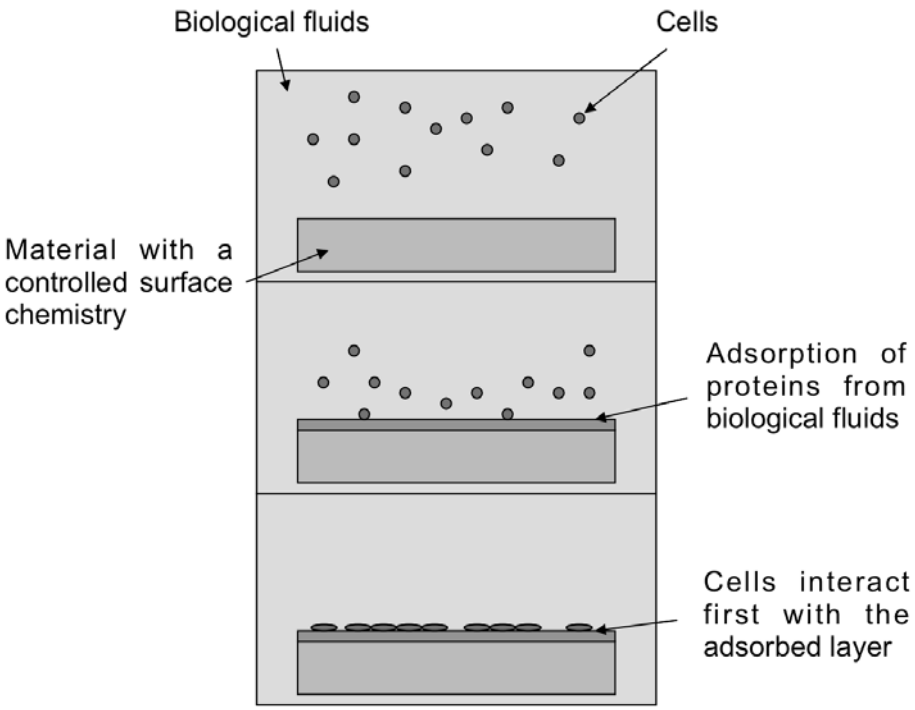

Figure 14 *Representation of the initial cell adhesion to a surface immersed in a biological fluid. The chemical properties of the surface determine the composition of the adsorbed layer and the conformation of the adhered proteins. When cells reach the surface they bind to specific ligands found in this layer of biomolecules* [60].

The chemical properties of the surface affect both the composition of the layer and the conformation (and thus, the functionality) of the adhered proteins. The situation is generally different *in vitro* than *in vivo*, due to the distinct chemical composition of cell culture media and physiological fluids. While cells cultured *in vitro* depend mainly on cell adhesive proteins from the serum to adhere (e.g. fibronectin and vitronectin), *in vivo* they are also accompanied by other proteins such as fibrinogen or albumin. One of the main contributions to cell adhesion from these molecules comes from the presence of the arginine-glycine-aspartic acid (RGD) amino acid sequence [61]. Cells can bind to this sequence through integrin receptors establishing stable bonds that evolve into focal complexes (see **Figure 15**). Focal complexes are bound intracellularly to actin filaments, participating in cytoskeleton organization and mechanotransduction, and are involved in the capacity of the cell to adhere, spread, divide and migrate. In

addition, the layer of adhered proteins may provide binding sites for growth factors, promoting cell differentiation, as observed in fibronectin [62].

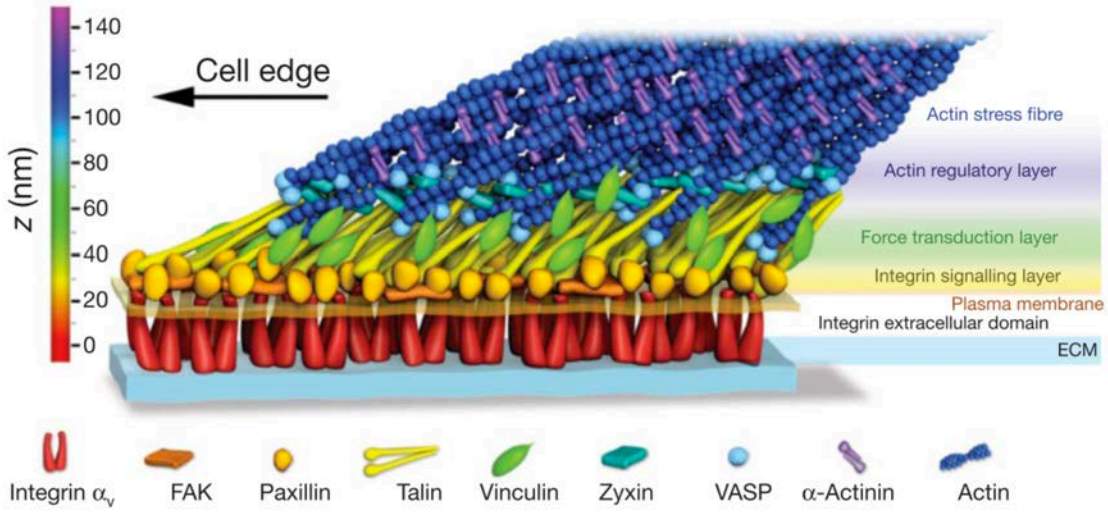

Figure 15 *Model of the proteins composition and position in a focal adhesion. Integrins (in red) can attach to the RGD sequence in the extracellular matrix. Once bound they gather together in large complexes called focal adhesions. These complexes are bound to the actin filaments (in blue) through a series of intracellular proteins* [63].

From the **physical point of view**, two main contributions can be found from surface properties: topography and stiffness. Surface topography can modify cell behavior in terms of adhesion, spreading, migration, differentiation, and gene expression [64–69]. The effects of topography depend on cell type but also on the scale of the features respect cell size [55] (see **Figure 16**). For macro-topographical features, much larger than cells, the increase in surface roughness favors a better bone-surface interlocking, ensuring mechanical stability [70]. On the other hand, at the micro- (1 - 10 μm) and sub-micrometric length scale (100 nm - 1 μm), both *in vivo* and *in vitro* studies show improved results by comparing micro-rough versus flat implants. In fact, most of the dental implants in the market take advantage of these observations, presenting an R_a ranged between 1-2 μm [70]. In this regard, *in vivo* studies reported higher bone-implant contact and higher torques needed to remove roughened screws as compared to flat

ones [71,72]. This may be attributed on the one hand to an enhanced micro-mechanical retention [73] and on the other hand to a higher number and activation of platelets on rougher surfaces (producing the fibrin clots that facilitate cell migration to the surface) [74,75]. *In vitro,* higher osteoblast differentiation and local factor production has been observed for micro-rough surfaces [76,77], although the exact mechanisms are still under debate.

In recent years, the importance of controlling nano-topography (< 100 nm) has also been highlighted. Integrin receptors interact with ligands at the nanometric length scale and the spacing, density, and distribution of adhesive nano-sites has been shown to highly affect integrin clustering and, thus, the adhesion and spreading quality [78]. Nano-features can affect not only cell adhesion [79,80], but also improve osteogenesis [81–83]. In fact, Dalby *et al.* [68] found that a certain degree of nano-feature disorder could influence stem cell phenotype, indicating that organization of the topography is as important as its size and shape. Due to the fact that bone presents a hierarchical structure at different length scales (i.e. from macro- to nano-), the mimicking of such combination has been addressed, with improved results respect to the use of only micro- or nano-features [84].

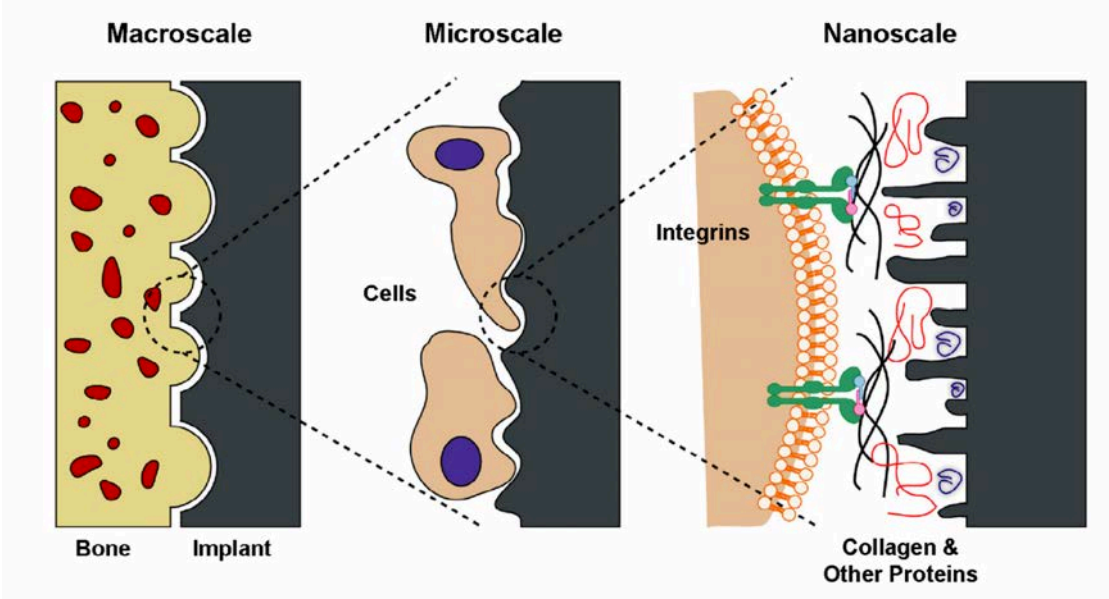

Figure 16 *Representation of the influence of topography at different length scales. At the macro-scale, mechanical bone-surface interlocking ensures primary stability of the implant. At the micro-scale, roughness introduces micro-mechanical stability as well as provides mechanical cues to cells that influence adhesion, spreading, proliferation, migration and differentiation. At the nano-scale, interactions at the integrin level affect focal adhesion and cytoskeleton organization, which triggers cell signaling from the mechanotransduction machinery* [55].

As mentioned before, stiffness is another physical property that can affect cell behavior. Indeed, the stiffness of the substrate where cells are growing can guide stem cell differentiation into specific lineages [85,86]. Cells can sense forces exerted by the matrix through the actin structures linked to focal adhesions. These forces result in intra-cellular signaling that can affect gene expression. Interestingly, this process is independent from the stimulation by soluble factors, but presents synergism with it. Thus, the stiffness of a biomaterial must be in concordance to the tissue it replaces. In the case of bone, rigid materials are preferred; in the case of other tissues such as muscle, softer materials are required [86].

In this regard, **Figure 17** displays how substrates with different stiffness affect the morphology of MSCs. When MSCs were grown on substrates with a stiffness

resembling brain tissue, muscle or the crosslinked collagen in osteoids, differentiation was guided to the lineage of each corresponding tissue: neurons, myoblasts or osteoblasts, respectively.

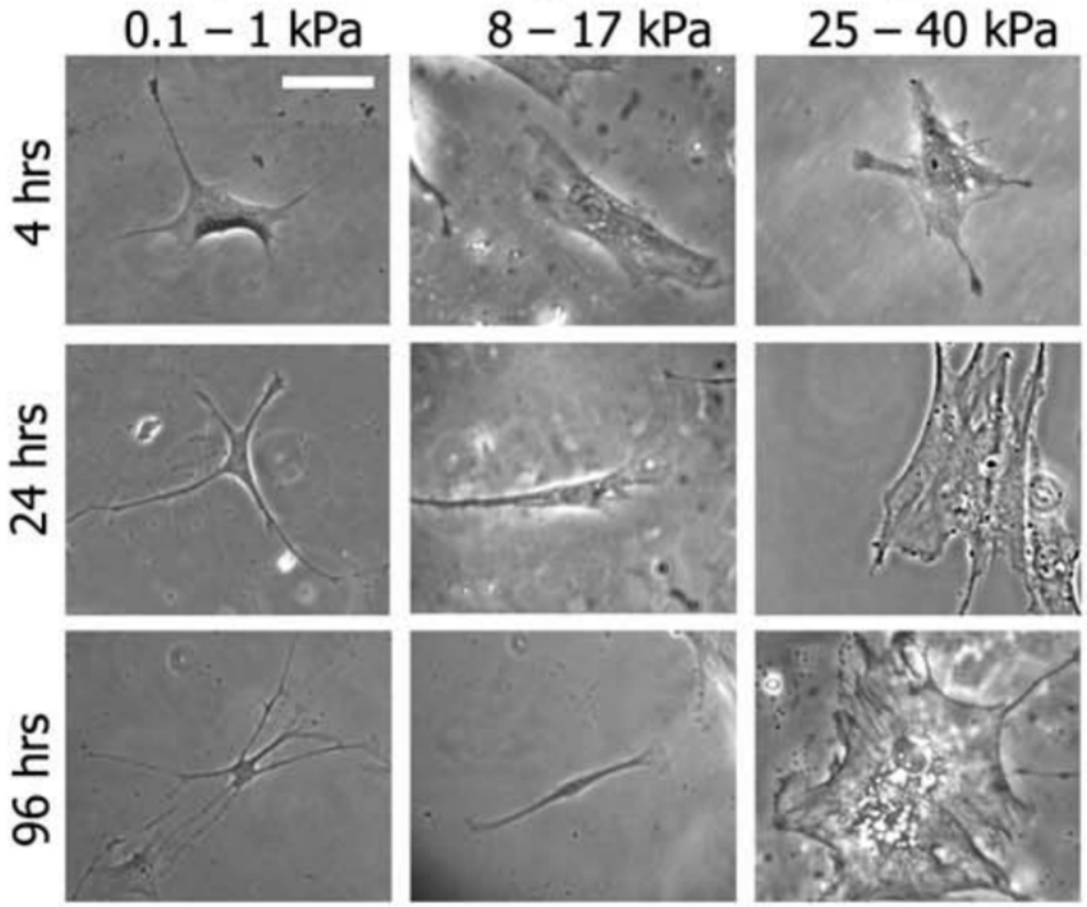

Figure 17 *Human MSCs cultured on substrates with different stiffness: 0.1-1 kPa (brain stiffness), 8-17 kPa (muscle stiffness) and 25-40 kPa (stiffness of crosslinked collagen of osteoids). After 96 hours of culture, cell morphology was completely different in the substrates: branched neuron-like cells in the softer substrates, spindle myoblast-like cells in the intermediate stiffness substrate, and polygonal cells in the stiffest one. Scale bar is 20 μm* [86].

Mineralized bone, as well as materials intended to replace bone (e.g. zirconia, titanium), present a higher stiffness than the one employed in the study of **Figure 17**. Thus, on such surfaces, MSCs tend to differentiate into osteoblasts. The Young's modulus of cortical bone, titanium and Y-TZP are listed in **Table 4**.

Table 4 *Young's modulus of typical materials for dental implants, as compared to bone.*

Material	**Young's Modulus (GPa)**
Cortical Bone	20
Ti6Al4V	110
3Y-TZP	210

It can be observed that the Young's modulus of both titanium alloys and zirconia ceramics are much higher than the one of human bone. This difference of stiffness is responsible of a mechanism known as "stress shielding" [87]. In the surgery of long bones, such as the femur, the higher stiffness of the prosthetic elements can "shield" the surrounding bone from experiencing the desired levels of stress. If the bone does not experience a certain level of mechanical stresses it gets progressively resorbed, which compromise the bone-implant function. However, in the dental field the "stress shielding" effect on the implant-jaw system has not been confirmed. In fact, recent studies based on numerical simulations have highlighted the benefits of using stiff materials [88].

Given the broad range of stimuli that the surface deliver to cells, both physical and chemical modifications are performed to implants in order to favor osteointegration. Such modifications may be oriented to provide a better mechanical retention, such as macro-roughening of the surface, or may be designed to improve interactions at the material-cell level such as facilitating adhesion, migration or cell differentiation.

1.4 Surface modification of zirconia based ceramics

1.4.1 Topographical modifications

1.4.1.1 Relevant techniques in zirconia dental prostheses

Commercial dental implants are generally roughened to promote faster and better implant-bone integration, obtaining improved bone-implant contact (BIC) and removal torques, *in vivo*. Modifications are mostly addressed to increase both surface area and macro-/micro- mechanical retention. However, the effect of micro- and nano-topography on bone-like cells, although probably present and beneficial, is not specifically targeted in such modifications. Thus, most of the employed techniques are directed towards a general increase in surface roughness at different length scales, but not towards the creation of particular topographies that trigger specific cell functions.

The most common techniques employed in Y-TZP implants include machining/grinding, sandblasting, chemical etching and laser patterning [89,90]. Other methods employed on titanium implants such as anodization are not suitable because of the lack of electrical conductivity of zirconia. While sandblasting and chemical etching produce random topographical features, grinding can produce directional (although also random) patterns. The three latter modifications (i.e. grinding, sandblasting and etching) are the most common and are employed in several commercial implants.

Among the techniques that allow creating specific pre-designed topographies, laser patterning stands out due to the possibility of creating features at the micron- and submicron- level [91,92]. Although its commercial use is still limited (e.g. Z systems, Oensingen, Switzerland) due to its lower processing speeds and the cost of the involved technology, research on this subject in recent years has highlighted the potential of the technique. In this regard, alternative methods able to create defined topographies, such as lithographic-based techniques, are also highly relevant in the research field due to their high resolution and flexibility but lack the processing speeds needed for commercial use.

One aspect that must be noted is that, in general, such techniques not only modify surface topography, but are also accompanied by microstructural changes and micro-damage that may influence LTD behavior and mechanical properties [93,94]. The changes introduced might be beneficial or not, and therefore, detailed characterization of the surface and its properties are required after such modifications. A brief description of the cited superficial treatments is outlined below:

Grinding: a surface finishing method similar to polishing, which involves coarser abrasive media. The surface of the material is in contact with a rotating grinding wheel, which consists on abrasive particles (usually diamond) embedded in a matrix, as depicted in **Figure 18**. The contact between these sharp particles and the material creates a combination of plastic flow and brittle fracture (i.e. micro-cracks, decohesion, etc.). In this sense, material removal takes place by chipping and the confluence of cracks from adjacent penetration sites [95]. If the depth of cut of the grinding wheel is sufficiently low, a ductile regime can be achieved, reducing surface damage [96]. This technique can be used both as a surface finishing procedure or to adjust the final shape of a component.

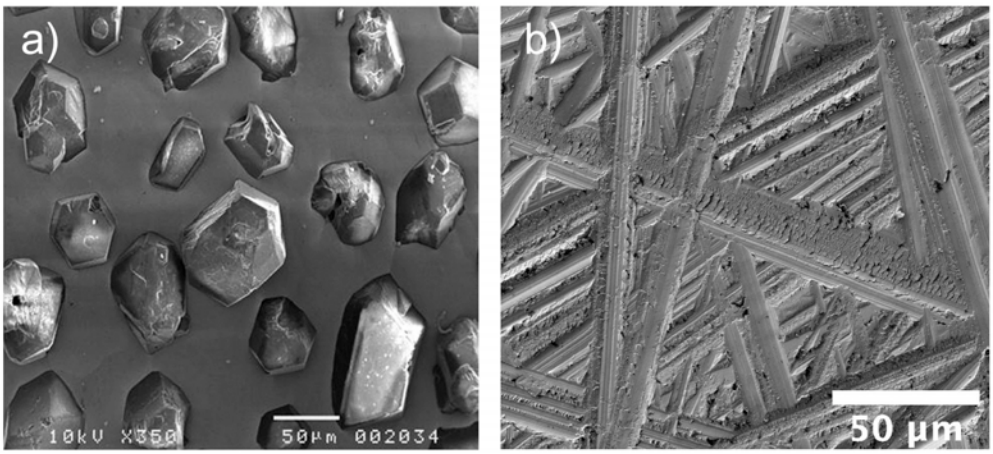

Figure 18 *SEM micrographs of a) surface of a bur. Embedded diamond particles can be observed* [97] *and b) 3Y-TZP surface after grinding. The tracks left by abrasive particles are evident.*

Sandblasting: this technique consists on the projection of a hard-ceramic particles jet onto the surface, generating plastic deformation and removing chunks of material (see **Figure 19a**). It has been widely used in dentistry to not only achieve a better osteointegration of implants [98], but also to enhance the bonding between dental crowns and luting cement or between the crown and the veneering porcelain, due to an increase in surface area and wettability [99,100]. The mechanism by which a particle from the jet is able to erode the material is based on the particular interaction particle-surface, which is similar in nature to a quasi-static indentation [101]. The high stresses around the collision zone create lateral and radial cracks that can propagate and lead to material pull out with successive impacts. Lateral cracks are responsible for material chipping while radial cracks penetrate through the material and are responsible for a reduction in strength. Depending on the particles' size, speed, and impact angle different values of roughness can be achieved. As some remnant particles may be strongly attached to the surface after the treatment, a biocompatible material must be chosen for the particles used. In this regard, materials such as alumina (Al_2O_3), titanium dioxide (TiO_2) or calcium phosphates are suitable for this purpose [98].

Chemical etching: this surface treatment consists on the dissolution of the material's surface by an alkali or an acid etchant, creating a roughness at the micro- and the nanometric length scale. Although Y-TZP presents a very high chemical inertness, it has been successfully etched with: hydrofluoric acid (HF), hypophosphorous acid (H_3PO_2), potassium hydroxide (KOH) and sodium hydroxide (NaOH); being HF the agent with the fastest etching rate [102–104].

Chemical etching is frequently used in combination with sandblasting in order to superimpose nano-roughness to a previously micro-roughened substrate [102], as shown in **Figure 19b**.

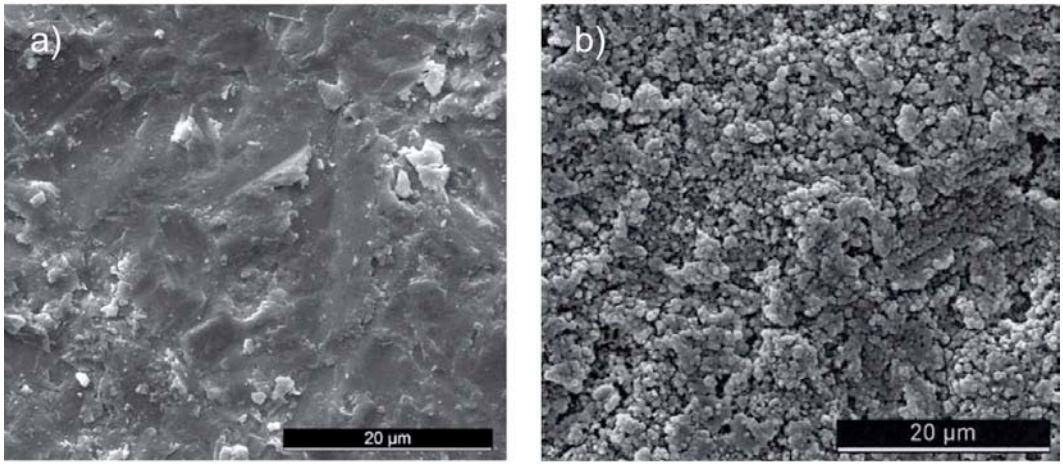

Figure 19 *SEM micrographs of a) sandblasted Y-TZP and b) sandblasted and alkali etched Y-TZP. The introduction of nano-roughness to sandblasted specimens can be clearly observed* [105].

Laser Patterning: this technique consists on the creation of a surface pattern by selectively removing material with a laser beam (see **Figure 20**). High density optical energy is required to melt, dissociate (break chemical bonds), vaporize and expulse material from the interaction zone [106]. Several types of lasers, working modes and techniques may be used, creating different types of laser-material interaction [107] that allow producing a wide range of patterns and topographies, including features at the micron- and submicron- length scale [108]. It is a non-contact technique, which avoids surface contamination as well as tool wear, which is especially relevant when machining hard ceramics.

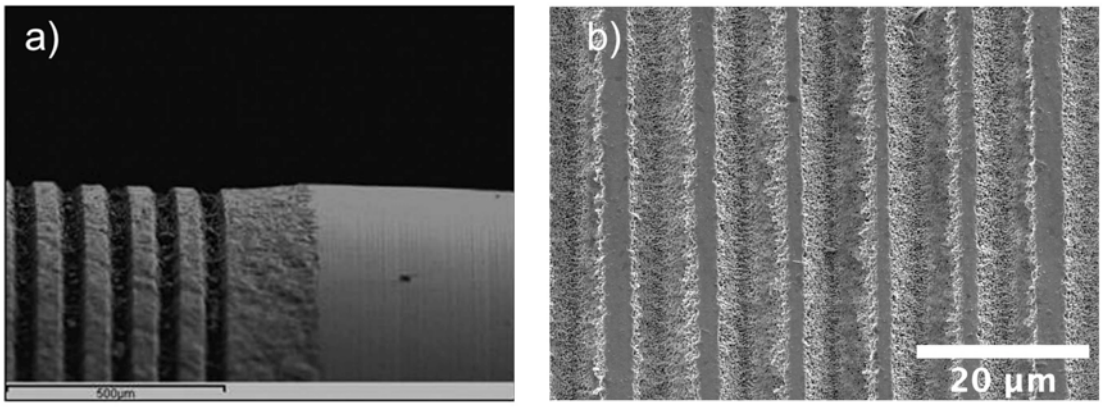

Figure 20 *SEM micrographs of a) laser patterned dental implant* [91] *and b) laser micro-patterning of 3Y-TZP.*

1.4.1.2 Grinding

Grinding and polishing are frequent steps in the production of Y-TZP components, both to provide an adequate surface finishing and to make adjustments to the shape of components. In the particular case of restorative dentistry, it is involved in many procedures, mostly in the CAD/CAM process (hard and soft machining), in the geometric adjustments made by dentists to fit the patient's needs, and as a roughening method to improve adhesion to veneers or cements. Thus, many efforts have been invested in understanding the surface changes after this process and its main effects on material's properties. On the other hand, and as described in **section 1.3.2**, the addition of surface roughness and the modification of surface topography can affect cellular behavior, which can be used as a tool to enhance the interaction with biological tissues. In this section the changes in microstructure, mechanical properties, LTD resistance and cellular behavior after surface grinding are presented in detail.

Microstructural features

Muñoz-Tabares *et al.* [109] described in detail the microstructural changes after grinding through transmission electron microscopy (TEM) inspection. As shown

in **Figure 21**, TEM observations revealed three different regions just below the surface:

1) A first layer was found, with a thickness around 300 nm. Due to the high strain produced during the abrasion of the surfaces, *in situ* recrystallization occurred, with grains of about 10-20 nm (compared to its original grain size of around 300-400 nm).
2) A second layer was identified, with a thickness of 500 nm. In this layer plastic deformation was found, with highly distorted grains in a direction parallel to the surface.
3) Below, a third layer of several microns thickness was observed, with abundant $t \rightarrow m$ phase transformation as evidenced by *m*- laths. In this region, compressive stresses were introduced due to such phase transformation.

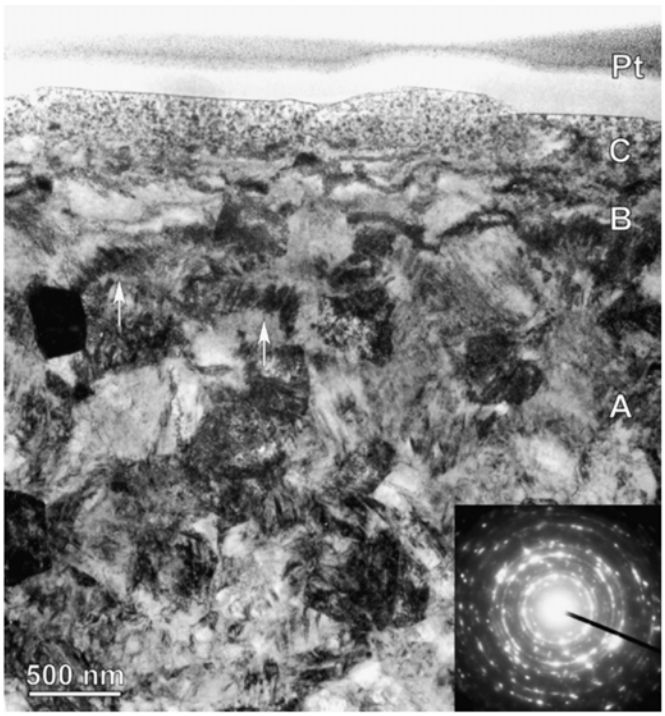

Figure 21 *TEM micrograph of ground 3Y-TZP. Three different layers can be identified. A first layer of recrystallized nano-grains is observed near the surface (C). Below, a region with highly distorted grains is present, with a layer thickness of*

around 500 nm (B). The rest of the lamella corresponds to equiaxed t- grains with a certain degree of t → m transformation (A) [109].

X-ray diffraction (XRD) has also been widely employed to study the effects of grinding processes in Y-TZP. The changes observed after evaluation of ground specimens by XRD are displayed in **Figure 22** and include:

a) An increase in the *m*- content due to the stress induced $t \rightarrow m$ transformation.
b) An asymmetric broadening of the $(101)_t$ peak. This was first reported by Hasegawa [110] and has been associated to the presence of rhombohedral (*r*) phase. According to several authors, such phase is only stable under high stresses and develops from the transformation from the cubic ($c \rightarrow r$) or the tetragonal phase ($t \rightarrow r$) [111,112]. Other authors, however, relate such broadening to a deformation in the *t*- lattice [113]. It can be reverted by annealing treatments at high temperature (>1000°C).
c) Texture, as revealed from the changes in intensity of the $(002)_t/(200)_t$ peaks. A reorientation of domains inside *t*- grains is triggered by the high biaxial stresses from the grinding process, with the *c* axis of the *t*- phase reoriented perpendicularly to the surface [109,114–116]. This process is known as ferroelastic switching. In the presence of external stresses, the tetragonal *a* axis can transform into *c*, and vice versa, absorbing part of the applied mechanical energy.
d) A certain degree of peak widening, suggesting the presence of residual stresses and grain size reduction, as confirmed by TEM measurements.

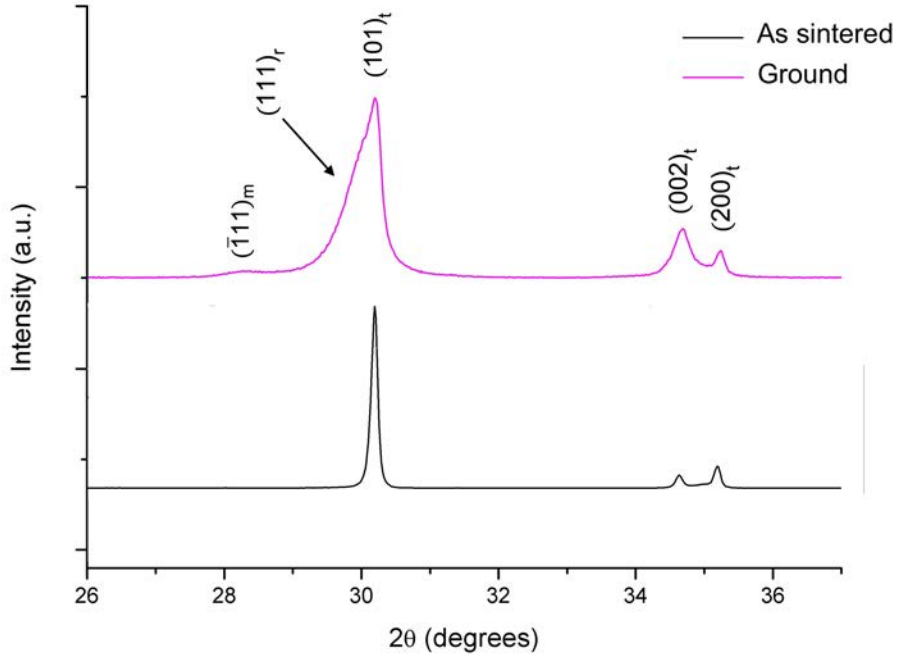

Figure 22 *XRD spectra of as sintered and ground 3Y-TZP specimens. Ground specimens present several characteristic features such as m-phase, asymmetric broadening of the* $(101)_t$ *peak and inversion of the* $(002)_t/(200)_t$ *peaks.*

As detailed above, several changes are introduced on the material's surface after grinding, which have a significant impact on mechanical properties and LTD resistance.

Mechanical properties

Mechanical properties may improve or worsen depending on the grinding conditions [109,117–120]. The main beneficial contribution comes from the stress induced $t \rightarrow m$ phase transformation. Such transformation is accompanied by a volume expansion of around 4% that creates a compressive layer of residual stresses on the surface [2], improving bending strength, fatigue and fracture toughness. However, when the induced flaws (e.g. scratches and cracks) are large enough to penetrate beyond the compressive layer, or when grinding parameters, such as the absence of coolant, promote an increase of temperature above the $m \rightarrow t$ phase transformation temperature (i.e. *m*- phase is reverted,

thus reducing the layer of compressive residual stresses), mechanical properties may drastically decrease [117,121].

Low temperature degradation

Low temperature degradation (also known as hydrothermal degradation or ageing) can also be hindered or not depending on the grinding conditions [93,122–124]. It has been shown that the changes introduced by grinding can delay hydrothermal degradation. The protection achieved is the result of the following changes in microstructure:

a) The layer of nano-grains that forms in the first nanometers of material are protected from the $t \rightarrow m$ phase transformation due to their reduced size [125]. Reducing grain size increases ΔU_{SE}, stabilizing the grains (see Eq. 1).
b) The layer of compressive residual stresses further stabilizes the *t*-phase [2,25]. Similarly to grain size, compressive stresses stabilize the *t*-phase by increasing ΔU_{SE}.
c) Reduction in domain size by ferroelastic switching can effectively prevent degradation, as shown by Jue *et al.* [126]. Formation of subdomains is analogous to reducing grain size.

Yet, under certain grinding conditions, these beneficial effects can be reduced or counteracted by extensive surface damage (allowing water to penetrate beyond the protective layer) or by the presence of too large amounts of *m*-phase on the surface [93,127].

Cellular response

The influence of ground surfaces on cell behavior is due to the increase in surface roughness and the introduction of particular surface features. As described in **section 1.3.2** an increase in superficial roughness can influence cell adhesion, spreading, migration, proliferation and differentiation. Regarding cell

adhesion and proliferation, some contradictory results can be found in literature. For example, Deligianni *et al.* [128] found an increase in both adhesion and proliferation on increasingly rough ground titanium surfaces. However, Anselme *et al.* [129][130] observed the opposite behavior. In this regard, decrease in proliferation may be related to the concomitant process of cell differentiation. Lincks *et al.* [131] compared smooth versus rough ground titanium surfaces and found an enhanced differentiation on the rough surfaces, indicated by a decrease in proliferation and an increase in alkaline phosphatase (ALP) and osteocalcin. Other authors have also found increased ALP activity on ground surfaces [132], indicating an enhanced osteogenic potential. Topographical features found on ground surfaces, in particular the formation of grooves, can also affect cellular behavior by favoring cell alignment (see **Figure 23**) and migration [65,133,134], which have an important role in many cellular processes such as cytoskeleton reorganization, membrane protein relocation, nucleus gene expression or extracellular matrix (ECM) remodeling [135]. Notably, most of the studies available are focused on titanium substrates, while scarce information is available for zirconia-based materials

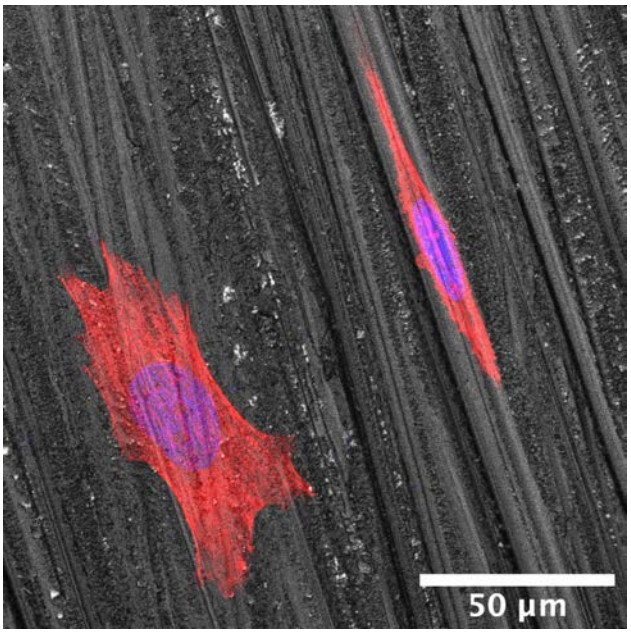

Figure 23 *Cells growing on a ground 3Y-TZP surface. Alignment of cell bodies along the grooves is observed. In red, cell cytoskeleton; in blue, cell nucleus. The image was obtained in the experimental work of this thesis.*

1.4.1.3 Laser micro-patterning

Laser applications are of interest for a variety of fields including the scientific, industrial, medical or military. They can be used to transmit information (e.g. telecommunications), gather information (e.g. measuring devices) or as a tool to modify matter (e.g. laser marking, cutting, welding, etc.), among others. Depending on the properties of the laser beam, such as wavelength or intensity, the mechanisms by which it interacts with matter can change, affecting surface chemistry, topography or phase composition in different ways [136]. In particular, when short pulses of high energy are employed, localized melting, vaporization or ablation are possible, which has been of especial interest in surface engineering. In this field, laser techniques have been employed to create micro-patterns on the surface of metallic [137], ceramic and polymeric components [138] by selectively removing material.

In order to create such patterns different techniques can be employed, including direct laser writing, projection patterning or direct laser interference patterning

(DLIP) [136]. The latter technique, DLIP, allows producing surface patterns by the inhomogeneous energy distribution produced by the interference of two or more laser beams. When coherent and linearly polarized beams are allowed to interfere on a surface, the particular intensity distribution depends on the wavelength, number of beams and their relative angles [139,140]. If beams are energetic enough, their interaction with the surface produces material removal and a surface pattern is created [92,141–144]. Different patterns depending on the number of beams are shown in **Figure 24**.

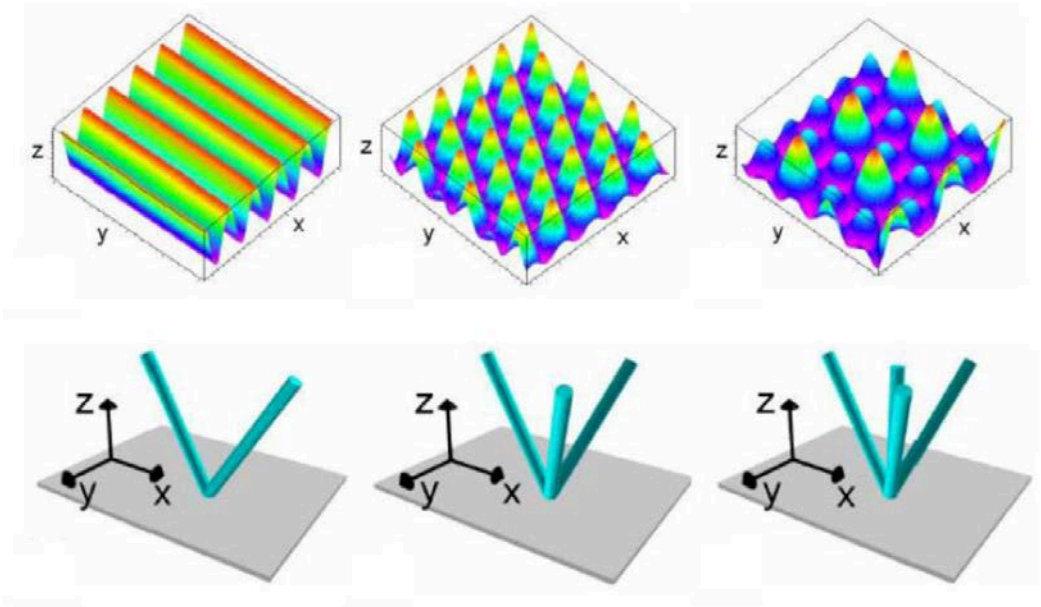

Figure 24 *Different intensity distribution patterns with two (left), three (center) and four (right) beams. On the top the intensity distribution is shown. On the bottom, the corresponding beam geometry* [142].

Several studies have successfully attempted to create micro-patterns on Y-TZP, and the majority focused on linear structures [91,92,145–152], achieving features at the micron scale. The most common approaches involve the use of laser equipment providing pulses at the nanosecond (mostly Nd:YAG at a wavelength of 1064 nm, or 532/355/266 nm by second and third-harmonic generation) or femtosecond time-scale (in general Ti:sapphire at a wavelength around 800 nm). Although both time regimes are suitable to micro-structure Y-

TZP, the nature of laser-material interaction is different, and therefore the produced topography, surface damage and microstructural changes are also different. The mechanisms underlying this effect are related to energy absorption, relaxation and the time-scale of the pulses involved, and are explained below [107,136,153].

Laser radiation is absorbed by the electrons of the target material. In Y-TZP (and most of dielectrics), the large gap between the valence and the conduction bands (≈4-5 eV [154,155]) restricts the linear absorption of photons to wavelengths in the ultraviolet (UV) or shorter. However, at high intensities such as in the case of short pulsed-lasers, non-linear optical processes take place and multi-photon absorption is possible. By this effect, several photons with energy lower than the band gap can be absorbed at the same time, and thus, lasers emitting at longer wavelengths can be employed (visible and infrared (IR)).

The incident energy from photons is thus transferred to free electrons, which are in an excited state. The time needed to transfer this energy to the lattice and reach an electron-lattice thermal equilibrium is in the order of 10^{-12} s. At this point, the duration of the pulse is critical. If laser pulses at the nanosecond (10^{-9} s) regime are delivered, electrons have enough time to transfer their energy to the lattice through electron-lattice collisions, and the main energy loss is heat conduction into the solid [107]. This way, material removal takes place mainly by thermal mechanisms (melting, vaporization, etc.) However, if the laser pulses are at the femtosecond regime (10^{-15} s), there is insufficient time to transfer the energy to the lattice and electrons are heated at high temperature almost instantaneously. Material removal is thus carried out by non-thermal processes, i.e. ablation (electrostatic ablation, Coulomb explosion, photolysis, etc.) [153].

In practice, in each time regime several mechanisms can take place simultaneously, although one of them is predominant. In Y-TZP, melting and vaporization are the main responsible for material removal in the nanosecond regime, while ablation is observed in the femtosecond. Thus, different surface features are observed after treatments in one or another regime.

Surface and microstructural changes

Materials patterned with nanosecond lasers present a surface layer with evident signs of melting and resolidification. Several defects can be observed, with the presence of cracks (due to thermal shock), pores and droplets [92,152]. Stresses generated by such cracks trigger the $t \rightarrow m$ phase transformation[152,156]. Slight texture in the *t*-phase has been also measured and due to resolidification some microstructural changes have been observed, such as recrystallization and columnar grain growth in the recast layer [156]. In contrast, femtosecond treated surfaces present a difference appearance, with features indicating ablation instead of melting. Scarce efforts have been dedicated to the study of the surface changes on Y-TZP after patterning with femtosecond lasers. Some sub-superficial micro-cracks and pores were observed by Stanciuc *et al.* [148] after patterning, as well as ripple formation under certain conditions [148,157]. In addition, very small amounts of phase transformation were found [91,149]. Characteristic features of laser-modified surfaces in both regimes are shown in **Figure 25**.

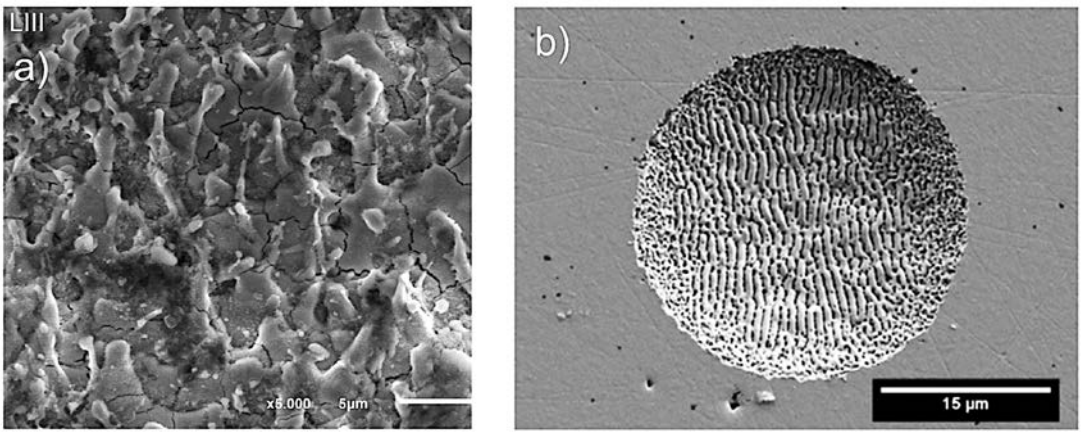

Figure 25 *SEM micrographs of the surface features of laser-modified Y-TZP. a) Surface appearance after modification with a nanosecond regime laser. A layer of resolidified material is visible, with the presence of droplets and cracks* [152]*. Scale bar is 5 µm. b) A pit produced with a femtosecond regime laser. Ripples are observed on the bottom of the pit* [148]*. Scale bar is 15 µm.*

Mechanical properties and low temperature degradation

Although of particular relevance, just a few works have studied mechanical properties and LTD resistance after such treatments. Daniel *et al.* [158] observed an increase in mechanical properties in the nanosecond regime, which attributed to compressive residual stresses and a reduced grain size. However, more recently, both Pereira *et al.* [152] and Roitero *et al.* [159] found a reduced strength but a slightly increased Weibull modulus. In particular, Roitero and coworkers attributed the reduced strength to the enlargement of pre-existing defects (i.e. pores) close to the surface.

Pereira *et al.* [152] found a worsening of the LTD resistance after laser patterning in the nanosecond pulse regime, which could be improved in some cases by a thermal treatment. Roitero *et al.* [94] obtained similar results. They found an overall decreased LTD resistance after laser patterning. Although compressive residual stresses favored slower phase transformation kinetics, the presence of a higher initial *m*-phase content (due to the laser-patterning process) decreased the overall ageing resistance. However, after a thermal treatment at 1200°C degradation was improved respect as-sintered specimens. Such improvements were related to the reversible $m \rightarrow t$ phase transformation, the presence of texture induced by the laser treatment, as well as the generation of a micro-cracked network on the surface (due to the laser treatment), which could potentially hinder autocatalytic phase transformation.

Cellular response

Laser machined micro-patterns on zirconia-based materials can modulate cell morphology. Different topographies have been produced such as pits [148] and linear structures [149–151,160,161]. While pits can just affect cell morphology (i.e. size, aspect ratio, circularity, etc.), linear structures can also promote cell alignment (see **Figure 26**). Several studies have shown improved response from cells of the bone lineage when growing on linearly patterned zirconia substrates. These enhancements include improved osteogenic differentiation from human

bone marrow stromal cells (BMSCs) [149], as well as increased ALP, mineralization and osteogenic gene upregulation in osteoblast-like cells [150,160,161]. In this regard, it has been shown that grooved patterns can guide stem cell differentiation, depending on the particular geometry of the grooves [162].

In vivo, micro-grooves can also improve implant performance. For instance, it has been shown that laser-ablated microgrooves on the implant collar can affect epithelial, fibroblastic and osteoblastic migratory patterns, influencing the orientation of the connective tissue fibers respect the implant surface [163]. The correct orientation of such fibers hinders the apical migration of the junctional epithelium, avoiding crestal bone loss. Laser patterned implant collars can limit the epithelial downgrowth, improve soft and bone tissue attachment, and influence bone remodeling so that improved bone quality is found adjacent to the implant [164].

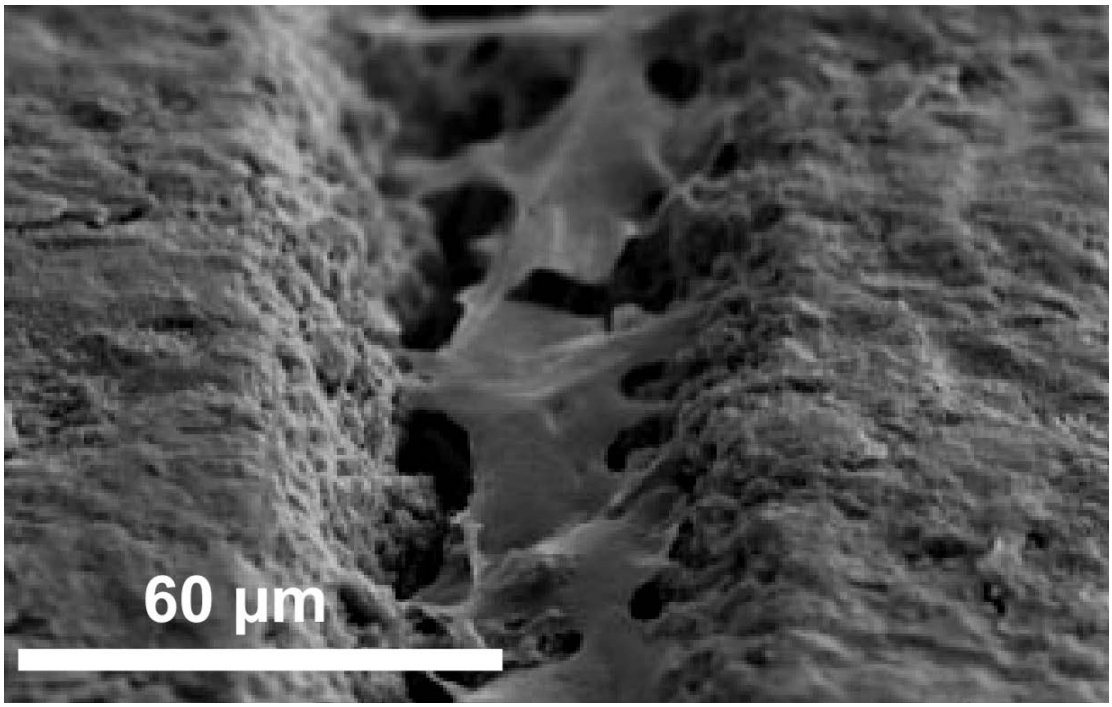

Figure 26 *Cells growing inside a laser-patterned groove on Y-TZP. Cell body extensions can be observed toward the micro-grooved walls* [160].

1.4.2 Chemical modifications - coatings

1.4.2.1 Biofunctional coatings: an overview

The surface of biomaterials can be chemically modified in order to add certain biological properties. One possibility is to alter the chemical properties of the surface itself. For example, surfaces can be treated with UV light in order to enhance their wettability [165]. However, these strategies depend largely on the material employed (i.e. expected performance cannot be directly extrapolated to different materials) and offer a relatively narrow range of possibilities. Another option consists on surface coatings [166,167], which can be designed to present specific biological cues and are easier to apply to different substrate materials. Coatings can be grouped into inorganic or organic, depending on the material from which they are produced. Some of the possibilities offered by this strategy are detailed below.

Inorganic coatings

The most common inorganic coatings in bone tissue engineering are based on ceramic inorganic materials, including *calcium phosphates (CaP)* [168] and *bioactive glasses* [169]. While CaP cements are a family of materials with similar composition to bone and teeth, bioactive glasses are based on mixtures of the oxides SiO_2–CaO–MgO–Na_2O–K_2O–P_2O_5. These coatings promote the deposition of a thin layer of biological apatite on the surface, which facilitates the adhesion and differentiation of host cells. They present a very good osteoconduction and can even promote osteogenesis [170,171]. Coatings can be produced by several techniques (e.g. plasma spraying or electrodeposition [168,169]) and have been mainly applied to titanium substrates but can also be employed on zirconia [172,173]. However, the control of composition and structure of the produced apatite is complex and the mechanical properties of thick coatings may present a poor performance [174,175]. An alternative to such coatings is the deposition of apatite through a biomimetic process. In this method a bone-like apatite layer is formed on the surface of a material after immersion in a simulated body fluid

(SBF), as shown in **Figure 27**. The deposited layer consists on amorphous or poorly crystalline ion-substituted calcium orthophosphates. The method proposed by Kokubo and coworkers [176,177], which entails a previous thermochemical treatment, is a good example of this approach and can be used on zirconia [178] as well as on various metals, including titanium.

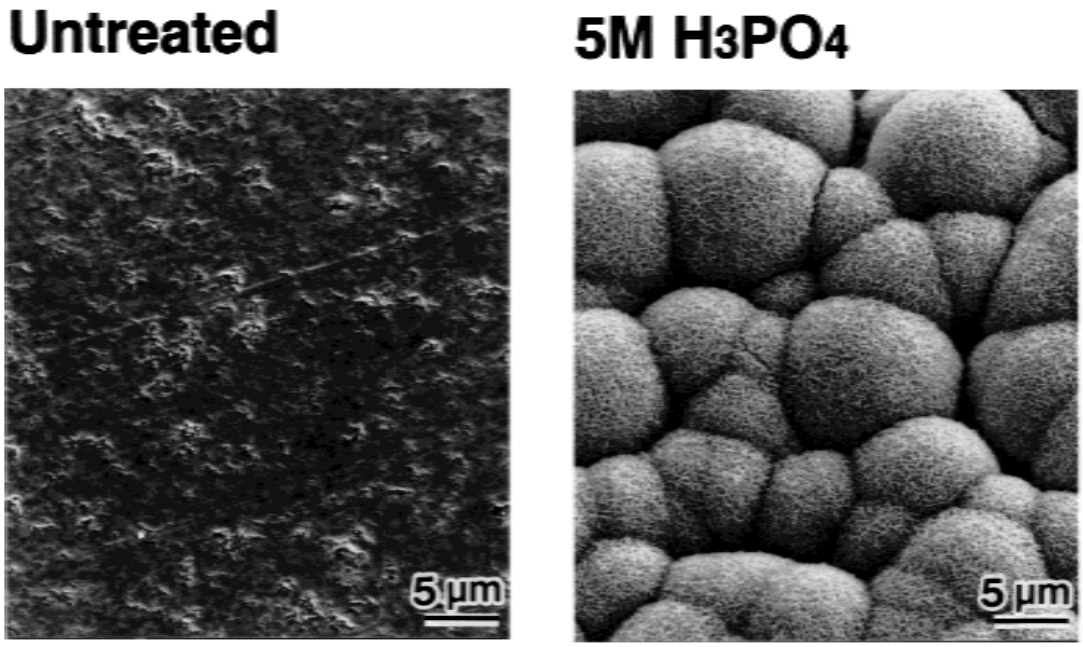

Figure 27 *SEM micrographs of the surfaces of 10Ce-TZP/Al_2O_3 composites which were either a) untreated or b) treated with 5M H_3PO_4, and subsequently immersed in SBF for 7 days. The surface treated with H_3PO_4 is fully covered by a layer of nucleated apatite* [178].

Organic coatings

These coatings are based on the immobilization of polymers on the surface, either from a synthetic or a natural origin. They are highly versatile as, to some extent, can be tuned to modify their properties in terms of density, morphology, thickness, hydrophobicity, degradability, etc. They may be aimed at mimicking the extracellular environment (i.e. the ECM), trigger specific cell functions, act as drug delivery systems, etc. They can be classified into *synthetic* and *natural coatings*, as schematized in **Figure 28**.

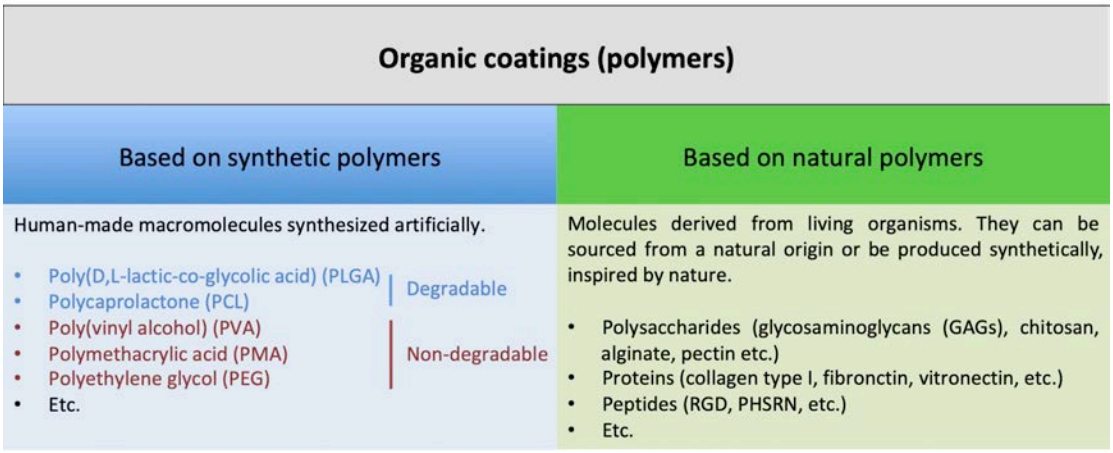

Figure 28 *Classification of organic coatings according to the origin of the polymers employed.*

Synthetic coatings are produced from human-made, artificially synthesized polymers. They can be degradable or non-degradable and are mainly employed to alter some chemical properties, such as the hydrophilic/hydrophobic behavior, or act as drug delivery systems. They are highly tunable, their physical properties can be modified depending on the specific application, and present low immunogenicity risks. However, their ability to deliver specific biological cues is limited. Degradable polymers are usually employed as drug-delivery agents and include poly(D,L-lactic-co-glycolic acid) (PLGA) [179] or polycaprolactone (PCL) [180]. Non-degradable polymers include poly(vinyl alcohol) (PVA), polymethacrylic acid (PMA) [181], or polyethylene glycol (PEG) [182].

In contrast to synthetic coatings, **natural coatings** are produced from molecules derived from living organisms. They can be sourced from a natural origin or be produced synthetically, inspired by nature. They can provide cell-specific interactions and are highly biocompatible and non-toxic. However, their synthesis is often more complex and when sourced from natural origins, both their composition and conformation cannot be entirely controlled. Natural coatings include a wide range of molecules including polysaccharides (e.g. glycosaminoglycans (GAGs), chitosan, alginate, pectin etc.), proteins derived from the ECM (e.g. collagen type I, fibronectin, vitronectin, etc.) and peptides.

While polysaccharides do not generally possess cell specific properties, they can provide biocompatible and stable structures to support other molecules, or favor protein adsorption and interaction with ECM molecules [183–186]. On the other side, ECM-derived proteins can present specific sites with biologic activity, including the presence of cell binding motives or the ability to entrap growth factors [62,187]. ECM proteins are complex molecules that can possess multiple functions, interact with other proteins and present unmasked functions that can be activated in the right moment by the right biological environment [188]. In the last decades, recombinant DNA technologies offer also the possibility to produce chimeric proteins that gather multiple biological functions [189]. However, there is a concern with the disease transmission and immunogenicity problems derived from the use of such proteins, as they are either derived from a natural source or produced by recombinant technologies in organisms such as bacteria or yeast [190]. In addition, the relatively large size of proteins may entail stability issues in varying conditions of pH and temperature. Another approach that circumvents such problems consists on the use of synthetic peptides, short sequences of amino acids. They can be derived from natural sources (e.g. ECM, soluble factors, etc.) or engineered for specific purposes, and can be easily synthesized by liquid or solid-phase chemistry. Peptides can present very different biological properties [191–193] and due to their smaller size are more stable than proteins and can be grafted at high surface concentrations. In addition, multifunctional coatings can be obtained if different peptides are combined [194–196].

The use of organic coatings on zirconia has been scarcely investigated. The available studies include the use of polydopamine coatings [197,198], as well as surface functionalization with proteins and peptides. In this regard, there is one study involving the functionalization with the insulin-like growth factor 1 (IGF-1) [199] and some additional works regarding the feasibility of the RGD peptidic functionalization [200–202]. Such studies are mainly focused on improving the cell adhesive properties of the zirconia surfaces.

1.4.2.2 Peptidic biofunctionalization: RGD and DWIVA

Peptides can display a wide range of biological properties, including cell-adhesion, angiogenesis, osteogenesis, antibacterial, antioxidative, antithrombotic, etc. For this reason, peptides have attracted the interest of the biomedical field, and especially of tissue engineering. In this regard, peptides have become a versatile tool to improve the performance of medical implants, as they can be successfully grafted to a wide range of materials.

RGD peptide

One of the most important properties of an implant's surface is the correct integration with the surrounding tissues. *In* vivo, cells can bind to the ECM mainly through integrins, a family of heterodimeric transmembrane receptors composed of two subunits, α and β. At least half of the known integrins can bind to a specific sequence found in several ECM proteins, the Arg-Gly-Asp (RGD) amino acid sequence [61]. This cell adhesive motif can be found in several proteins including fibronectin, vitronectin, fibrinogen, osteopontin, bone sialoprotein and collagen. Once bound to the ECM, integrins oligomerize. Intracellularly, integrins promote clustering of several proteins, which are linked to actin filaments, thus establishing a link between the cell cytoskeleton and the ECM. Such complexes formed by integrins and intracellular protein aggregates (which include structural and signaling molecules such as talin, vinculin or α-actinin) are called focal adhesions [203]. The establishment of focal adhesions allows for a strong bond with the ECM and, importantly, the mechanical sensing by the cell of its extracellular environment (i.e. mechanotransduction). The adhesion of cells to the ECM through integrins mediate several cellular processes including proliferation, migration, differentiation and apoptosis [61].

Surface functionalization with RGD peptides has been therefore widely employed *in vitro* and *in vivo* to mimic the cell adhesion to the ECM on the surface of biomaterials [195,196,201,202]. RGD provides strong cell attachment sites allowing cells not only to adhere to the substrate, but also to sense the

properties of the biomaterial. Thanks to the formation of a well-developed cytoskeleton, cells can respond to the biomaterial's cues such as surface topography [78] or mechanical properties [86].

DWIVA peptide

Bone morphogenetic protein 2 (BMP-2) is a growth factor that belongs to the transforming growth factor *β* (TGF-β) super family. It has an important role in the development of bone, cartilage and in bone regeneration [204]. Importantly, BMP-2 can induce the differentiation of MSCs into osteoblast precursors, and promote their maturation [205]. Recombinant human BMP-2 has been employed in spinal fusion surgeries, although several problems including ectopic bone formation have been reported [206,207]. The use of peptides derived from BMP-2 may retain its osteogenic properties while reducing potential side effects. Moreover, peptidic functionalization of the prosthesis surface allows reducing the dose employed and avoiding its diffusion off the target, as it happens with soluble growth factors. Among the different BMP-2 derived peptides that have been found to present osteogenic properties, the *DWIVA* sequence is of particular interest due to its activity and small size [208–212]. It is derived from the wrist epitope of the human BMP-2 and includes overlapping sequences of BMP receptor I and BMP receptor II binding sites. It has shown enhanced *in vivo* bone growth around functionalized titanium implants and mineral granules, as well as increased *in vitro* osteogenesis in osteoblast-like MC3T3 cells and differentiation in MSCs [208–210].

Notably, Oliver-Cervelló *et al.* [213] studied the effects of the combined action of the RGD and the DWIVA peptides. The authors employed a peptidic platform to graft both peptides in a geometrically controlled manner on the surface. It was observed that the combination RGD-DWIVA promoted a larger increase in cell adhesion and osteogenic differentiation as compared to the presence of RGD or DWIVA alone, thus presenting a synergistic effect.

1.4.2.3 Coating strategies for peptides: L-DOPA

Different techniques can be employed to attach a biomolecule to a biomaterial's surface. The most general classification differentiates between those routes that are physical (physisorption) or chemical (covalent bonding).

Physisorption relies on electrostatic interactions (e.g. hydrogen bonding, van der Waals forces, hydrophobic interactions etc.) between the molecule and the surface. It is a simple and fast method and prevents alterations of the biomolecule, but leads to relatively unstable bonds, which can be affected by slight changes in pH or temperature. Covalent bonding, however, involves more steps but provides stronger grafting properties and is generally preferred. In this category, silane coupling agents are the most commonly employed to functionalize surfaces of metallic oxides [214]. The process begins with the reaction between the trialkoxy group of the silane and the hydroxyl groups of the surface, which must be previously activated (e.g. with an alkaline etching, plasma treatment, etc.). At the other end of the silane, a functional group (e.g. amino, vinyl, phenyl, etc.) offers the possibility of carrying out further reactions until the biomolecule is coupled [201,215,216].

Although this method is highly effective in providing strong and stable bonds, it involves multiple steps and the use of toxic solvents. In this regard, alternative biomimetic strategies have been developed. Among them, it is of particular interest the use of L-3,4-dihydroxyphenylalanine (L-DOPA), a molecule derived from the adhesive proteins found in marine mussels [217].

This molecule can bind to both organic and inorganic substrates [218,219] thanks to the chemistry of its catechol unit, which can bind non-covalently or covalently (see **Figure 29**). At an acidic pH the catechol is capable of establishing hydrogen bonds, π-π electron interactions, cation-π interactions, or coordinating with metal oxides. In this regard, it was found that the pull-of force required to separate a L-DOPA molecule from titanium (i.e. the passivated surface of titanium) was at around 800 pN, which is approximately the 40% of the strength

of a covalent bond (2000 pN for a carbon–silicon bond). However, at basic pH the catechol is oxidized into a quinone form and can crosslink covalently. In this state it can polymerize or react with other functional groups [219]. Thanks to its simplicity and high flexibility, this molecule can be employed as a one-step anchoring unit to provide a strong adhesion with a wide range of materials.

In the case of zirconia, similarly to titanium, the L-DOPA molecule can attach to the surface due to its ability to coordinate with metallic oxides. A few studies can be found on the functionalization of zirconia with L-DOPA and other related molecules (e.g. dopamine, polydopamine) [197,198].

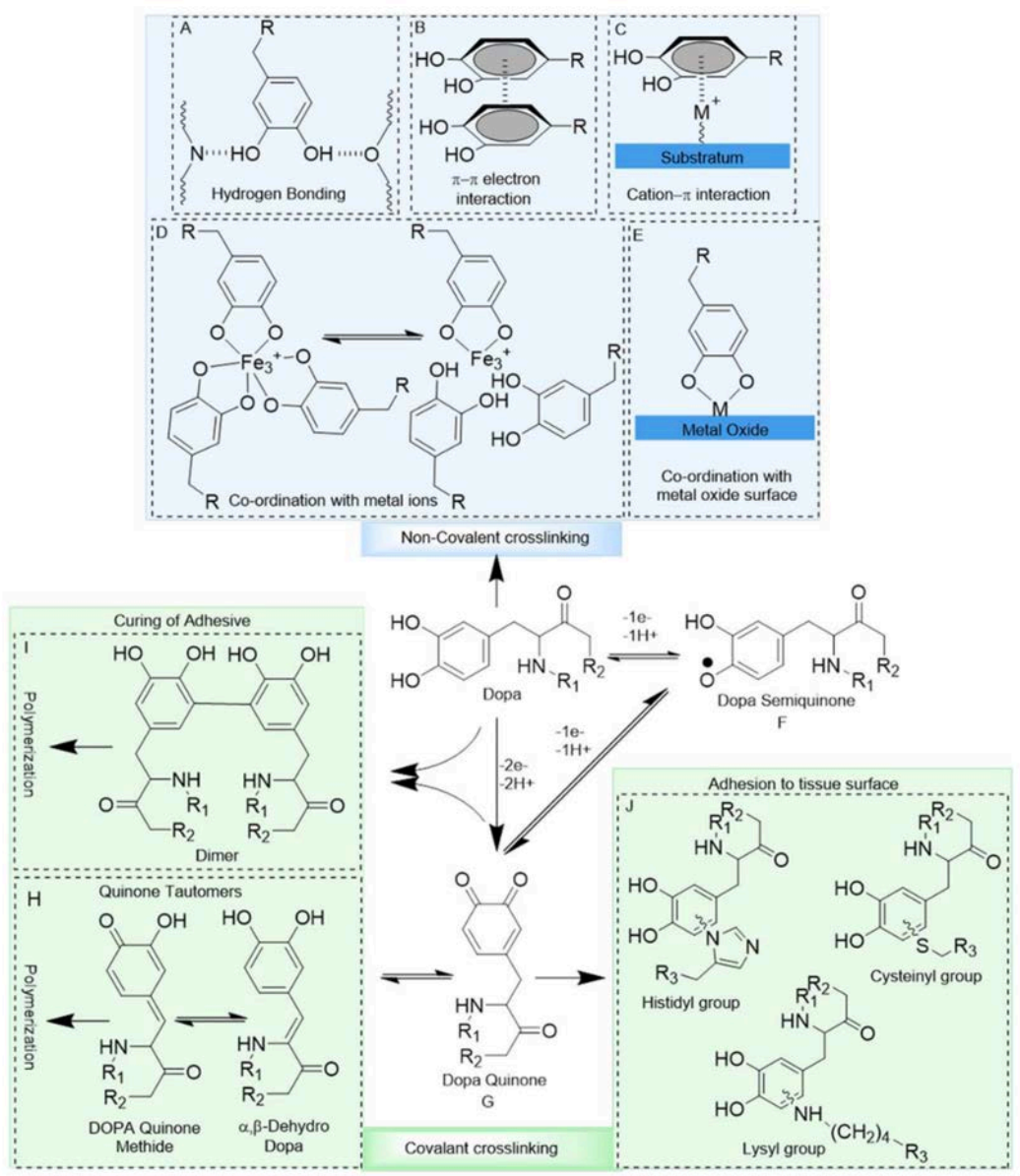

Figure 29 *Schematic representation of the possible interactions of the catechol found in L-DOPA. In its reduced form, non-covalent interactions are found (blue blocks). However, in its oxidized state it can establish covalent bonds (green blocks). Reproduced from* [219].

1.5 State of the art of dual surface modification in zirconia

Although surface topographical modification of Y-TZP is quite common both at the research level and the dental field, the use of biofunctional coatings is still scarce for this material. In this aspect, the most common approach is the modification with inorganic coatings, including bioglass and hydroxyapatite (HA) [220,221]. In contrast, organic coatings have been barely explored on these materials. The few available studies include L-DOPA and polydopamine coatings [197,198,202], the RGD peptide [200–202] and IGF-1 [199]. However, no works are found in the literature combining both approaches: *topographical modification* and *organic coatings*.

Chapter 2
Aim and structure of the thesis

2 Aim and structure of the thesis

2.1 Aim of the thesis

Since the first dental implants developed by Brånemark [222], titanium has become the "gold standard" in oral implantology. Over time, the original designs as well as the surface properties have been extensively modified in order to accelerate healing time [223]. Roughened surfaces and hydroxyapatite coatings were introduced in the 1980's. In this sense, roughened implants have been obtained by employing techniques such as sandblasting, chemical etching, laser structuring and/or anodic oxidation. On the other hand, inorganic coatings have also been explored, including the well-known hydroxyapatite, and others such as carbon, bioactive glass, titanium dioxide films and fluoride surface treatments. More recently, the release of drugs (e.g. bisphosphonates and statins), antibiotics (e.g. tetracycline) and growth factors (e.g. bone morphogenetic proteins and transforming growth factor $\beta 1$) have been introduced, as well as the study of organic coatings including synthetic peptides and recombinant proteins.

In contrast to the long and successful history of titanium, zirconia-based ceramics began their journey in prosthetic dentistry in the early 2000's, after suffering an unexpected setback in the hip replacement field. The technological challenges to surface modify a hard ceramic coupled with the critical changes in the LTD behavior, further slowed the introduction of these materials in the biomedical field. Nowadays, zirconia is the preferred choice to produce several dental parts, but its application as an implant is still reduced. Yet, some of the improvements performed on titanium implants have also been employed in zirconia including grinding, sandblasting, chemical etching, laser patterning and hydroxyapatite coatings.

In this context, the present Ph.D. Thesis will investigate topography-modifying treatments in 3Y-TZP able to improve the implant-tissue integration. The induced surface damage, phase transformation and changes in LTD resistance will be evaluated, as well as its biological effects on cell cultures. The most promising surface treatment will be further functionalized with a peptidic

platform to enhance its osteogenic and cell adhesive properties. Thus, the main goal of this Ph.D. Thesis is to combine two surface treatments on 3Y-TZP able to improve its tissue integration potential, one of physical and one of chemical nature. Throughout this Ph.D. Thesis it will be shown that, similarly to titanium, zirconia–based ceramics can be surface-modified with advanced and highly tunable methods, avoiding extensive surface damage or LTD worsening, and importantly, with industrial applicability.

Two surface treatments were chosen: grinding/polishing and laser micro-patterning. Both of them can increase the average roughness (R_a) at the micro- and sub-micrometric length scale as well as introduce directional features that can guide cell growth. However, the surface modifications are achieved by different principles, entirely mechanically in the case of grinding/polishing and thermally in the case of laser micro-patterning. Hence, differently affected microstructures (i.e. grain refinement, micro-cracks, phase transformation, etc.) and surface damage are expected. Both present their advantages and drawbacks. While grinding/polishing is faster and cheaper, laser micro-patterning can produce more reproducible and homogeneous structures. As described before, the one displaying the best outcome will be further functionalized with an osteogenic and cell adhesive peptidic platform, including the RGD and DWIVA sequences.

2.2 Structure of the thesis

The content of this Ph.D. Thesis is presented as a compendium of publications:

- In *Paper I* the changes on the surface and the subsurface after grinding/polishing 3Y-TZP will be evaluated. In particular, topographical changes, the presence of surface damage, changes in microstructure, phase transformation and residual stresses will be discussed. For this purpose, different treatments in terms of grinding severity and directionality will be compared. Results are published in "J. Minguela, S. Slawik, F. Mücklich, M.P. Ginebra, L. Llanes, C. Mas-Moruno, J.J. Roa, *Evolution of microstructure and residual stresses in gradually ground/polished 3Y-TZP*, J. Eur. Ceram. Soc. 40 (2020) 1582–1591".

- In *Paper II* the influence of grinding/polishing on mechanical properties, LTD resistance and cell behavior will be analyzed. The properties observed will be explained on the basis of the surface changes reported in *Paper I*. Results are published in "J. Minguela, M.P. Ginebra, L. Llanes, C. Mas-Moruno, J.J. Roa, *Influence of grinding/polishing on the mechanical, phase stability and cell adhesion properties of yttria-stabilized zirconia*, J. Eur. Ceram. Soc. 40 (2020) 4304–4314".

- In *Paper III* 3Y-TZP will be micro-patterned with a femtosecond laser. Surface damage, microstructure, phase transformation, residual stresses and LTD resistance will be analyzed. The surface will also be functionalized with a dual RGD/DWIVA peptidic platform. The rationale for selecting laser patterning over grinding for functionalization is detailed in *Annex A.* The effects on cell behavior derived from both the topography and the biomolecule will be discussed. Results are published in "J. Minguela, D.W. Müller, F. Mücklich, L. Llanes, M.P. Ginebra, J.J. Roa, C. Mas-Moruno, *Peptidic biofunctionalization of laser patterned dental zirconia: a biochemical-topographical approach*, Mat. Sci. Eng. C 125 (2021) 112096".

- In *Annex A* the rationale and the experimental procedure for selecting an optimal topography-modification technique will de detailed. A technique is selected between grinding and laser micro-patterning, to be further functionalized with the biomolecule in *Paper III*.

Chapter 3
Summary of the main results

3 Summary of the main results

3.1 Effects of the topographical modification techniques

Two main surface treatments able to modify topography at different length scales were studied: grinding/polishing and laser-patterning.

Grinding/polishing

In *Papers I* and *II* the main subsurface changes after grinding/polishing were characterized by means of advanced characterization techniques (i.e. field emission scanning electron microscopy; focused ion beam; confocal micro-Raman spectroscopy, etc.). The surface properties were also investigated and correlated to the observed subsurface changes. For this purpose, gradually ground/polished specimens were produced, yielding four different topographies of increasing roughness (grades 1–4) and two different textures (unidirectionally, U, and multidirectionally, M).

Regarding *Paper I*, it was found that several changes take place on the subsurface after grinding/polishing, which are correlated with the severity of the abrasion. A layer of recrystallized nano-grains was found on the ground surfaces. The thickness of this layer increased in agreement with the abrasion severity employed. Even in mildly polished specimens (1-M/U), a partially recrystallized layer could be observed. The $t \rightarrow m$ stress-induced phase transformation took place, following the same trend as displayed by surface recrystallization. As expected, due to the expansive nature of the $t \rightarrow m$ phase transformation, a layer of residual compressive stresses could be detected, reaching 1.4 GPa in the most severely ground surfaces. Simple mathematical equations relating surface average roughness (S_a), monoclinic volume fraction (V_m) and residual surface stresses could be obtained. Although the observed changes after grinding/polishing can be beneficial for the mechanical properties and the LTD resistance of the surface, damage in the form of flakes was observed in the most severely abraded specimens (4-M/U), associated to

subsurface micro-cracks. A summary of the main results presented in this work can be found on **Figure 30**.

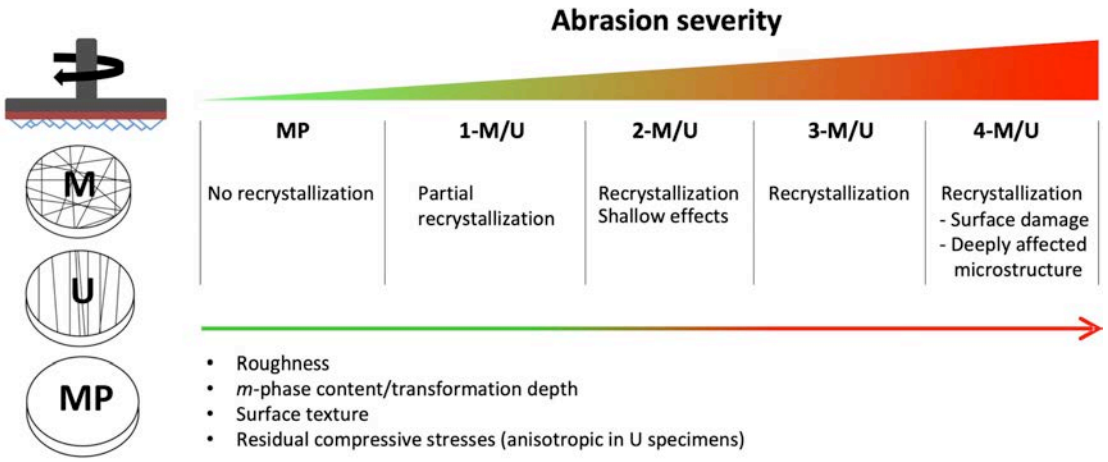

Figure 30 *Summary of the main results of Paper I. Abrasion severity is labeled from 1 to 4. Grinding directionality with M or U. MP specimens correspond to a mirror-like polished specimen employed as a reference.*

In *Paper II,* the observations made in *Paper I* were employed to explain the changes in surface properties after grinding/polishing. Contact damage response improved thanks to the layer of residual compressive stresses. In addition, the anisotropic compressive residual stresses in unidirectionally ground specimens led to anisotropic mechanical properties. LTD behavior improved with grinding/polishing and was maximum at intermediate levels of abrasion (2/3-M/U). However, in severely abraded specimens surface damage was the responsible for a drastic decrease in the LTD protection (4-M/U). Finally, human sarcoma osteogenic (SaOS-2) cells were cultured on the modified surfaces. Although no improvement in cell adhesion was detected as compared to flat reference specimens, contact guidance was observed in unidirectionally ground specimens. This only happened on the surfaces with the two highest roughness grades (S_a > 150 nm) and was evidenced by cell elongation and alignment along the grooves (3/4-U). A schematized summary of the main results presented in this work can be found on **Figure 31.**

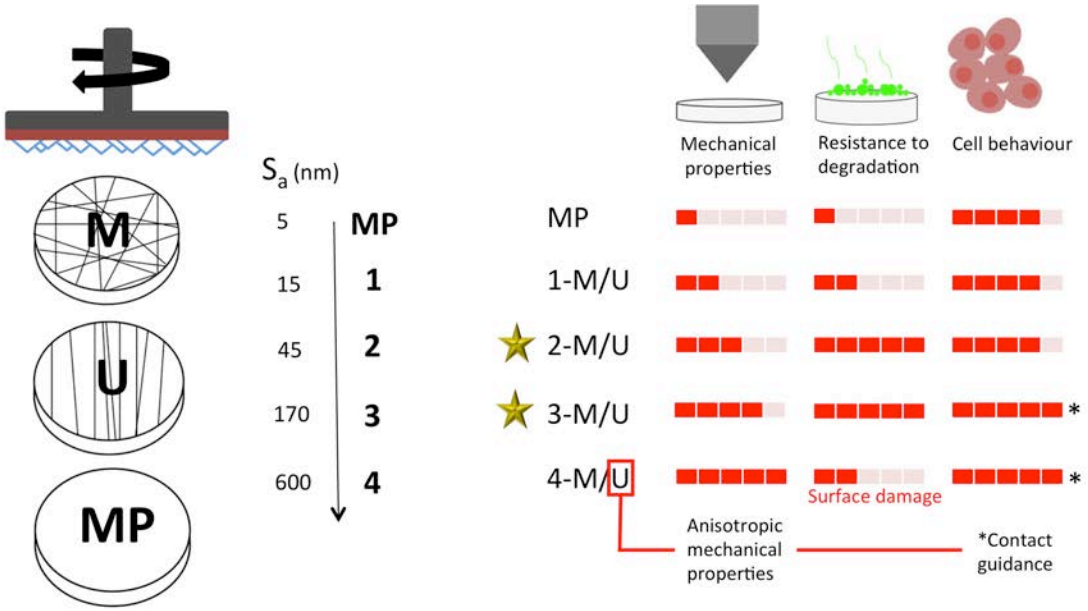

Figure 31 *Summary of the main results of Paper II. Abrasion severity is labeled from 1 to 4. Grinding directionality with M or U. MP specimens correspond to a mirror-like polished specimen employed as a reference. As depicted, 2-M/U and 3-M/U showed moderate to good mechanical properties, excellent resistance to LTD and optimal cellular responses, including cell contact guidance for 3-M/U.*

Laser patterning

In *Paper III* a linear micro-pattern was produced on the surface of 3Y-TZP with a femtosecond laser. The technique employed, direct laser interference patterning (DLIP), ensured a fast, reproducible and homogeneous pattern. In this regard, the selection of the femtosecond regime allowed decreasing the surface damage and microstructural changes on the subsurface, as compared to other pulse time regimes. In the first part of *Paper III* the effects of the laser on topography, microstructure, phase transformation, residual stresses and LTD were investigated.

Briefly, two patterns with different periodicities were produced: 3 and 10 µm. The patterns were homogeneous and a nano-topography was observed on the bottom of the valleys. It was found that just small traces

of *m*-phase were produced after modification with this technique. As a result, the residual stress state was very low, similar to the one prior to laser patterning. Damage was found on the bottom of the valleys in the form of nano-cracks and nano-pores, which was limited to the first 500 nm under the surface. Regarding LTD, accelerated tests in water steam showed that the laser treatment reduced the LTD resistance. This was related to: 1) the presence of nano-cracks, 2) small traces of *m*-phase induced by the laser treatment and 3) the increase in surface area. However, if a post-laser thermal treatment was carried out, LTD resistance was recovered and even improved with respect to the reference specimens. Thermal treatments can revert the *m*-phase to *t*-phase and relief residual stresses. The improvement respect to reference specimens was related to the nano-topography found on the bottom of the valleys, which could have a similar effect as reducing the grain size. Color changes on the surface were also observed after the laser modification. However, a thermal treatment was also able to recover the whitish look of 3Y-TZP. **Figure 32** displays a schematized summary of the main changes observed after the laser modification.

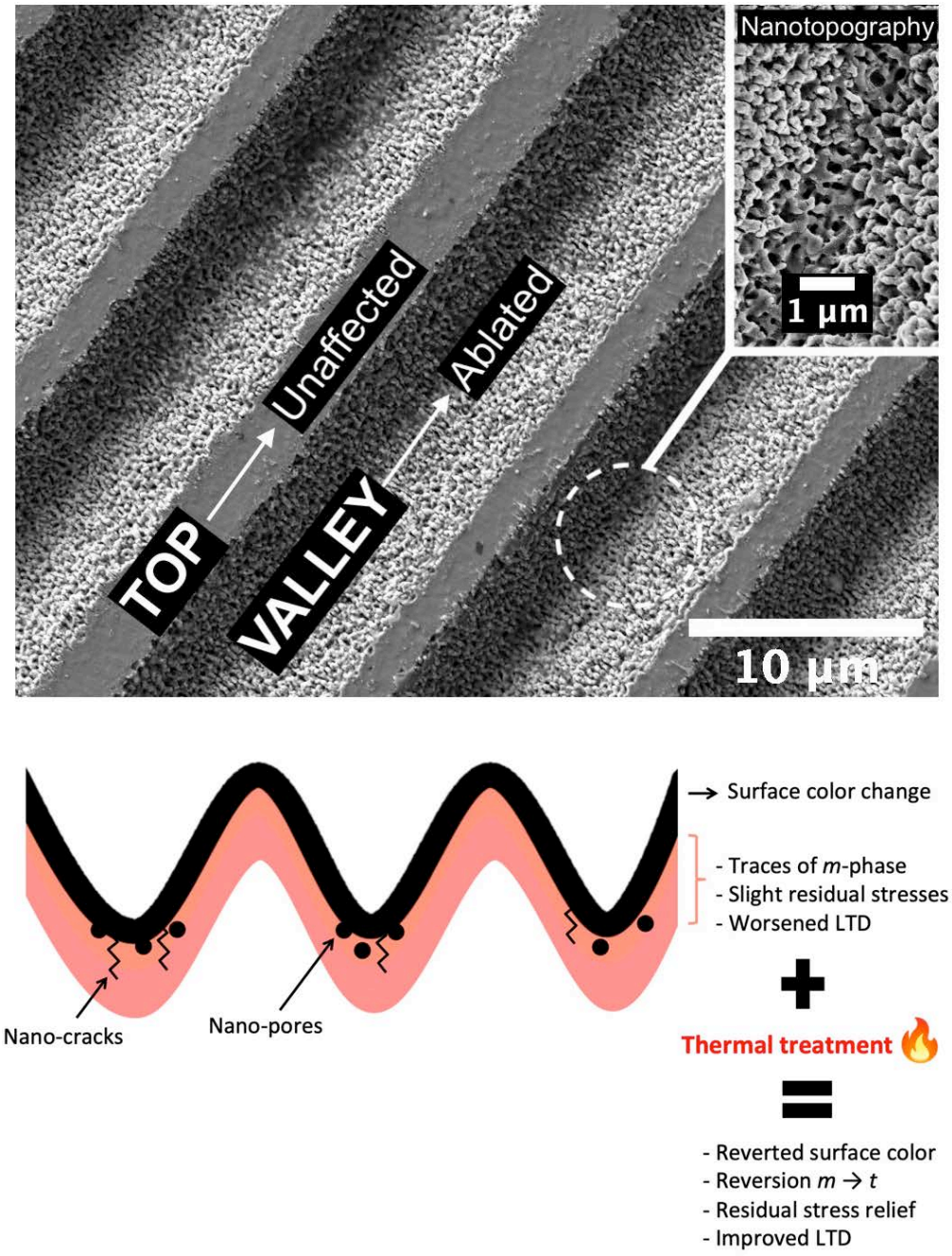

Figure 32 *Summary of the main results obtained after the characterization of laser-patterned 3Y-TZP surfaces (corresponding to the first part of Paper III). The results shown correspond to surfaces patterned with a periodicity of 10 µm.*

Similarly to the case of unidirectionally ground/polished samples, the produced laser patterned specimens could guide cell growth (MSCs) with an evident contact guidance, promoting cell alignment and elongation.

3.2 Selection of a topographical modification technique

The last part of the Ph.D. Thesis was dedicated to investigate the possible synergisms between topographical and biochemical modifications on cell behavior. However, prior to this, one of the techniques able to modify surface topography had to be chosen. In *Annex A*, a cell adhesion assay was employed to analyze and compare the effects of the topographies produced by grinding/polishing and laser patterning on cell adhesion and morphology. The most optimal surface treatment (i.e. grinding or laser-patterning) was selected. Peptide-functionalized versions of all the specimens were also included in this experiment.

It was found that while in *Paper II* the unidirectionally ground specimens could effectively produce a contact guidance in SaOS-2 cells, in the larger MSCs employed in this experiment the effects were highly reduced. This could be related to the limited size of the features that can be produced by grinding without generating excessive damage. In contrast, cells growing on the laser-patterned specimens displayed highly elongated bodies and were aligned with the grooved pattern. The advantage of laser micro-patterns over grinding lie on the ability of producing different periodicities and depths with a limited surface damage. In contrast, the increase of roughness in ground surfaces (i.e. pattern depth) is always associated with higher levels of surface damage. For these reasons, laser patterning was chosen as the best technique to proceed with surface biofunctionalization.

3.3 The combined effects of topography and peptidic biofunctionalization

In the second part of *Paper III*, laser patterned-samples were functionalized with a peptidic biomolecule including the cell-adhesive RGD and the osteogenic DWIVA motives, aiming at investigating the combined effects and possible synergies between topographical features and chemical biofunctionalization. A scheme of the rationale behind this study can be found in **Figure 33**.

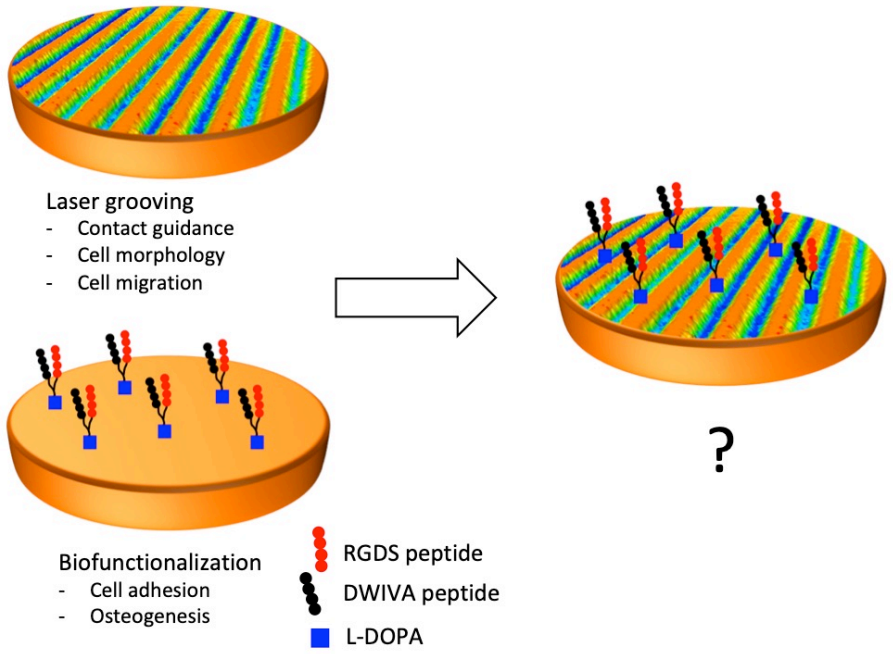

Figure 33 *Two different strategies were employed in order to improve the tissue integration potential of 3Y-TZP surfaces, one of topographical and one of biochemical nature. The main known effects on human cells from each strategy are detailed on the figure.*

In the first place, a higher concentration of the peptidic biomolecule attached to the patterned surfaces was observed, as compared to flat specimens, due to the increase in surface area.

Moreover, the patterns guided cellular attachment and migration. On these surfaces, cells with elongated bodies parallel to the grooves were observed. Cell migration was greatly enhanced in the patterning direction as compared to flat specimens, while movement in the perpendicular direction was highly reduced.

As for the peptidic platform, improved cell attachment, well-developed cytoskeletons and larger cell area were observed, but no effects regarding cell migration were detected.

Although some osteogenic potential was found in 10L specimens (i.e. the ones grooved with a periodicity of 10 μm), the largest effects were observed from the biomolecule, which favored upregulation of several genes related to osteoblastic differentiation in all the surfaces.

Hence, the combination of topographical features and the peptidic platform provided a powerful tool to tune and enhance cellular responses, which indicate potential to improve tissue integration. As schematized in **Figure 34**, while topographical features could guide cellular growth, the biomolecule improved cell attachment and osteogenic properties.

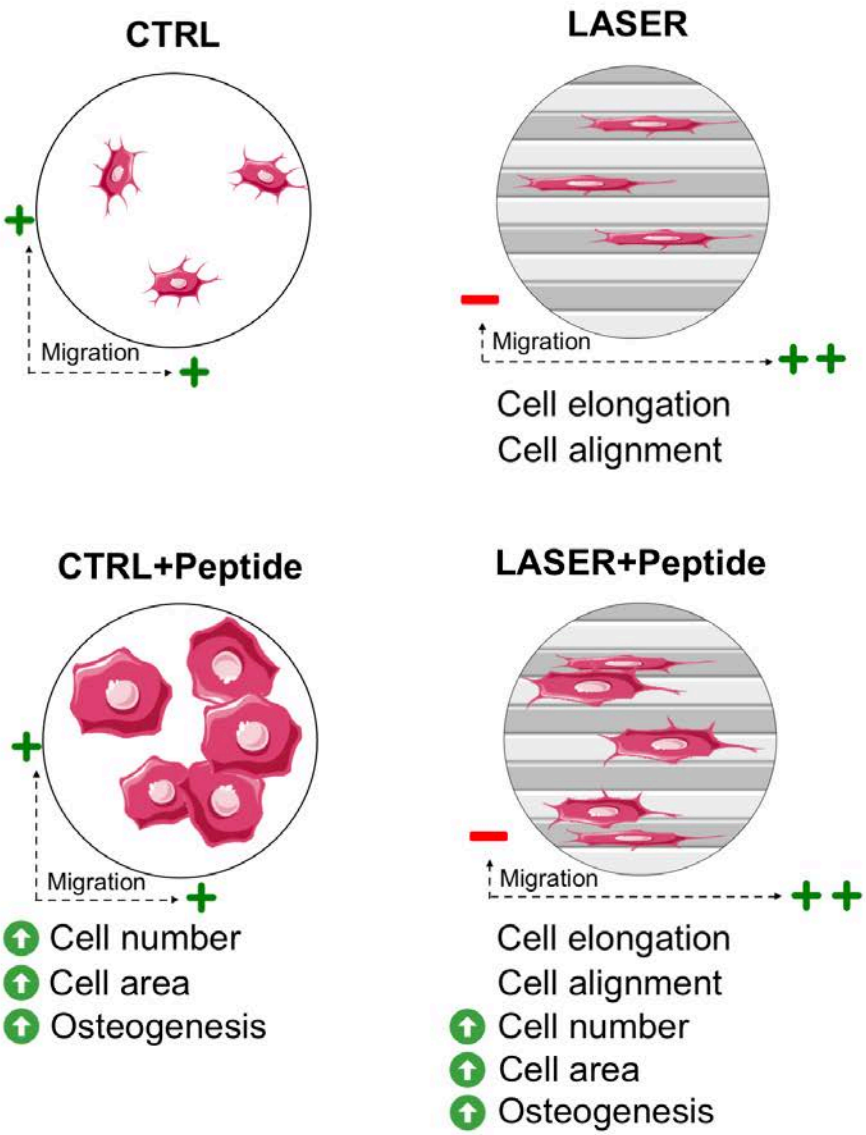

Figure 34 *Scheme of the main results obtained from the characterization of cell response on laser treated and functionalized specimens. CTRL samples correspond to mirror-like polished specimens employed as a flat topography reference.*

Chapter 4
Paper I

Evolution of microstructure and residual stresses in gradually ground/polished 3Y-TZP

Available at:

https://www.sciencedirect.com/science/article/abs/pii/S0955221919307289

Journal of the European Ceramic Society 40 (2020) 1582–1591

Contents lists available at ScienceDirect

Journal of the European Ceramic Society

journal homepage: www.elsevier.com/locate/jeurceramsoc

Original Article

Evolution of microstructure and residual stresses in gradually ground/polished 3Y-TZP

J. Minguela[a,b,c], S. Slawik[d], F. Mücklich[d], M.P. Ginebra[a,c,e], L. Llanes[b,c], C. Mas-Moruno[a,c,*], J.J. Roa[b,c,*]

[a] Biomaterials, Biomechanics and Tissue Engineering Group (BBT), Department of Materials Science and Metallurgical Engineering, Universitat Politècnica de Catalunya, 08019 Barcelona, Spain
[b] Center for Structural Integrity, Reliability and Micromechanics of Materials (CIEFMA), Department of Materials Science and Metallurgical Engineering, Universitat Politècnica de Catalunya, 08019 Barcelona, Spain
[c] Barcelona Research Center in Multiscale Science and Engineering, Universitat Politècnica de Catalunya, 08019 Barcelona, Spain
[d] Functional Materials, Department of Materials Science and Engineering, Saarland University, 66123 Saarbruecken, Germany
[e] Institute for Bioengineering of Catalonia (IBEC), Barcelona Institute of Technology (BIST), 08028 Barcelona, Spain

ARTICLE INFO

Keywords:
Zirconia
Grinding
Microstructure
Phase transformation
Residual stresses

ABSTRACT

A comprehensive study of progressively ground/polished 3Y-TZP was performed with the aim of better understanding the mechanisms driving the microstructural modifications observed after such procedures, and identifying the processing parameters leading to optimal microstructures (i.e. ageing-protective and damage-free). Gradually ground/polished surfaces were produced, yielding four different topographies of increasing roughness (grades 1–4) and two different textures (unidirectionally, U, and multidirectionally, M). Phase transformation, microstructure and residual stresses were investigated by means of advanced characterization techniques. It was found that low-roughness mildly ground/polished specimens (i.e. 2-M/U) presented a nanometric layer with the ageing-related protective features generally associated with coarsely ground specimens. A lower limit for grain refinement in terms of surface abrasion was also found, in which partial recrystallization took place (i.e. 1-M/U). A mathematical relation was established between average surface roughness (S_a), monoclinic volume fraction (V_m) and surface compressive residual stresses, demonstrating that if the processing parameters are controlled, both V_m and residual stresses can be predicted by the measurement of S_a.

1. Introduction

Polycrystalline tetragonal zirconia doped with 3 mol.% yttria (usually referred to as either 3Y-TZP or 3Y-ZrO_2) has been widely used as a structural ceramic due to its outstanding mechanical properties [1]. For instance, in the case of prosthodontics, several components are produced using zirconia-based materials such as implants, abutments, crowns, bridges and endodontic posts and cores [2–4]. During the manufacture process, several shaping and surface finishing steps are commonly involved, including computer-aided design/computer-aided manufacturing (CAD/CAM) machining, drilling, cutting, grinding or polishing. All of them are known to introduce surface defects as well as microstructural and crystallographic changes [5–8].

Grinding processes are routinely used as finishing steps; and thus, microstructural changes after such surface treatments have been studied in detail. In this regard, a close inspection of ground specimens by Muñoz-Tabares *et al.* [5] revealed three different microstructural layers just below the surface: 1) a first zone of recrystallized nano-grains in the range of 10–20 nm; 2) a plastically deformed zone; and 3) a layer where abundant stress-induced tetragonal (t) to monoclinic (m) transformation ($t \rightarrow m$) took place, generating residual compressive stresses.

As a result of its ability to generate such changes, grinding has attracted researchers interest as a means of modifying surface properties. Both mechanical behaviour [9,10] and ageing resistance [11,12] can be modified through the introduction of compressive stresses (as well as detrimental cracks and flaws), but also in response to the presence of nano-grains and the reduction in domain size by ferroelastic switching [7,13,14]. In particular, the addition of a thin layer of residual compressive stresses can improve mechanical properties and is able to stabilize the t-phase, hindering the nucleation and propagation of the m-phase in the so-called hydrothermal degradation process [15], also known as ageing or low-temperature degradation [16]. In this aspect,

* Corresponding authors at: Barcelona Research Center in Multiscale Science and Engineering, Universitat Politècnica de Catalunya, 08019 Barcelona, Spain.
E-mail addresses: carles.mas.moruno@upc.edu (C. Mas-Moruno), joan.josep.roa@upc.edu (J.J. Roa).

https://doi.org/10.1016/j.jeurceramsoc.2019.10.057
Received 30 July 2019; Received in revised form 21 October 2019; Accepted 29 October 2019
Available online 04 November 2019
0955-2219/

the presence of a nanograined layer on the surface has also proven to be beneficial, displaying a protective effect due to the reduced grain size [17,18].

As a consequence of the intense changes introduced after severe grinding, most of the published data are related to the effects produced by this harsh condition. However, microstructural effects obtained using softer procedures are commonly neglected; and thus, structural information of intermediate surface states is lost. Hence, a comprehensive study including milder polishing/ grinding procedures would be of relevance, because i) the characterization of intermediate stages can expand the current knowledge about the mechanisms driving microstructural modifications, and ii) the screening of different and progressive surface states can serve to identify and optimize the processing parameters leading to the best microstructured surfaces (i.e. in terms of ageing resistance and surface damage).

Within this context, in the present work a comprehensive characterization study was carried out, including surface conditions that range from mirror-like polished to coarsely ground. Special emphasis was put on intermediate conditions, with the main goal of studying the changes and evolution from a free of defects bulk-like material into a severely affected surface, in terms of microstructure, phase transformation and residual stresses.

2. Experimental procedure

2.1. Specimen preparation

Specimens were produced from zirconia powders stabilized with 3 mol.% yttria (TZ-3YSB-E, Tosoh, Japan). The powders were shaped by uniaxial pressing at 50 MPa, followed by cold isostatic pressing at 288 MPa. The green bodies were then sintered in air at 1450 °C for two hours with heating and cooling rates of 3 °C/min (LHT 02/17, Nabertherm). By this method, 15 mm diameter disc-shaped specimens were obtained. In order to characterize the starting material, specimens were mirror-like polished and grain size, density, hardness and indentation fracture toughness were measured. Grain size was evaluated by thermally etching the samples, and subsequent examination of them by Field Emission Scanning Electron Microscopy (FESEM, Carl Zeiss Neon 40). Five images per sample in three different specimens were taken in order to have statistical significance and the linear interception method was used. Density was characterized by the Archimedes method in distilled water. Finally, hardness was obtained from 1 kgf Vickers indentations and fracture toughness was calculated with the method proposed by Niihara et al. [19] using 30 kgf indentations. Four indentations per specimen in three different specimens were used for both measurements. The properties of the starting material are summarized in Table 1.

2.2. Superficial modification: grinding/polishing treatments

Different surface finish conditions were obtained by polishing the samples in a Buehler Ecomet4 automatic polishing machine, coupled with an Automet2 power head. Four different roughness grades and two different patterns were produced: multidirectional (M) and unidirectional (U) grooves. Besides, one mirror-like polished specimen (MP) was used as a reference. Table 2 shows the codes for the different specimens tested as well as the different parameters employed to superficially modify each sample.

Table 1
Summary of the main microstructural and mechanical properties of the starting 3Y-TZP material.

Grain size (μm)	0.32 ± 0.12
Density ($g{\cdot}cm^{-3}$)	6.08 ± 0.01
Hardness (GPa)	13.46 ± 0.34
Indentation fracture toughness (MPa·√m)	5.09 ± 0.02

2.3. Surface characterization

Surface roughness of the obtained topographies was measured by white light interferometry (WLI, Veeco Wyko 9300 N T). FESEM was employed in order to observe general appearance, topographical features and surface damage right after treatment. Aiming to get detailed information of the sub-surface, cross-sections were prepared by means of Focused Ion Beam (FIB, Carl Zeiss Neon 40) using a Ga^+ source. Prior to FIB milling, a protective thin platinum layer was deposited on the region of interest. Current as well as acceleration voltage were continuously decreased down to a final polishing stage at 500 pA and 30 kV.

Crystalline phases were determined by X-Ray Diffraction (XRD) and confocal micro-Raman Spectroscopy. XRD (D8-Advance, Bruker) was carried on both Bragg-Brentano symmetric geometry configuration ($k_{\alpha-1}$ Johansson Typ monochromator in the primary side, parallel plate collimator with a LynxEye detector in the secondary side) and grazing incidence angle at $\omega = 1^\circ$ (Goebel mirror in the primary side, parallel plate collimator with scintillation detector in the secondary side). The analysis was performed from $26^\circ \leq 2\theta \leq 37^\circ$ on a diffractometer using Cu K_α radiation (40 kV and 40 mA) with 0.02° step size and 1 s/step. For Bragg-Brentano symmetric configuration the penetration depth of the incident X-rays (i.e. the thickness of the sample, where 90% of the information recorded in a diffractogram is gathered) at $2\theta = 30^\circ$ is around 5 μm according to the Lambert-Beer's law, while on the grazing incidence angle experiment it is reduced to around 300 nm. The volume fraction of the monoclinic phase (V_m) was calculated with the equation proposed by Toraya et al. [20], as follows:

$$V_m = \frac{1.311[I_m(\bar{1}11) + I_m(111)]}{1.311[I_m(\bar{1}11) + I_m(111)] + I_t(101)} \quad (1)$$

where I_m and I_t correspond to the intensities of the monoclinic and tetragonal peaks, respectively.

In-depth *m*-phase distribution was characterized with confocal micro-Raman spectroscopy (inVia Qontor, Renishaw) with a Nd:YAG laser (wavelength 532 nm, integration time 0.1 s). Phase maps under the surface were obtained. To do that the discs were cut in half, as depicted in Fig. 7e, and the cross-sections were mirror-like polished. Volume fraction of *m*-phase was quantified by using the equation proposed by Katagiri et al. [21]:

$$V_m = \frac{I_m^{181} + I_m^{190}}{2.2I_t^{147} + I_m^{181} + I_m^{190}} \quad (2)$$

where I_m and I_t correspond to the integrated intensities of the monoclinic and tetragonal bands, respectively. Numbers indicate Raman shift in cm^{-1}.

In order to reveal the microstructure and be able to study the surface recrystallization effect, some specimens were thermally etched (1100 °C for 1 h, with heating and cooling rates of 12 °C/min) and subsequently observed by FESEM.

Surface residual stresses were calculated with the $\sin^2\psi$ method by XRD analysis (Empyrean, PANalytical) using Cu K_α radiation (40 kV and 40 mA). An X-ray lens with cross aperture (primary side) and parallel plate collimator with 0D proportional counter detector (secondary side) were employed. The tetragonal $(101)_t$ peak found at $2\theta = 30.2^\circ$ was used for the stress calculations, at Chi angles from -60° to +60° in 13 steps. The use of a peak at low 2θ was necessary to obtain an X-Ray penetration depth similar to the thickness of the stressed layer. The loss of sensitivity at small 2θ angles was reduced by using parallel plate collimators on the secondary side [22]. As the stress measurements performed in the $(101)_t$ may be influenced by surrounding peaks, such as the $(111)_t$, some of the spectra were deconvoluted with the PANalytical HighScore Plus software, in order to

Table 2
Summary of the codes and grinding/polishing parameters of the superficially modified specimens.

Roughness grade	Pattern direction		Code	Grinding/polishing parameters				
				Disk/cloth	Diamond slurry	Load (KPa)	rpm	
-	-		MP	Ground and polished with water-based diamond slurries (30μm - 6μm - 3μm) with a final alumina suspension (0.02 μm) step in a Struers MD-Nap.				Mirror-like polishing
1	Multidirectional (M)	Unidirectional (U)	1-M	Struers MD-Dac	9 μm	50	150 + lubricant	Polishing
			1-U					
2			2-M	Struers MD-Plan	30 μm		150 + lubricant	Polishing
			2-U					
3			3-M	Struers MD-Piano 220	-		300 + water cooling	Grinding
			3-U					
4			4-M	Struers MD-Piano 80	-		300 + water cooling	Grinding
			4-U					

obtain more accurate values. Given the high amount of recorded spectra, this methodology was only performed in selected samples. In order to characterize the anisotropy of the stress state, measurements were done along three different directions on the surface ($\Phi = 0^\circ$, 45° and 90°). For samples with unidirectional scratches, $\Phi = 0^\circ$ and $\Phi = 90^\circ$ correspond to a direction parallel and perpendicular to the grooves, respectively. For samples with multidirectional grooves, the angles were chosen arbitrarily. Stress analysis was performed by using the PANalytical X'Pert Stress plus software. The X-ray elastic constants (XECs) used for such calculations were S_1 = -1.58 TPa^{-1} and $\frac{1}{2}S_2$ = 6.50 TPa^{-1} [23].

A piezo-spectroscopic technique was also employed in order to obtain cross-sectional macro-stress maps of the *t*-phase. This technique has already been used by other authors for the assessment of stresses in zirconia-based materials [24–26]. Stresses can change the frequency of vibrational modes and induce shifts in Raman bands. These Raman shifts can be related to hydrostatic stress through the following equation:

$$\Delta\omega = 3\Pi_t\langle\sigma\rangle_t \quad (3)$$

where $\Delta\omega$ is the Raman band shift in cm^{-1}, $\langle\sigma\rangle_t$ is the average hydrostatic stress in the tetragonal phase in GPa and Π_t is the uniaxial piezo-spectroscopic coefficient for the chosen tetragonal band in cm^{-1}/ GPa. In order to know the piezo-spectroscopic coefficient, a calibration process is necessary. In this work, piezo-spectroscopic coefficients determined by Pezzotti and Porporati in 3Y-TZP have been used [25] for the *t* band found around 146 cm^{-1}. Raman band positions were obtained by fitting the data to Gaussian curves with commercially available software (WiRE 4.4, Renishaw). Residual stresses were calculated from the spectroscopic data obtained in cross-sections.

3. Results and discussion

The overlapping of individual abrasions during grinding/polishing procedures, progressively eroded the surface resulting in a characteristic grooved topography. Fig. 1 shows the FESEM micrographs of the studied surfaces after grinding/polishing. The average surface roughness (S_a) obtained by WLI is summarized at the top and the bottom of the micrographs for the M and U specimens, respectively. A clear linear pattern is observed in all the images. By choosing the adequate abrasive and polishing dynamics, the obtained topographical features were finely tailored, including different surface roughness and patterning texture. While M conditions presented multidirectionally oriented scratches, U conditions were constituted by almost parallel grooves. From 1 to 4, an increase in roughness with deeper valleys and higher peaks was noticed, in accordance with the use of rougher abrasive particles. Likewise, for the roughest condition, more evident and extended signs of damage were present. For conditions 1 to 3, the lack of visible surface cracks, smooth and homogeneous tracks without chipping, and the presence of serrated and irregular edges, which indicated that extruded material at the sides of the grooves (ploughing) had been detached, pointed out to ductile material removal mechanisms. At sufficiently low cutting depths, plastic flow is more energetically favourable than brittle fracture, and is the responsible for material removal even in intrinsically fragile materials [27]. Hence, a surface free of defects from brittle fracture events was obtained. Despite brittle regime was not reached in any of the studied specimens, in the case of the rougher structures (i.e. 4-M/U) additional damage mechanisms (e.g. flaking, material detachment and micro-cracks) were activated, as depicted in Fig. 2. On such specimens, due to the higher friction between the abrading particles and the surface, extensive damage in the form of micro-cracking was observed along some of the grooves. Fig. 2 presents a magnified FESEM micrograph showing this kind of surface defects, related to ductile flaking [28]. This created a track of aligned semi-circular flakes, such as the ones observed in Fig. 2a. Material detachment also occurred in some of the most damaged grooves, revealing the sub-surface grainy microstructure (Fig. 2b, zones marked as A, B, C and D).

The effects of abrasion in such procedures are not only limited to topographical modifications and surface damage, but are also able to introduce crystalline phase transformations, lattice distortions and texture [5]. As shown in Fig. 3a, where the results of XRD experiments in Bragg-Brentano symmetric geometry are displayed, several crystallographic changes were identified after modifying the surface. While MP and 1-M spectra overlapped almost entirely, 2-M, 3-M and 4-M presented important alterations, progressively intensified with the severity of the applied abrasion. As the diamond particles erode the material, the accompanying shearing and tensile stresses in the sub-surface destabilize the metastable *t* phase, which undergoes a martensitic transformation into *m* one [29]. Accordingly, the most evident change in spectra after grinding was the increase in the content of *m*-phase at the surface, as shown in Figs. 3b and d, which increased almost linearly to a maximum of V_m = 7% in 4-M. Furthermore, in the left side of the $(101)_t$ a tail was observed, increasing in intensity from 2-M to 4-M. This peak was first proposed to be associated with a rhombohedral phase (*r*-phase) [30], arising from the transformation of cubic grains ($c \rightarrow r$) under high stresses, or from the transformation of the tetragonal phase ($t \rightarrow r$), as suggested by other authors [31,32]. It has also been associated with lattice distortions produced after grinding [33].

One of the known mechanisms of zirconia to accommodate stresses

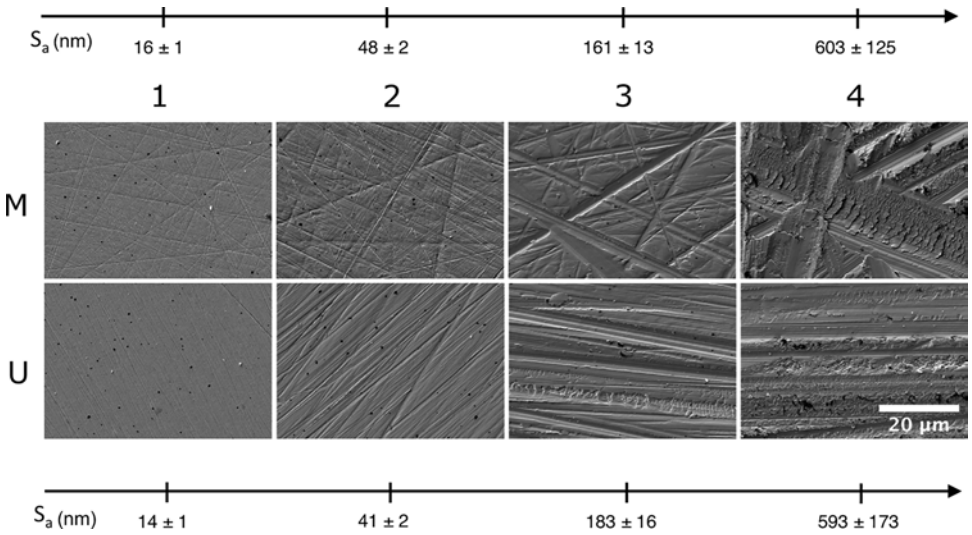

Fig. 1. FESEM micrographs of the different topographies obtained. Multidirectional (M) patterns are displayed in the first row, while unidirectional (U) patterns are presented in the second. From left to right, increasing levels of roughness, 1–4 (more information available in Table 2). On the top and bottom, average surface roughness (S_a) in nm is available for the M and U patterns, respectively.

is the ferroelastic switching of domains [7,13]. Under high biaxial stresses such as the ones produced during grinding, the *c*-axis of the *t* phase reorients perpendicularly to the surface [5,34,35]. This domain reorientation promotes the onset of texture (i.e. a preferential crystallographic orientation), as revealed by the changes of the $(002)_t$ / $(200)_t$ intensity relation [7]. Figs. 3c and 3e display the relation between these two peaks, showing that similarly to the increase in *m*-phase, as the abrasion gets more severe, an increase in texture is noticed. Regarding surface directionality, M and U specimens showed no significant differences (results not shown) and hence just diffractograms for the M specimens are presented.

The high strain introduced after surface mechanical treatments can produce changes in microstructure, which are able to affect material's properties such as the hydrothermal degradation behaviour [17]. As shown in Fig. 4a, three distinctive microstructural regions were observed under the surface of 3Y-TZP after grinding (labelled as regions 1, 2 and 3), in a 4-M cross-sectioned specimen. These microstructural features are in agreement with previous studies [6,35] and are described in detail by Muñoz-Tabares et al. [5]. As reported in [5], *in-situ* recrystallization occurs in the first nanometres (in a layer of about 300 nm), where a refined microstructure is observed. Due to the high strain, progressive misorientation of dislocation cells lead to the formation of new nano-sized grains, in the range of 10–20 nm (region 1). Below (region 2), plastically deformed grains in a direction parallel to the surface are observed, followed by a third layer of bulk-like grains in which monoclinic laths are identified (region 3). Two monoclinic laths found in this region are shown in the inset of Fig. 4a. It should be noted that, in the present work, shallow micro-cracks extending parallel to the surface were observed in the first region, linked to the flakes observed in Fig. 2. The steep difference in properties between the nano-sized and the plastically deformed layer and the fact that flaking is intrinsically parallel to the surface, may avoid its propagation to deeper regions.

Although microstructure after grinding and other procedures involving intense abrasion have been thoroughly studied [5,6,8,35,36] changes after mild procedures such as polishing are quite unknown. Fig. 4b shows the microstructure of 2-M specimens, polished with a 30 µm diamond slurry, as detailed in Table 2. Less intense microstructural modifications were present in this case, and just two defined zones were observed: a very shallow first layer of nano-sized grains, with a thickness smaller than 100 nm; and a second layer of bulk-like

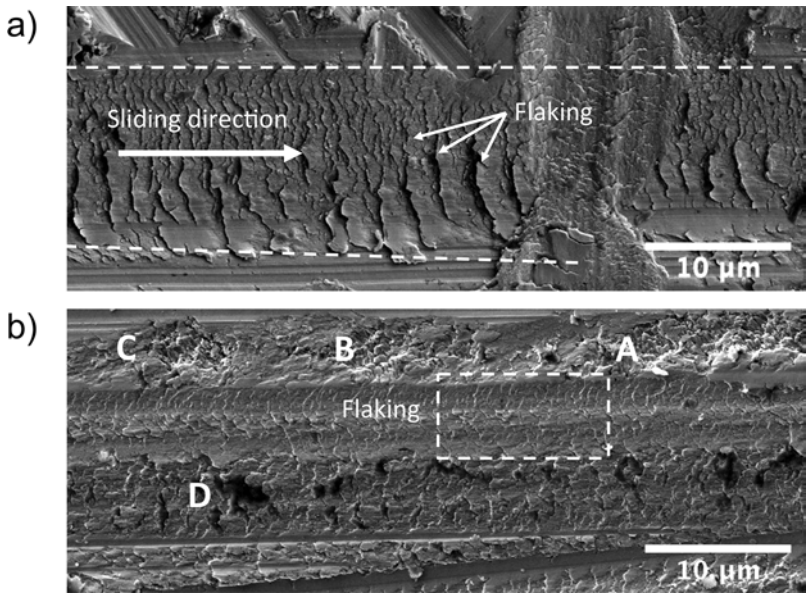

Fig. 2. Different modes of surface damage for the specimens 4-M/U. a) Flakes left by a particle sliding from left to right in 4-M. Dotted lines delimit the edge of the groove and b) damage in 4-U. The dotted square outlines an area with flaking. Labels A, B, C and D identify zones with material detachment.

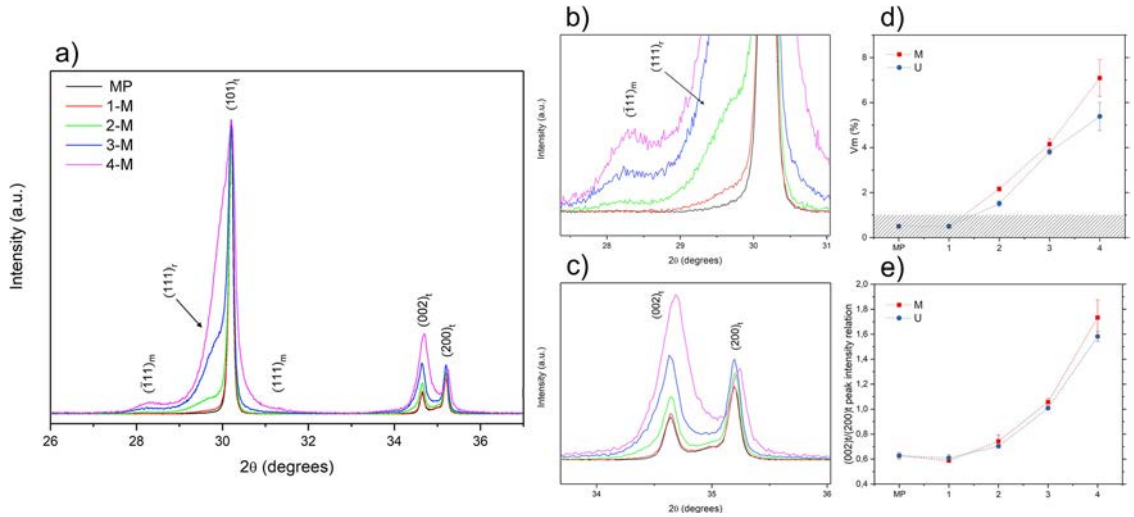

Fig. 3. Results of the XRD experiments in Bragg-Brentano symmetric geometry, n = 3. a) XRD spectra of representative specimens, b) and c) magnifications of the $(\bar{1}11)_m$ peak and the $(002)_t$ /$(200)_t$ tetragonal doublet, respectively. d) m-phase volume fraction. Dashed area corresponds to the detection limit of the technique, V_m = 1%. e) $(002)_t$ /$(200)_t$ intensity relation.

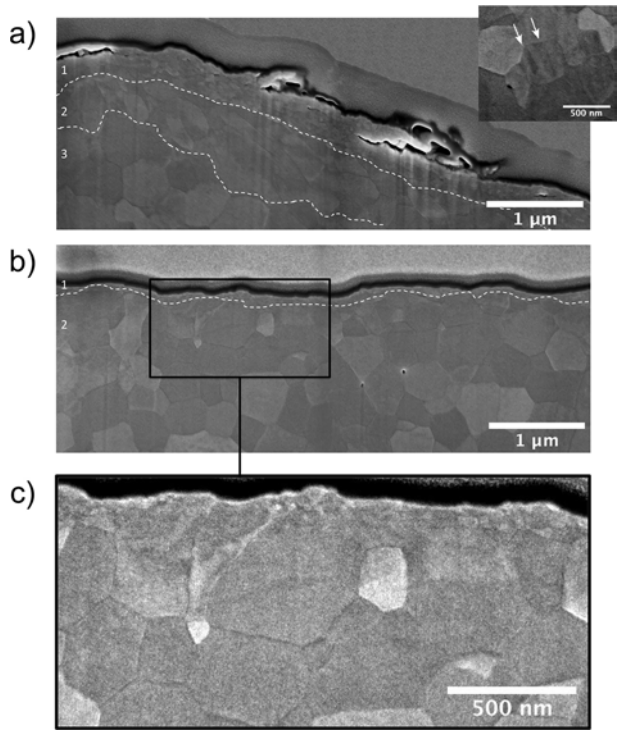

Fig. 4. Sub-superficial microstructure of a) 4-M and b) 2-M specimen. c) Magnification of a region in 2-M. Dashed lines in a) and b) delimit the different regions. Inset in a) identify two monoclinic laths (see white arrows). Note that a very shallow layer of nano-grains is discerned in c), without any sign of plastic deformation.

material where no deformed grains and no monoclinic twins were observed. As illustrated in Fig. 4c, a magnification of the first micron under the surface presented no signs of plastically deformed grains with a sudden transition between an extremely shallow refined layer and the bulk-like material.

A nano-sized grain layer, as the ones observed in Fig. 4, can successfully protect zirconia-based materials from ageing [17]. Grinding has been used for such purpose [11], but for many applications surface roughness or micro-damage produced after these treatments may not be acceptable. The present results evidence that softer procedures, leading to lower levels of surface damage and roughness, may also introduce some of the protective features generally associated with coarsely ground zirconia.

In order to have a better insight about grain refinement, M specimens were thermally etched. Thermal etching is carried out in polished surfaces and involves a mass transport away from grain boundaries, so that grooves develop and boundaries become visible [37]. Fig. 5 shows the surface microstructure after thermally etching the specimens at 1100 °C for 1 h. MP specimen presented a grain size distribution around 300 nm, in agreement with values reported by other authors working with similar conditions (Fig. 5a) [5,38]. Instead, 2-M, 3-M and 4-M (Figs. 5c, d and e), displayed a layer of recrystallized nano-grains covering the surface, in accordance with the presence of a superficial nano-sized grain layer (Fig. 4). As reported by other authors after high resolution TEM observations, the dynamically recrystallized grains present a size in the order of 20 nm [5], but grow during the annealing process depending on the chosen etching temperature [35]. In the case of 1-M (Fig. 5b), however, an intermediate behaviour was observed, with a combination of both bulk-like and nano-sized grains. As shown in the magnification of Fig. 5f, the surface presented a bimodal distribution with large grains in the order of 300–400 nm (left side of the micrograph) and small ones below 100 nm (right side of the micrograph). Accordingly, the surface of 1-M seemed to be in the limit of strain required for nano-structuring, with just some of the grains accumulating enough strain to fully recrystallize. The experiments carried out suggest that under the used conditions (i.e. load, speed, polishing equipment, etc.) a polishing procedure providing a surface roughness as low as $S_a = 16 \pm 1$ nm is able to initiate the recrystallization process, highlighting the extreme sensitivity of 3Y-TZP to be surface modified.

As it has been shown by different techniques (e.g. XRD, FESEM and FIB/FESEM), important structural changes occurred on the very first nm of the surface upon grinding. Due to the reduced thickness of the affected layer, the evaluation of crystalline phases on an even smaller scale seems necessary. For such purpose, XRD in grazing incidence of 1° was performed in a superficial layer of around 300 nm. Results for M specimens are displayed in Fig. 6a. If compared to Fig. 3, MP and 1-M spectra were still similar to each other, although in this case both of them showed a slight hump on the left side of $(101)_t$, a little amount of *m*-phase (Fig. 6b), as well as higher $(002)_t/(200)_t$ ratio (Fig. 6c). For the rest of specimens, a significant increase in *m* phase and texture was appreciated. For these conditions, 2-M, 3-M and 4-M, $(101)_t$ was shifted around 0.5° to lower angles, giving way either to the $(111)_r$, or to a peak produced by the distortion of the tetragonal lattice [33]. Content of *m*-

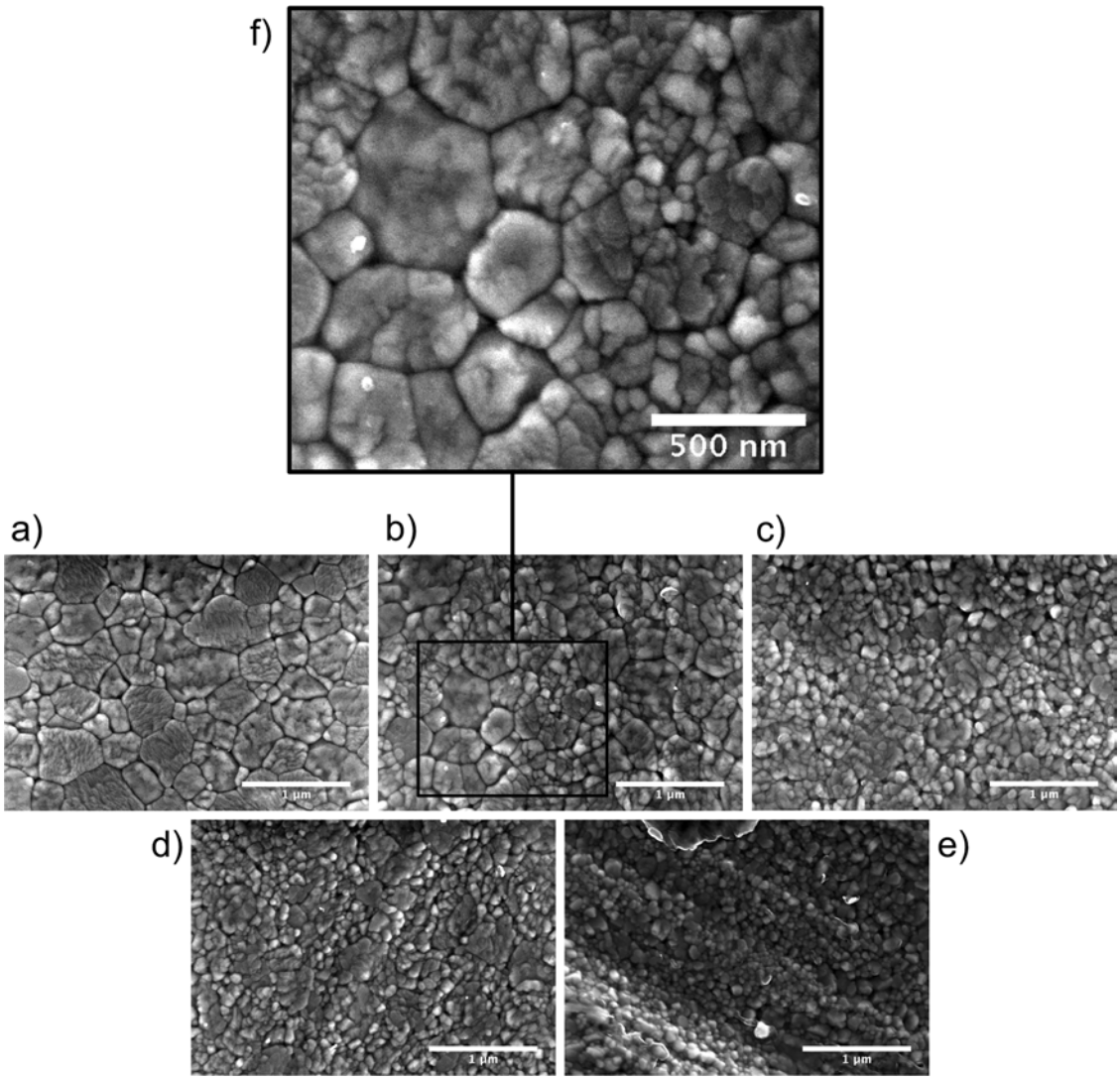

Fig. 5. FESEM micrographs of the thermally etched specimens. a) MP b) 1-M c) 2-M d) 3-M e) 4-M, f) magnification of 1-M. Micrographs show: a) bulk-like sized grains. c), d) and e) surface covered by recrystallized nano-grains. b) Intermediate behaviour with both bulk-like and nano-sized grains.

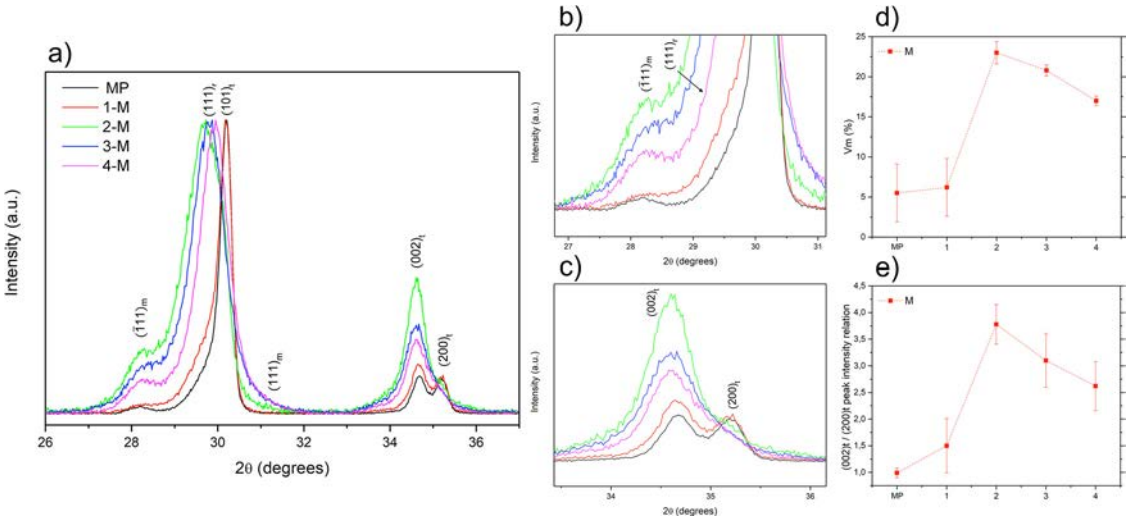

Fig. 6. Results of the XRD experiments in grazing incidence at 1°, n = 3. a) XRD spectra of representative specimens, b) and c) magnifications of the $(\bar{1}11)_m$ peak and the $(002)_t$ /$(200)_t$ tetragonal doublet, respectively. d) m-phase volume fraction and e) $(002)_t$ /$(200)_t$ intensity relation.

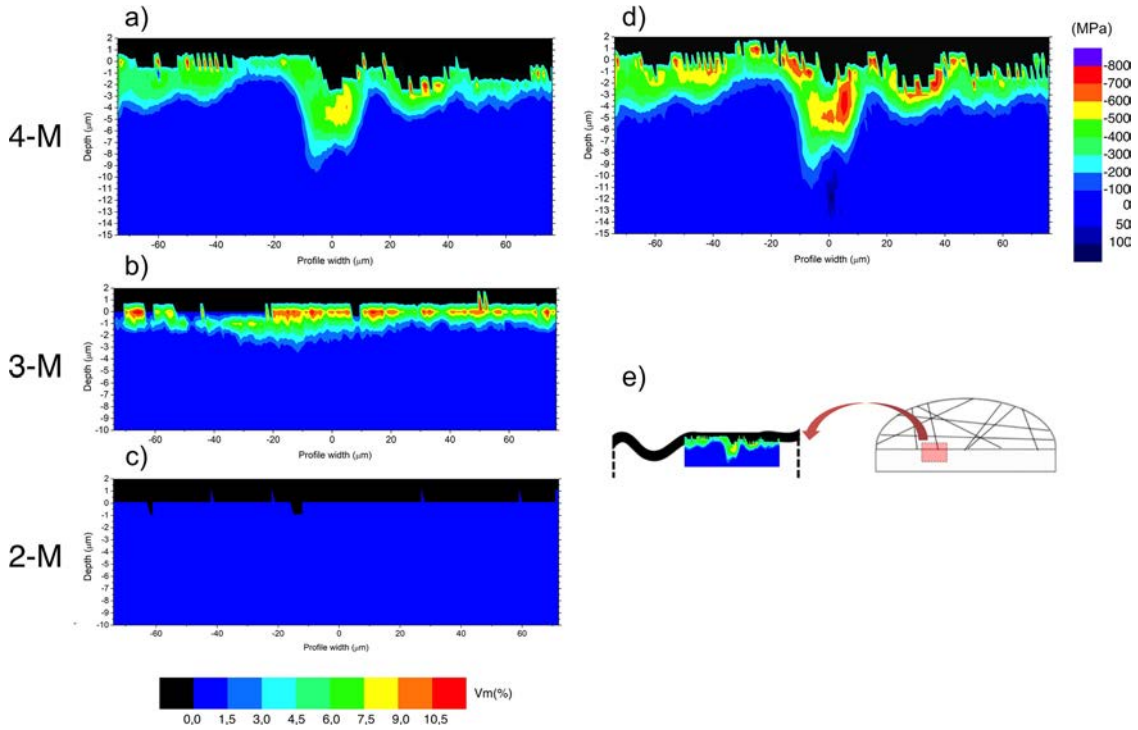

Fig. 7. Results of the cross-sectional confocal micro-Raman spectroscopy measurements. a) to c) m-phase distribution in cross-sections 4-M, 3-M and 2-M, respectively. d) Residual stress profile of the t-phase in 4-M and e) diagram showing the measured regions. Note that black areas correspond to bakelite, while dark blue areas correspond to the bulk non-transformed material. (For interpretation of the references to colour in this figure legend, the reader is referred to the web version of this article.)

phase is plotted in Fig. 6d, while the $(002)_t$ /$(200)_t$ intensity relation is presented in Fig. 6e. It can be observed that the trend followed in Figs. 3d and e for symmetric Bragg-Brentano geometry is not seen in this case. There is a large gap from MP and 1-M specimens to 2-M, which presented the highest amounts of *m*-phase and texture, even higher than in specimens 3-M and 4-M. These results suggest that 2-M mildly polished specimens present a shallow layer of very high *m* content and texture. Similar results have been obtained by other authors [39], although they attributed this behaviour to measurement errors due to surface roughness. In this configuration, X-Ray penetration depth is similar to the height of surface roughness, leading to increased scattering and reduced signal intensity. Whether this is the reason for the observed trend, it is difficult to know. Although the standard deviation of results is low, the fact that measurements were done in specimens with high gradients in depth [5], combined with the important differences in surface roughness, make it difficult to establish trustworthy comparisons. In addition, the equation proposed by Toraya et al. [20] for *m*-phase quantification does not include the particular case in which *r*-phase is present. For this reason, especially in the case of grazing incidence measurements where very high amounts of *r*-phase are identified, additional care should be taken on quantitative interpretation of the results. What is clear is that on the very first nanometres of material, even softly polished specimens such as 2-M present a highly affected microstructure with both refined grains and significant amounts of texture and phase transformation. In the particular case of 1-M, although microstructural differences respect to MP were identified after thermal etching (e.g. partial recrystallization), XRD spectra did not show significant differences.

As a result of its relation to surface properties, much importance has been given in this and other works to the presence of *m*-phase on the surface [40,41]. If too high *m* amounts are generated during surface treatments, both mechanical properties and ageing resistance can be detrimentally affected. However, if the *m* content is sufficiently low, its effects can turn beneficial. The $t \rightarrow m$ martensitic transformation is accompanied by a 4% volume expansion in the unit cell, creating a layer of compressive stresses on the surface. These residual stresses can improve mechanical properties [9] and provide a better resistance to degradation [15]. In order to further study the extent of phase transformation in the treated specimens, samples were cross-sectioned (see scheme in Fig. 7e) and studied by confocal micro-Raman spectroscopy. This technique allows to quantitatively assess both crystalline phases [41] and residual stresses [25]. Fig. 7a to c show the in-depth distribution of the *m*-phase of specimens 4-M, 3-M and 2-M, respectively. Fig. 7d displays the obtained stress distribution in 4-M. Figs. 7a and d evidence the close relation between *m*-phase and residual stresses, presenting an overlap of their profiles in both location and magnitude. Phase transformation is maximum on the surface and decreases with depth [40].

As expected, in our study transformation depths and monoclinic content increased with the severity of the applied treatment. While in 4-M phase transformation reached a depth of 5 µm, in the case of 3-M such transformation was not produced beyond 3 µm. In addition, a wavy pattern was observed in 4-M, with higher transformation depths below the largest grooves. No transformation was observed in 2-M, although XRD clearly showed the presence of *m*-phase. As the samples were embedded in bakelite for edge retention, the spectra obtained in the first one or two microns was significantly affected by bakelite's background and the rounding effect, which may had hidden the presence of very shallow layers of *m*-phase. Regarding residual stresses in 4-M, following phase transformation, they extended below the surface until a depth of approximately 5 µm, decreasing progressively and reaching a maximum value of around −700 MPa in the areas where maximum *m*-phase was found. All the stresses were of compressive nature, except for a small region in which tensile stresses were identified. Tensile stresses below the compressed zone are commonly reported [42] and necessary in terms of force equilibrium.

Finally, to characterize the surface stress state in all the specimens, X-ray stress analysis was carried. Fig. 8 summarizes the results

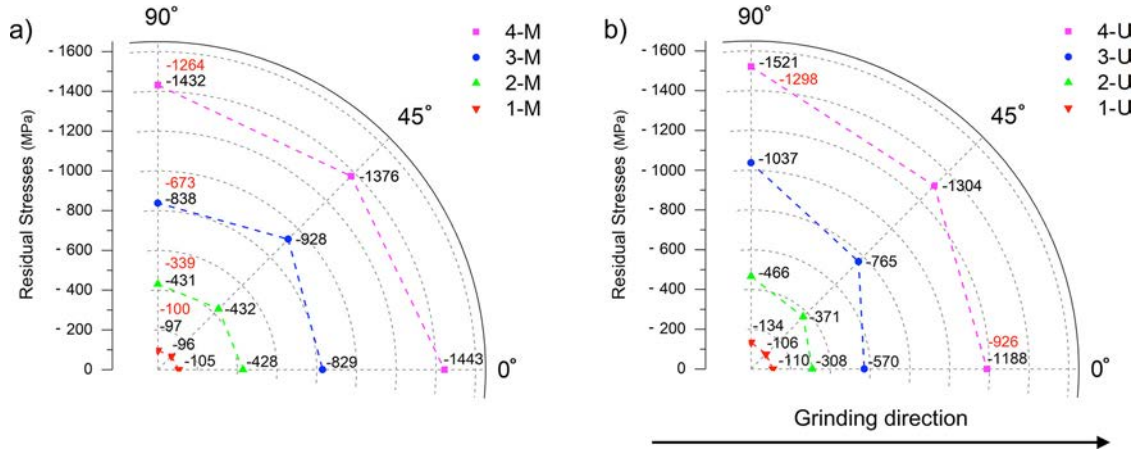

Fig. 8. Residual stresses distribution in the t-phase measured by X-ray stress analysis. n = 1 a) M samples. b) U samples. Numbers in red correspond to the stress values obtained after peak deconvolution. The arrow in b) points to the grinding direction. For each specimen, measurements along three different directions are shown: at 0°, 45° and 90°. (For interpretation of the references to colour in this figure legend, the reader is referred to the web version of this article.)

obtained. MP sample revealed a slight compressive isotropic stress state of around −70 MPa (results not shown). For the rest of the conditions, intensity of residual stresses gradually increased with the use of coarser abrasives (i.e. as the total monoclinic content of the surface increased), reaching a value of around -1.4 GPa in the roughest samples. Although in all the cases the nature of the stresses was compressive, a clear difference between M and U was observed. In the first case, the stress state was identical regardless of the measured direction. For U, however, significantly lower stresses were present along the grinding direction, leaving the surface under an anisotropic stress state. This behaviour has been already observed in other ceramics, including zirconia [43–45]. As discussed by Wobker and Tönshoff [46], it may be explained by the largest plastic deformation perpendicularly to the grinding direction. Measurements performed with deconvoluted spectra displayed slightly lower stress values (see red values), although the trend was identical regardless of how data was treated, as shown in Fig. 8.

Easily unnoticed, the magnitude of stresses in specimens polished with diamond slurries could be higher than initially expected. For instance, residual stresses in 2-M specimens were around three times lower than in the roughest grade used (i.e. 4-M/U). However, the monoclinic layer directly responsible for generating these stresses was also more than three times thinner. Taking into account the thickness in which values are averaged by X-rays, this suggests that the residual stress state in the very first layer of material in 2-M/U (i.e. the first micron) could be comparable to the one in 4-M/U, which agrees with the high *m* content found in grazing incidence angle XRD (Fig. 6). Another important feature is that the stress values found in 4-M are higher than the ones calculated by using Raman spectroscopy (Fig. 7). A possible explanation lies on the fact that, in the latter case, the polished cross-section is a free surface and stresses may be partly released. This in turn may affect the validity of the hypothesis used for the Raman stress calculation (i.e. hydrostatic stress state). Such differences highlight that although accurate stress profiles are obtained by using Raman piezo-spectroscopic techniques (as demonstrated by the *m*-phase/stress maps full overlapping), stress calculation may need additional considerations, especially in the case of cross-sectioned specimens. Thus, in this case, reference values for surface stresses should be the ones determined by XRD.

The sliding contact between diamond particles and the surface directly translates into a topographical modification. As shown, not only surface topography is altered, but also the $t \rightarrow$ m transformation is activated, which in turn generates a compressed superficial layer. As a consequence, a certain degree of correlation is expected not only between residual stresses and content of *m*–phase, but also with surface roughness. Fig. 9 displays the relation between residual stresses, surface's monoclinic volume fraction (V_m) and average surface roughness (S_a) for the M conditions. As it can be observed, stresses and surface V_m display a clear linear relationship. As higher *m*-phase is produced, higher compressive residual stresses are present on the surface. Furthermore, under the used conditions (i.e. in terms of load, coolant use, polishing/grinding products used, etc.) both compressive residual stresses and V_m can be predicted with the S_a. In other words, if all the processing parameters are controlled, a simple predictive model can be obtained, in which a measure of surface roughness (either by WLI or surface profilometry) can be used to estimate both V_m and the residual stress state.

Grinding has been extensively used in the literature to improve ageing resistance on zirconia-based materials. However, heavily ground samples may display worsened mechanical behaviour due to surface damage. To the best of our knowledge, here it is shown for the first time that polished specimens with low surface roughness and no damage are capable of also presenting protective features generally associated with ground specimens. For mildly polished samples, the affected region is reduced to a nanometric layer, in contrast to ground specimens, in which such region extends to the micrometric length scale. Surface recrystallization together with a significant *m*–phase content and texture in the first nanometres under the surface were found. The specimens produced and characterized in this work provide an overview of the relation between surface finishing (i.e. surface roughness) and its associated microstructural features. In this sense, if the processing parameters are controlled, it is possible to find simple mathematical equations relating surface roughness, monoclinic content and residual stresses. The high sensitivity to surface treatments displayed by 3Y-TZP even after mild procedures show that slight changes in processing parameters can have a significant influence in the final properties of the very first layer of material, with particular relevance in applications were a high control of the surface is needed.

4. Conclusions

A range of surfaces gradually ground/polished by increasing abrasion severity have been studied. The following conclusions may be drawn:

- Increasing the abrasion severity produces a higher total content of *m*-phase and transformation depths, which correlates with higher compressive residual stresses. Unidirectionally ground specimens present an anisotropic stress state.
- Polishing with diamond slurries (i.e. 2-M/U) generates a two-layer microstructure, with an extremely shallow (< 100 nm) refined layer

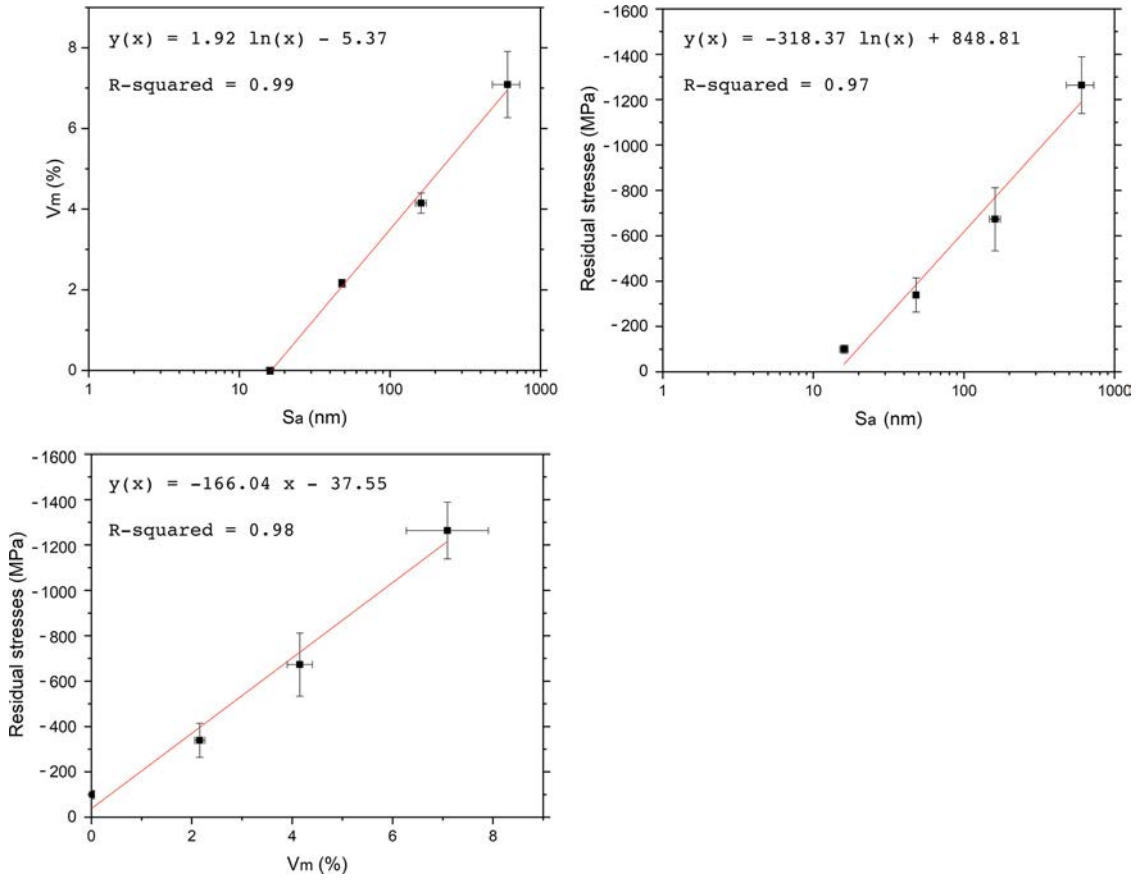

Fig. 9. Relation between residual stresses, monoclinic volume fraction (V_m) and average surface roughness (S_a), for the M specimens (1-M to 4-M). The more accurate stress values obtained after peak deconvolution were used.

followed by bulk-like material. Very importantly, in these specimens no surface damage is detected and XRD analysis of the very near surface (i.e. a layer < 300 nm) reveals high amounts of *m*-phase and texture (in a similar range to coarsely ground samples). This is different from the changes observed after coarse grinding: a three-layer microstructure with evident signs of surface damage.

- Surface recrystallization occurs in a wide range of ground/polished surfaces, even after relatively soft procedures. The transition from bulk-like to recrystallized surfaces have been identified in polished surfaces with a roughness as low as $S_a = 16 \pm 1$ nm, in which partial recrystallization is observed.
- Under controlled processing parameters, a simple mathematical relation can be obtained relating average surface roughness, *m* content and residual stresses.

Declaration of Competing Interest

The authors declare that they have no known competing financial interests or personal relationships that could have appeared to influence the work reported in this paper.

Acknowledgements

This work was supported by the Ministerio de Ciencia, Innovación y Universidades (MAT2017-83905-R, MINECO/FEDER), the Generalitat de Catalunya (2017 SGR-933 and SGR-1165) and the CREATe-Network Project, Horizon 2020 Program of the European Commission (RISE Project Nr. 644013). J. Minguela has been supported by a predoctoral fellowship from the Barcelona Research Center in Multiscale Science and Engineering of the UPC. J.J. Roa acknowledges the Serra Hunter programme and M-P. Ginebra the ICREA Academia Award, both from the Generalitat de Catalunya. C. Mas-Moruno thanks the Spanish Government for a Ramon y Cajal grant.

References

[1] E.P. Butler, Transformation-toughened zirconia ceramics, Mater. Sci. Technol. 1 (6) (1985) 417–432.
[2] T. Miyazaki, T. Nakamura, H. Matsumura, S. Ban, T. Kobayashi, Current status of zirconia restoration, J. Prosthodont. Res. 57 (4) (2013) 236–261.
[3] H.J. Conrad, W.J. Seong, I.J. Pesun, Current ceramic materials and systems with clinical recommendations: a systematic review, J. Prosthet. Dent. 98 (5) (2007) 389–404.
[4] I. Denry, J.R. Kelly, State of the art of zirconia for dental applications, Dent. Mater. 24 (3) (2008) 299–307.
[5] J.A. Muñoz-Tabares, E. Jiménez-Piqué, J. Reyes-Gasga, M. Anglada, Microstructural changes in ground 3Y-TZP and their effect on mechanical properties, Acta Mater. 59 (17) (2011) 6670–6683.
[6] J. Barceinas-Sanchez, W. Rainforth, Transmission electron microscopy study of a 3Y-TZP worn under dry and water-lubricated sliding conditions, J. Am. Ceram. Soc. 82 (6) (1999) 1483–1491.
[7] K. Mehta, J.F. Jue, A.V. Virkar, Grinding-induced texture in ferroelastic tetragonal zirconia, J. Am. Ceram. Soc. 73 (6) (1990) 1777–1779.
[8] L. Melk, J. Mouzon, M. Turon, F. Akhtar, M.L. Antti, M. Anglada, Surface microstructural changes of spark plasma sintered zirconia after grinding and annealing, Ceram. Int. 42 (14) (2016) 15610–15617.
[9] T.K. Gupta, Strengthening by surface damage in metastable tetragonal zirconia, J. Am. Ceram. Soc. 63 (1–2) (1980) 117.
[10] C.J. Ho, H.C. Liu, W.H. Tuan, Effect of abrasive grinding on the strength of Y-TZP, J. Eur. Ceram. Soc. 29 (12) (2009) 2665–2669.
[11] J.A. Muñoz-Tabares, M. Anglada, Hydrothermal degradation of ground 3Y-TZP, J. Eur. Ceram. Soc. 32 (2) (2012) 325–333.
[12] M. Inokoshi, K. Vanmeensel, F. Zhang, J. De Munck, G. Eliades, S. Minakuchi, I. Naert, B. Van Meerbeek, J. Vleugels, Aging resistance of surface-treated dental zirconia, Dent. Mater. 31 (2) (2015) 182–194.
[13] J.F. Jue, J. Chen, A.V. Virkar, Low-temperature aging of T'-zirconia: the role of microstructure on phase-stability, J. Am. Ceram. Soc. 74 (8) (1991) 1811–1820.
[14] A.V. Virkar, J.F. Jue, P. Smith, K. Mehta, K. Prettyman, The role of ferroelasticity in toughening of brittle materials, Phase Transitions 35 (1) (1991) 27–46.
[15] S. Deville, J. Chevalier, L. Gremillard, Influence of surface finish and residual

stresses on the ageing sensitivity of biomedical grade zirconia, Biomaterials 27 (10) (2006) 2186–2192.
[16] J. Chevalier, L. Gremillard, S. Deville, Low-temperature degradation of zirconia and implications for biomedical implants, Annu. Rev. Mater. Res. 37 (1) (2007) 1–32.
[17] P.J. Whalen, F. Reidinger, R.F. Antrim, Prevention of low-temperature surface transformation by surface recrystallization in yttria-doped tetragonal zirconia, J. Am. Ceram. Soc. 72 (2) (1989) 319–321.
[18] P.F. Becher, M.V. Swain, Grain-Size-Dependent transformation behavior in polycrystalline tetragonal zirconia, J. Am. Ceram. Soc. 75 (3) (1992) 493–502.
[19] K. Niihara, R. Morena, D.P. Hasselman, Evaluation of K_{ic} of brittle solids By the indentation method with low crack to indent ratios, J. Mater. Sci. Lett. 1 (1) (1982) 13–16.
[20] H. Toraya, M. Yoshimura, S. Somiya, Calibration curve for quantitative analysis of the monoclinic-tetragonal ZrO_2 system by x-ray diffraction, J. Am. Ceram. Soc. 67 (6) (1984) p. C-119-C-121.
[21] T.M.G. Katagiri, H. Ishida, A. Ishitani, "Direct determination by raman microprobe of the transformation zone size in Y_2O_3 containing Tetragonal ZrO_2 polycrystal," Sci. Technol. Zirconia III, Ed. by S. Somiya, N. Yamamoto, H. Yanagida, Am. Ceram. Soc. (1988) 537–544.
[22] A.C. Vermeulen, Considerations for collecting reliable XRD residual stress data across the full 2Theta range, JCPDS -International Cent. Diffr. Data (2006) 133–142.
[23] B. Eigenmann, B. Scholtes, E. Macherauch, Grundlagen und Anwendung der röntgenographischen Spannungsermittlung an Keramiken und Metall-Keramik-Verbundwerkstoffen, Materwiss. Werksttech. 20 (9) (1989) 314–325.
[24] V. Sergo, D.R. Clarke, W. Pompe, Deformation bands in ceria-stabilized tetragonal Zirconia/Alumina: I, measurement of internal stresses, J. Am. Ceram. Soc. 78 (3) (1995) 633–640.
[25] G. Pezzotti, A.A. Porporati, Raman spectroscopic analysis of phase-transformation and stress patterns in zirconia hip joints, J. Biomed. Opt. 9 (2) (2004) 372.
[26] G. Pezzotti, K. Yamada, S. Sakakura, R.P. Pitto, Raman spectroscopic analysis of advanced ceramic composite for hip prosthesis, J. Am. Ceram. Soc. 91 (4) (2008) 1199–1206.
[27] T.G. Bifano, T.A. Dow, R.O. Scattergood, Ductile-regime grinding: a New technology for machining brittle materials, J. Eng. Ind. 113 (2) (1991) 184.
[28] N. Jochum, Zerspanung Ultraharter Keramik Am Beispiel Einer Dreigliedrigen Zahnbrücke, ETH Zürich, (2013).
[29] R.H.J. Hannink, P.M. Kelly, B.C. Muddle, Transformation toughening in zirconia-containing ceramics, J. Am. Ceram. Soc. 83 (3) (2000) 461–487.
[30] H. Hasegawa, Rhombohedral phase produced in abraded surfaces of partially stabilized zirconia (PSZ), J. Mater. Sci. Lett. 2 (3) (1983) 91–93.
[31] Y. Kitano, Y. Mori, A. Ishitani, T. Masaki, Rhombohedral phase in Y_2O_3-partially-stabilized ZrO_2, J. Am. Ceram. Soc. 71 (1) (1988) pp. C-34-C–36.
[32] D.J. Kim, H.J. Jung, H.J. Kim, t→r phase transformation of tetragonal zirconia alloys by grinding, J. Mater. Sci. Lett. 14 (4) (1995) 285–288.
[33] J. Kondoh, Origin of the hump on the left shoulder of the X-ray diffraction peaks observed in Y_2O_3-fully and partially stabilized ZrO_2, J. Alloys Compd. 375 (1–2) (2004) 270–282.
[34] A.V. Virkar, Ferroelastic domain switching as a toughening mechanism in tetragonal zirconia, J. Am. Ceram. Soc. 71 (7) (1988) p. C-362-C-364.
[35] J.J. Roa, M. Turon-Vinas, M. Anglada, Surface grain size and texture after annealing ground zirconia, J. Eur. Ceram. Soc. 36 (6) (2016) 1519–1525.
[36] J.A. Muñoz-Tabares, E. Jiménez-Piqué, J. Reyes-Gasga, M. Anglada, Microstructural changes in 3Y-TZP induced by scratching and indentation, J. Eur. Ceram. Soc. 32 (15) (2012) 3919–3927.
[37] W.W. Mullins, Theory of thermal grooving, J. Appl. Phys. 28 (3) (1957) 333–339.
[38] R.K. Chintapalli, A. Mestra Rodriguez, F. Garcia Marro, M. Anglada, Effect of sandblasting and residual stress on strength of zirconia for restorative dentistry applications, J. Mech. Behav. Biomed. Mater. 29 (2014) 126–137.
[39] M. Strasberg, A.A. Barrett, K.J. Anusavice, J.J. Mecholsky, J.C. Nino, Influence of roughness on the efficacy of grazing incidence X-ray diffraction to characterize grinding-induced phase changes in yttria-tetragonal zirconia polycrystals (Y-TZP), J. Mater. Sci. 49 (4) (2014) 1630–1638.
[40] L. Gremillard, S. Grandjean, J. Chevalier, A new method to measure monoclinic depth profile in zirconia-based ceramics from X-ray diffraction data, Int. J. Mater. Res. 101 (1) (2010) 88–94.
[41] J.A. Muñoz Tabares, M.J. Anglada, Quantitative analysis of monoclinic phase in 3Y-TZP by raman spectroscopy, J. Am. Ceram. Soc. 93 (6) (2010) 1790–1795.
[42] R. Samuel, S. Chandrasekar, T.N. Farris, R.H. Licht, Effect of residual stresses on the fracture of Ground ceramics, J. Am. Ceram. Soc. 72 (10) (1989) 1960–1966.
[43] K. Li, T.W. Liao, Surface/subsurface damage and the fracture strength of ground ceramics, J. Mater. Process. Technol. 57 (3–4) (1996) 207–220.
[44] D. Johnson-Walls, A.G. Evans, D.B. Marshall, M.R. James, Residual stresses in machined ceramic surfaces, J. Am. Ceram. Soc. 69 (1) (1986) 44–47.
[45] B. Eigenmann, E. Macherauch, Determination of inhomogeneous residual stress states in surface layers of machined engineering ceramics by synchrotron X-rays, Nucl. Instruments Methods Phys. Res. Sect. B Beam Interact. with Mater. Atoms 97 (1–4) (1995) 92–97.
[46] H.G. Wobker, H.K. Tönshoff, High efficiency grinding of structural ceramics, in "Machining of advanced materials", NIST Special Publication 847 (1993) 171–184.

Chapter 5
Paper II

Influence of grinding/polishing on the mechanical, phase stability and cell adhesion properties of yttria-stabilized zirconia

Available at:

https://www.sciencedirect.com/science/article/abs/pii/S0955221920302302

Journal of the European Ceramic Society 40 (2020) 4304–4314

Contents lists available at ScienceDirect

Journal of the European Ceramic Society

journal homepage: www.elsevier.com/locate/jeurceramsoc

Original Article

Influence of grinding/polishing on the mechanical, phase stability and cell adhesion properties of yttria-stabilized zirconia

J. Minguela[a,b,c], M.P. Ginebra[a,c,d], L. Llanes[b,c], C. Mas-Moruno[a,c,*], J.J. Roa[b,c,*]

[a] Biomaterials, Biomechanics and Tissue Engineering Group (BBT), Department of Materials Science and Engineering, Universitat Politècnica de Catalunya - BarcelonaTECH, 08019 Barcelona, Spain
[b] Center for Structural Integrity, Micromechanics and Reliability of Materials (CIEFMA), Department of Materials Science and Engineering, Universitat Politècnica de Catalunya - BarcelonaTECH, 08019 Barcelona, Spain
[c] Barcelona Research Center in Multiscale Science and Engineering, Universitat Politècnica de Catalunya - BarcelonaTECH, 08019 Barcelona, Spain
[d] Institute for Bioengineering of Catalonia (IBEC), Barcelona Institute of Technology (BIST), 08028 Barcelona, Spain

ARTICLE INFO

Keywords:
Zirconia
Grinding
Mechanical properties
Hydrothermal degradation
Cell adhesion

ABSTRACT

The changes in mechanical properties, hydrothermal degradation and cell adhesion were studied in 3Y-TZP under two different superficial modification patterns (uni- and multidirectional) with a surface roughness ranging from 16 to 603 nm. In this sense, mechanical properties (i.e. hardness, indentation fracture toughness and scratch) and accelerated tests in water steam were measured to evaluate the influence of the surface treatments on the superficially modified layer. Moreover, a detailed characterization through micro-Raman spectroscopy and X-Ray diffraction was performed. Finally, SaOS-2 osteoblasts were used for the evaluation of the cell adhesion behaviour on the surfaces. Overall, ground/polished specimens increased the mechanical properties and ageing resistance of mirror-like polished specimens, although resistance to degradation was maximum at intermediate conditions ($S_a \approx 40-180$ nm). The studied surfaces allowed cell attachment, but promoted contact guidance (i.e. cell alignment) only on unidirectionally ground surfaces above $Sa = 150$ nm.

1. Introduction

Zirconia-based materials have gained increasing attention during the last years in restorative dentistry, and are now used to produce several prosthetic elements, such as crowns, bridges, endodontic posts and cores, abutments and dental implants [1,2]. Among the different zirconia compositions available, yttria-doped zirconia (Y-TZP) is still the most commonly used solution, although other compositions such as ceria-doped or zirconia-alumina composites are also employed in order to improve zirconia's ageing resistance [1–5] (also known as hydrothermal degradation or low-temperature degradation [6]), at the expense of certain mechanical properties [7,8]. The superior properties of zirconia, which include high strength, toughness, hardness and wear resistance; and especially its whitish colour resembling natural teeth, have been decisive for the development of new advanced ceramic solutions in dentistry [9].

Due to the harsh environment of the oral cavity, dental materials present many challenges from the mechanical [10] and chemical [11] point of view. On the one hand, cyclic contact loads from chewing as well as sliding loads from food and teeth abrasion can introduce flaws on the surface, which may compromise the long-term reliability of the prosthesis. On the other hand, after long periods in contact with moisture, yttria-stabilized zirconia may be affected by hydrothermal degradation [12,13]. When kept for a long time in a humid environment, a martensitic phase transformation from the metastable tetragonal (t) phase to the monoclinic (m) one takes place spontaneously on the surface. This transformation is associated with an m-volume expansion of around 4 % that generates micro-cracks through which water can penetrate into the material and further degrade it until the final failure. However, many restorative elements (e.g. dental implants) should not only preserve its structural integrity for several years, but also display a proper biological interaction [14] both in the short and long term. In the particular case of dental implants, the surface plays a key role, interacting with bone and guiding the biological response towards a proper osseointegration and mechanical stability.

Since it is indeed the surface that provides the features that will largely decide the success of an implant, the ability of modifying and fine-tuning its properties has been a subject of study. Extensive research has been carried out to investigate the changes in microstructure,

* Corresponding authors at: Barcelona Research Center in Multiscale Science and Engineering, Universitat Politècnica de Catalunya - BarcelonaTECH, 08019 Barcelona, Spain.
E-mail addresses: carles.mas.moruno@upc.edu (C. Mas-Moruno), joan.josep.roa@upc.edu (J.J. Roa).

https://doi.org/10.1016/j.jeurceramsoc.2020.03.049
Received 9 December 2019; Received in revised form 20 March 2020; Accepted 24 March 2020
Available online 03 April 2020
0955-2219/

mechanical properties and/or hydrothermal degradation of Y-TZP materials after surface treatments such as sandblasting [15,16], grinding [17–19], chemical etching [20,21] or laser patterning [22,23].

As a surface-modifying technique, grinding/polishing is known to affect the properties of Y-TZP. Several changes are introduced on the surface and subsurface depending on the severity of the treatment such as increased roughness, microstructural modifications, residual stresses, cracks, etc. as detailed by Muñoz-Tabares et al. [17]. The consequences of such changes inevitably leave their imprint on the material's properties, mainly in terms of mechanical and hydrothermal degradation behaviour. In the first case, the layer of residual compressive stresses originating from the expansive stress-induced $t \rightarrow m$ transformation enhances the mechanical properties of the surface, as long as the introduced damage is controlled [15,17,24–27] In the second case, hydrothermal degradation can be delayed by certain microstructural features associated with grinding procedures [18,28–30] such as the reduction in grain size in the dynamically recrystallized surface [31], the *t*-phase stabilizing effect of the residual compressive layer [32,33], and the reduction in domain size by ferroelastic switching, as shown by Jue et al. [34].

On the other hand, the changes in surface topography introduced by such procedures may be used as a tool to improve biological response. In this regard, grinding as well as sandblasting and chemical etching have been used, mostly in titanium surfaces, as a means to improve osseointegration [35,36]. Both eukaryotic and prokaryotic cells can be affected by the topographical cues of the substrate in which they are adhered [37,38]. In particular, osseointegration of biomedical implants can be enhanced by increasing surface roughness, both in the macroscale because of a better bone-surface interlocking [39,40], and in the micro- and nano- scale because of the beneficial influence of roughness in osteoblasts activity [41–43], displaying higher levels of adhesion and extracellular matrix deposition [44].

Although the individual mechanisms able to affect surface properties after grinding are known, predicting the outcome of their combined effects after a specific treatment is still challenging. Most of the available studies are based on the comparison of a few grinding treatments, relying solely on the *m*-phase content to explain the observed differences, without providing a detailed characterization of the surface. As a result, different studies report contradictory outcomes from apparently similar treatments, as it is the unique combination in terms of microstructure, surface defects and residual stresses after each treatment what dictates the final properties of the material. Therefore, it is of paramount importance to study how increasingly severe treatments affect surface properties, and to relate such properties with the microstructural features of the surface. This will allow: i) to understand and rationalize differences found among conflicting studies, and ii) to gather the necessary knowledge in order to smartly design surface microstructure and obtain materials with the desired mechanical, ageing and cell instructive properties. For this reason, in the present work a series of gradually ground/polished 3Y-TZP surfaces were prepared. The chosen material resembled low-translucency 3Y-TZP, mainly employed in veneered restorations as well as dental implants and abutments. Mechanical properties, ageing resistance and cell adhesion performance were studied and related to the particular features of each surface [45]. Within this context, the hypotheses under examination are:

- Grinding/polishing are able to modify surface properties.
- Different abrasion degrees can lead to different surface properties.
- The increase in surface properties is not necessarily in direct correlation with the abrasion severity employed.

2. Experimental procedure

2.1. Sample preparation

Specimens were produced from zirconia powders stabilized with 3 mol% yttria (TZ-3YSB-E, Tosoh). Powders were cold isostatically pressed at 288 MPa and sintered at 1450 °C for 2 h, with constant heating and cooling rates of 3 °C/min. Disc-shaped specimens of 15 mm diameter and 2 mm thickness were obtained by this procedure. Grain size determined by the linear interception method was found to be 0.32 ± 0.12 μm and density was above 99 % of the theoretical one.

2.2. Grinding/Polishing treatments

Specimens were gradually ground/polished (Ecomet4, Buehler) in order to obtain progressive levels of surface roughness and abrasion severity. Four different roughness grades (1–4) and two different directionalities were obtained: aligned (unidirectional, U) and random grooves (multidirectional, M). A mirror-like polished surface (labelled as MP) was also included in all the experiments as a reference. Further details about the procedure and the codes used to identify the specimens can be found in [45]. The main microstructural and crystallographic features, residual stresses and surface damage of the studied specimens are summarized in Table 1 [45].

2.3. Surface characterization

Roughness parameters were obtained by White Light Interferometry (WLI, Wyko 9300 N T, Veeco). Measurements were performed in regions of 150μm × 150 μm by stitching four images taken at a magnification of 50×. Surface parameters were obtained with the Veeco's Vision® software. Tilt was corrected and a filter was used in the flattest conditions in order to separate roughness from waviness. For this purpose, a Robust Gaussian short wavelength pass filter with a spatial cut-off at 0.01 mm was selected. A description of the roughness parameters studied in this work can be found in Refs. [46–48].

Wettability of the surfaces was determined by static contact angle (CA, OCA15 Plus, Dataphysics) with the sessile drop method [49]. Measurements were done at room temperature with ultrapure Milli-Q water (3 μL drop volume) and contact angle determined by Laplace-Young fitting with SCA 20® software (Dataphysics).

For both WLI and CA, values shown are the mean of three different measurements in three different specimens.

2.4. Mechanical characterization

In order to determine the Vickers hardness (HV) and indentation fracture toughness (K_{Ic}), four indentations per specimen in three different samples were made on the surfaces, at 10 kgf and 30 kgf. 10 kgf indentations were used for Vickers hardness calculations, while the cracks originated at the corners of 30 kgf indentations were measured to calculate apparent indentation fracture toughness with the equation proposed by Niihara et al. [50]. The orientation of indentations was arbitrary, regardless of the groove's direction. However, to determine the presence of anisotropic properties after grinding, 30 kgf indentations were performed again in 4-U samples, in order to induce cracks running parallel or perpendicular to the grooves. Indentation size and crack length were determined by Field Emission Scanning Electron Microscopy (FESEM, Carl Zeiss Neon 40) imaging.

Scratch tests [51] were carried out on a CMS Revetest using a Rockwell C diamond tip (200 μm radius), increasing the load linearly from 0 N to 200 N, with a scratch length of 5 mm and an advancing speed of 1 mm/min. Three scratches were done per specimen, with one specimen per condition. After the tests, specimens were observed under FESEM. Some of the specimens were also cut transverse to the scratches, near the end of the tracks, in order to observe the sub-superficial damage induced at one particular load. The cross-sections were polished and observed with a Confocal Laser Scanning Microscope (CLSM, Lext OLS3100 Olympus).

Table 1
Summary of the microstructure, phase composition, residual stresses and surface damage of the specimens used in the present work [45]. U_T and U_P indicate residual stresses measured transverse or parallel to the grinding grooves (in unidirectionally ground specimens).

Specimen code	Subsurface microstructural features	Monoclinic content (penetration depth = 5 μm) (Vm%)		GIXRD 1° Monoclinic content (penetration depth = 300 nm) (Vm%)	Residual stresses (MPa)			Damage
MP	Bulk-like 300 nm equiaxed grains.	0 %		3.9 %	-70			No
		M	U	M	M	U_T	U_P	
1-M/U	No data. Thermal etching revealed partial recrystallization of nano-sized grains on the surface.	0 %	0%	5.1 %	-99	-134	-110	No
2-M/U	Layer (<100 nm) with nano-sized grains on the surface, followed by bulk-like microstructure.	2.2 %	1.5 %	24.1 %	-430	-466	-308	No
3-M/U	No data. By comparing to literature it is expected to be similar to 4-M/U [17].	4.1 %	3.8 %	21.6 %	-865	-1037	-570	No
4-M/U	Layer (< 300 nm) with nano-sized grains on the surface. Followed by ≈500 nm layer with highly deformed grains. Final layer with bulk-like grains with visible monoclinic laths.	7.1 %	5.4%	16.7 %	-1417	-1521	-1188	Surface micro-flaking linked to subsurface cracks.

2.5. Hydrothermal degradation

Accelerated degradation tests in water steam were performed at 134 °C and 2 bars of pressure (Micro8, Selecta) [52]. Monoclinic phase (*m*-phase) was quantified by X-Ray Diffraction (XRD, D8-Advance, Bruker) in Bragg-Brentano symmetric geometry using Cu K_α radiation (40 kV and 40 mA) with 0.02° step size, 1 s/step and a 2θ range of $26° \leq 2\theta \leq 37°$. In order to study $t \rightarrow m$ transformation kinetics, XRD spectra were collected at different degradation times (at 0, 2.5, 5, 10, 15, 20, 30, 40 and 50 h). Monoclinic content was calculated with the equation proposed by Toraya et al. [53]. For each condition and time point, the monoclinic fraction of three different specimens was averaged.

Samples degraded for 50 h, which correspond to the last time point used, were cut and the cross-section was mirror-polished. CLSM was employed to observe the extent of the transformed layer. *m*-phase maps in the cross-sections were also obtained using Confocal micro-Raman spectroscopy (Cm-RS, inVia Qontor, Renishaw) with a Nd:YAG laser (wavelength 532 nm, integration time 0.1 s). *m*-phase was quantified by using the equation proposed by Katagiri et al. [54].

2.6. Cell adhesion study

Human sarcoma osteogenic (SaOS-2) cells (ATCC) at passage 15–17 were cultured in Mc Coy's 5A medium supplemented with 10 % (v/v) foetal bovine serum (FBS), 2 % (v/v) 4-(2-hydroxyethyl)-1-piperazineethanesulfonic acid (HEPES), 1 % (w/v) sodium pyruvate, 50 μg/mL streptomycin, 50 U/ mL penicillin, and 1 % (w/v) L-glutamine. Cells were maintained at 37 °C in a humidified atmosphere containing 5 % (v/v) CO_2, changing culture medium every three days. This cell line represents a well established cellular model to study osteoblast-like responses on biomaterials [55,56]. After reaching 80 % confluence, cells were trypsinized (Trypsin-EDTA) and seeded at a concentration of 10,000 cells/specimen in the same medium used for cell culture. Cells were allowed to attach and spread for 24 h and then they were gently washed with PBS, fixed with paraformaldehyde (PFA, 4 % w/v in PBS) for 30 min and permeabilized with 0.05 % (w/v) Triton X-100 in PBS for 20 min. Actin fibers were stained by incubating with TRITC-conjugated phalloidin (1:300, in permeabilizing buffer) for 1 h and nuclei were stained using 4′,6-diamidino-2- phenylindole (DAPI) (1:1000, in PBS-glycine 20 mM) for 2 min, both in the dark. Between all steps, samples were rinsed three times with PBS-glycine for 5 min. All reagents were purchased from Sigma–Aldrich, unless otherwise noted. Specimens were mounted in Mowiol 4–88, examined under a fluorescence CLSM (CLSM, LSM 800, Carl Zeiss) and images were processed using Fiji/Image-J package [57] to calculate cell-shape parameters. Assays were done with triplicates, and repeated twice.

2.7. Statistical analysis

Values in all graphs are displayed as mean ± standard deviation. Statistical comparison of values was based on ANOVA using Tukey's test for pair-wise comparisons ($p < 0.05$). Differences were also analysed with the non-parametric Mann-Whitney test. The software used for statistical analysis was Minitab® 18.1.

3. Results and discussion

3.1. Topographical characterization

As depicted in the WLI images of Fig. 1, during specimen preparation the use of distinct grit sizes and polishing dynamics allowed to obtain a range of topographies, combining different roughnesses and directionalities. As coarser abrasives were used, an increase in roughness was observed (i.e. specimens from 1 to 4). As plotted in Fig. 2a and visually depicted in Fig. 2e, S_a increased by a factor larger than or equal to three between consecutive roughness grades, and no significant differences were present between M and U specimens. An evident textured directional pattern was present in U specimens, while grooves in

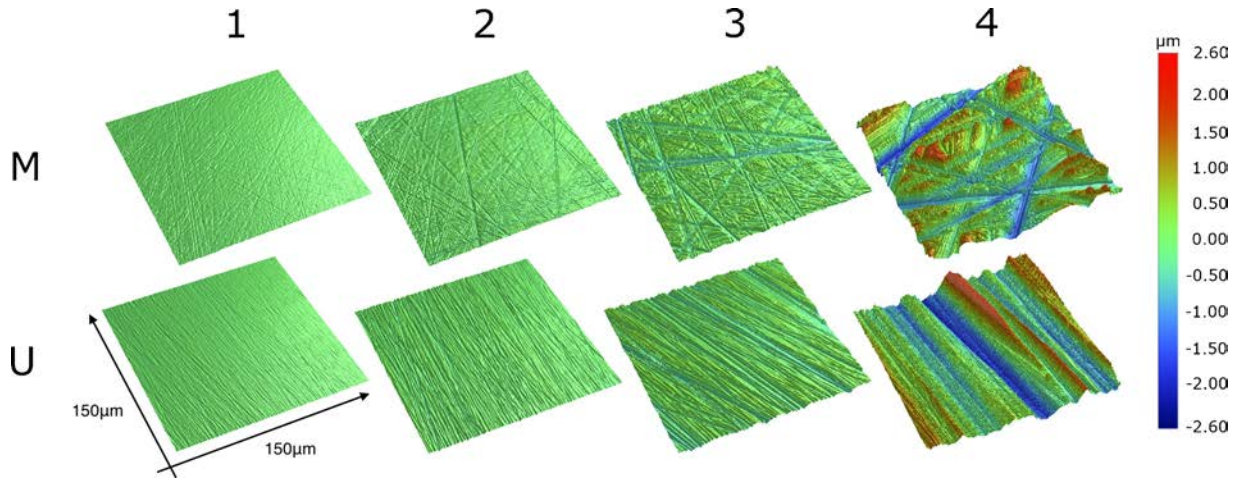

Fig. 1. WLI topographical images of the specimens after surface modification. From left to right, increasing levels of roughness, 1 to 4. Multidirectional (M) patterns are displayed on the top, while unidirectional (U) patterns are displayed on the bottom.

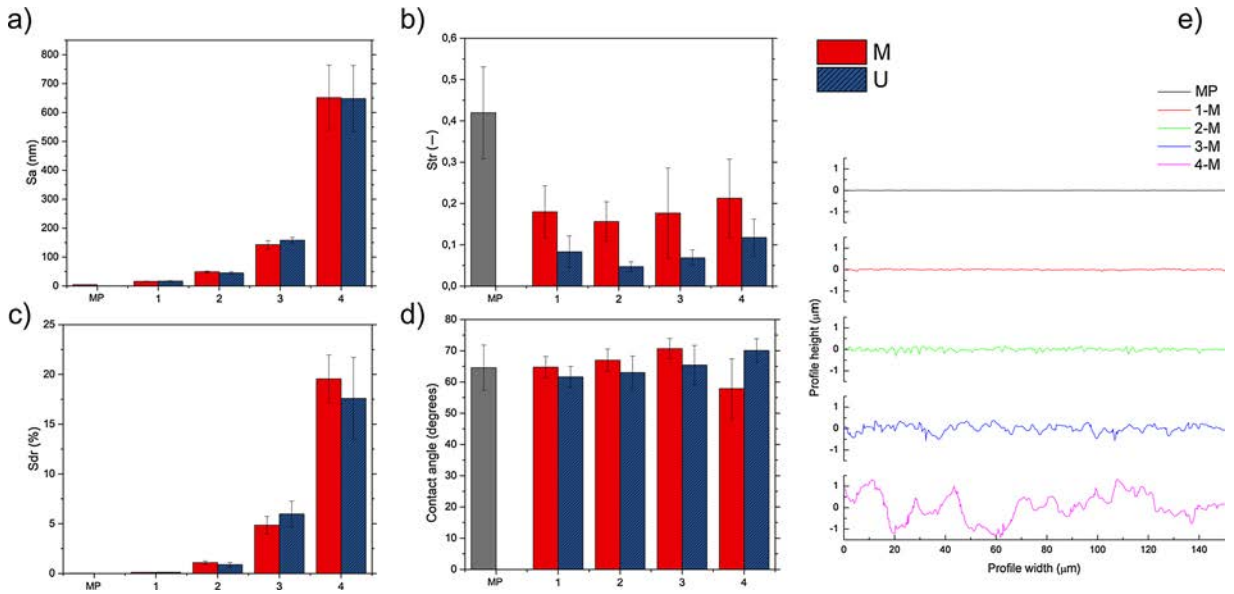

Fig. 2. Roughness parameters, contact angle and surface profile in ground/polished specimens. a) Arithmetic average height (S_a), b) Texture aspect ratio (S_{tr}), c) Developed interfacial area ratio (S_{dr}), d) Contact angle and e) Surface profile of heights.

M samples showed a random arrangement. This texture was further confirmed by S_{tr} (Fig. 2b), indicating a stronger anisotropy in all U specimens. A gradual increase in surface area was also noticed, which according to S_{dr} (Fig. 2c) increased to about 20 % in the case of 4-M/U. Although grinding/polishing introduced evident topographical modifications on the surfaces, contact angles (Fig. 2d) remained almost constant between 60° and 70°. This may be attributed to the relatively narrow S_a range of the studied surfaces, with similar differences as found by other authors in this material [58].

3.2. Mechanical characterization

The interaction between abrasive particles and the surface is not only limited to topographical modifications. As the diamond abrasives erode the surface, shearing and tensile stresses induce a $t \rightarrow m$ transformation, reaching several microns deep [17,45]. The volume expansion of the *m*-phase induces a compressive stress state on the surface that can exceed the GPa, which may affect its mechanical properties [17,59]. 10 kgf HV test results are presented in Fig. 3a, in which no significant differences were observed. However, in the case of K_{Ic} a clear increasing trend was detected. Fig. 3b shows the results of K_{Ic} for M and U specimens, both presenting the same behaviour. As rougher abrasives were used (i.e. higher compressive state on the surface, as shown in Table 1), statistically higher values were obtained. 4-M/U specimens showed an increase of 1.5 MPa·√m as compared to MP, which represents an improvement of around 30 %. In order to study if the anisotropic stress state found in unidirectionally ground specimens (see Table 1) can result in anisotropic mechanical properties, further indentations were done in 4-U specimens, this time aligning the originated cracks in two different directions: parallel and perpendicular to the grooves. According to results presented in Fig. 3c, despite the high variability in crack length measurements, a significantly increased K_{Ic} parallel to the grinding grooves was detected. As depicted in Fig. 3d, the higher stresses perpendicular to the grinding direction were able to hamper crack propagation along the grooves.

In order to evaluate the effects of this stressed layer on flaw development after a sliding contact, scratch tests were carried out in M specimens and surface damage was evaluated by FESEM. Micrographs in Fig. 4a correspond to the last part of the scratch tracks, showing the region under applied loads between 120 − 200 N. Images of the polished cross-sections near the end of the tracks, under loads above 180 N, are displayed in Fig. 4c and 4d. From the top view it is observed that lateral cracks formed along the tracks at high loads, except for specimen

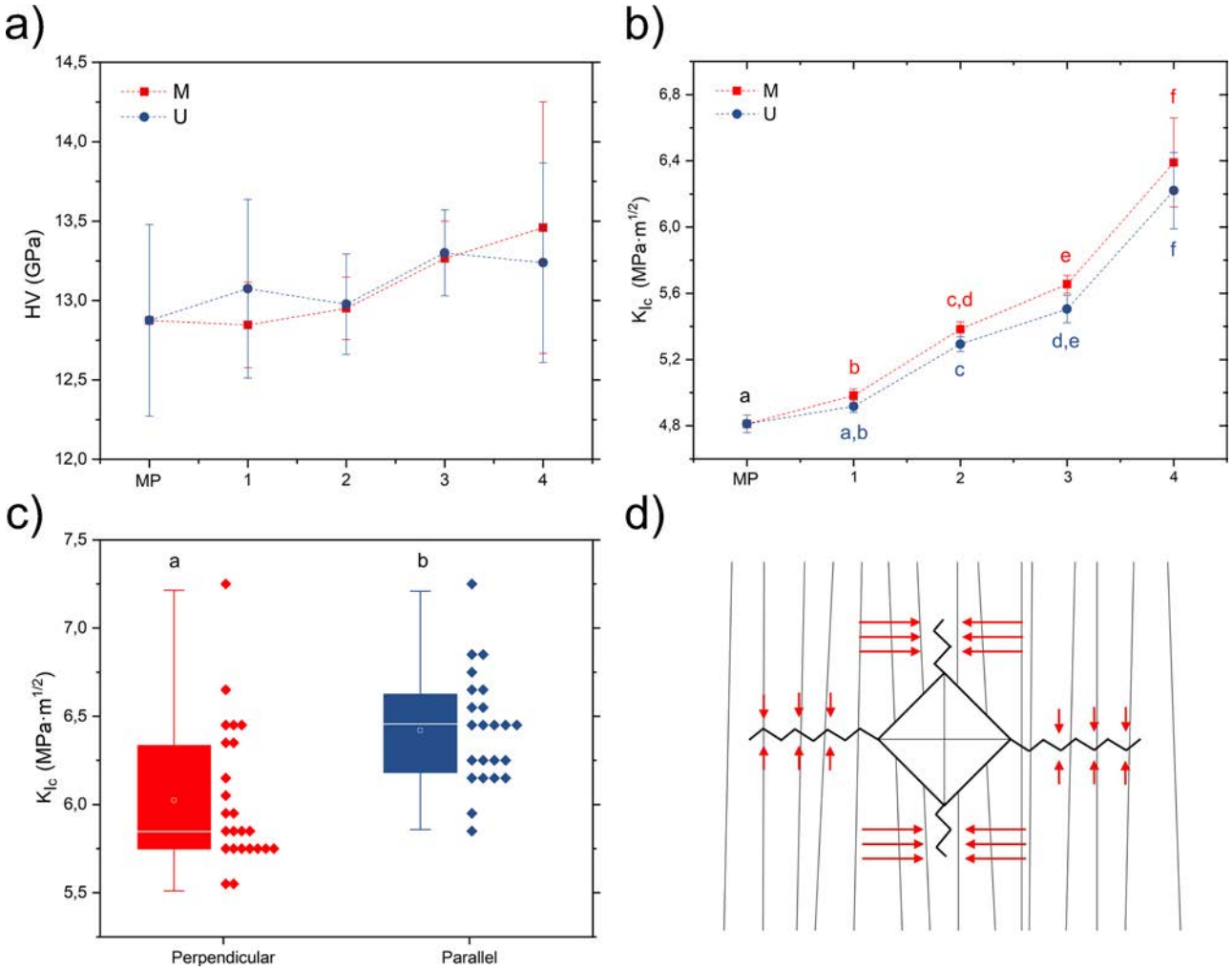

Fig. 3. Mechanical surface properties of the studied specimens. a) Vickers hardness, b) Apparent indentation fracture toughness, c) Apparent indentation fracture toughness in 4-U specimens along two different directions: perpendicular and parallel to the grinding grooves. d) Schematic representation of the influence of residual surface stresses on indentation crack length. Red arrows depict the intensity and direction of the residual stresses. Anisotropic stress states in unidirectionally ground specimens led to anisotropic mechanical behaviour. Groups identified by the same letter are not statistically different ($p > 0.05$). (For interpretation of the references to colour in the Figure, the reader is referred to the web version of this article).

4-M in which no cracks were visible. A magnification of the final section in 4-M is presented in Fig. 4b. Yet, once the cross-sections were evaluated, all the specimens presented sub-surface lateral cracks, generated at the centre of the track (where stresses are maximum) and propagating laterally up to the surface. As shown in Fig. 4d, MP specimen presented two symmetric lateral cracks at each side of the track. In the case of 4-M, cracks were also observed, with less symmetry and irregular length. While in MP they were wide and reached the surface open, allowing for a clear identification in the top view, cracks in 4-M were narrow and their intersection with the surface was difficult to detect. Such differences between crack morphology may be related to two different factors found in coarsely ground specimens. On one hand, the presence of a shallow layer of compressive stresses on the surface (around 6 − 7 μm thickness [45]). It may avoid crack opening in a similar fashion as observed in the K_{Ic} experiments. On the other hand, possibly to a lower extent, the highly distorted microstructure under the first micron. It may deflect or hinder crack propagation, as observed in severe plastically deformed materials [60]. The obtained results demonstrate that the changes undergone after grinding/polishing procedures are able to improve surface mechanical properties, in particular crack propagation after contact damage events, by improving apparent fracture toughness. A close relation thus exists between surface mechanical response and the layer of residual stresses.

3.3. Hydrothermal degradation

Fig. 5 plots the transformation kinetics of both M (Fig. 5a) and U (Fig. 5b) specimens after degradation in water steam. Degradation kinetics showed that unlike the grinding directionality, whose influence was minor, the severity of the abrasion (i.e. grit size) critically influenced the degradation behaviour. All the ground/polished specimens exhibited an improved resistance to hydrothermal degradation, as compared to MP specimens. However, both too soft and too aggressive treatments failed to provide protection against degradation over time. In contrast, 2-M/U and 3-M/U, presenting intermediate roughness, displayed an excellent resistance to degradation. The former in particular showed no signs of increase in the monoclinic content even after 50 h in water steam, which corresponds to roughly 150 years in vivo [52], much longer than the expected lifetime of any biomedical implant. Fig. 6 shows CLSM images and a *m*-phase mapping of the cross-sections in all M specimens as well as in MP after 50 h of degradation. MP specimens presented the maximum transformation depth, with a homogeneous fully degraded layer of about 10 − 11 μm. Meanwhile, both 2-M and 3-M were free of degradation. Specimens 1-M and 4-M presented partial transformation of the surface, with a similar degree of transformation but a different distribution of the monoclinic material. On one hand, transformation in 4-M was very heterogeneous and seemed to be nucleated around specific spots, leaving

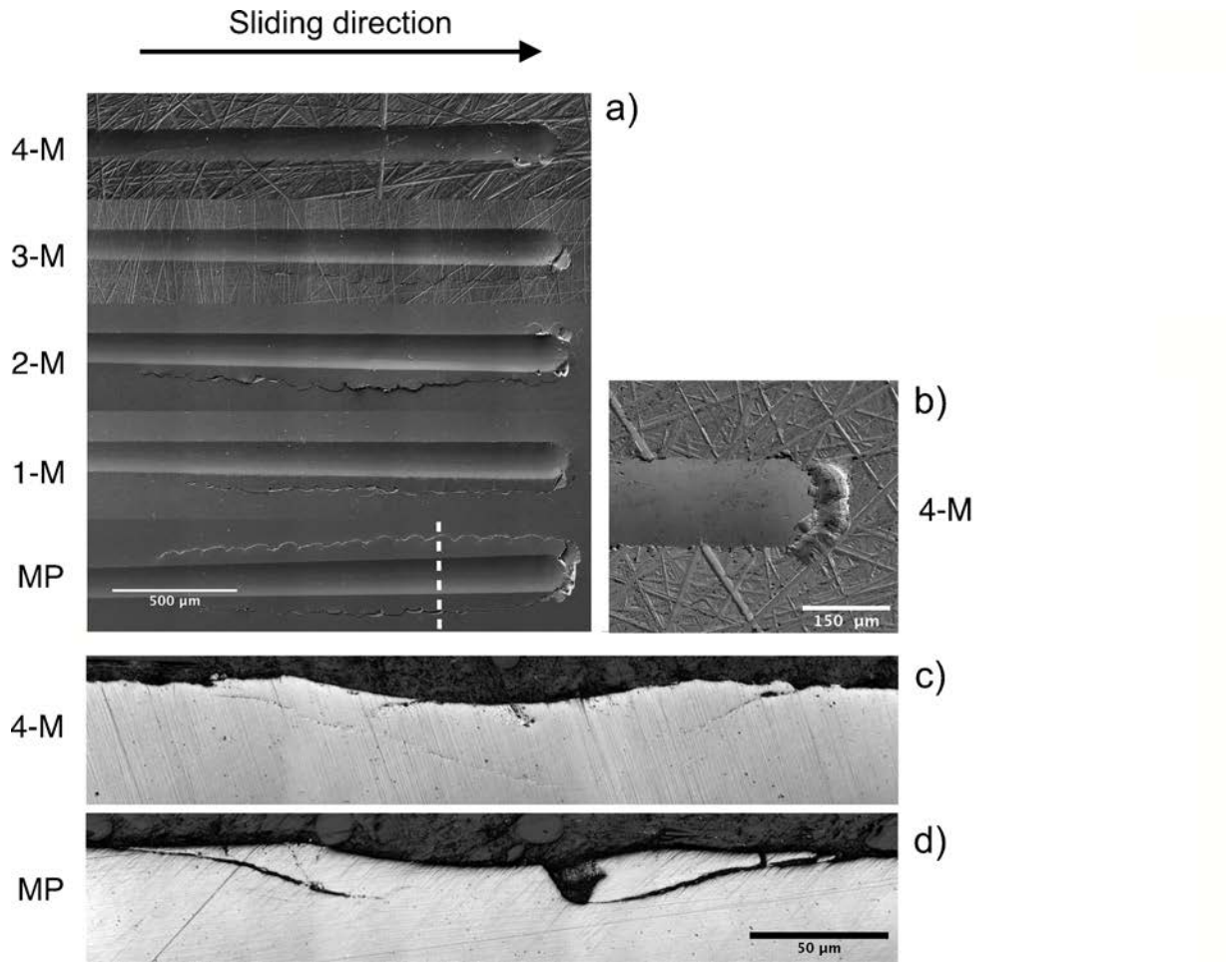

Fig. 4. a) FESEM micrographs of the tracks left after scratch tests in M specimens. Note that no cracks were visible on the surface of 4-M. Dashed line in MP indicates how specimens were cross-sectioned to obtain figures c) and d). b) Magnification of the last section of the track in a 4-M specimen. c) and d) CLSM cross sectional images of the last section of the scratch at loads above 180 N in 4-M and MP specimens, respectively. Lateral cracks could be observed in both specimens, presenting different morphologies.

other surface regions with lower amounts of *m*-phase. On the other hand, 1-M presented a layer-like structure with maximum transformation in the surface region, decreasing with depth. Nevertheless, both 1-M and 4-M displayed lower transformation depths as compared to MP.

Several of the microstructural features observed after grinding/polishing procedures are known to have a protective effect against

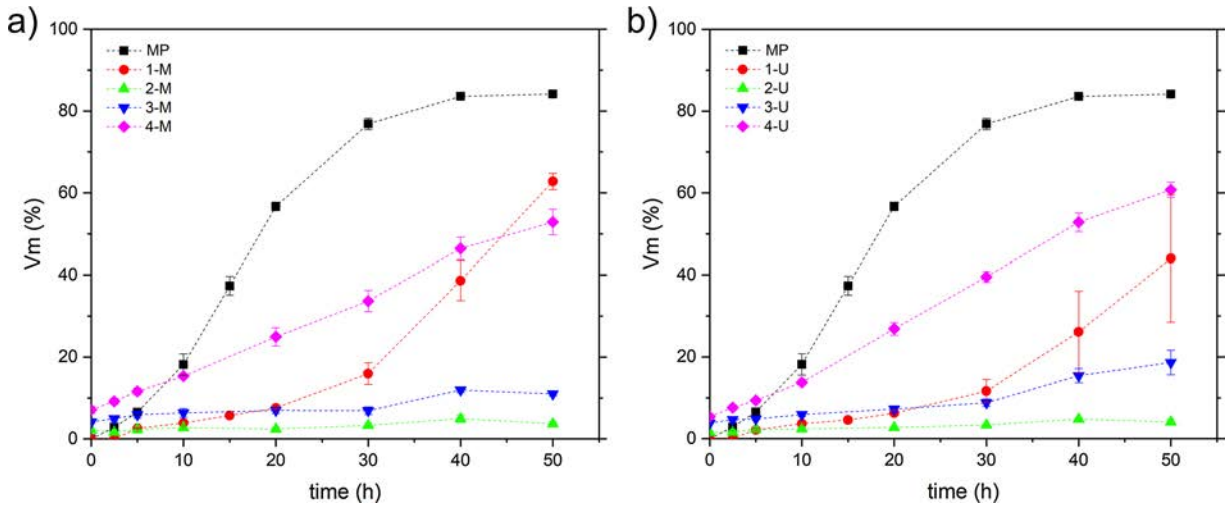

Fig. 5. Degradation kinetics in water steam. The evolution of the monoclinic volume fraction is plotted against degradation time. a) M specimens and b) U specimens. No degradation was observed in 2-M/U specimens and just a slight increase in the monoclinic content could be appreciated in 3-M/U specimens. The 20 % V_m left to reach a full *m*-phase material in MP specimens, corresponded to non-transformable cubic (*c*) phase.

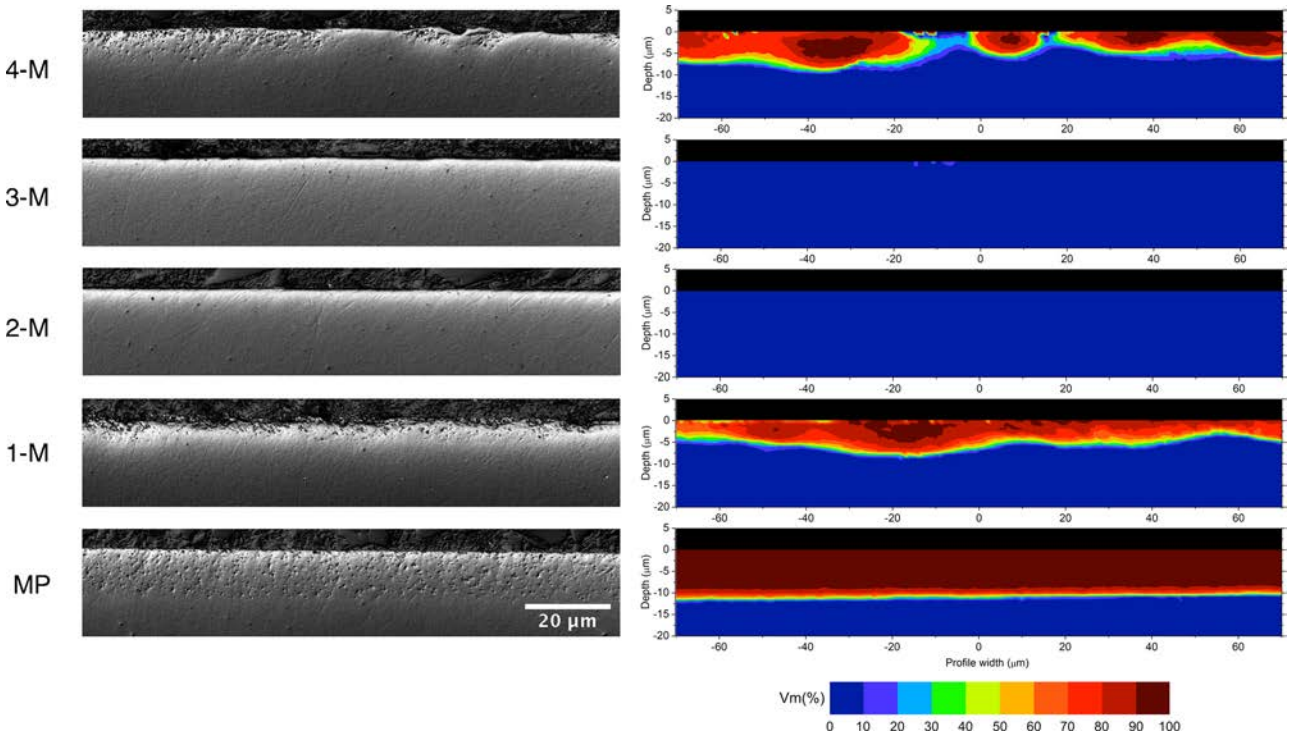

Fig. 6. Cross-sections of the degraded specimens after 50 h in water steam. On the left, CLSM images. On the right, *m*-phase distribution determined by confocal micro-Raman spectroscopy. Note that for each condition, CLSM and phase images were taken from the same specimen but probing different regions.

ageing. Reduction in grain size after surface recrystallization [31], as well as in domain size due to ferroelastic switching [34], and presence of a layer of residual compressive stresses [33] are known to delay low temperature degradation through different mechanisms. The behaviour shown by the studied specimens can be explained in terms of the presence of such features, as summarized in Table 1. Both 2-M/U and 3-M/U, presenting an excellent resistance, displayed a recrystallized surface of nano-grains, a certain amount of domain switching (i.e. texture as shown by $(002)_t$ /$(200)_t$ XRD intensity relation), as well as a layer of residual compressive stresses [45]. 3-M/U was ground with resin-bonded and relatively large diamond particles, presenting an affected layer of several microns deep. 2-M/U was polished with smaller diamond particles in water-based slurries, involving a milder process that reduced the affected region to a very shallow but intense layer, in the first micron of material. However, both of them were able to effectively protect the surface. In fact, similar degradation resistance in softly polished specimens have been recently reported [30] with 15 µm diamond polishing. As the grinding/polishing varied from this optimal finishing, degradation started to occur. While 1-M/U seemed not to present enough protective features, 4-M/U showed a deterioration of the achieved protection. Regarding the former, XRD spectra performed in a previous study [45], showed to be very similar to the one in the mirror-polished (MP) with almost no changes even in grazing incidence measurements, lacking the protection of surface texture and the residual stresses following the $t \rightarrow m$ transformation. However, 1-M/U's surface was found to present partial recrystallization, which seemed to have a positive effect, as degradation was clearly improved respect to MP. In fact, ageing in this specimen presented a degradation similar to 4-M/U, in which a very severe grinding had been applied. It is important to highlight that a surface finishing as smooth as the one in 1-M/U, with a S_a =16 nm, was able to introduce the microstructural changes needed for the delay of ageing.

The key point to enhance ageing resistance through microstructural tailoring, is thus not to introduce large changes, but just the adequate ones. This could be observed in the case of 4-M/U, where degradation was higher than in 2-M/U and 3-M/U, even though the former exhibited the largest microstructural changes. The decrease in performance for this specimen was related to surface damage. As evidenced in Fig. 7a and 7b, where the surfaces of 3-M and 4-M specimens are shown right after grinding (i.e. not degraded), regions with extensive damage in the form of micro-cracks could be observed in 4-M. This is different to the scenario found in the rest of the specimens, where ductile material removal mechanisms took place exclusively. In order to study whether the worsening of the degradation behaviour was indeed related to such surface state, a superficial *m*-phase map was obtained in one of the 4-M specimens degraded for 50 h. Fig. 7c shows the obtained phase map along with an optical micrograph of the corresponding region. While most of the surface presented damaged material (labelled as A), a damage-free track with a whitish surface crossed the measured region almost horizontally (labelled as B). Phase mapping clearly revealed that the entire surface was degraded except for the damage-free track, which was totally resistant to degradation. In fact, one damaged track crossed the non-transformed region, acting as a nucleating zone for the *m*-phase (labelled as C). As shown in our previous study [45], as the diamond particle size increases, material removal mechanisms tend to change from ductile to brittle, favouring the presence of damaged regions and allowing water to bypass the protective layer. Thus, if microstructural tuning through grinding procedures is to be performed for ageing-protective reasons, a balance must be achieved between the introduction of beneficial features and the prevention of surface micro-damage.

3.4. Cell adhesion study

Surface topography of biomaterials is known to affect cell behaviour [61]. Indeed, it is well accepted that roughness can influence (positively or not) the adhesion, proliferation and differentiation of osteoblastic cells [42,43,62,63]. However, the majority of works have generally focused on titanium and studies on other materials, e.g. Y-TZP, are needed.

Fig. 8 displays the results obtained in the cell adhesion assays. As shown in Fig. 8a, the number of adherent SaOS-2 was very similar on all

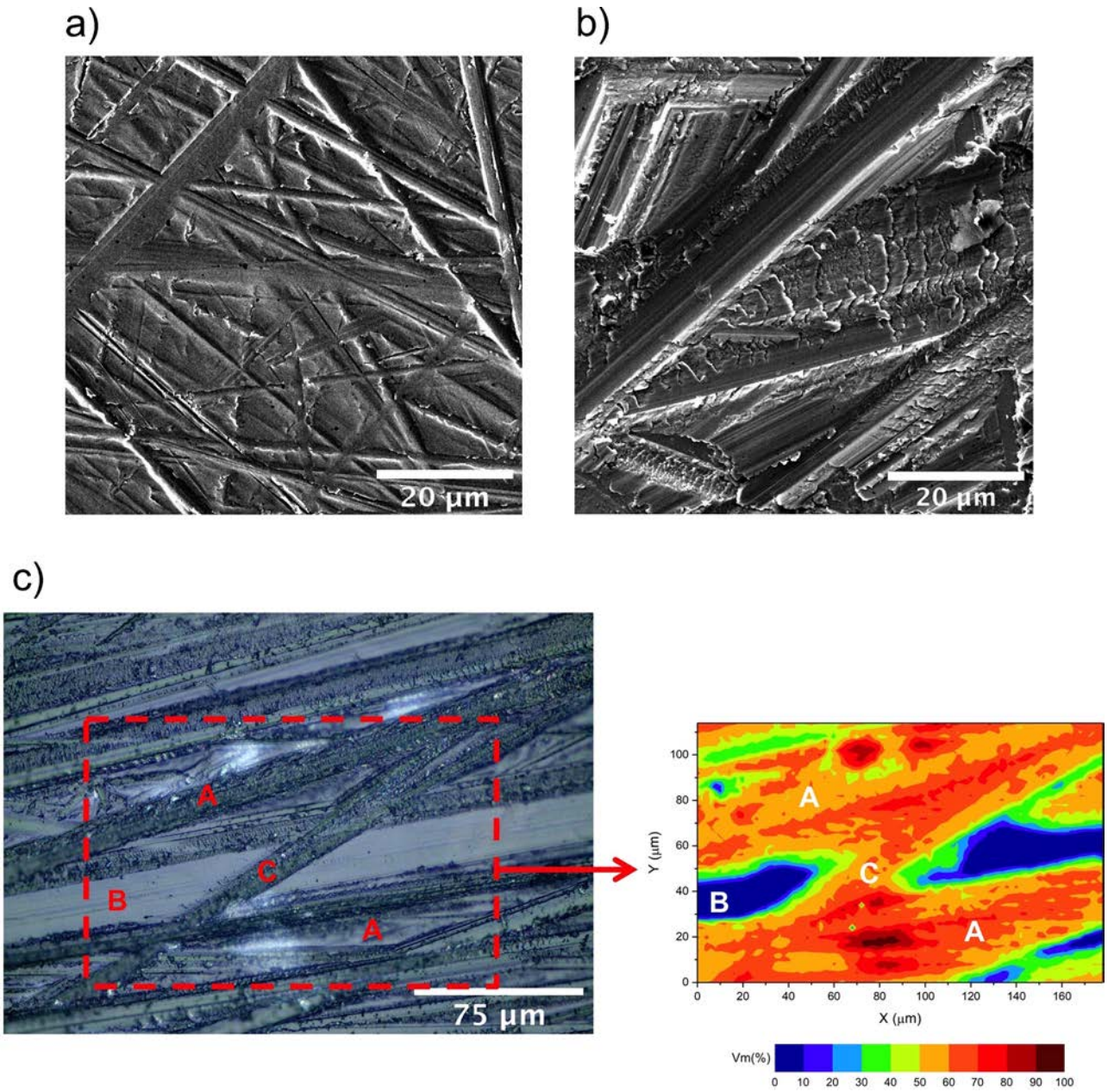

Fig. 7. FESEM micrograph of the surface in a) 3-M and b) 4-M specimens right after grinding (i.e. not degraded). Extensive damage could be seen in 4-M surface, with the presence of micro-cracks and flaking, while 3-M presented a smoother damage-free surface, with evident signs of plastic material removal mechanisms. c) Insight on the degradation behaviour of 4-M specimens. On the left, optical microscopy image of a 4-M specimen surface degraded for 50 h. On the right, *m*-phase mapping of the outlined region through confocal micro-Raman spectroscopy. Labels A indicate large regions were micro-damage was observed on the ground tracks. Label B identifies a track (in whitish colour) with no damage, where mainly ductile removal mechanisms took place. Label C shows a damaged track crossing the damage-free region.

the studied surfaces, without statistically significant differences as a function of the surface topography. In detail, neither an increase in surface roughness (i.e. Sa values) nor the presence of a pattern texture (M/U) seemed to influence cell attachment. In contrast, cell morphology and orientation were dependent on the topography. This effect can be observed in Fig. 8b and 8c, where for both 3-U and 4-U, a slight decrease in cell area (statistically significant for 4-U) and an increase in the aspect ratio (statistically significant for 3-U and 4-U), i.e. a more elongated cell shape, were observed. As depicted in Fig. 8d the morphological changes in 3-U and 4-U were related to a strong alignment in the direction of the grinding grooves, which was only detected on these two surfaces. For the rest of the specimens no alignment was observed, displaying similar morphological features as those found in the mirror-like polished MP specimen. These results indicate that roughness alone does not directly affect cell area or their aspect ratio, but in combination with oriented patterns is able to favour cell alignment above a certain roughness level, changing cell morphology. Previous data already reported such effect on ground titanium surfaces [64,65], as well as in other materials [66]. The ability to induce cell alignment has been a subject of interest for many researchers, as a means of affecting cell behaviour. In fact, it has been shown to trigger cytoskeleton reorganization, and to affect extracellular matrix remodelling, cell migration, membrane protein relocation and gene expression [67]. Herein we propose the existence of a threshold larger or equal to Sa = 150 nm to effectively induce cell alignment on unidirectionally ground Y-TZP. Fig. 8e and 8f show two fluorescence CLSM images of stained cells in

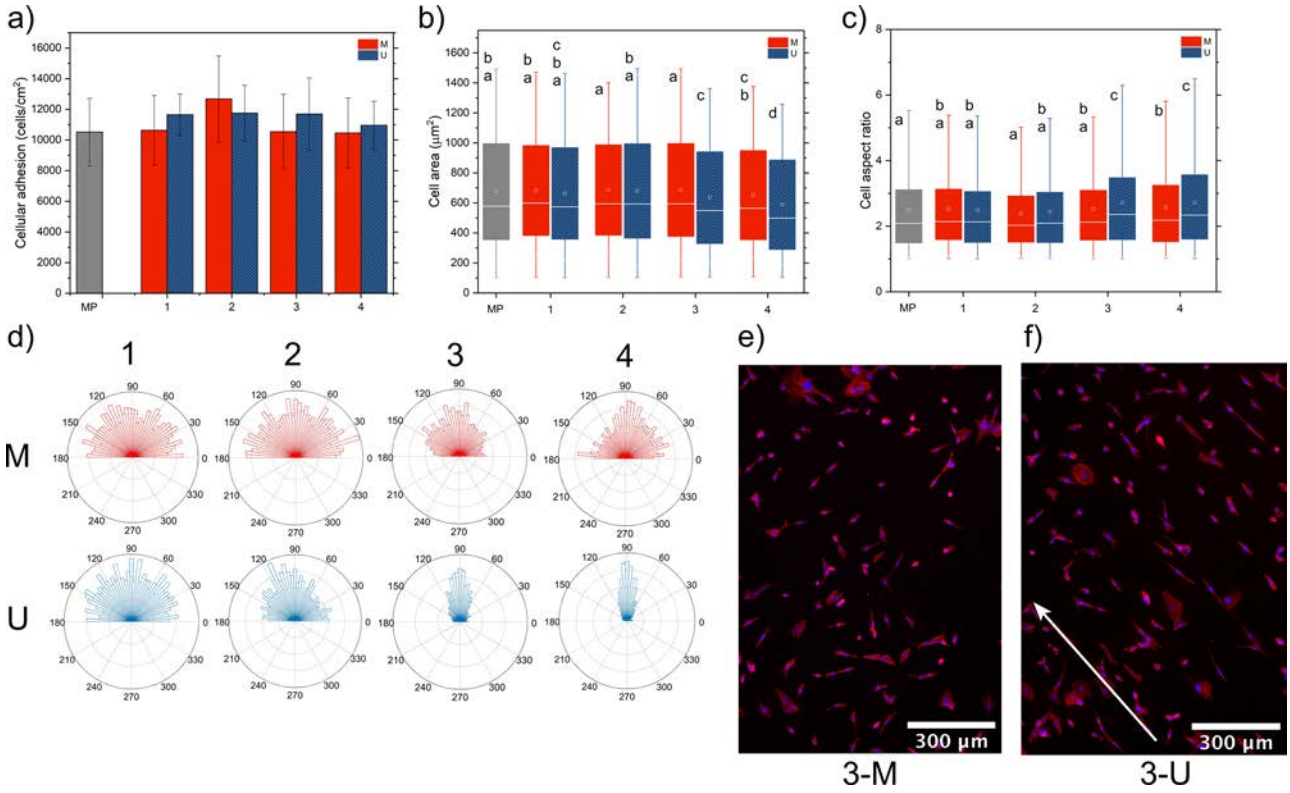

Fig. 8. SaOS-2 adhesion results after 24 h of incubation in FBS-supplemented medium. a) Cellular adhesion (cells/cm^2), b) cell area (μm^2) and c) cell aspect ratio. d) Angular histogram of cell orientation. Each bar of the histogram represents the relative cell number aligned to a specific angle on the surface. In U specimens 90° corresponds to the grinding direction. e) and f) Fluorescence CLSM images of the cells cultured on specimens 3-M and 3-U, respectively. Actin filaments are stained with TRITC-conjugated phalloidin (red), and cell nuclei with DAPI (blue). White arrow in f) points to the grinding direction. Groups identified by the same letter are not statistically different ($p > 0.05$). (For interpretation of the references to colour in the Figure, the reader is referred to the web version of this article).

specimens 3-M and 3-U. An alignment in 3-U in the direction of grinding is clearly noticed, while cells are randomly spread onto 3-M surfaces.

4. Conclusions

Microstructural and crystallographic changes after surface grinding/polishing were able to greatly affect both mechanical properties and hydrothermal degradation resistance of 3Y-TZP. Furthermore, topographical changes (i.e. unidirectional grooves) efficiently promoted osteoblasts alignment. Although the increase in properties showed a significant direct correlation with abrasion severity, surface damage introduced in the coarsest grinding worsened ageing resistance. In particular, it was observed that:

- The layer of compressive residual stresses as a result of the $t \rightarrow m$ transformation resulted in an increase in apparent fracture toughness, which hindered the propagation of superficial cracks, as well as the opening of subsurface cracks reaching the surface, the latter as observed in scratch tests. The studied mechanical properties improved with grinding.
- In order to protect 3Y-TZP from ageing, it was shown that coarse grinding is not only unnecessary, but can be counterproductive. Instead, intermediate conditions (in terms of grit size), including both grinding and rough polishing, could protect the surface from degradation, even in damage-free specimens with a roughness as low as $S_a = 45$ nm. In this regard, zirconia showed to be highly responsive to surface mechanical treatments. Even specimens polished until a surface roughness of $S_a = 16$ nm displayed an important degree of surface protection.
- All the topographical modifications performed allowed cell attachment and presented contact guidance when unidirectionally ground above a certain roughness level.

Declaration of Competing Interest

The authors declare that they have no known competing financial interests or personal relationships that could have appeared to influence the work reported in this paper.

Acknowledgements

This work was supported by the Ministerio de Ciencia, Innovación y Universidades (MAT2017-83905-R, MINECO/FEDER), the Generalitat de Catalunya (2017 SGR-933 and SGR-1165) and the CREATe-Network Project, Horizon 2020 Program of the European Commission (RISE Project Nr. 644013). J. Minguela has been supported by a predoctoral fellowship from the Barcelona Research Center in Multiscale Science and Engineering of the UPC. M-P. Ginebra acknowledges the ICREA Academia Award from the Generalitat de Catalunya. C. Mas-Moruno thanks the Spanish Government for a Ramon y Cajal grant. J.J. Roa acknowledges the Serra Hunter programme from the Generalitat de Catalunya.

References

[1] H.J. Conrad, W.J. Seong, I.J. Pesun, Current ceramic materials and systems with clinical recommendations: a systematic review, J. Prosthet. Dent. 98 (2007) 389–404.
[2] T. Miyazaki, T. Nakamura, H. Matsumura, S. Ban, T. Kobayashi, Current status of zirconia restoration, J. Prosthodont. Res. 57 (2013) 236–261.
[3] J.R. Kelly, I. Denry, Stabilized zirconia as a structural ceramic: an overview, Dent. Mater. 24 (2008) 289–298.
[4] I. Denry, J.R. Kelly, State of the art of zirconia for dental applications, Dent. Mater.

24 (2008) 299–307.
[5] I. Denry, J.R. Kelly, Emerging ceramic-based materials for dentistry, J. Dent. Res. 93 (2014) 1235–1242.
[6] T. Kosmač, A. Kocjan, Ageing of dental zirconia ceramics, J. Eur. Ceram. Soc. 32 (2012) 2613–2622.
[7] K. Tsukuma, M. Shimada, Strength, fracture toughness and Vickers hardness of CeO_2-stabilized tetragonal ZrO_2 polycrystals (Ce-TZP), J. Mater. Sci. 20 (1985) 1178–1184.
[8] M. Turon-Vinas, J.J. Roa, F.G. Marro, M. Anglada, Mechanical properties of 12Ce-ZrO_2/3Y-ZrO_2 composites, Ceram. Int. 41 (2015) 14988–14997.
[9] P.F. Manicone, P.R. Iommetti, L. Raffaelli, An overview of zirconia ceramics: basic properties and clinical applications, J. Dent. 35 (2007) 819–826.
[10] B.C. Spies, J. Nold, K. Vach, R.J. Kohal, Two-piece zirconia oral implants withstand masticatory loads: an investigation in the artificial mouth, J. Mech. Behav. Biomed. Mater. 53 (2016) 1–10.
[11] V. Lughi, V. Sergo, Low temperature degradation -aging- of zirconia: a critical review of the relevant aspects in dentistry, Dent. Mater. 26 (2010) 807–820.
[12] J. Chevalier, L. Gremillard, S. Deville, Low-temperature degradation of zirconia and implications for biomedical implants, Annu. Rev. Mater. Res. 37 (2007) 1–32.
[13] J. Chevalier, L. Gremillard, A.V. Virkar, D.R. Clarke, The tetragonal-monoclinic transformation in zirconia: lessons learned and future trends, J. Am. Ceram. Soc. 92 (2009) 1901–1920.
[14] A.G. Gristina, Biomaterial-centered infections: microbial adhesion versus tissue integration, Science 237 (1987) 1588–1595.
[15] T. Kosmač, Č. Oblak, P. Jevnikar, N. Funduk, L. Marion, The effect of surface grinding and sandblasting on flexural strength and reliability of Y-TZP zirconia ceramic, Dent. Mater. 15 (1999) 426–433.
[16] R.K. Chintapalli, A. Mestra Rodriguez, F. Garcia Marro, M. Anglada, Effect of sandblasting and residual stress on strength of zirconia for restorative dentistry applications, J. Mech. Behav. Biomed. Mater. 29 (2014) 126–137.
[17] J.A. Muñoz-Tabares, E. Jiménez-Piqué, J. Reyes-Gasga, M. Anglada, Microstructural changes in ground 3Y-TZP and their effect on mechanical properties, Acta Mater. 59 (2011) 6670–6683.
[18] J.A. Muñoz-Tabares, M. Anglada, Hydrothermal degradation of ground 3Y-TZP, J. Eur. Ceram. Soc. 32 (2012) 325–333.
[19] J.J. Roa, M. Turon-Vinas, M. Anglada, Surface grain size and texture after annealing ground zirconia, J. Eur. Ceram. Soc. 36 (2016) 1519–1525.
[20] Q. Flamant, F. García Marro, J.J. Roa Rovira, M. Anglada, Hydrofluoric acid etching of dental zirconia. Part 1: etching mechanism and surface characterization, J. Eur. Ceram. Soc. 36 (2016) 121–134.
[21] Q. Flamant, M. Anglada, Hydrofluoric acid etching of dental zirconia. Part 2: Effect on flexural strength and ageing behavior, J. Eur. Ceram. Soc. 36 (2016) 135–145.
[22] E. Roitero, F. Lasserre, J.J. Roa, M. Anglada, F. Mücklich, E. Jiménez-Piqué, Nanosecond-laser patterning of 3Y-TZP: damage and microstructural changes, J. Eur. Ceram. Soc. 37 (2017) 4876–4887.
[23] E. Roitero, M. Ochoa, M. Anglada, F. Mücklich, E. Jiménez-Piqué, Low temperature degradation of laser patterned 3Y-TZP: enhancement of resistance after thermal treatment, J. Eur. Ceram. Soc. 38 (2018) 1742–1749.
[24] C.J. Ho, H.C. Liu, W.H. Tuan, Effect of abrasive grinding on the strength of Y-TZP, J. Eur. Ceram. Soc. 29 (2009) 2665–2669.
[25] G.K.R. Pereira, M. Amaral, R. Simoneti, G.C. Rocha, P.F. Cesar, L.F. Valandro, Effect of grinding with diamond-disc and -bur on the mechanical behavior of a Y-TZP ceramic, J. Mech. Behav. Biomed. Mater. 37 (2014) 133–140.
[26] G.K.R. Pereira, S. Fraga, A.F. Montagner, F.Z.M. Soares, C.J. Kleverlaan, L.F. Valandro, The effect of grinding on the mechanical behavior of Y-TZP ceramics: a systematic review and meta-analyses, J. Mech. Behav. Biomed. Mater. 63 (2016) 417–442.
[27] M. Inokoshi, F. Zhang, K. Vanmeensel, J. De Munck, S. Minakuchi, I. Naert, J. Vleugels, B. Van Meerbeek, Residual compressive surface stress increases the bending strength of dental zirconia, Dent. Mater. 33 (2017) e147–e154.
[28] P.J. Whalen, F. Reidinger, R.F. Antrim, Prevention of low-temperature surface transformation by surface recrystallization in yttria-doped tetragonal zirconia, J. Am. Ceram. Soc. 72 (1989) 319–321.
[29] T. Kosmač, Č. Oblak, L. Marion, The effects of dental grinding and sandblasting on ageing and fatigue behavior of dental zirconia (Y-TZP) ceramics, J. Eur. Ceram. Soc. 28 (2008) 1085–1090.
[30] M. Inokoshi, K. Vanmeensel, F. Zhang, J. De Munck, G. Eliades, S. Minakuchi, I. Naert, B. Van Meerbeek, J. Vleugels, Aging resistance of surface-treated dental zirconia, Dent. Mater. 31 (2015) 182–194.
[31] P.F. Becher, M.V. Swain, Grain-size-Dependent transformation behavior in poly-crystalline tetragonal zirconia, J. Am. Ceram. Soc. 75 (1992) 493–502.
[32] R.H.J. Hannink, P.M. Kelly, B.C. Muddle, Transformation toughening in zirconia-containing ceramics, J. Am. Ceram. Soc. 83 (2000) 461–487.
[33] S. Deville, J. Chevalier, L. Gremillard, Influence of surface finish and residual stresses on the ageing sensitivity of biomedical grade zirconia, Biomaterials. 27 (2006) 2186–2192.
[34] J.F. Jue, J. Chen, A.V. Virkar, Low-temperature aging of t'-Zirconia: the role of microstructure on phase-stability, J. Am. Ceram. Soc. 74 (1991) 1811–1820.
[35] J. Lincks, B.D. Boyan, C.R. Blanchard, C.H. Lohmann, Y. Liu, D.L. Cochran, D. Dean, Z. Schwartz, Response of MG63 osteoblast-like cells to titanium and titanium alloy is dependent on surface roughness and composition, Biomaterials 19 (1998) 2219–2232.
[36] U. Hempel, T. Hefti, M. Kalbacova, C. Wolf-Brandstetter, P. Dieter, F. Schlottig, Response of osteoblast-like SAOS-2 cells to zirconia ceramics with different surface topographies, Clin. Oral Implants Res. 21 (2010) 174–181.
[37] F.F.B. Hulshof, B. Papenburg, A. Vasilevich, M. Hulsman, Y. Zhao, M. Levers, N. Fekete, M. de Boer, H. Yuan, S. Singh, N. Beijer, M.A. Bray, D.J. Logan, M. Reinders, A.E. Carpenter, C. van Blitterswijk, D. Stamatialis, J. de Boer, Mining for osteogenic surface topographies: in silico design to in vivo osseo-integration, Biomaterials. 137 (2017) 49–60.
[38] S. Erramilli, J. Genzer, Influence of surface topography attributes on settlement and adhesion of natural and synthetic species, Soft Matter 15 (2019) 4045–4067.
[39] L. Sennerby, A. Dasmah, B. Larsson, M. Iverhed, Bone tissue responses to surface-modified zirconia implants: a histomorphometric and removal torque study in the rabbit, Clin. Implant Dent. Relat. Res. 7 (2005) s13–s20.
[40] M. Gahlert, T. Gudehus, S. Eichhorn, E. Steinhauser, H. Kniha, W. Erhardt, Biomechanical and histomorphometric comparison between zirconia implants with varying surface textures and a titanium implant in the maxilla of miniature pigs, Clin. Oral Implants Res. 18 (2007) 662–668.
[41] J.Y. Martin, Z. Schwartz, D.M. Schraub, J. Simpson, J. Lankford, D.D. Dean, D.L. Cochran, Effect of titanium surface roughness on proliferation, differentiation, and protein synthesis of human osteoblast-like cells (MG63), J. Biomed. Mater. Res. 29 (1995) 389–401.
[42] H. Ito, H. Sasaki, K. Saito, S. Honma, Y. Yajima, M. Yoshinari, Response of osteoblast-like cells to zirconia with different surface topography, Dent. Mater. J. 32 (2013) 122–129.
[43] R.A. Delgado-Ruíz, G. Gomez Moreno, A. Aguilar-Salvatierra, A. Markovic, J.E. Mate-Sánchez, J.L. Calvo-Guirado, Human fetal osteoblast behavior on zirconia dental implants and zirconia disks with microstructured surfaces, An experimental in vitro study, Clin. Oral Implants Res. 27 (2016) e144–e153.
[44] B.D. Boyan, T.W. Hummert, D.D. Dean, Z. Schwartz, Role of material surfaces in regulating bone and cartilage cell response, Biomaterials 17 (1996) 137–146.
[45] J. Minguela, S. Slawik, F. Mücklich, M.P. Ginebra, L. Llanes, C. Mas-Moruno, J.J. Roa, Evolution of microstructure and residual stresses in gradually ground/polished 3Y-TZP, J. Eur. Ceram. Soc. 40 (2020) 1582–1591.
[46] W.P. Dong, P.J. Sullivan, K.J. Stout, Comprehensive study of parameters for characterising three- dimensional surface topography. III: parameters for characterising amplitude and some functional properties, Wear 178 (1994) 29–43.
[47] W.P. Dong, P.J. Sullivan, K.J. Stout, Comprehensive study of parameters for characterising three-dimensional surface topography. IV: parameters for characterising spatial and hybrid properties, Wear 178 (1994) 45–60.
[48] E.S. Gadelmawla, M.M. Koura, T.M.A. Maksoud, I.M. Elewa, H.H. Soliman, Roughness parameters, J. Mater. Process. Technol. 123 (2002) 133–145.
[49] R.J. Good, Contact angle, wetting and adhesion: a critical review, J. Adhes. Sci. Technol. 6 (1992) 1269–1302.
[50] K. Niihara, R. Morena, D.P. Hasselman, Evaluation of klc of brittle solids by the indentation method with low crack to indent ratios, J. Mater. Sci. Lett. 1 (1982) 13–16.
[51] S.K. Lee, R. Tandon, M.J. Readey, B.R. Lawn, Scratch damage in zirconia ceramics, J. Am. Ceram. Soc. 83 (2000) 1428–1432.
[52] J. Chevalier, B. Cales, J.M. Drouin, Low-temperature aging of Y-TZP ceramics, J. Am. Ceram. Soc. 82 (1999) 2150–2154.
[53] H. Toraya, M. Yoshimura, S. Somiya, Calibration curve for quantitative analysis of the monoclinic-tetragonal ZrO2 system by X-Ray diffraction, J. Am. Ceram. Soc. 67 (1984) C119–C121.
[54] T.M.G. Katagiri, H. Ishida, A. Ishitani, Direct determination by Raman Microprobe of the transformation zone size in Y2O3 containing tetrag- onal ZrO2 polycrystal, Sci. Technol. Zirconia III, Ed. By S. Somiya, N. Yamamoto, H. Yanagida, J. Am. Ceram. Soc. (1988) 537–544.
[55] R. Fraioli, F. Rechenmacher, S. Neubauer, J.M. Manero, J. Gil, H. Kessler, C. Mas-Moruno, Mimicking bone extracellular matrix: integrin-binding peptidomimetics enhance osteoblast-like cells adhesion, proliferation, and differentiation on titanium, Colloids Surf. B Biointerfaces 128 (2015) 191–200.
[56] M. Hoyos-Nogués, F. Velasco, M.P. Ginebra, J.M. Manero, F.J. Gil, C. Mas-Moruno, Regenerating bone via multifunctional coatings: the blending of cell integration and bacterial inhibition properties on the surface of biomaterials, ACS Appl. Mater. Interfaces 9 (2017) 21618–21630.
[57] J. Schindelin, I. Arganda-Carreras, E. Frise, V. Kaynig, M. Longair, T. Pietzsch, S. Preibisch, C. Rueden, S. Saalfeld, B. Schmid, J.Y. Tinevez, D.J. White, V. Hartenstein, K. Eliceiri, P. Tomancak, A. Cardona, Fiji: An open-source platform for biological-image analysis, Nat. Methods 9 (2012) 676–682.
[58] N. Al-Haj Husain, M. Özcan, A study on topographical properties and surface wettability of monolithic zirconia after use of diverse polishing instruments with different surface coatings, J. Prosthodont. 27 (2018) 429–442.
[59] A. Juy, M. Anglada, Strength and grinding residual stresses of Y-TZP with duplex microstructures, Eng. Fail. Anal. 16 (2009) 2586–2597.
[60] T. Leitner, A. Hohenwarter, W. Ochensberger, R. Pippan, Fatigue crack growth anisotropy in ultrafine-grained iron, Acta Mater. 126 (2017) 154–165.
[61] C. Mas-Moruno, B. Su, M.J. Dalby, Multifunctional coatings and nanotopographies: toward cell instructive and antibacterial implants, Adv. Healthc. Mater. 8 (2019) 1801103.
[62] C. Mas-Moruno, P.M. Dorfner, F. Manzenrieder, S. Neubauer, U. Reuning, R. Burgkart, H. Kessler, Behavior of primary human osteoblasts on trimmed and sandblasted Ti6Al4V surfaces functionalized with integrin αvβ3-selective cyclic RGD peptides, J. Biomed. Mater. Res. - Part A. 101 A (2013) 87–97.
[63] T. Hirano, H. Sasaki, S. Honma, Y. Furuya, T. Miura, Y. Yajima, M. Yoshinari,

Proliferation and osteogenic differentiation of human mesenchymal stem cells on zirconia and titanium with different surface topography, Dent. Mater. J. 34 (2015) 872–880.
[64] E. Eisenbarth, P. Linez, V. Biehl, D. Velten, J. Breme, H.F. Hildebrand, Cell orientation and cytoskeleton organisation on ground titanium surfaces, Biomol. Eng. 19 (2002) 233–237.
[65] H. Huang, C. Ho, T. Lee, T. Lee, K. Liao, F. Chen, Effect of surface roughness of ground titanium on initial cell adhesion, Biomol. Eng. 21 (2004) 93–97.
[66] K. Shimizu, H. Fujita, E. Nagamori, Alignment of skeletal muscle myoblasts and myotubes using linear micropatterned surfaces ground with abrasives, Biotechnol. Bioeng. 103 (2009) 631–638.
[67] Y. Li, G. Huang, X. Zhang, L. Wang, Y. Du, T.J. Lu, F. Xu, Engineering cell alignment in vitro, Biotechnol. Adv. 32 (2014) 347–365.

Chapter 6
Paper III

Peptidic biofunctionalization of laser patterned dental zirconia: a biochemical - topographical approach

Available at:

https://www.sciencedirect.com/science/article/abs/pii/S0928493121002356

Materials Science & Engineering C 125 (2021) 112096

Contents lists available at ScienceDirect

Materials Science & Engineering C

journal homepage: www.elsevier.com/locate/msec

Peptidic biofunctionalization of laser patterned dental zirconia: A biochemical-topographical approach

J. Minguela [a,b,c], D.W. Müller [d], F. Mücklich [d], L. Llanes [b,c], M.P. Ginebra [a,c,e], J.J. Roa [b,c], C. Mas-Moruno [a,c,*]

[a] Biomaterials, Biomechanics and Tissue Engineering Group (BBT), Department of Materials Science and Engineering, Universitat Politècnica de Catalunya-BarcelonaTECH, 08019 Barcelona, Spain
[b] Center for Structural Integrity, Reliability and Micromechanics of Materials (CIEFMA), Department of Materials Science and Engineering, Universitat Politècnica de Catalunya-BarcelonaTECH, 08019 Barcelona, Spain
[c] Barcelona Research Center in Multiscale Science and Engineering, Universitat Politècnica de Catalunya-BarcelonaTECH, 08019 Barcelona, Spain
[d] Functional Materials, Department of Materials Science and Engineering, Saarland University, 66123 Saarbruecken, Germany
[e] Institute for Bioengineering of Catalonia (IBEC), Barcelona Institute of Technology (BIST), 08028 Barcelona, Spain

ARTICLE INFO

Keywords:
Zirconia
Laser patterning
Surface functionalization
Peptides
Osteointegration

ABSTRACT

A dual approach employing peptidic biofunctionalization and laser micro-patterns on dental zirconia was explored, with the aim of providing a flexible tool to improve tissue integration of restorations. Direct laser interference patterning with a femtosecond Ti:Sapphire laser was employed, and two periodic grooved patterns were produced with a periodicity of 3 and 10 μm. A platform containing the cell-adhesive RGD and the osteogenic DWIVA peptides was used to functionalize the grooved surfaces. Topography and surface damage were characterized by confocal laser scanning (CLSM), scanning electron and scanning transmission electron microscopy techniques. The surface patterns exhibited a high homogeneity and subsurface damage was found in the form of nano-cracks and nano-pores, at the bottom of the valleys. Accelerated tests in water steam were carried out to assess hydrothermal degradation resistance, which slightly decreased after the laser treatment. Interestingly, the detrimental effects of the laser modification were reverted by a post-laser thermal treatment. The attachment of the molecule was verified trough fluorescence CLSM and X-ray photoelectron spectroscopy. Finally, the biological properties of the surfaces were studied in human mesenchymal stem cells. Cell adhesion, morphology, migration and differentiation were investigated. Cells on grooved surfaces displayed an elongated morphology and aligned along the patterns. On these surfaces, migration was greatly enhanced along the grooves, but also highly restricted in the perpendicular direction as compared to flat specimens. After biofunctionalization, cell number and cell area increased and well-developed cell cytoskeletons were observed. However, no effects on cell migration were found for the peptidic platform. Although some osteogenic potential was found in specimens grooved with a periodicity of 10 μm, the largest effects were observed from the biomolecule, which favored upregulation of several genes related to osteoblastic differentiation in all the surfaces.

1. Introduction

Yttria-stabilized tetragonal zirconia polycrystal (Y-TZP) is used to produce several components employed in restorative dentistry, including dental implants, which are screwed into the jawbone and provide mechanical stability to the prosthesis [1]. The success of this procedure largely depends on the capacity of the implanted material to osteointegrate, i.e. establish a direct implant-to-bone contact [2], which will ensure the mechanical stability and long-lasting performance of the implant. However, the foreign body response triggered by the biomaterial after the surgery may also result in the formation of a collagenous fibrous layer encapsulating the implant; and thus, compromise its clinical viability. In this regard, although excellent outcomes have been recently reported for Y-TZP based ceramic implants, with a calculated 5-

* Corresponding author at: Biomaterials, Biomechanics and Tissue Engineering Group (BBT), Department of Materials Science and Engineering, Universitat Politècnica de Catalunya-BarcelonaTECH, 08019 Barcelona, Spain.
E-mail address: carles.mas.moruno@upc.edu (C. Mas-Moruno).

https://doi.org/10.1016/j.msec.2021.112096
Received 27 January 2021; Received in revised form 25 March 2021; Accepted 8 April 2021

year survival rate of 98.4% (95% CI 91.6, 99.9) [3], long-term studies are still needed. In the case of titanium, for instance, implant survival rates at 10 years are close to 95% [4]. Moreover, it should be taken into account that it is estimated that 5.5–6 million implants are placed each year only in Europe [5]. Therefore, even if the percentage of dental implant failure is low, in absolute values a large number of patients need a revision surgery every year, and the consequences are often catastrophic. The reasons for failure are varied and still not completely understood. They are often related to the initial foreign body response, but also to other events disbalancing the osteointegration process, including peri-implantitis, non-optimal implant design, traumatic handling, new loading conditions after losing adjacent teeth, and general health aspects [6]. In particular, further improvement of osteointegration at the implant surface is still necessary as [7]:

- In healthy subjects the osteointegration of a dental implant is a slow process. An early or immediate loading is not possible, which has negative effects in terms of patient morbidity and healthcare costs.
- The placement of implants is counter indicated in clinically compromised patients, where impaired osteointegration is observed. Such conditions include diabetes mellitus, osteoporosis, radiotherapy in neck and head or smoking addiction [8,9].

For these reasons, surface modification (e.g. topographical or biochemical) of implants has been widely employed in order to enhance bone formation at the material-tissue interface and achieve a proper biological seal at the gum level [10,11].

Surface topography can improve tissue integration in several ways. Firstly, surface roughness favors cell adhesion [12] and allows for better mechanical interlocking when in contact with bone [13]. Secondly, surface texture can influence cell behavior. For example, grooved surfaces can display contact guidance and favor cell migration, which is of special interest in applications where tissue growth over a surface must be guided [14,15], including dental implants [16–18]. In addition, both micro-[19,20] and nano- [11,21] topographical features can modify gene expression through cellular mechanotransduction. Indeed, changes in the organization of the cytoskeleton can trigger signaling pathways that (up)regulate the expression of genes involved in osteodifferentiation. It is the case of linear patterns, in which different groove/ridge combinations can guide human mesenchymal stem cell (hMSC) differentiation into several lineages, including the osteogenic one [22–24].

However, due to its particular properties, surface modification of Y-TZP remains challenging as compared to other materials used in dentistry such as titanium. Y-TZP is a relatively hard and brittle-like material [25]; thus, its surface can only withstand limited amounts of plastic deformation before presenting surface damage [26,27]. Accordingly, milder treatments must be employed if excessive crack formation, chipping or stress-induced phase transformation (from tetragonal to monoclinic phase, $t \rightarrow m$) are to be avoided. Consequently, relatively low values of surface average roughness (R_a) are obtained. Due to its chemical inertness, etching is only limited to a few aggressive reagents [28], and other methods such as anodization are not possible due to the lack of electronic conductivity. The effect of such treatments on the hydrothermal degradation of Y-TZP has to be taken in particular consideration. After extended exposure to water, some Y-TZP formulations can undergo a spontaneous phase transformation from *t*- to the more stable *m*-phase, which is associated with crack formation and weakening [29,30]. Excessive surface damage can facilitate this process [31,32], and as a consequence suitable methods for surface modification are limited, especially in biomedical applications.

Among the methods that have been successfully employed to superficially modify the topography of Y-TZP there are mechanical, chemical and thermal-based techniques, including sandblasting, grinding [26], chemical etching [28] and laser micro-patterning [33]. Of particular interest is laser patterning, which stands out as an efficient means of producing detailed and reproducible topographies at different length scales (e.g. grooves [34], pits [35], grits [36] or other textures) with relatively fast processing speed. Besides, as a non-contact technique it presents additional advantages, such as the absence of tool wear and surface contamination. Y-TZP surface has been successfully structured with lasers working on different regimes and employing different techniques [33,34,37–39]. In particular, direct laser interference patterning (DLIP) represents a promising technique for industrial use thanks to its ability to produce periodical patterns (mostly grooves, although other patterns are possible) in a single step, with higher processing speeds as compared to other techniques (e.g. laser writing or lithographic techniques) and resolutions at the micron- and sub-micron level [40–43]. Notably, it is possible to engrave such patterns in complex 3D structures, such as the body of threaded dental implants [44].

Just a few works are available about DLIP structuring of Y-TZP surfaces [24,32,33,41,43,45–47] and its influence on damage and hydrothermal degradation, which are only known in the nanosecond pulse duration regime [32,41,46], but not in the femtosecond one. Likewise, cellular behavior on Y-TZP grooved substrates has been scarcely characterized, whether produced by DLIP or direct writing. The available information agrees in that the grooved topographies (as it has been widely characterized in other materials [19,48]) can influence cell morphology, and that differentiation into the osteogenic lineage may be enhanced [24,36,49–51].

Alternatively, biochemical surface modifications may also be used in order to improve the osteointegrative potential of biomedical surfaces. Such modifications are generally based on the extracellular matrix (ECM) of bone, either its mineral inorganic part (e.g. calcium phosphate coatings) or its organic components (e.g. collagen, fibronectin, etc.) [11,52]. Of particular relevance are those organic molecules able to trigger receptor-specific cell functions, especially proteins [53], growth factors [54,55], peptides and related analogues [56,57]. In the particular case of peptidic molecules, several works have explored the functionalization of dental materials to enhance their surface properties and bioactivity [58]. These works include the use of antibacterial peptides [59,60], peptides that can reinforce epithelial sealing [61] and peptides that are osteogenic [62] or can improve the bone healing process [63], among others.

The main advantage of using synthetic peptides lies on their specificity, reduced size, and higher stability against enzymatic degradation and environmental changes such as pH or temperature. Although the most well-known peptide in tissue engineering is the RGD sequence [64], with a predominant role in cell-adhesion, other peptides have shown potential to improve bone healing and osteointegration [65]. In this regard, several peptide sequences have been found to present osteoinductive properties [66], such as those derived from the bone morphogenetic protein 2 (BMP-2) [67,68]. BMP-2 induces osteoblastic differentiation by binding to type I and type II BMP receptors (BMPRs). Lee et al. [69] studied a BMP-2 derived peptide (DWIVA) and found an increased osteoblastic differentiation of human bone marrow stromal cells through Smad signal transduction. Subsequently, it was recently demonstrated that combining this peptide with the RGD motif synergistically promoted integrin and BMPR signaling, inhibiting myotube formation on C2C12 cells and activating their transdifferentiation into the osteogenic lineage [70]. Notably, this study showed that the combination RGD-DWIVA in a geometrically controlled manner increased cell adhesion and promoted BMP-dependent signaling in a larger extent as compared to the presence of RGD or DWIVA only.

Within this context, the aim of the present work was to study the combination of topographical and biochemical modifications on Y-TZP biomaterials, and evaluate their effects at the surface level and its biological influence on hMSCs. Grooved laser patterns were created with two different periodicities: one with features of only a few microns, much below the cell body size, 3 μm; the other one with larger grooves, in a closer range to the cell size, 10 μm. DLIP technique was employed in order to ensure both periodicity and high processing speeds with

industrial applicability. The femtosecond regime was chosen because previous studies reported extended surface damage [46] and limitations in terms of pattern depth for the nanosecond regime [33]. A detailed topographical and microstructural characterization of the modified surfaces was carried out to analyze surface damage and changes in surface properties. To the best knowledge of the authors, these effects have not been investigated for such treatment. Additionally, the patterned surfaces were also functionalized with a dual peptidic platform [71], including the RGD and the BMP-2-derived DWIVA sequences [70], to further tune hMSC behavior. Interestingly, the biofunctionalization of Y-TZP has been scarce and limited to cell adhesive peptides [72–74]. Studies expanding the potential of peptidic functionalization to other areas (e.g. osteogenesis) are missing, and to date no studies combining topographical and biochemical modifications on this material can be found.

Thus, the main objective of this study was to investigate for the first time the combination of ultrashort pulsed direct laser interference patterning (USP-DLIP) and chemical functionalization on Y-TZP and explore the potential synergisms between topographical and biochemical cues (Fig. 1). Such combined approach may improve the tissue integrative properties and osteogenic potential of Y-TZP surfaces and provide new insights for the design of long-term functional dental implants.

2. Experimental procedure

2.1. Material processing

2.1.1. Sample preparation

Disc-shaped samples of 15 mm diameter were produced from zirconia powders stabilized with 3 mol% yttria (TZ-3YSB-E, Tosoh). Briefly, powders were cold isostatically pressed at 288 MPa and sintered at 1450 °C for 2 h (constant heating and cooling rates of 3 °C/min) obtaining a material with a grain size of 0.32 ± 0.12 μm and a density above 99% of the theoretical one. All the samples were mirror-like polished using suspensions of diamond particles with decreasing particle size (30 μm – 6 μm – 3 μm) with a final polishing step using an alumina suspension of 0.02 μm particle size. Some samples were not further modified to be used as reference specimens, labeled as CTRL. Further details about sample preparation and characterization can be found elsewhere [75]. After polishing, samples were cleaned in an ultrasonic bath in 6-minute washes, as follows: cyclohexane (x 2), acetone (x 2), deionized water (x 2), ethanol (x 2) and acetone (x 2). Finally, samples were dried in a N_2 stream.

2.1.2. Laser patterning

In order to obtain surface patterns, DLIP was employed. In this technique, an inhomogeneous fluence distribution is produced on the surface due to the interference of two or more laser beams, originating a periodical pattern [15,76]. The particular geometry of the patterns depends on the number of interfering beams as well as the optical setup. Surface patterning was carried out by using a Ti:Sapphire laser source emitting ultrashort pulses of 100 fs at Full Width Half Maximum (FWHM) with a centered wavelength λ of 800 nm. A detailed description of the optical setup employed in this work can be found in [43]. Briefly, an aperture defines the working beam diameter while a wave plate adjusts the polarization angle of the laser beam perpendicular to the generated pattern orientation in the first section of the optical setup. Further on, the femtosecond pulsed seed beam is divided by a Diffractive Optical Element (DOE), while the individual coherent beams are finally overlapped on the sample surface by means of a lens system. The beam-overlap induces a line-like interference pattern. The periodicity Π is defined by

$$\Pi = \frac{\lambda}{2\ tan\left(\frac{\theta}{2}\right)} \quad (1)$$

where θ is the incidence angle between the individual beams [43]. An alteration of Π can be achieved by changing the distance between DOE and the focusing lens system. The sample was mounted on a (x,y) motorized stage. In order to fully structure specimen surfaces, laser pulses were synchronized with the motorized stage. An optimization process was carried out adjusting laser power, stage speed and pulse overlapping in relation to the DOE-lens system spacing until homogeneous linear patterns were obtained of either 3 or 10 μm periodicity. Such laser-treated specimens were labeled as 3L and 10L, respectively. Samples were subsequently cleaned and dried as described above.

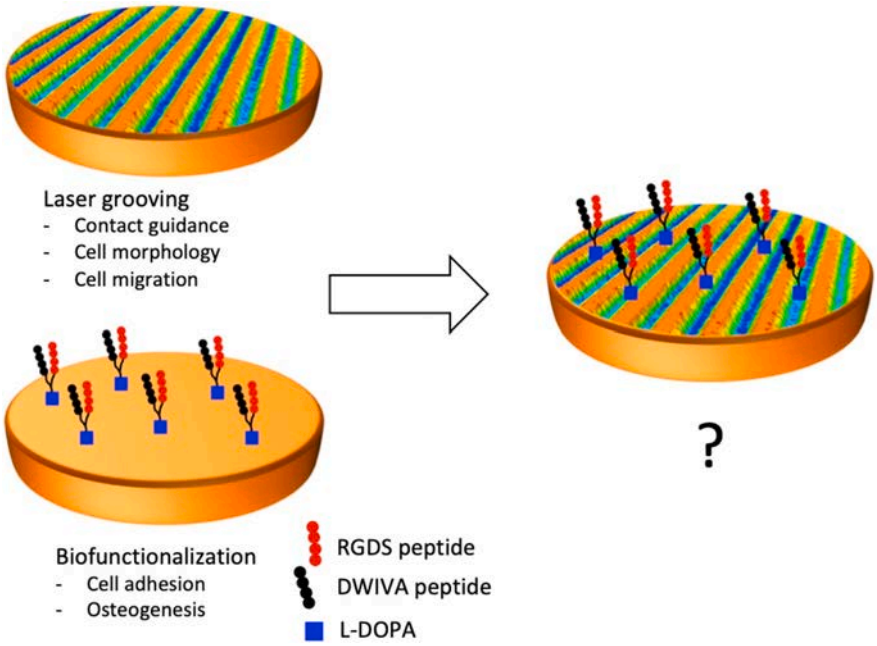

Fig. 1. Scheme of the rationale behind this study. Two different strategies were employed in order to improve the tissue integration potential of zirconia surfaces, one of topographical and one of biochemical nature. The main known effects on human cells from each strategy are detailed on the figure.

2.2. Biofunctionalization process

2.2.1. Biomolecule synthesis

The coating molecule (labeled as P) was produced using standard solid-phase peptide synthesis protocols and characterized as described elsewhere [70]. As shown in Fig. 2, the peptidic platform contains the bioactive sequences RGDS and DWIVA, and two units of L-3,4-dihydroxyphenylalanine (L-DOPA) as surface anchoring points. An analogue with 5(6)-carboxyfluorescein was also synthesized to perform characterization studies with fluorescent methods.

2.2.2. Surface functionalization

Samples were coated overnight with a 150 μL drop at 100 μM of the peptidic platform (P) solution. As previously indicated, some samples were functionalized with the fluorescently labeled platform, for characterization purposes. Next, samples were rinsed thrice with deionized water and dried in a N_2 stream. Specimens functionalized with the peptide were labeled as CTRL-P, 3L-P and 10L-P. A summary with all the specimens and labels used in this work can be found in Table 1.

2.3. Surface characterization

2.3.1. Surface changes induced by the laser treatment

Changes in surface topography were visualized by Field Emission Scanning Electron Microscopy (FESEM, Carl Zeiss Neon 40). Roughness parameters and surface profiles were obtained using a Confocal Laser Scanning Microscope (CLSM, Olympus Lext OLS3100). For such purpose, three specimens were evaluated per surface condition, and three images of 96 μm × 128 μm were taken on each specimen.

Crystalline phases were determined by X-Ray Diffraction (XRD, Bruker D8-Advance) in Bragg-Brentano symmetric geometry configuration. The analysis was performed from $26° \leq 2\theta \leq 37°$ on a diffractometer using Cu Kα radiation (40 kV and 40 mA) with 0.02° step size and 1 s/step. The volume fraction (V_m) of the monoclinic phase (m) was calculated with the equation proposed by Toraya et al. [77]. The residual stress state of the surfaces was characterized with the $\sin^2\psi$ method [78] by XRD analysis (Empyrean, PANalytical) using Cu Kα radiation (40 kV and 40 mA). With the same methodology employed in a previous study [75], the tetragonal $(101)_t$ peak found at $2\theta = 30.2°$ was used for the stress calculations, at Chi angles from −60° to +60° in 13 steps. Measurements were performed along three directions on the surface: $\Phi = 0°$, 45° and 90°, in order to identify possible stress anisotropies. In this case, $\Phi = 0°$ and $\Phi = 90°$ corresponded to a direction parallel and perpendicular to the grooved patterns, respectively. Analysis was performed by using the PANalytical X'Pert Stress plus software. Crystalline phases were determined in triplicates, while residual stresses were determined in duplicates.

In order to characterize the microstructure resulting from the laser modification, thin lamellas of the subsurface were obtained by Focused Ion Beam (FIB, FEI Helios Nanolab Dualbeam 600) and deposited on a copper grid. The lamellas were then observed under Scanning Transmission Electron Microscopy (STEM, Carl Zeiss Neon 40) to reveal the subsurface microstructure.

Hydrothermal degradation resistance (also known as ageing or low-temperature degradation (LTD)) of the specimens after surface patterning was investigated. More information about this phenomenon can be found in Ref. [29]. In such process, the $t \rightarrow m$ transformation, of expansive nature, spontaneously takes place on the surface in the

Table 1
Labels and description of the studied surface conditions.

Label	Description
CTRL	Mirror-like polished. Used as a flat topography reference.
3L	Laser patterned with a periodicity of 3 μm.
10L	Laser patterned with a periodicity of 10 μm.
CTRL-P	CTRL specimens functionalized with the peptidic platform.
3L-P	3L specimens functionalized with the peptidic platform.
10L-P	10L specimens functionalized with the peptidic platform.

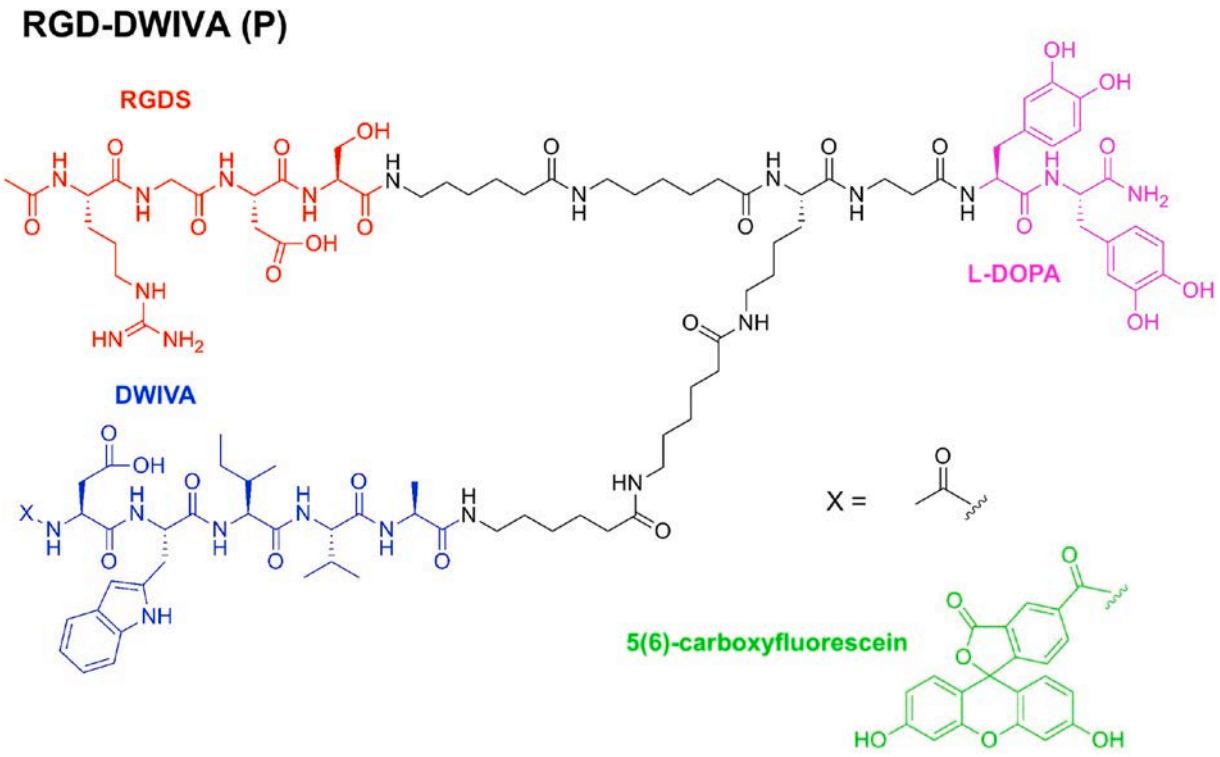

Fig. 2. Chemical structure of the biomolecule. The RGDS and the DWIVA sequences are highlighted in different colors, as well as the L-DOPA based anchoring unit. In the fluorescently labeled biomolecule, 5(6)-carboxyfluorescein was bound to the N-terminus of DWIVA. (For interpretation of the references to color in this figure legend, the reader is referred to the web version of this article.)

presence of moisture. It is associated with the onset of micro-cracks and is able to progress autocatalytically to the bulk material [79]. LTD is of great concern, especially in the biomedical field, where it has been responsible for the catastrophic failure of medical prostheses. In order to evaluate the resistance to LTD of Y-TZP materials, accelerated tests can be carried out in water steam, as reported elsewhere [29,80]. Hence, specimens were degraded in an autoclave at 134 °C and 2 bars of pressure (Selecta Micro8) for 30 h. V_m was determined by XRD at several timepoints, and the *m*-phase content was plotted against degradation time. Three specimens per condition were used.

2.3.2. Attachment of the biomolecule

The presence of the peptides on the surface after biofunctionalization was verified through the changes in the surface nitrogen content. This was evaluated by using X-Ray Photoelectron Spectroscopy (XPS) and determining the percentage of the N1s signal. XPS spectra were acquired with a non-monochromatic Al anode X50 source, operating at 150 W at a pressure below 7.5×10^{-9} mbar. A Phoibos 150 MCD-9 detector (SPECS Surface Nano Analysis GmbH) was employed. To record high-resolution spectra, detector pass energy was fixed at 20 eV with 0.05 eV steps. The obtained spectra were analyzed using Casa XPS software. All binding energies were referenced to the signal of C1s. Measurements were acquired in duplicates.

To further study the attachment of the biomolecule and its distribution, a fluorescently-labeled version of the peptide was employed. Surfaces functionalized with such peptides were observed under fluorescence CLSM (Carl Zeiss LSM 800). Three images were taken on each specimen, and three different specimens were studied per condition. The data obtained was analyzed using Fiji/ImageJ.

Finally, the peptide surface density was determined following the method reported in [70]. For such purpose, samples coated with the fluorescently-labeled peptides were used in duplicates. After functionalization, the peptidic platforms were detached off the surfaces with 500 μL of an aqueous solution of NaOH 1 M for 12 min at 70 °C. The supernatants were collected. In parallel, a standard curve of the same fluorescent peptide was prepared in NaOH 1 M, with concentrations ranging from 0 nM to 2500 nM. 50 μL of both the supernatants and each concentration of the standard curve were pipetted into a black 96-well plate. The fluorescence (λ excitation = 485 nm, λ emission = 528 nm) was read in a multimode reader (Synergy HTX multimode reader, BioTek). The standard curve was finally used to determine the surface density of the peptide.

2.4. Biological characterization

2.4.1. Cell culture

Bone-marrow derived hMSCs were purchased from ATCC and cultured in Advanced Dulbecco's Modified Eagle's Medium (DMEM) supplemented with 10% (*v*/v) fetal bovine serum (FBS), 50 U/mL penicillin, 50 μg/mL streptomycin and 1% (*w/v*) L-glutamine. Cells were maintained at 37 °C, in a humidified atmosphere containing 5% (v/v) CO_2, changing culture medium three times per week. Cells were detached with trypsin-EDTA and replated on a new flask after reaching 80% confluence. All reagents were purchased from Sigma–Aldrich, unless otherwise specified.

Before conducting all cellular experiments, samples were disinfected for 15 min in 70% (v/v) ethanol and subsequently washed thrice with phosphate-buffered saline (PBS). Experiments were carried out in 24-well plates, as sample size closely matched this diameter.

2.4.2. Cell adhesion

In the cell adhesion assay, hMSCs at passage 6 were seeded at a concentration of 5000 cells/well in serum-free medium and incubated at 37 °C and 5% (v/v) CO_2 containing atmosphere. After 6 h, medium was aspired and non-adherent cells removed by carefully washing with PBS. Cells were fixed with paraformaldehyde (PFA, 4% w/v in PBS) for 30 min and permeabilized with 0.05% (w/v) Triton X-100 in PBS for 20 min. Actin fibers were stained by incubating with TRITC-conjugated phalloidin (1:300, in permeabilizing buffer) for 1 h and nuclei were stained using 4′,6-diamidino-2- phenylindole (DAPI) (1:1000, in PBS-glycine 20 mM) for 2 min, both in the dark. Between all steps, samples were rinsed three times with PBS-glycine for 5 min. Specimens were mounted in Mowiol 4–88, examined under a fluorescence CLSM (Carl Zeiss LSM 800) and images were processed using Fiji/Image-J package [81] to calculate cell-shape parameters. The experiment was performed using triplicates.

Once all images were obtained, the samples were immersed in PBS at room temperature for two days, while gently shaking. The mounting medium was dissolved and the coverslips removed. Cells were then dehydrated through immersion in increasing concentrations of ethanol and observed under FESEM.

Cell adhesion after one day was also evaluated with the Alamar Blue assay (Invitrogen, ThermoFisher Scientific). In this case, hMSCs at passage 4 were employed, seeding an initial concentration of 5000 cells/well in serum-free medium. Cells were maintained as described before. After 6 h, non-adherent cells were rinsed and carefully aspired, and complete medium (i.e. FBS supplemented) was added. After one day, cell number was determined with the Alamar Blue assay. Briefly, medium was replaced by 10% (v/v) Alamar Blue reagent in complete medium for 2 h. After the time was reached, the fluorescence of the reagent was measured following the manufacturer's instructions in a multimode reader (Synergy HTX multimode reader, BioTek), and compared to a standard curve relating cell number and fluorescence intensity. Three biological and three technical replicates were used.

2.4.3. Cell migration

In order to study cell migration, silicon culture-inserts (Ibidi) were placed on the surface of the samples. 20,000 hMSCs at passage 5 were seeded in each insert in complete medium, following the volumes recommended by the manufacturer. Cells were left to attach for 24 h, and the inserts were then removed, leaving a confluent layer with a squared shape of approximately 7 × 7 mm at the center of the samples. Non-adherent cells were rinsed and fresh medium was added. At this point, some specimens were carefully washed with PBS, fixed with PFA (4% w/v in PBS) for 30 min and stored at 4 °C in PBS. These specimens were used as a reference, in order to determine the initial cell layer shape and size just after removing the inserts. The rest of the specimens were incubated for an additional 72 h. During this period, cells started migrating to the rest of the surface. After the time was finished, the specimens were washed with PBS and fixed with PFA. Cells were permeabilized with 0.05% (w/v) Triton X-100 in PBS for 20 min and stained in a 0.5% (w/v) toluidine blue solution for 10 min. Samples were rinsed until the excess dye was removed and dried in a N_2 stream. The stained samples were visualized under a stereomicroscope system (Olympus SZX16) and images analyzed with Fiji/Image-J package. The cell layer size and shape of all specimens was measured, and compared to the reference specimens. An explanatory scheme of this experiment can be found in Fig. 10a. Each condition was evaluated by triplicate.

2.4.4. Cell differentiation

15,000 cells/well of hMSCs at passage 4 were seeded in all the cell differentiation experiments. Cells were seeded in serum-free medium for 6 h, and non-adherent cells were then carefully aspired and medium replaced by a complete one.

The genetic expression of several genes related to hMSC differentiation was analyzed. After an incubation time of 7 days, total RNA was extracted and purified using the RNeasy Mini Kit (Qiagen). RNA was quantified using a Take3 Micro-Volume Plate (BioTek) and a Synergy HTX multimode reader (BioTek). Equal RNA amounts for each sample were retrotranscribed to cDNA using the Maxima First Strand cDNA Synthesis Kit (ThermoFisher Scientific). RT-qPCR were performed using the PowerUp SYBR Green Master Mix (Applied Biosystems) and specific

primers (see Table 2) in a MIC qPCR cycler (Bio Molecular Systems). The genes tested were: runt-related transcription factor 2 (RUNX2), alkaline phosphatase (ALP), collagen type I (COL-1) and osterix (OSX). Three biological and three technical replicates were tested for each condition studied. The fold change of gene expression was obtained after normalizing the values to CTRL specimens and to the housekeeping gene GAPDH. Detailed calculations have been described elsewhere [82].

Alkaline phosphatase (ALP) activity, a marker associated with the early stages of osteogenesis, was also investigated. After an incubation period of 14 days, cells were rinsed with PBS, lysed with 500 μL of mammalian protein extraction reagent (mPER, ThermoFisher Scientific) and ALP activity measured as indicated by the manufacturer. A colorimetric assay based on the conversion of *p*-nitrophenyl phosphate (pNPP) into p-nitrophenol (pNP) was employed (SensoLyte® pNPP Alkaline Phosphatase Assay Kit, AnaSpec Inc.). The results were expressed as nanograms of ALP and normalized by the number of cells on each surface. The number of cells was measured prior to protein extraction on the same day, by employing the Alamar Blue assay. Three biological and three technical replicates were used.

2.4.5. Statistical analysis

Values in graphs are displayed as mean ± standard deviation. Statistical differences were assessed by ANOVA using Tukey's test for pairwise comparisons ($p < 0.05$). Differences were further analyzed and confirmed with the non-parametric Mann-Whitney test. The software employed was Minitab® 18.1.

3. Results and discussion

3.1. Laser patterning

As displayed in Fig. 3, CLSM was used to obtain the most relevant topographical parameters after laser modification. By adjusting the optical setup, periodicity could be controlled and set at the desired values: 3.03 ± 0.16 μm (3L) and 9.92 ± 0.36 μm (10L). Such periodicities were chosen with respect to cell size. One periodicity was set to only have a few microns, much below the cell body size (3L), and the other one was set to obtain larger grooves, closer to the range of the cell (i.e. 10L). In contrast to previous results obtained with nanosecond lasers [33], the use of DLIP in the femtosecond regime presented less limitations in terms of pattern depth, which in the present case were 3.04 ± 0.48 μm in 10L, and 0.99 ± 0.19 μm in 3L. Accordingly, the measured surface average roughness (S_a) was found to be 1030 ± 110 nm in 10L and 370 ± 20 nm in 3L. The roughness before sample patterning is represented by the CTRL specimens, which was initially 20 ± 10 nm.

The possibility of producing grooves with larger depths without losing pattern definition is important, as different depths can have different effects on cell behavior [83,84]. In addition, surfaces with larger S_a values are known to present better osteointegration in vivo [85,86].

The large differences in terms of the achievable depths between DLIP in both regimes (i.e. nano- and femto-) owes to changes in the nature of laser-material interaction. In the nanosecond regime, material removal is produced by a combination of ablation and melting. In this regime, pulse duration is higher than the electron-phonon relaxation time. Electrons transfer the absorbed energy to the lattice and a thermal equilibrium is reached, leading to heat conduction to the surrounding material [87]. As a consequence, after nanosecond pulsed DLIP irradiation, material is selectively molten in the regions of maximum fluence and pushed to cold areas due to thermocapillarity (i.e. Marangoni effect [88]), producing a grooved topography. Roitero et al. [33] found that, by this method, a trade-off exists between pattern depth and quality. That is, higher depth was accompanied by lower pattern definition.

However, in the femtosecond regime, due to the ultrashort pulse duration below the electron-phonon relaxation time [89], material removal is mainly driven by evaporative ablation. In this regime, electrons are heated almost instantly to high temperatures before an energy transfer to the lattice takes place. This results in cold ablation (i.e. direct vaporization and ion break-off), minimizing thermal damage [87,90]. In brief, the transition from melting to ablation (from nano- to femtosecond regime) in DLIP structuring of zirconia allowed to obtain both higher depth and pattern definition, demonstrating the clear advantage of using ultrashort pulses. This can be observed in Fig. 4 where FESEM micrographs of the laser modified surface are presented.

As displayed in these images, groove edges were clearly defined, presenting a sharp transition between ablated and non-ablated regions. However, the nano-topography on the valleys differed between both specimens. While 3L presented an array of periodic line-like substructures, 10L presented a more stochastic nano-topography (see magnifications in Fig. 4). Similar sub-structures have been observed when employing different pulse energy or pulse number in the same materials and lasers [35]. Interestingly, although the ripples observed in the bottom of 3L valleys were similar to the feature characteristics of laser-induced periodic substructures (LIPSS) [91], their orientation was aligned parallel to the linear polarization angle of the beam and thus appeared to follow a different formation mechanism compared to classic LIPSS. The formation of such ripples has also been identified in other materials patterned in similar conditions, and its nature is still not clear [43]. In addition to nano-topography, more evident signs of micromelting were present in 3L as compared to 10L, as evidenced by the presence of droplets and recast material.

A closer inspection of 10L surfaces is presented in Fig. 5 along STEM micrographs of different sub-surface regions. Fig. 5a presents a general view of 10L surface. Fig. 5b and d correspond to the magnification of two areas: the valleys and the top of the grooves, respectively. Micrographs clearly displayed that material on the top of the grooves remained unaltered, without the presence of any feature indicating microstructural modifications after laser irradiation. However, a sharp transition was observed between this region and the ablated valleys.

Most dielectric materials, such as Y-TZP, present a too wide bandgap to absorb single photons at the wavelengths employed. However, at sufficiently high photon intensity, nonlinear absorption processes become predominant and significant multiphoton absorption can take place. The free excited electrons that are generated can then gain enough kinetic energy (through single photon absorption) to excite further electrons into the conduction band, leading to an electron avalanche ionization [92]. This process is generally accepted as the main mechanism of photon absorption by semiconductors and insulators and explains the ability of ultrashort-pulsed lasers to ablate such materials [93].

In the case of the present work, once a threshold of incoming photon intensity was surpassed, nonlinear absorption mechanisms dominated and ablation started, explaining the sudden transition between the non-ablated and the ablated regions. Hence, below the ablation threshold no changes were produced either in the surface (Fig. 5d) or in the sub-surface (Fig. 5e). However, once the ablation threshold was surpassed, material was clearly ablated. Apart from evaporative ablation, which was the main material removal mechanism, topography of the valleys suggested that a slight melting was produced, as observed in Fig. 5b. A large number of cavities could be observed, presumably due to the

Table 2
Sequences of the primers employed.

Primer	Sequence (5′-3′)
RUNX2	F AAATGCCTCCGCTGTTATGAA
	R GCTCCGGCCCACAAATCT
ALP	F ATCTTTGGTCTGGCTCCCATG
	R TTTCCCGTTCACCGTCCAC
COL-1	F AGGTCCCCCTGGAAAGAA
	R AATCCTCGAGCACCCTGA
OSX	F TGCTTGAGGAGGAAGTTCAC
	R AGGTCACTGCCCACAGAGTA

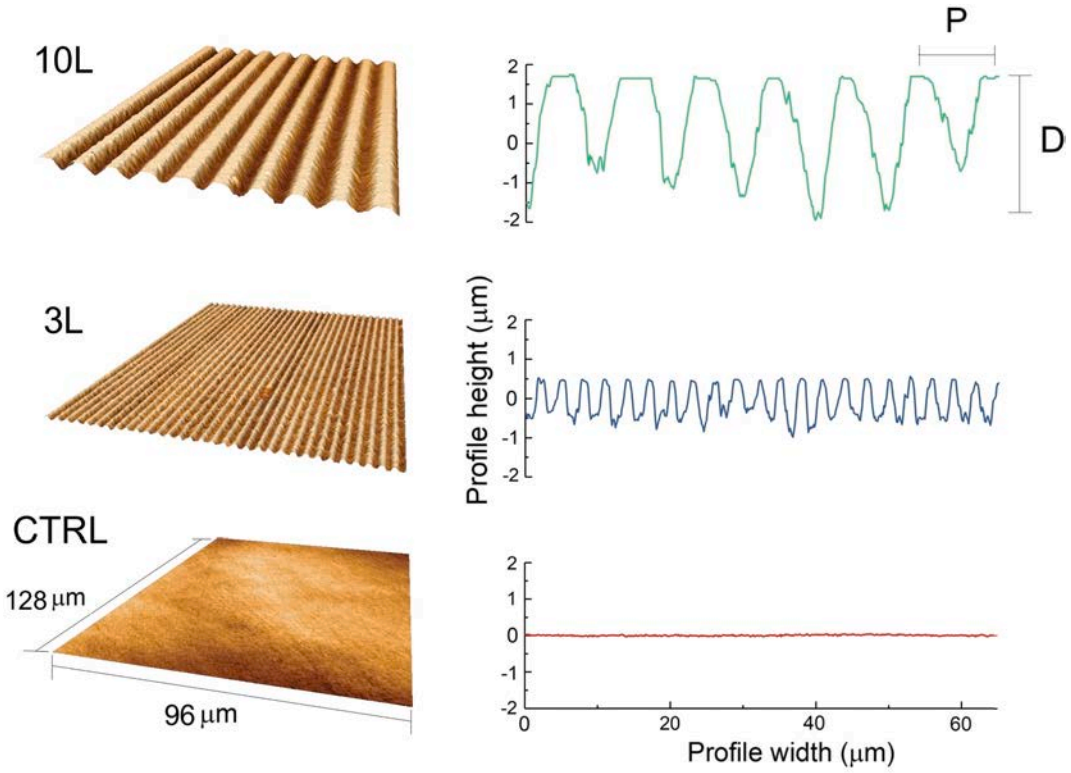

	Sa (μm)	P (μm)	D (μm)
10L	1.03 ± 0.11	9.92 ± 0.36	3.04 ± 0.48
3L	0.37 ± 0.02	3.03 ± 0.16	0.99 ± 0.19
CTRL	0.02 ± 0.01	-	-

Fig. 3. From left to right: 3D reconstruction of the micro-patterned surfaces and roughness profiles. *P* and *D* indicate pattern periodicity and depth, respectively.

occurrence of localized boiling, creating an intricate nano-topography. Although most of the pores seemed to be connected to the surface, STEM images revealed some pores below the surface, always in the first 500 nm of material (Fig. 5c). Nano-cracks originated on this layer as well, as a result of the high temperature gradients after material resolidification.

Stress-induced $t \rightarrow m$ phase transformation can take place around cracks in the laser-affected layer of Y-TZP [46]. In fact, it was observed that a subtle $t \rightarrow m$ phase transformation took place in both 3L and 10L after laser modification, where traces of the *m*-phase remained lower than $V_m = 3\%$ (and above the detection limits of the equipment $V_m > 1\%$). No other changes were detected after laser modification. The corresponding XRD spectra of the 2θ region between 26° and 37° is presented in Fig. 6a.

Although the *m*-phase content found was low, the superficial nucleation of *m*-phase coupled to the presence of small cracks may affect hydrothermal degradation resistance of Y-TZP surfaces. For this reason, accelerated degradation tests were carried out in water steam [32,80]. Degradation kinetics of CTRL, 3L and 10L surfaces are displayed in Fig. 6b. In order to revert the detrimental consequences of *m*-phase after laser patterning and to relief possible residual stresses, a thermal treatment can be applied. As an example, 10L specimens were selected and heated up to 1200 °C for 1 h with a cooling and heating rate of 5 °C/min. These specimens were labeled as 10L-TT and included in the degradation experiment.

It can be noticed that both 3L and 10L behaved worse than the CTRL specimens, displaying an earlier increase in the *m*-phase content. As explained, the nano-cracks, through which water can easily penetrate the material, coupled with a pre-existing amount of *m*-phase and the increase in surface area after laser treatment, may explain such performance. However, the thermal treatment (TT) reverted the negative consequences of the laser modification, and even improved significantly the behavior respect to CTRL specimens. The recovery of properties after the TT is explained by the total reversion $m \rightarrow t$ of the *m*-phase traces and the release of residual stresses [32,94]. However, the increase in the resistance respect CTRL specimens is more difficult to rationalize, and may be explained by the changes in nano-topography of the surface. The size of the protrusions originated on the valleys in 10L samples (see Fig. 5b) are below the average grain size (300 nm). This may have the same effect as reducing the grain size of the first layer of grains, which could hinder *m*-phase nucleation [95].

As shown in the image included in Fig. 6b, after the laser treatment the surface changed its color into a reddish/brownish one. Many other authors have already reported the color change in zirconia after laser modification [38,46,51,96], which is generally associated with the formation of color centers [46,96]. As it can be observed on the image, the whitish color was recovered after the thermal treatment.

Fig. 6c plots the residual stresses found in 10L and CTRL specimens. The presence of residual stresses due to the thermal effects of the laser can influence mechanical properties and LTD [97]. The laser treatment

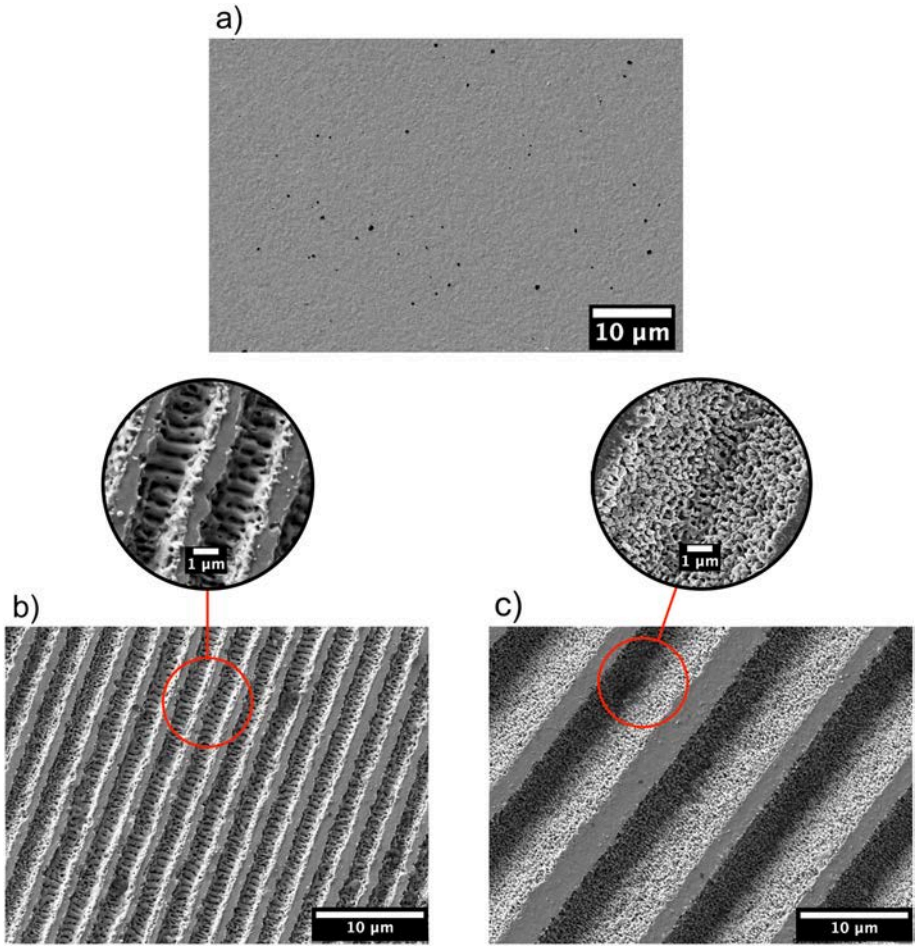

Fig. 4. FESEM micrographs of the studied surfaces of a) CTRL, b) 3L and c) 10L specimens. Black particles in CTRL specimens correspond to Al_2O_3 inclusions present in the Y-TZP feedstock.

introduced slightly tensile stresses along the pattern and slightly compressive ones perpendicularly, as compared to CTRL. Compressive stresses can stabilize the *t*-phase and delay LTD. In this case, the values found were relatively low, of similar magnitude to those that can be found on mildly polished surfaces [75]. On the other hand, tensile stresses can facilitate the degradation process [31]. Their relative impact on the LTD behavior of the surface is complex and depends on several factors, including stabilizer content, grain size, alumina content, etc. However, the tensile stresses obtained lie below the limit recommended to avoid LTD ($\sigma < 300$ MPa) [98].

In the light of the obtained results, a thermal treatment (TT) should be carried out after laser patterning. The main benefits are listed below:

- Although LTD degradation cannot be totally hindered in 3Y-TZP, these materials are designed to delay its detrimental effects beyond the expected lifespan of the prostheses. An earlier degradation increases the probabilities of a premature mechanical failure. As shown, LTD resistance can be worsened after laser patterning, but a TT can effectively revert its negative consequences.
- From the aesthetic point of view, preserving the surface color of the prostheses is of particular interest for the final application. One of the advantages of using zirconia instead of titanium lies in its whitish and more natural appearance. Laser patterning changes the surface color, but this process can be reverted after a TT.
- Residual stresses can affect LTD. In particular, tensile stresses can worsen the degradation resistance. A TT can relieve the residual stresses introduced by the laser patterning process [31].

3.2. Surface functionalization

In order to improve the biological effects of the surface patterns, specimens were biofunctionalized with a dual platform combining a well-known cell-adhesive peptide (RGD) and an osteoinductive peptide (DWIVA). The presence of the peptides after functionalization was determined by different methods. Fig. 7a shows the images obtained by fluorescence CLSM of the surfaces after functionalizing with a fluorescent version of the platform. All the functionalized samples presented a certain degree of fluorescence, with a higher intensity in the laser treated specimens as compared to the flat CTRL-P. The peptide was detached from these surfaces with NaOH and the fluorescence of the supernatant measured and compared to a standard curve relating fluorescence intensity against platform concentration. Fig. 7b plots the obtained peptide concentration on the surface of the samples. Similar to Fig. 7a, the presence of the platform was confirmed in the functionalized specimens and a higher amount was found in the laser-modified surfaces, with 10L presenting the highest content. Finally, the surface chemical composition of the functionalized specimens was studied by XPS (non-fluorescent platform). Fig. 7c shows the atomic percentage of nitrogen (N1s signal) on the surface (as compared to the total content of Zr, Y and O), which is directly related to the presence of peptide bonds and amino acid side chains of the peptidic backbone. Results were in agreement with the trend obtained in the quantification experiment (Fig. 7b). All the functionalized samples displayed a clear increase in the nitrogen content, which was maximum in the laser-patterned samples.

These experiments clearly showed that the anchoring molecule used in the peptidic platform was effective in attaching the biomolecule to the

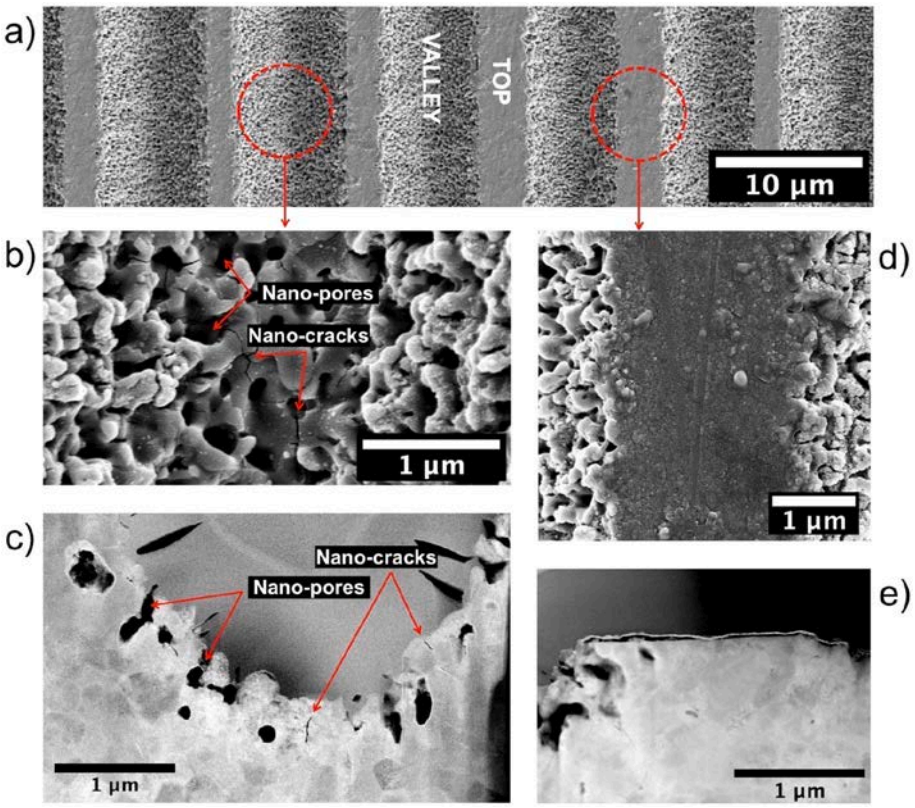

Fig. 5. Surface features of 10L specimens. a) General micrograph view of 10L surface, b) magnification of the valley nano-topography with the presence of nano-pores and nano-cracks, c) STEM micrograph of the valley subsurface, d) magnification of the top of the grooves where no signs of surface modification are observed and e) STEM micrograph of the subsurface in the top of the grooves.

surface of zirconia. L-DOPA is one of the main components of the adhesive proteins employed by marine mussels to anchor surfaces in seawater [99]. It can strongly bind to both organic and inorganic substrates [100] and its properties have been exploited, among other applications, to coat biomedical surfaces including zirconia [74,101]. The higher surface concentration of the platform observed in the laser-modified specimens can be explained by the increase in surface area, which was due not only to the grooves but also to the nano-topographies observed on the bottom of the valleys. In this regard, while the primary pattern (i.e. the grooves) increased the surface area in both 3L and 10L by a factor close to 1.6 with respect to a flat surface (Wenzel's roughness factor for a rectangular profile), the nanotopography in 10L presented more intricate features (see Fig. 4), further increasing surface area as compared to 3L. Accordingly, the highest values of peptide attachment were found in 10L. The presence of peptides entrapped inside the nano-topographies (nano-pores) cannot be discarded and may have also increased the values obtained during the peptide quantification.

3.3. Cell response on the patterned/biofunctionalized surfaces

3.3.1. Cell-adhesion

Fig. 8 presents the results obtained in the cell-adhesion assay, evaluating cell morphology 6 h after cell seeding. The behavior observed was determined by the combined effects of the two modifications studied: surface patterns and the biomolecule.

The effects of laser patterning on cell morphology were studied by comparing CTRL, 3L and 10L. As shown in Fig. 8a, cells cultured on the patterned surfaces underwent a drastic shape change. Cell body stretched along the grooves and thinned in the perpendicular direction, displaying a large increase in aspect ratio (Fig. 8e), as compared to the round-shaped cells growing in CTRL. Apart from the morphological changes, the most evident effect of laser patterns was the alignment of cells along the grooves, with more than 90% of the cells aligned at ±15° of the pattern direction in both 3L and 10L (Fig. 8f). Regarding cell number, no significant differences were found (Fig. 8b). In summary, topography greatly affected cell morphology due to a significant contact guidance. FESEM micrographs of both 3L and 10L are shown in Fig. 9c to f. The alignment effect is obvious on the images. A cell body extension growing on a ridge can be observed in Fig. 9e. Cells could also establish contact with the nano-topography, as evidenced in Fig. 9f, where filopodia extending from the cell body (right part of the image) anchored to the lateral side of a valley (left part of the image).

On the other hand, the effects of the biomolecule were also studied, as well as its combination with surface patterns. In the case of flat specimens, CTRL-P displayed important differences with respect to its non-functionalized equivalent, CTRL. When free of the biochemical stimuli of the peptides, CTRL specimens displayed relatively small, star-shape cell bodies, with evident cell projections (see magnification attached to Fig. 8a CTRL and Fig. 9a). On such surfaces, non-specific cell-material interactions were expected, with an establishment of weak bonds based on electrostatic interactions, hydrogen bonding, etc. Under such conditions, a poorly developed cell cytoskeleton and a reduced cell area were observed. In contrast, biofunctionalized surfaces displayed a two-fold increase in surface area (Fig. 8d), with polygonal cell bodies displaying well-developed bundles of actin filaments (see magnification attached to Fig. 8a CTRL-P and Fig. 9b). In the latter condition, due to the cell-adhesion properties of the biomolecule employed, a higher number of cells attached to the surface (Fig. 8b). This improvement in the number of cells on the functionalized specimens is in well agreement with the literature [56,64,70] and was corroborated by an adhesion assay with Alamar Blue. Following an incubation time of 24 h after cell seeding, the functionalized specimen presented a higher number of adhered cells, as shown in Fig. 8c.

In contrast to flat specimens, the combination of the peptidic

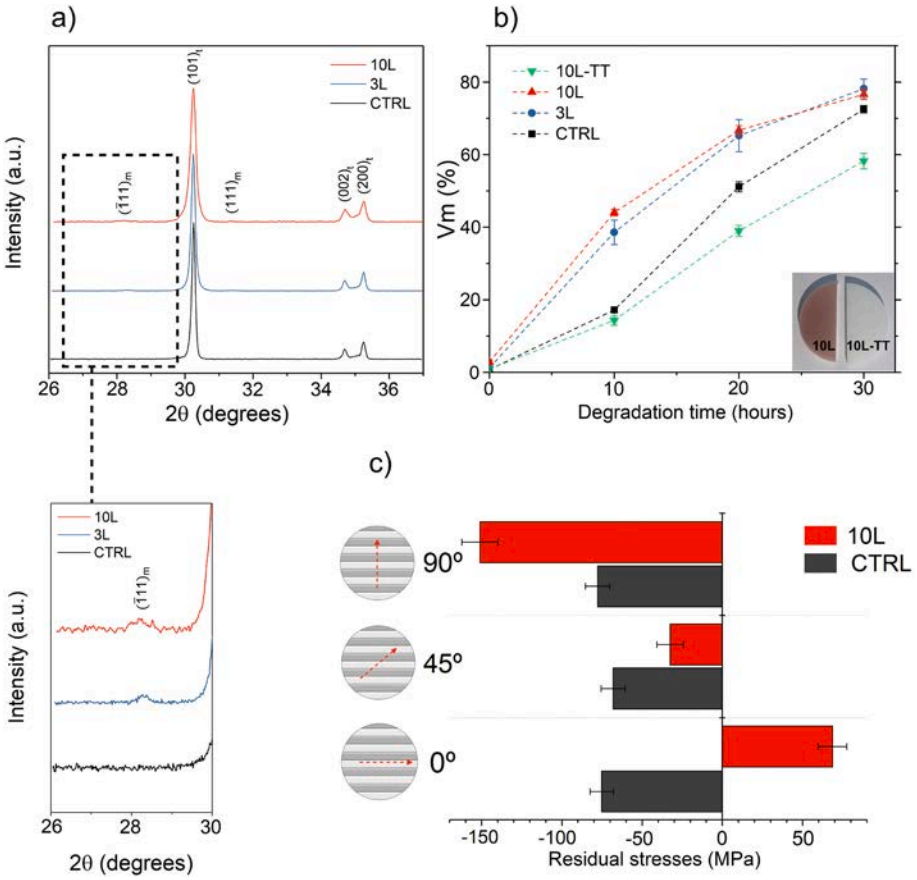

Fig. 6. Results of the XRD experiments. a) XRD spectra of the studied specimens. Just minor changes were observed with small traces of *m*-phase in the laser treated specimens. In the magnification below, x/y axis relation has been modified to clearly show the presence of *m*-phase traces. b) Degradation kinetics in water steam. The increase in *m*-phase content is plotted against degradation time. A picture depicting the recovery of the white color of 10L after thermal treatment is included. c) Residual surface stresses in 10L and CTRL specimens measured by XRD. In 10L, 0° correspond to a direction parallel to the grooves. Positive and negative values correspond to tensile and compressive stresses respectively.

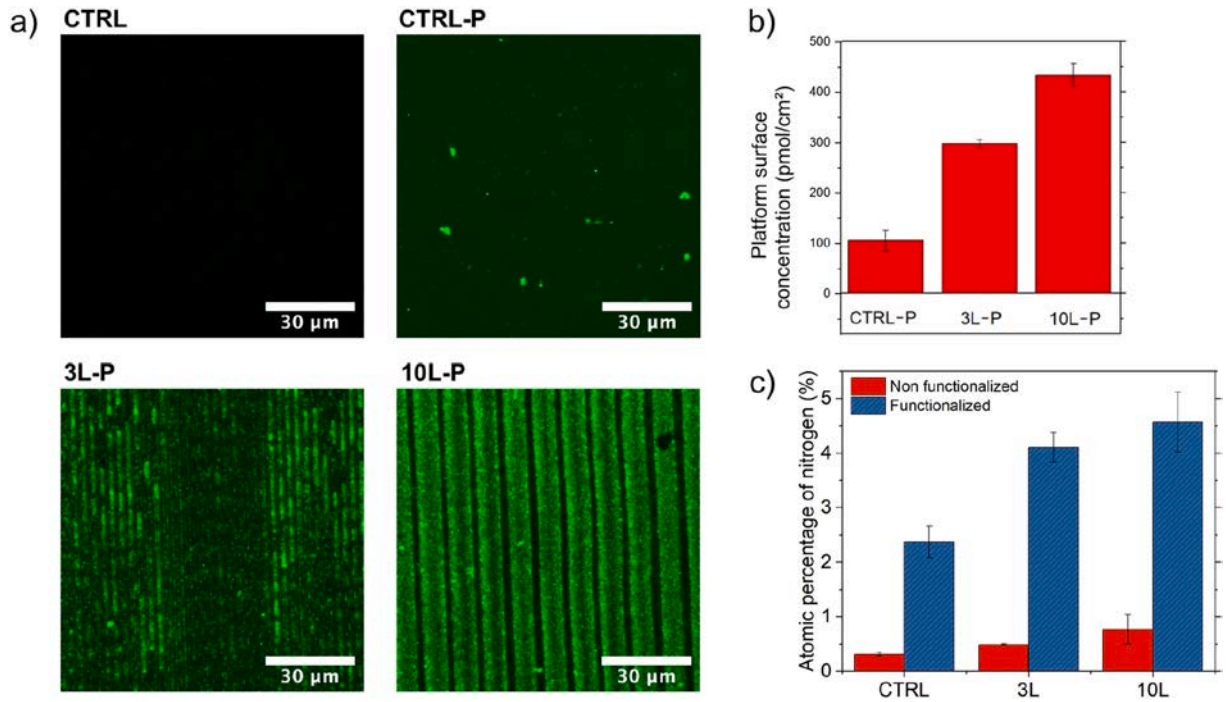

Fig. 7. Characterization of the presence of peptides on the surfaces. a) Fluorescence CLSM of the specimens functionalized with the fluorescently-labeled peptidic platforms. b) Results of the peptide quantification by detachment of the fluorescently-labeled peptidic platforms. c) Atomic percentage of nitrogen (N1s signal) on the surfaces (non-fluorescent platform was used).

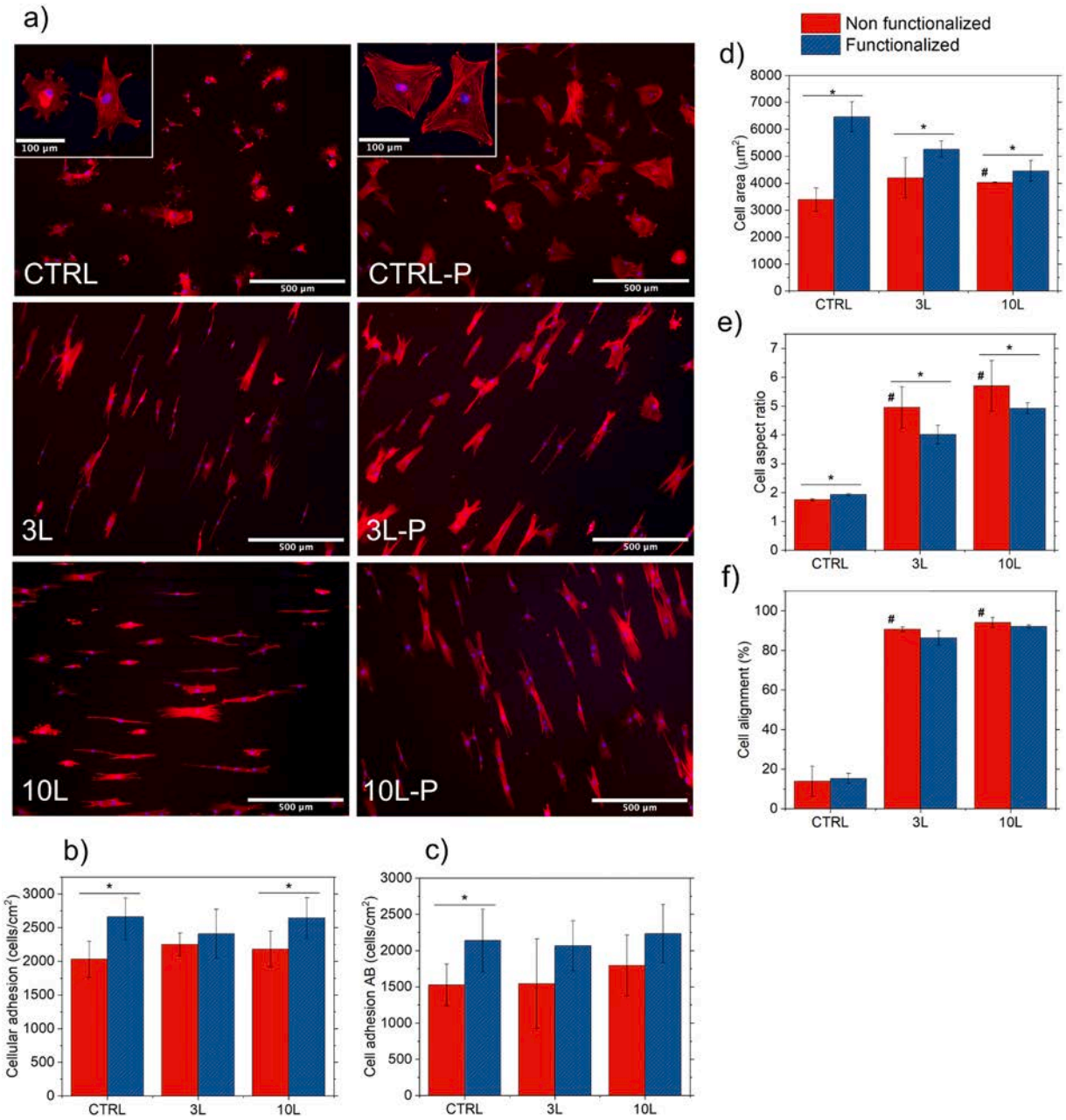

Fig. 8. hMSCs adhesion results after 6 h in serum free medium. a) Representative images of the studied specimens under fluorescence CLSM. Actin filaments were stained with TRITC-conjugated phalloidin (red), and cell nuclei with DAPI (blue). b) Cellular adhesion (cells/cm^2), c) cellular adhesion by the AlamarBlue assay 24 h after cell seeding (cells/cm^2), d) cell area (μm^2), e) cell aspect ratio and f) cell alignment (%). Cell alignment was defined as the percentage of cells aligned along a direction ±15° respect to the pattern direction. Red bars correspond to the non-functionalized specimens while blue bars represent specimens functionalized with the peptidic platform. * indicates statistical differences between functionalized and non-functionalized specimens with the same topography (e.g. 10L vs. 10L-P). # indicates statistical differences between 10L or 3L with respect to CTRL, analyzing only the effect of topography, without functionalization ($p < 0.05$). (For interpretation of the references to color in this figure legend, the reader is referred to the web version of this article.)

platform with the laser-patterned surfaces did not display such drastic differences. Cell morphology of non-functionalized 3L and 10L specimens did not differ significantly from that exhibited by the functionalized versions 3L-P and 10L-P, in both cases presenting an elongated spindle-shape. In this case, the effect of the topography prevailed markedly over the biochemical cues. As expected, although standard deviation was high, the main trend showed higher cell number in all functionalized specimens as compared to their non-functionalized equivalents (Fig. 8b and c). As in CTRL specimens, but to a lower extent, the effect of RGD resulted in a higher cell area (Fig. 8d). In this case, a lower degree of thinning perpendicularly to the grooves was observed, as compared to 3L and 10L. This translated into a lower aspect ratio, which still was much higher respect to CTRL and CTRL-P (Fig. 8e). In terms of cell alignment, the peptidic platform did not introduce significant changes, displaying both 3L-P and 10L-P an alignment degree around 90% (Fig. 8f).

Overall, laser pattering mainly affected cell-shape and alignment, without significant changes in cell number. Once the surfaces were biofunctionalized, large changes were observed in flat CTRL specimens, mainly in terms of a higher cell body area and a well-developed cell cytoskeleton. In laser-patterned surfaces such changes were reduced. No differences in cytoskeleton organization or alignment were observed

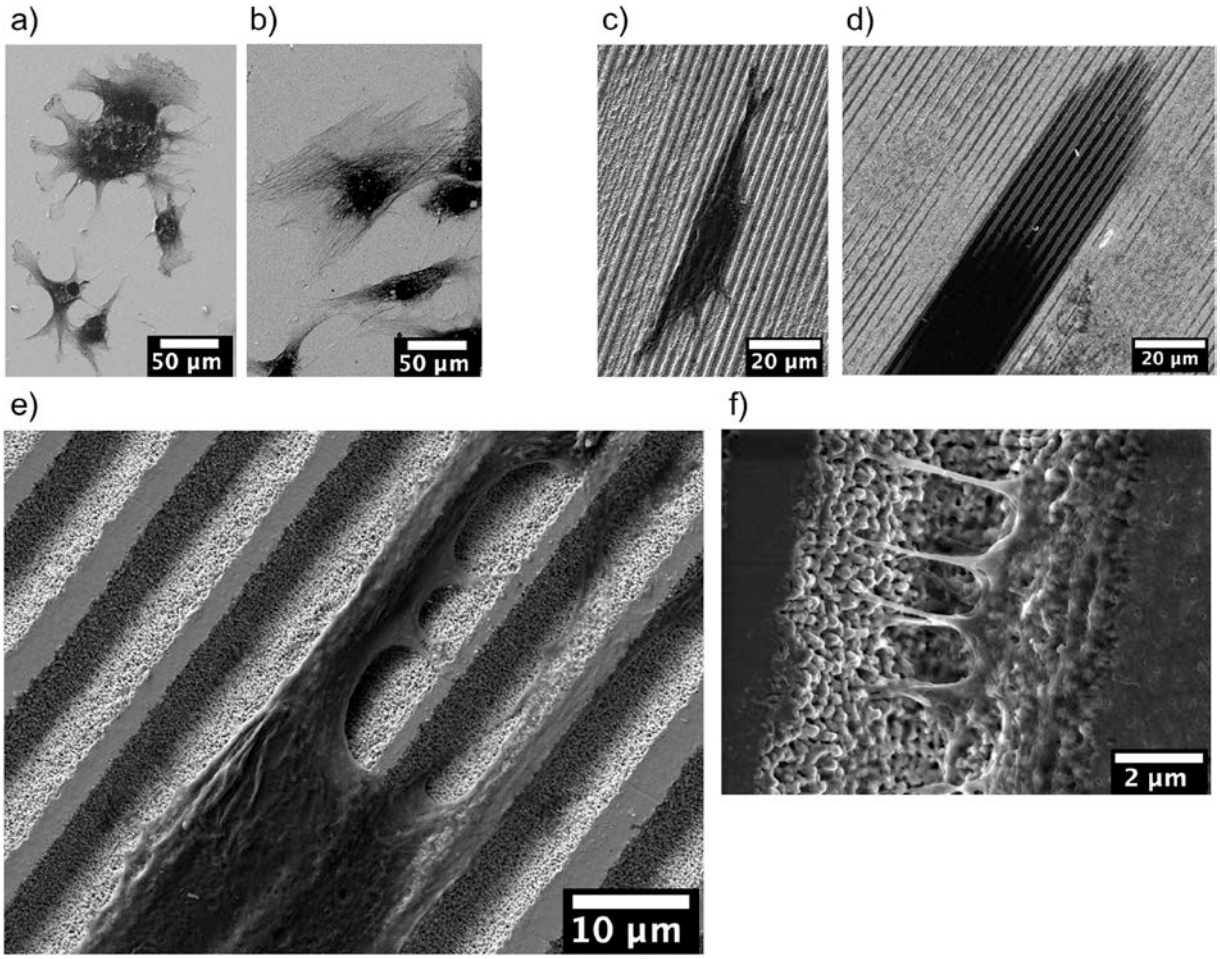

Fig. 9. FESEM micrographs of the specimens employed in the cell adhesion assay. a) CTRL; b) CTRL-P; c) and d) 3L; e) and f) 10L.

after functionalization, and lower changes in cell area were detected as compared to the case CTRL vs. CTRL-P. The presence of RGD-DWIVA increased cell number in all specimens, although the obtained values were not statistically significant in some cases due to a high variability.

3.3.2. Cell migration

Fig. 10 clearly shows that topographical cues have a strong influence on cellular migration. As observed in the plot from Fig. 10c as well as on the images displayed in Fig. 10b, cells migrated isotropically on the CTRL specimens. In contrast, both laser patterned specimens showed high anisotropy, with a significantly enhanced migration along the grooves, but hampering considerably the displacement across the grooves. While the movement parallel to the grooves was more than doubled in 3L and 10L respect to CTRL, in the perpendicular direction displacement was less than half the distance observed in CTRL. In addition, the peptidic platform did not show any significant influence on the migration behavior. The lack of visible differences in the functionalized specimens may be related to the presence of FBS in the medium, which could have masked the effects of the peptide. The trends observed here have also been reported by other authors [48,102], with grooves facilitating migration along its direction, but hindering it perpendicularly.

The mechanism by which grooved substrates can affect cellular migration are related to the morphological changes after attachment on such topographies. As shown in Fig. 8 and Fig. 9, cells tended to align when grown on grooved surfaces [103,104]. The reasons for such alignment can vary depending on the size of the grooves, changing from a more geometrical guidance in grooves larger or equal to the cell size, to a more fundamental way when topographical cues are in the nano-scale and can interact with cell membrane receptors. In particular, Fujita et al. [105] proposed a mechanism by which fragmented focal adhesions in the perpendicular direction led to cell protrusion retraction, while long focal adhesion along the grooves favored more stable cellular protrusions; thus, favoring cell elongation along the pattern. The consequences of this asymmetric morphology can affect cell migration. In fact, directed cell migration is based on an asymmetric cell situation, with a leading and a trailing edge [106]. This process consists of the formation of stable protrusions on the leading edge of the cell and its restriction on the laterals, which can be governed by the grooved topography. Thanks to the actin-rich leading protrusions and the detachment of the trailing edge, cells can successfully migrate.

In vivo application of such effects in the dental field has been also proposed. For instance, it has been shown that laser-ablated microgrooves in the implant collar can affect epithelial, fibroblastic and osteoblastic migratory patterns, influencing the orientation of the connective tissue fibers with respect to the implant surface [107]. The correct orientation of such fibers hinders the apical migration of the junctional epithelium, avoiding crestal bone loss. Laser patterned implant collars can limit the epithelial downgrowth, improve soft and bone tissue attachment, and influence bone remodeling so that improved bone quality is found adjacent to the implant [16]. Microgrooved surfaces not only present the ability of guiding soft tissues but can also guide bone growth. It has been observed that on these surfaces bone is guided parallel to the grooves. When a chamber with multiple channels was placed on canine femurs, micro-grooved titanium surfaces promoted the highest levels of bone ingrowth into the channels as

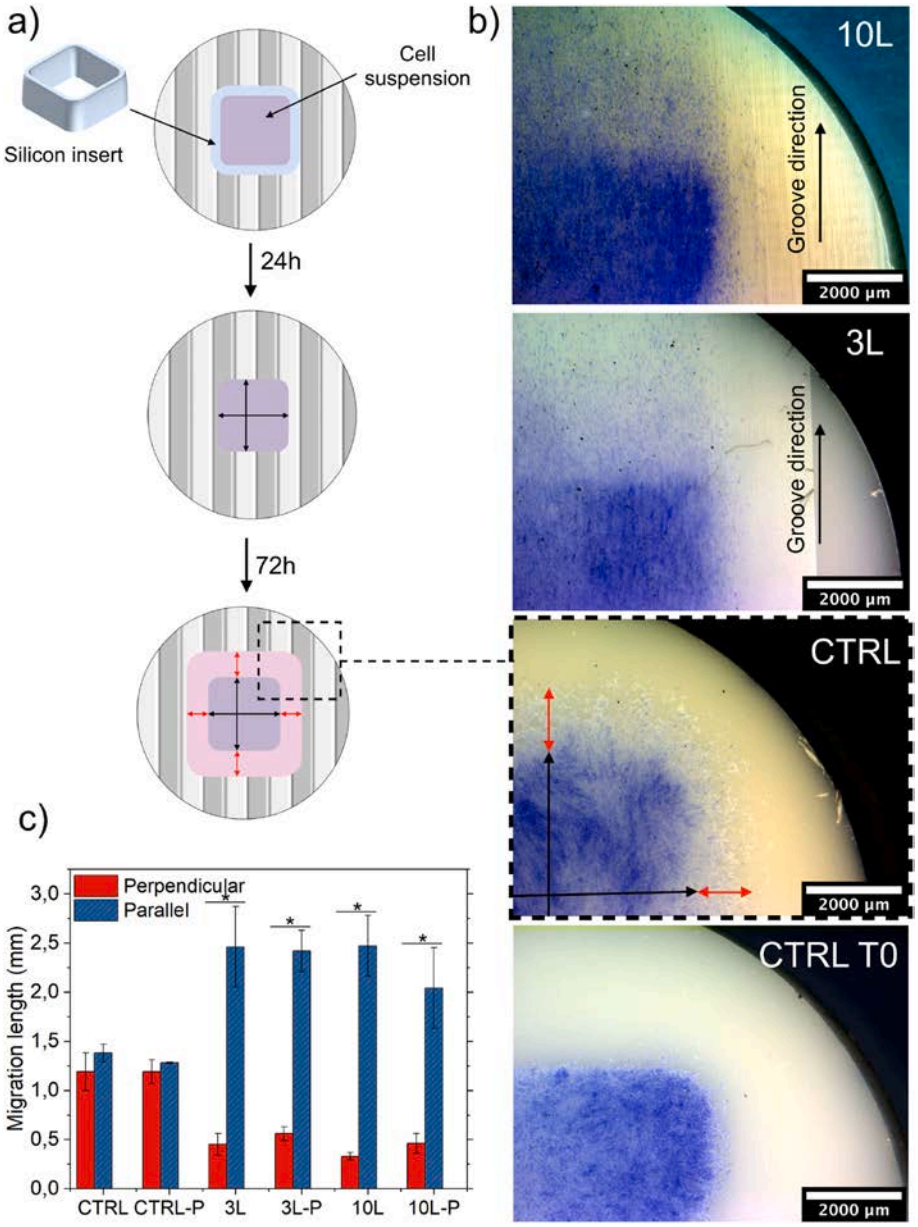

Fig. 10. Results of the cell migration experiments. a) Scheme of the experimental procedure: 1- a cell suspension was seeded in a cell-culture insert; 2- after 24 h a confluent layer had grown and the insert was removed; 3- after an additional 72 h cells migrated across the surface. b) Optical micrographs of the toluidine blue stained cells after migrating during 72 h. CTRL T0 indicates the reference specimen obtained just after removing the insert. c) Migration length (mm) for the studied specimens in two directions: parallel and perpendicular to the grooves. In CTRL specimens (without grooves) two orthogonal directions were chosen arbitrarily. * indicates statistical differences between the migration length in the parallel and the perpendicular direction for a particular specimen. (For interpretation of the references to color in this figure legend, the reader is referred to the web version of this article.)

compared to other surfaces. In this case, the authors of the study concluded that micro-grooves could result in a clinically valuable implant design, favoring rapid bone ingrowth and a strong bone-to-implant interface [108]. These results are in agreement with the in vitro migration experiments detailed in the present work, where a significantly enhanced migration was observed along the grooved patterns.

3.3.3. *Osteogenic potential*

Topography can effectively influence stem cell fate [11,21]. In particular, certain grooved substrates have been found to promote osteogenic differentiation [23,36,49]. This effect may be related to the changes in cell shape and cytoskeletal tension, which are known to regulate stem cell lineage commitment [109]. Moreover, biofunctionalization with bone growth factor derived peptides can enhance the osteodifferentiation of stem cells. Among the different BMP-2 derived peptides that have been found to present osteogenic properties, the DWIVA sequence is of particular interest due to its activity and small size [69,110–113]. It is derived from a fragment of the human BMP-2 that corresponds to overlapping sequences in BMPR-I and BMPR-II binding sites, and has shown enhanced in vivo bone growth around functionalized titanium implants and mineral granules, as well as increased in vitro osteogenesis in osteoblast-like MC3T3 cells and differentiation in hMSCs [69,110,111]. In addition, we recently reported that the DWIVA peptide can act synergistically with the RGD sequence in inducing integrin-BMPR crosstalk and mediating BMP-signaling [70]. Indeed, we demonstrated that the combination of RGD and DWIVA in a geometrically controlled manner within a peptidic platform (Fig. 2) promoted a larger increase in cell adhesion and osteogenic signaling as compared to the presence of RGD or DWIVA alone. Thus, the effects observed in the present study both in terms of cell adhesion and osteogenesis cannot be attributed to either one of the two peptides alone, but rather to the synergistic combination of both.

Gene expression was investigated at the early stages of osteogenic differentiation. For this purpose, the expression of early osteogenic markers was analyzed, including RUNX2, ALP, OSX and COL-1. Fig. 11a to d show the hMSCs expression levels of these genes after 7 days of culture. In this regard, the effect of topography was uneven. While 3L

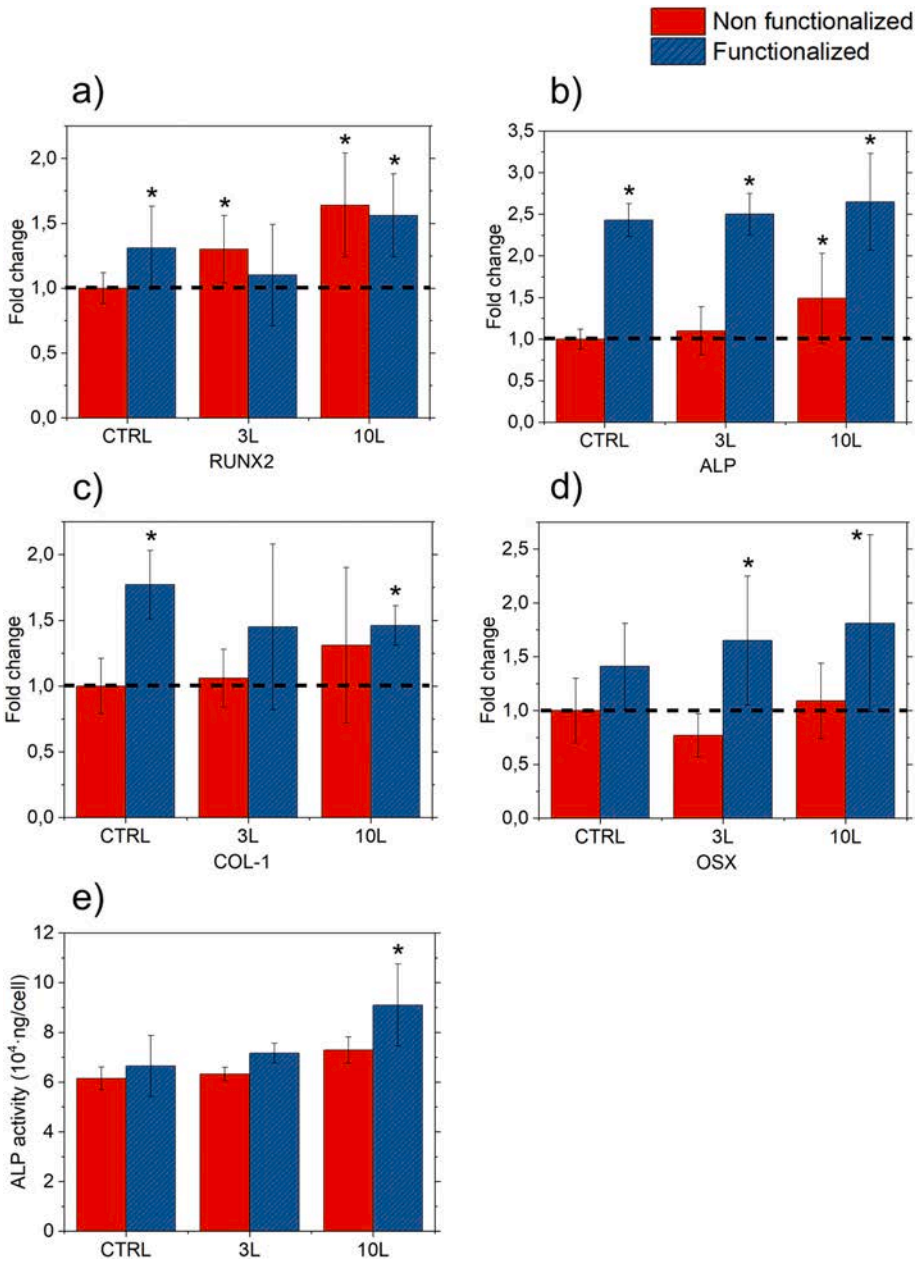

Fig. 11. Influence of topography and the peptidic platform on hMSCs. Expression levels of different genes related to osteoblastic differentiation are presented as follows: a) RUNX2, b) ALP, c) COL-1 and d) OSX. Results were normalized respect to the expression level of the housekeeping gene GAPDH and are represented as relative fold change to CTRL. e) ALP activity after 14 days of culture. In graphs a) to d) * indicates a statistically significant overexpression with respect to non-functionalized CTRL ($p < 0.05$). In e) * indicates an enhanced ALP activity with respect to non-functionalized CTRL ($p < 0.05$).

presented similar expression levels to CTRL specimens, 10L displayed a significant 1.5-fold upregulation of both RUNX2 and ALP. In contrast, the effect of the peptidic platform was relatively uniform in all the surfaces, with three of the studied genes upregulated: ALP (2.5-fold), COL-1 (1.5-fold) and OSX (1.5-fold), regardless of the studied topography. ALP activity was also measured after 14 days of culture (Fig. 11e). Small differences were observed except for 10L-P, which presented the highest level of activity. Differences between ALP at gene and protein level may be attributed to the time delay between the gene expression and the protein activity characterization, 7 and 14 days after cell seeding, respectively. Such differences suggest an early stimulation of hMSCs by the RGD/DWIVA peptides.

In summary, although the studied topographies (i.e. 10L) possessed a certain degree of osteogenic properties, the largest effects were observed from the RGD-DWIVA platform, which enhanced the differentiation potential of all the surfaces.

On the basis of the obtained results, the two modifications studied can be successfully combined. On the one hand the micro-patterns were responsible for a significant contact guidance, leading to an enhanced cell migration along the grooves, but a limited movement across the pattern. The clinical relevance of the directed movement of cells on a surface lies mainly on the control over tissue growth. At the gum level, grooves can hinder the apical downgrowth of the junctional epithelium, while at the bone level they can direct bone growth, promoting a faster ingrowth along the implant thread. On the other hand, the peptide-based platform favored the adhesion of a larger cell number as well as their spreading, facilitating the development of the cell cytoskeleton, which mediates mechanotransduction. A proper cell-to-implant adhesion is crucial for the differentiation of osteoblasts, although it is not the only requirement. In this regard, it was confirmed that the peptidic platform could successfully deliver osteogenic cues, stimulating cell differentiation. In conclusion, the dual strategy presented can act both at controlling the tissue growth around the implant and facilitating the bone formation at the surface.

4. Conclusions

In order to improve the tissue integration potential of zirconia surfaces, this work explored the combination of topographical and biochemical modifications. USP-DLIP was successful at producing defined micro-patterns on the surface of zirconia at a low cost in terms of surface damage. In particular, if a post-laser thermal treatment is applied, the main detrimental consequences of the patterning process can be reverted. The patterns were combined with a dual RGD/DWIVA peptidic platform. Thanks to the L-DOPA anchoring molecule, the peptide-based platform successfully attached to the surface of zirconia in a single step process, avoiding the use of toxic solvents.

The effects derived from the two surface modifications could be combined. Notably, the presence of the peptidic platform did not mask the effects derived from surface topography. While the grooves were mainly associated with contact guidance (cell alignment, elongation and migration) the peptidic platform improved cell adhesion (cell number and spreading) and introduced osteogenic potential to the surface.

The combination of surface topographical features obtained by laser micro-patterning and biofunctionalization with organic molecules provides a flexible tool to improve 3Y-TZP surfaces. Future works must be addressed to find the most suitable combinations at the different implant levels (e.g. gum and bone), exploring different surface topographies and using alternative peptides with additional properties (e.g. antibacterial). In addition, an investigation of the anchoring stability provided by the L-DOPA residues in a clinically relevant scenario is needed.

CRediT authorship contribution statement

Conceptualization: J. Minguela, J.J. Roa, C. Mas-Moruno.
Methodology: J. Minguela, D.W. Müller.
Investigation: J. Minguela.
Resources: F. Mücklich, L. Llanes, M.P. Ginebra, J.J. Roa, C. Mas-Moruno.
Writing - Original Draft: J. Minguela.
Writing - Review & Editing: All authors.
Supervision: J.J. Roa, C. Mas-Moruno.
Funding acquisition: F. Mücklich, L. Llanes, M.P. Ginebra, J.J. Roa, C. Mas-Moruno.

Declaration of competing interest

The authors declare that they have no known competing financial interests or personal relationships that could have appeared to influence the work reported in this paper.

Acknowledgements

This work was supported by the Ministerio de Ciencia, Innovación y Universidades (MAT2017-83905-R, MINECO/FEDER), the Generalitat de Catalunya (2017 SGR-933 and SGR-1165) and the CREATe-Network Project, Horizon 2020 Program of the European Commission (RISE Project Nr. 644013). J. Minguela has been supported by a predoctoral fellowship from the Barcelona Research Center in Multiscale Science and Engineering of the UPC. D.W. Müller is supported by funding from the European Regional Development Fund (EFRE, Interreg Großregion, Project: “Pulsatec”). M-P. Ginebra acknowledges the ICREA Academia Award and J.J. Roa the Serra Hunter program, both from the Generalitat de Catalunya. C. Mas-Moruno thanks the Spanish Government for a Ramon y Cajal grant.

References

[1] N. Cionca, D. Hashim, A. Mombelli, Zirconia dental implants: where are we now, and where are we heading? Periodontol. 2000 (73) (2017) 241–258.
[2] T. Albrektsson, B. Chrcanovic, M. Jacobsson, A. Wennerberg, Osseointegration of implants – a biological and clinical overview, JSM Dent Surg 2 (2017) 1022.
[3] M. Balmer, B.C. Spies, R.J. Kohal, C.H.F. Hämmerle, K. Vach, R.E. Jung, Zirconia implants restored with single crowns or fixed dental prostheses: 5-year results of a prospective cohort investigation, Clin. Oral Implants Res. 31 (2020) 452–462.
[4] D. Schwartz-Arad, N. Kidron, E. Dolev, A long-term study of implants supporting overdentures as a model for implant success, J. Periodontol. 76 (2005) 1431–1435.
[5] B. Klinge, M. Lundström, M. Rosén, K. Bertl, A. Klinge, A. Stavropoulos, Dental implant quality register—a possible tool to further improve implant treatment and outcome, Clin. Oral Implants Res. 29 (2018) 145–151.
[6] T. Albrektsson, C. Dahlin, T. Jemt, L. Sennerby, A. Turri, A. Wennerberg, Is marginal bone loss around oral implants the result of a provoked foreign body reaction? Clin. Implant. Dent. Relat. Res. 16 (2014) 155–165.
[7] X. Chen, Y. Li, C. Aparicio, Biofunctional coatings for dental implants, in: S. Nazarpour (Ed.), Thin Film. Coatings Biol. Biol. Med. Physics, Springer, Biomed. Eng, 2013.
[8] N. Donos, E. Calciolari, Dental implants in patients affected by systemic diseases, Br. Dent. J. 217 (2014) 425–430.
[9] B.R. Chrcanovic, T. Albrektsson, A. Wennerberg, Smoking and dental implants: a systematic review and meta-analysis, J. Dent. 43 (2015) 487–498.
[10] A. Civantos, E. Martínez-Campos, V. Ramos, C. Elvira, A. Gallardo, A. Abarrategi, Titanium coatings and surface modifications: toward clinically useful bioactive implants, ACS Biomater. Sci. Eng. 3 (2017) 1245–1261.
[11] C. Mas-Moruno, B. Su, M.J. Dalby, Multifunctional coatings and nanotopographies: toward cell instructive and antibacterial implants, Adv. Healthc. Mater. 8 (2019) 1801103.
[12] O. Zinger, G. Zhao, Z. Schwartz, J. Simpson, M. Wieland, D. Landolt, B. Boyan, Differential regulation of osteoblasts by substrate microstructural features, Biomaterials 26 (2005) 1837–1847.
[13] D. Li, S.J. Ferguson, T. Beutler, D.L. Cochran, C. Sittig, H.P. Hirt, D. Buser, Biomechanical comparison of the sandblasted and acid-etched and the machined and acid-etched titanium surface for dental implants, J. Biomed. Mater. Res. 60 (2002) 325–332.
[14] Q. Zhang, H. Dong, Y. Li, Y. Zhu, L. Zeng, H. Gao, B. Yuan, X. Chen, C. Mao, Microgrooved polymer substrates promote collective cell migration to accelerate fracture healing in an in vitro model, ACS Appl. Mater. Interfaces 7 (2015) 23336–23345.
[15] R. Schieber, F. Lasserre, M. Hans, M. Fernández-Yagüe, M. Díaz-Ricart, G. Escolar, M.P. Ginebra, F. Mücklich, M. Pegueroles, Direct laser interference patterning of CoCr alloy surfaces to control endothelial cell and platelet response for cardiovascular applications, Adv. Healthc. Mater. 6 (2017) 1700327.
[16] S. Weiner, J. Simon, D.S. Ehrenberg, B. Zweig, J.L. Ricci, The effects of laser microtextured collars upon crestal bone levels of dental implants, Implant. Dent. 17 (2008) 217–228.
[17] B. Chehroudi, T.R.L. Gould, D.M. Brunette, Titanium-coated micromachined grooves of different dimensions affect epithelial and connective-tissue cells differently in vivo, J. Biomed. Mater. Res. 24 (1990) 1203–1219.
[18] D.W. Hamilton, C.J. Oates, A. Hasanzadeh, S. Mittler, Migration of periodontal ligament fibroblasts on nanometric topographical patterns: influence of filopodia and focal adhesions on contact guidance, PLoS One 5 (2010), e15129.
[19] M.J. Dalby, M.O. Riehle, S.J. Yarwood, C.D.W. Wilkinson, A.S.G. Curtis, Nucleus alignment and cell signaling in fibroblasts: response to a micro-grooved topography, Exp. Cell Res. 284 (2003) 274–282.
[20] F.F.B. Hulshof, B. Papenburg, A. Vasilevich, M. Hulsman, Y. Zhao, M. Levers, N. Fekete, M. de Boer, H. Yuan, S. Singh, N. Beijer, M.A. Bray, D.J. Logan, M. Reinders, A.E. Carpenter, C. van Blitterswijk, D. Stamatialis, J. de Boer, Mining for osteogenic surface topographies: in silico design to in vivo osseo-integration, Biomaterials 137 (2017) 49–60.
[21] M.J. Dalby, N. Gadegaard, R. Tare, A. Andar, M.O. Riehle, P. Herzyk, C.D. W. Wilkinson, R.O.C. Oreffo, The control of human mesenchymal cell differentiation using nanoscale symmetry and disorder, Nat. Mater. 6 (2007) 997–1003.
[22] S. Watari, K. Hayashi, J.A. Wood, P. Russell, P.F. Nealey, C.J. Murphy, D. C. Genetos, Modulation of osteogenic differentiation in hMSCs cells by submicron topographically-patterned ridges and grooves, Biomaterials 33 (2012) 128–136.
[23] G. Abagnale, M. Steger, V.H. Nguyen, N. Hersch, A. Sechi, S. Joussen, B. Denecke, R. Merkel, B. Hoffmann, A. Dreser, U. Schnakenberg, A. Gillner, W. Wagner, Surface topography enhances differentiation of mesenchymal stem cells towards osteogenic and adipogenic lineages, Biomaterials 61 (2015) 316–326.
[24] A. Carvalho, L. Cangueiro, V. Oliveira, R. Vilar, M.H. Fernandes, F.J. Monteiro, Femtosecond laser microstructured alumina toughened zirconia: a new strategy to improve osteogenic differentiation of hMSCs, Appl. Surf. Sci. 435 (2018) 1237–1245.
[25] R.H.J. Hannink, P.M. Kelly, B.C. Muddle, Transformation toughening in zirconia-containing ceramics, J. Am. Ceram. Soc. 83 (2000) 461–487.
[26] T. Kosmač, Č. Oblak, P. Jevnikar, N. Funduk, L. Marion, Strength and reliability of surface treated Y-TZP dental ceramics, J. Biomed. Mater. Res. 53 (2000) 304–313.
[27] I.L. Denry, J.A. Holloway, Microstructural and crystallographic surface changes after grinding zirconia-based dental ceramics, J. Biomed. Mater. Res. - Part B Appl. Biomater. 76 (2006) 440–448.
[28] Q. Flamant, F. García Marro, J.J. Roa Rovira, M. Anglada, Hydrofluoric acid etching of dental zirconia. Part 1: etching mechanism and surface characterization, J. Eur. Ceram. Soc. 36 (2016) 121–134.
[29] J. Chevalier, L. Gremillard, S. Deville, Low-temperature degradation of zirconia and implications for biomedical implants, Annu. Rev. Mater. Res. 37 (2007) 1–32.

[30] E. Jiménez-Piqué, A. Ramos, J.A. Muñoz-Tabares, A. Hatton, F. Soldera, F. Mücklich, M. Anglada, Focused ion beam tomography of zirconia degraded under hydrothermal conditions, J. Eur. Ceram. Soc. 32 (2012) 2129–2136.

[31] S. Deville, J. Chevalier, L. Gremillard, Influence of surface finish and residual stresses on the ageing sensitivity of biomedical grade zirconia, Biomaterials 27 (2006) 2186–2192.

[32] E. Roitero, M. Ochoa, M. Anglada, F. Mücklich, E. Jiménez-Piqué, Low temperature degradation of laser patterned 3Y-TZP: enhancement of resistance after thermal treatment, J. Eur. Ceram. Soc. 38 (2018) 1742–1749.

[33] E. Roitero, F. Lasserre, M. Anglada, F. Mücklich, E. Jiménez-Piqué, A parametric study of laser interference surface patterning of dental zirconia: effects of laser parameters on topography and surface quality, Dent. Mater. 33 (2017) e28–e38.

[34] R.A. Delgado-Ruíz, J.L. Calvo-Guirado, P. Moreno, J. Guardia, G. Gomez-Moreno, J.E. Mate-Sánchez, P. Ramirez-Fernández, F. Chiva, Femtosecond laser microstructuring of zirconia dental implants, J. Biomed. Mater. Res. - Part B Appl. Biomater. 96 (B) (2011) 91–100.

[35] A.M. Stanciuc, Q. Flamant, C.M. Sprecher, M. Alini, M. Anglada, M. Peroglio, Femtosecond laser multi-patterning of zirconia for screening of cell-surface interactions, J. Eur. Ceram. Soc. 38 (2018) 939–948.

[36] A. Carvalho, L. Grenho, M.H. Fernandes, A. Daskalova, A. Trifonov, I. Buchvarov, F.J. Monteiro, Femtosecond laser microstructuring of alumina toughened zirconia for surface functionalization of dental implants, Ceram. Int. 46 (2020) 1383–1389.

[37] N. Bärsch, K. Werelius, S. Barcikowski, F. Liebana, U. Stute, A. Ostendorf, Femtosecond laser microstructuring of hot-isostatically pressed zirconia ceramic, J. Laser Appl. 19 (2007) 107–115.

[38] S. Heiroth, J. Koch, T. Lippert, A. Wokaun, D. Günther, F. Garrelie, M. Guillermin, Laser ablation characteristics of yttria-doped zirconia in the nanosecond and femtosecond regimes, J. Appl. Phys. 107 (2010), 014908.

[39] J. Li, L. Ji, Y. Hu, Y. Bao, Precise micromachining of yttria-tetragonal zirconia polycrystal ceramic using 532 nm nanosecond laser, Ceram. Int. 42 (2016) 4377–4385.

[40] F. Mücklich, A. Lasagni, C. Daniel, Laser interference metallurgy - using interference as a tool for micro/nano structuring, Int. J. Mater. Res. 97 (2006) 1337–1344.

[41] C. Daniel, B.L. Armstrong, J.Y. Howe, N.B. Dahotre, Controlled evolution of morphology and microstructure in laser interference-structured zirconia, J. Am. Ceram. Soc. 91 (2008) 2138–2142.

[42] A.F. Lasagni, Laser interference patterning methods: possibilities for high-throughput fabrication of periodic surface patterns, Adv. Opt. Technol. 6 (2017) 1–11.

[43] D.W. Müller, T. Fox, P.G. Grützmacher, S. Suarez, F. Mücklich, Applying ultrashort pulsed direct laser interference patterning for functional surfaces, Sci. Rep. 10 (2020) 3647.

[44] C. Zwahr, D. Günther, T. Brinkmann, N. Gulow, S. Oswald, M. Grosse Holthaus, A. F. Lasagni, Laser surface pattering of titanium for improving the biological performance of dental implants, Adv. Healthc. Mater. 6 (2017) 1600858.

[45] C. Daniel, J. Drummond, R.A. Giordano, Improving flexural strength of dental restorative ceramics using laser interference direct structuring, J. Am. Ceram. Soc. 91 (2008) 3455–3457.

[46] E. Roitero, F. Lasserre, J.J. Roa, M. Anglada, F. Mücklich, E. Jiménez-Piqué, Nanosecond-laser patterning of 3Y-TZP: damage and microstructural changes, J. Eur. Ceram. Soc. 37 (2017) 4876–4887.

[47] E. Roitero, M. Anglada, F. Mücklich, E. Jiménez-Piqué, Mechanical reliability of dental grade zirconia after laser patterning, J. Mech. Behav. Biomed. Mater. 86 (2018) 257–263.

[48] S. Lenhert, M.B. Meier, U. Meyer, L. Chi, H.P. Wiesmann, Osteoblast alignment, elongation and migration on grooved polystyrene surfaces patterned by Langmuir-Blodgett lithography, Biomaterials 26 (2005) 563–570.

[49] R.A. Delgado-Ruíz, G. Gomez Moreno, A. Aguilar-Salvatierra, A. Markovic, J. E. Mate-Sánchez, J.L. Calvo-Guirado, Human fetal osteoblast behavior on zirconia dental implants and zirconia disks with microstructured surfaces. An experimental in vitro study, Clin. Oral Implants Res. 27 (2016) e144–e153.

[50] Y. Taniguchi, K. Kakura, K. Yamamoto, H. Kido, J. Yamazaki, Accelerated osteogenic differentiation and bone formation on zirconia with surface grooves created with fiber laser irradiation, Clin. Implant. Dent. Relat. Res. 18 (2016) 883–894.

[51] L. Goyos-Ball, C. Prado, R. Díaz, E. Fernández, A. Ismailov, T. Kumpulainen, E. Levänen, R. Torrecillas, A. Fernández, The effects of laser patterning 10CeTZP-Al_2O_3 nanocomposite disc surfaces: osseous differentiation and cellular arrangement in vitro, Ceram. Int. 44 (2018) 9472–9478.

[52] R. Tejero, E. Anitua, G. Orive, Toward the biomimetic implant surface: biopolymers on titanium-based implants for bone regeneration, Prog. Polym. Sci. 39 (2014) 1406–1447.

[53] M.A. Wronska, I.B. O'Connor, M.A. Tilbury, A. Srivastava, J.G. Wall, Adding functions to biomaterial surfaces through protein incorporation, Adv. Mater. 28 (2016) 5485–5508.

[54] A. Cipitria, M. Salmeron-Sanchez, Mechanotransduction and growth factor signalling to engineer cellular microenvironments, Adv. Healthc. Mater. 6 (2017) 1700052.

[55] S. Trujillo, C. Gonzalez-Garcia, P. Rico, A. Reid, J. Windmill, M.J. Dalby, M. Salmeron-Sanchez, Engineered 3D hydrogels with full-length fibronectin that sequester and present growth factors, Biomaterials 252 (2020) 120104.

[56] C. Mas-Moruno, R. Fraioli, F. Rechenmacher, S. Neubauer, T.G. Kapp, H. Kessler, αvβ3- or α5β1-integrin-selective peptidomimetics for surface coating, Angew. Chemie - Int. Ed. 55 (2016) 7048–7067.

[57] R. Fraioli, S. Neubauer, F. Rechenmacher, B.M. Bosch, K. Dashnyam, J.H. Kim, R. A. Perez, H.W. Kim, F.J. Gil, M.P. Ginebra, J.M. Manero, H. Kessler, C. Mas-Moruno, Control of stem cell response and bone growth on biomaterials by fully non-peptidic integrin selective ligands, Biomater. Sci. 7 (2019) 1281–1285.

[58] N.G. Fischer, E.A. Münchow, C. Tamerler, M.C. Bottino, C. Aparicio, Harnessing biomolecules for bioinspired dental biomaterials, J. Mater. Chem. B 8 (2020) 8713–8747.

[59] Z. Wang, Y. Shen, M. Haapasalo, Antibiofilm peptides against oral biofilms, J. Oral Microbiol. 9 (2017) 1327308.

[60] K.V. Holmberg, M. Abdolhosseini, Y. Li, X. Chen, S.U. Gorr, C. Aparicio, Bio-inspired stable antimicrobial peptide coatings for dental applications, Acta Biomater. 9 (2013) 8224–8231.

[61] Z. Liu, S. Ma, X. Lu, T. Zhang, Y. Sun, W. Feng, G. Zheng, L. Sui, X. Wu, X. Zhang, P. Gao, Reinforcement of epithelial sealing around titanium dental implants by chimeric peptides, Chem. Eng. J. 356 (2019) 117–129.

[62] M. Yakufu, Z. Wang, Y. Wang, Z. Jiao, M. Guo, J. Liu, P. Zhang, Covalently functionalized poly(etheretherketone) implants with osteogenic growth peptide (OGP) to improve osteogenesis activity, RSC Adv. 10 (2020) 9777–9785.

[63] P. Sevilla, A. Cirera, J. Dotor, F.J. Gil, P. Galindo-Moreno, C. Aparicio, In vitro cell response on CP-Ti surfaces functionalized with TGF-β1 inhibitory peptides, J. Mater. Sci. Mater. Med. 29 (2018) 73.

[64] E. Ruoslahti, RGD and other recognition sequences for integrins, Annu. Rev. Cell Dev. Biol. 12 (1996) 697–715.

[65] R. Visser, G.A. Rico-Llanos, H. Pulkkinen, J. Becerra, Peptides for bone tissue engineering, J. Control. Release 244 (2016) 122–135.

[66] F.R. Maia, S.J. Bidarra, P.L. Granja, C.C. Barrias, Functionalization of biomaterials with small osteoinductive moieties, Acta Biomater. 9 (2013) 8773–8789.

[67] Y. Suzuki, M. Tanihara, K. Suzuki, A. Saitou, W. Sufan, Y. Nishimura, Alginate hydrogel linked with synthetic oligopeptide derived from BMP-2 allows ectopic osteoinduction in vivo, J. Biomed. Mater. Res. 50 (2000) 405–409.

[68] X. Niu, Q. Feng, M. Wang, X. Guo, Q. Zheng, Porous nano-HA/collagen/PLLA scaffold containing chitosan microspheres for controlled delivery of synthetic peptide derived from BMP-2, J. Control. Release 134 (2009) 111–117.

[69] J.Y. Lee, J.E. Choo, Y.S. Choi, J.S. Suh, S.J. Lee, C.P. Chung, Y.J. Park, Osteoblastic differentiation of human bone marrow stromal cells in self-assembled BMP-2 receptor-binding peptide-amphiphiles, Biomaterials 30 (2009) 3532–3541.

[70] L. Oliver-Cervelló, H. Martin-Gómez, L. Reyes, F. Noureddine, E.A. Cavalcanti-Adam, M.-P. Ginebra, C. Mas-Moruno, An engineered biomimetic peptide regulates cell behavior by synergistic integrin and growth factor signaling, Adv. Healthc. Mater. 10 (2021) 2001757.

[71] C. Mas-Moruno, R. Fraioli, F. Albericio, J.M. Manero, F.J. Gil, Novel peptide-based platform for the dual presentation of biologically active peptide motifs on biomaterials, ACS Appl. Mater. Interfaces 6 (2014) 6525–6536.

[72] S.K. Hsu, H.C. Hsu, W.F. Ho, C.H. Yao, P.L. Chang, S.C. Wu, Biomolecular modification of zirconia surfaces for enhanced biocompatibility, Thin Solid Films 572 (2014) 91–98.

[73] E. Fernandez-Garcia, X. Chen, C.F. Gutierrez-Gonzalez, A. Fernandez, S. Lopez-Esteban, C. Aparicio, Peptide-functionalized zirconia and new zirconia/titanium biocermets for dental applications, J. Dent. 43 (2015) 1162–1174.

[74] Z. Yang, M. Liu, Y. Yang, M. Zheng, Y. Yang, X. Liu, J. Tan, Biofunctionalization of zirconia with cell-adhesion peptides via polydopamine crosslinking for soft tissue engineering: effects on the biological behaviors of human gingival fibroblasts and oral bacteria, RSC Adv. 10 (2020) 6200–6212.

[75] J. Minguela, S. Slawik, F. Mücklich, M.P. Ginebra, L. Llanes, C. Mas-Moruno, J. J. Roa, Evolution of microstructure and residual stresses in gradually ground/polished 3Y-TZP, J. Eur. Ceram. Soc. 40 (2020) 1582–1591.

[76] A. Rosenkranz, M. Hans, C. Gachot, A. Thome, S. Bonk, F. Mücklich, Direct laser interference patterning: tailoring of contact area for frictional and antibacterial properties, Lubricants 4 (2016) 2–15.

[77] H. Toraya, M. Yoshimura, S. Somiya, Calibration curve for quantitative analysis of the monoclinic-tetragonal ZrO2 system by X-ray diffraction, J. Am. Ceram. Soc. 67 (1984) C-119–C-121.

[78] I.C. Noyan, J.B. Cohen, Residual Stress - Measurement by Diffraction and Interpretation, Springer-Verlag, 1987.

[79] J.A. Muñoz-Tabares, E. Jiménez-Piqué, M. Anglada, Subsurface evaluation of hydrothermal degradation of zirconia, Acta Mater. 59 (2011) 473–484.

[80] J. Chevalier, B. Cales, J.M. Drouin, Low-temperature aging of Y-TZP ceramics, J. Am. Ceram. Soc. 82 (1999) 2150–2154.

[81] J. Schindelin, I. Arganda-Carreras, E. Frise, V. Kaynig, M. Longair, T. Pietzsch, S. Preibisch, C. Rueden, S. Saalfeld, B. Schmid, J.Y. Tinevez, D.J. White, V. Hartenstein, K. Eliceiri, P. Tomancak, A. Cardona, Fiji: an open-source platform for biological-image analysis, Nat. Methods 9 (2012) 676–682.

[82] K.J. Livak, T.D. Schmittgen, Analysis of relative gene expression data using real-time quantitative PCR and the 2-ΔΔCT method, Methods 25 (2001) 402–408.

[83] P. Clark, P. Connolly, A.S.G. Curtis, J.A.T. Dow, C.D.W. Wilkinson, Topographical control of cell behaviour: II. Multiple grooved substrata, Development 108 (1990) 635–644.

[84] X.F. Walboomers, W. Monaghan, A.S.G. Curtis, J.A. Jansen, Attachment of fibroblasts on smooth and microgrooved polystyrene, J. Biomed. Mater. Res. 46 (1999) 212–220.

[85] L. Sennerby, A. Dasmah, B. Larsson, M. Iverhed, Bone tissue responses to surface-modified zirconia implants: a histomorphometric and removal torque study in the rabbit, Clin. Implant. Dent. Relat. Res. 7 (2005) s13–s20.

[86] A. Wennerberg, T. Albrektsson, Effects of titanium surface topography on bone integration: a systematic review, Clin. Oral Implants Res. 20 (2009) 172–184.
[87] Y.L. Yao, H. Chen, W. Zhang, Time scale effects in laser material removal: a review, Int. J. Adv. Manuf. Technol. 26 (2005) 598–608.
[88] T.D. Bennett, D.J. Krajnovich, C.P. Grigoropoulos, P. Baumgart, A.C. Tam, Marangoni mechanism in pulsed laser texturing of magnetic disk substrates, J. Heat Transf. Asme 119 (1997) 589–596.
[89] B.J. Von Der Linde, D., K. Sokolowski-Tinten, Laser – solid interaction in the femtosecond time regime, Appl. Surf. Sci. 109–110 (1997) 1–10.
[90] J. Krüger, W. Kautek, Ultrashort pulse laser interaction with dielectrics and polymers, Adv. Polym. Sci. 168 (2004) 247–289.
[91] R. Wagner, J. Gottmann, A. Horn, E.W. Kreutz, Subwavelength ripple formation induced by tightly focused femtosecond laser radiation, Appl. Surf. Sci. 252 (2006) 8576–8579.
[92] B. Rethfeld, Unified model for the free-electron avalanche in laser-irradiated dielectrics, Phys. Rev. Lett. 92 (2004) 1–4.
[93] M.D. Shirk, P.A. Molian, A review of ultrashort pulsed laser ablation of materials, J. Laser Appl. 10 (1998) 18–28.
[94] J.J. Roa, M. Turon-Vinas, M. Anglada, Surface grain size and texture after annealing ground zirconia, J. Eur. Ceram. Soc. 36 (2016) 1519–1525.
[95] P.F. Becher, M.V. Swain, Grain-size-dependent transformation behavior in polycrystalline tetragonal zirconia, J. Am. Ceram. Soc. 75 (1992) 493–502.
[96] N. Mansour, K. Mansour, E.W. Van Stryland, M.J. Soileau, Diffusion of color centers generated by two-photon absorption at 532 nm in cubic zirconia, J. Appl. Phys. 67 (1990) 1475–1477.
[97] J. Minguela, M.P. Ginebra, L. Llanes, C. Mas-Moruno, J.J. Roa, Influence of grinding/polishing on the mechanical, phase stability and cell adhesion properties of yttria-stabilized zirconia, J. Eur. Ceram. Soc. 40 (2020) 4304–4314.
[98] V. Lughi, V. Sergo, Low temperature degradation -aging- of zirconia: a critical review of the relevant aspects in dentistry, Dent. Mater. 26 (2010) 807–820.
[99] E.W. Danner, Y. Kan, M.U. Hammer, J.N. Israelachvili, J.H. Waite, Adhesion of mussel foot protein Mefp-5 to mica: an underwater superglue, Biochemistry 51 (2012) 6511–6518.
[100] H. Lee, N.F. Scherer, P.B. Messersmith, Single-molecule mechanics of mussel adhesion, Proc. Natl. Acad. Sci. 103 (2006) 12999–13003.
[101] M. Liu, J. Zhou, Y. Yang, M. Zheng, J. Yang, J. Tan, Surface modification of zirconia with polydopamine to enhance fibroblast response and decrease bacterial activity in vitro: a potential technique for soft tissue engineering applications, Colloids Surfaces B Biointerfaces 136 (2015) 74–83.
[102] B. Ann Dalton, X. Frank Walboomers, M. Dziegielewski, M.D.M. Evans, S. Taylor, J.A. Jansen, J.G. Steele, Modulation of epithelial tissue and cell migration by microgrooves, J. Biomed. Mater. Res. 56 (2001) 195–207.
[103] A. Curtis, C. Wilkinson, Topographical control of cells, Biomaterials 18 (1997) 1573–1583.
[104] Y. Li, G. Huang, X. Zhang, L. Wang, Y. Du, T.J. Lu, F. Xu, Engineering cell alignment in vitro, Biotechnol. Adv. 32 (2014) 347–365.
[105] S. Fujita, M. Ohshima, H. Iwata, Time-lapse observation of cell alignment on nanogrooved patterns, J. R. Soc. Interface 6 (2009) S269–S277.
[106] R.J. Petrie, A.D. Doyle, K.M. Yamada, Random versus directionally persistent cell migration, Nat. Rev. Mol. Cell Biol. 10 (2009) 538–549.
[107] M. Nevins, M. Camelo, M.L. Nevins, P. Schupbach, D.M. Kim, Connective tissue attachment to laser-microgrooved abutments: a human histologic case report, Int. J. Periodontics Restor. Dent 32 (2012) 385–392.
[108] S.R. Frenkel, J. Simon, H. Alexander, M. Dennis, J.L. Ricci, Osseointegration on metallic implant surfaces: effects of microgeometry and growth factor treatment, J. Biomed. Mater. Res. 63 (2002) 706–713.
[109] R. Mcbeath, D.M. Pirone, C.M. Nelson, K. Bhadriraju, C.S. Chen, Cell shape, cytoskeletal tension, and RhoA regulate stem cell lineage commitment, Dev. Cell 6 (2004) 483–495.
[110] Y.-J. Seol, Y.-J. Park, S.-C. Lee, K.-H. Kim, J.-Y. Lee, T.-I. Kim, Y.-M. Lee, Y. Ku, I.-C. Rhyu, S.-B. Han, C.-P. Chung, Enhanced osteogenic promotion around dental implants with synthetic binding motif mimicking bone morphogenetic protein (BMP)-2, J. Biomed. Mater. Res. Part A 77A (2006) 599–607.
[111] J.-B. Park, J.-Y. Lee, H.-N. Park, Y.-J. Seol, Y.-J. Park, S.-H. Rhee, S.-C. Lee, K.-H. Kim, T.-I. Kim, Y.-M. Lee, Y. Ku, I.-C. Rhyu, S.-B. Han, C.-P. Chung, Osteopromotion with synthetic oligopeptide–coated bovine bone mineral in vivo, J. Periodontol. 78 (2007) 157–163.
[112] L. Falcigno, G. D'Auria, L. Calvanese, D. Marasco, R. Iacobelli, P.L. Scognamiglio, P. Brun, R. Danesin, M. Pasqualin, I. Castagliuolo, M. Dettin, Osteogenic properties of a short BMP-2 chimera peptide, J. Pept. Sci. 21 (2015) 700–709.
[113] Y. Oki, K. Kirita, S. Ohta, S. Ohba, I. Horiguchi, Y. Sakai, T. Ito, Switching of cell proliferation/differentiation in thiol-maleimide clickable microcapsules triggered by in situ conjugation of biomimetic peptides, Biomacromolecules 20 (2019) 2350–2359.

Chapter 7
Main conclusions and relevance of the findings

7 Main conclusions and relevance of the findings

The main conclusions of the work gathered in this thesis will be summarized and discussed below, highlighting the relevance of the most remarkable findings.

Grinding/polishing

Grinding/polishing procedures not only affect surface roughness, but also microstructure and phase composition of 3Y-TZP. The stresses generated by the abrading particles trigger the *m*-phase transformation. In turn, the expansive nature of this phase transformation generates a residual compressive surface layer. In the light of the results obtained, surface roughness, monoclinic volume fraction (V_m) and the value of residual stresses can be mathematically related. This observation is not trivial. If the manufacturing conditions of zirconia parts are controlled, the residual stress state and *m*-phase content of the ground parts can be deduced by using a simple profilometer. This procedure is relatively cheap, simple, readily available and fast, and avoids the use of more expensive and complex equipment, such as X-ray diffractometers or Raman spectrometers.

On the other hand, severe microstructural changes are found on the surface of ground and polished specimens. The main changes are due to surface grain recrystallization. Although it is a phenomenon that has been previously reported in this material, the work conducted along this Ph.D. Thesis demonstrates that recrystallization takes place in a wide range of grinding/polishing procedures, and not only on coarsely ground surfaces. Even after relatively mild procedures, surface recrystallization can be observed. In this regard, the transition from bulk-like to recrystallized surfaces was identified in polished surfaces with a roughness as low as S_a = 16 ± 1 nm, in which partial recrystallization was observed. The consequences of these findings are very important. LTD experiments showed that mildly polished surfaces can present excellent protective features. Surfaces with low roughness (S_a < 50 nm) had the same protective properties as ground specimens, showing an excellent resistance even after 50 hours in water steam (equivalent to more than 150 years *in vivo*). In this

regard, even the specimens polished to a S_a = 16 nm displayed a significant degree of protection respect to mirror-like polished specimens (S_a = 5 nm). After 20 hours in water steam (equivalent to 60 years *in vivo*) they presented a monoclinic content of V_m < 10 %, while mirror-like polished surfaces presented already a severely degraded surface with V_m = 60 %. These results must be highlighted, as most of the literature available has overlooked such effects.

As also reported previously by other authors, if too coarse grinding is employed, the resistance to LTD can be worsened. Although other works have related the worsening of properties to surface damage, no evidences were given on this relation. In the present Ph.D. Thesis, a clear relation is found between degradation of the surface and damage in the form of flakes, which were associated to subsurface micro-cracks.

From these observations, it can be concluded that 3Y-TZP is highly susceptible to changes after surface mechanical treatments. A special emphasis must be placed on this sentence, as small changes on the surface can have catastrophic effects on the performance of 3Y-TZP final parts. Recent history of zirconia has sadly evidenced this fact.

Finally, regarding mechanical properties, the layer of residual compressive stresses generated after grinding can improve contact damage properties.

Laser patterning

DLIP technique can be employed to micro-pattern ceramic materials in the femtosecond pulse regime, such as 3Y-TZP. Although one recent work has employed this technique and this time regime successfully (with a five-fold longer pulse duration), it is the first time that such a good pattern definition is achieved, and that grooves with a periodicity as low as 3 μm are ablated. The results obtained in this Ph.D. thesis also highlight the potential industrial application of this technique, which allows creating homogeneous and defined

features of only a few microns in 3Y-TZP materials. No other technique with equivalent processing speed has yet achieved these results.

The effects in the subsurface of DLIP laser-patterned 3Y-TZP in the nanosecond regime have been recently studied. However, no clues on the effects in the femtosecond regime existed until now. In contrast to the nanosecond time regime, where extensive melting of the surface is produced, the material removal mechanism in the femtosecond regime is mainly governed by ablation. While material in the top of the peaks remains unaltered, material on the bottom of the valleys is ablated, producing a stochastic grainy nano-topography. Surface damage in the form of nano-cracks and nano-pores can be found on the valleys, but limited to a layer of 500 nm below the surface. Just traces of *m*- phase can be detected after these procedures and very low residual stresses are generated, in the range of the ones found in mirror-like polished specimens. LTD is slightly worsened, but after a thermal treatment it can be reverted, even improving the LTD resistance of the base material.

Femtosecond regime DLIP shows a clear potential to be employed in creating micro- and nano-topographies on biomedical surfaces, where surface damage must be reduced and features of only a few micrometers are required.

Biological effects of the topographies and surface functionalization

Grooved topographies have been obtained by two methods: grinding/polishing and laser micro-patterning. None of the surfaces showed a significant increase in cell attachment, although when the grooves were parallel, contact guidance could be observed. In the case of ground/polished surfaces, this was only observed in surfaces above a certain roughness threshold (S_a > 150 nm) and just in the smaller SaOS-2, but not in the larger MSCs. The roughness degree that can be achieved by grinding without producing excessive surface damage is limited. Thus, the topographical features obtained with this method may not be enough to efficiently guide the growth of larger cells. This problem can be solved by

producing the grooves by laser micro-patterning, where the cost of producing deeper features is less detrimental in terms of surface damage.

Laser grooved surfaces can guide cellular growth, inducing cell alignment, elongation and cell migration along the pattern. In the perpendicular direction, however, migration is limited. This effect has been already used *in vivo* in dog models where micro-textured collars showed reduced epithelial downgrowth and greater bone attachment.

Regarding the peptidic platform employed, the L-DOPA-based anchoring molecule can successfully attach to 3Y-TZP. The effects from the dual RGD-DWIVA platform are kept once the molecule attaches to the surface. Functionalized surfaces present more cells, better spread and with well-developed cytoskeletons. The molecule introduces osteogenic properties to the surfaces by upregulating several osteogenesis-related genes. Importantly, the effects derived from the topography are not masked by the biomolecule, and are also kept in functionalized specimens. Thus, by combining the laser micro-patterns and the peptidic platform cell growth can be guided, and improved adhesion and osteogenic cues are provided.

The combination of surface topography and biofunctionalization carried out in this Ph.D. Thesis show that the effects from both strategies are compatible and can be combined to tailor the surface properties. Of note, such dual approach was never investigated before on 3Y-TZP. By studying other topographies and employing other peptides, more properties can be introduced to 3Y-TZP surfaces, depending on the specific application. This dual functionalization can thus become a powerful tool to improve the tissue integration and healing success of 3Y-TZP dental implants.

References

[1] R.B. Heimann, H.D. Lehmann, Bioceramics – A Historical Perspective, in: Bioceram. Coatings Med. Implant., Wiley, 2015: pp. 1–10.

[2] R.H.J. Hannink, P.M. Kelly, B.C. Muddle, Transformation toughening in zirconia-containing ceramics, J. Am. Ceram. Soc. 83 (2000) 461–487.

[3] O. Ruff, F. Ebert, Beiträge zur Keramik hochfeuerfester Stoffe. l. Die Formen des Zirkondioxyds, Zeitschrift Für Anorg. Und Allg. Chemie 180 (1929) 19–41.

[4] O. Ruff, F. Ebert, E. Stephan, Beiträge zur Keramik hochfeuerfester Stoffe II. Das System ZrO_2-CaO, Zeitschrift Für Anorg. Und Allg. Chemie 180 (1929) 215–224.

[5] R.C. Garvie, R.H. Hannink, R.T. Pascoe, Ceramic steel?, Nature 258 (1975) 703–704.

[6] I. Nettleship, R. Stevens, Tetragonal zirconia polycrystal (TZP)-A review, Int. J. High Technol. Ceram. 3 (1987) 1–32.

[7] P.H. Rieth, J.S. Reed, A.W. Naumann, Fabrication and flexural strength of ultrafine- grained yttria-stabilized zirconia, Am. Ceram. Soc. Bull 55 (1976) 717–721.

[8] T.K. Gupta, J.H. Bechtold, R.C. Kuznicki, L.H. Cadoff, B.R. Rossing, Stabilization of tetragonal phase in polycrystalline zirconia, J. Mater. Sci. 12 (1977) 2421–2426.

[9] S. Ban, Reliability and properties of core materials for all-ceramic dental restorations, Jpn. Dent. Sci. Rev. 44 (2008) 3–21.

[10] J.R. Kelly, I. Denry, Stabilized zirconia as a structural ceramic: An overview, Dent. Mater. 24 (2008) 289–298.

[11] J. Chevalier, L. Gremillard, Ceramics for medical applications: A picture for the next 20 years, J. Eur. Ceram. Soc. 29 (2009) 1245–1255.

[12] I. Birkby, R. Stevens, Applications of Zirconia Ceramics, Key Eng. Mater. 122–124 (1996) 527–552.

[13] C. Piconi, G. Maccauro, F. Muratori, E. Brach Del Prever, Alumina and zirconia ceramics in joint replacements., J. Appl. Biomater. Biomech. 1 (2003) 19–32.

[14] M. Peters, B. Saruhan-Brings, U. Schulz, Advanced Coatings for Blades of Future Aero Engines, in: Proc. CEAS 2009 Eur. Air Sp. Conf., Manchester, UK, 2009: pp. 1–9.

[15] J.E. Shigley, A. Gilbertson, S. Eaton-Magaña, Characterization of colorless coated cubic zirconia (Diamantine), Gems Gemol. 48 (2012) 18–30.

[16] S. Shukla, S. Seal, Mechanisms of room temperature metastable tetragonal phase stabilisation in zirconia, Int. Mater. Rev. 50 (2005) 45–64.

[17] University of Cambridge, DoITPoMS TLP Library. Available at:https://www.doitpoms.ac.uk/tlplib/fuel-cells/sofc_electrolyte.php (accessed November 24, 2020).

[18] J. Chevalier, L. Gremillard, A. V. Virkar, D.R. Clarke, The tetragonal-monoclinic transformation in zirconia: Lessons learned and future trends, J. Am. Ceram. Soc. 92 (2009) 1901–1920.

[19] F.F. Lange, Transformation toughening - Part 1 Size effects associated with the

thermodynamics of constrained transformations, J. Mater. Sci. 17 (1982) 225–234.

[20] R.M. McMeeking, A.G. Evans, Mechanics of Transformation-Toughening in Brittle Materials, J. Am. Ceram. Soc. 65 (1982) 242–246.

[21] K. Kobayashi, H. Kuwajima, T. Masaki, Phase change and mechanical properties of ZrO_2-Y_2O_3 solid electrolyte after ageing, Solid State Ionics 3–4 (1981) 489–493.

[22] M. Yoshimura, Phase stability of zirconia, Am. Ceram. Soc. Bull. 67 (1988) 1950–1955.

[23] J. Chevalier, B. Cales, J.M. Drouin, Low-temperature aging of Y-TZP ceramics, J. Am. Ceram. Soc. 82 (1999) 2150–2154.

[24] J. Chevalier, What future for zirconia as a biomaterial?, Biomaterials 27 (2006) 535–543.

[25] S. Deville, J. Chevalier, L. Gremillard, Influence of surface finish and residual stresses on the ageing sensitivity of biomedical grade zirconia, Biomaterials 27 (2006) 2186–2192.

[26] L. Gremillard, S. Grandjean, J. Chevalier, A new method to measure monoclinic depth profile in zirconia-based ceramics from X-ray diffraction data, Int. J. Mater. Res. 101 (2010) 88–94.

[27] J.A. Muñoz-Tabares, E. Jiménez-Piqué, M. Anglada, Subsurface evaluation of hydrothermal degradation of zirconia, Acta Mater. 59 (2011) 473–484.

[28] T. Kosmač, A. Kocjan, Ageing of dental zirconia ceramics, J. Eur. Ceram. Soc. 32 (2012) 2613–2622.

[29] J. Chevalier, L. Gremillard, S. Deville, Low-temperature degradation of zirconia and implications for biomedical implants, Annu. Rev. Mater. Res. 37 (2007) 1–32.

[30] X. Guo, Low temperature degradation mechanism of tetragonal zirconia ceramics in water: role of oxygen vacancies, Solid State Ionics 112 (1998) 113–116.

[31] X. Guo, T. Schober, Water incorporation in tetragonal zirconia, J. Am. Ceram. Soc. 87 (2004) 746–748.

[32] H. Schubert, F. Frey, Stability of Y-TZP during hydrothermal treatment: Neutron experiments and stability considerations, J. Eur. Ceram. Soc. 25 (2005) 1597–1602.

[33] T. Duong, A.M. Limarga, D.R. Clarke, Diffusion of water species in yttria-stabilized zirconia, J. Am. Ceram. Soc. 92 (2009) 2731–2737.

[34] E. Jiménez-Piqué, A. Ramos, J.A. Muñoz-Tabares, A. Hatton, F. Soldera, F. Mücklich, M. Anglada, Focused ion beam tomography of zirconia degraded under hydrothermal conditions, J. Eur. Ceram. Soc. 32 (2012) 2129–2136.

[35] G. Maccauro, C. Piconi, W. Burger, L. Pilloni, E. De Santis, F. Muratori, I.D. Learmonth, Fracture of a Y-TZP ceramic femoral head. Analysis of a fault, J. Bone Jt. Surg. - Ser. B 86 (2004) 1192–1196.

[36] W.A. Johnson, R.F. Mehl, Reaction kinetics in processes of nucleation and growth, Trans. Am. Inst. Min. Met. Pet. Eng. 135 (1939) 416–441.

[37] V. Lughi, V. Sergo, Low temperature degradation -aging- of zirconia: A critical review of the relevant aspects in dentistry, Dent. Mater. 26 (2010) 807–820.

[38] J.R. Kelly, I. Nishimura, S.D. Campbell, Ceramics in dentistry: Historical roots and current perspectives, J. Prosthet. Dent. 75 (1996) 18–32.

[39] J.R. Kelly, Ceramics in restorative and prosthetic dentistry, Annu. Rev. Mater. Sci. 27 (1997) 443–468.

[40] J.D. Helmer, T.D. Driskell, Research on bioceramics. Symp. on use of ceramics as surgical implants, South Carolina (USA): Clemson University, 1969.

[41] P. Christel, A. Meunier, J.M. Dorlot, J.M. Crolet, J. Witvoet, L. Sedel, P. Boutin, Biomechanical Compatibility and Design of Ceramic Implants for Orthopedic Surgery, Ann. N. Y. Acad. Sci. 523 (1988) 234–256.

[42] I. Denry, J.R. Kelly, State of the art of zirconia for dental applications, Dent. Mater. 24 (2008) 299–307.

[43] B. Stawarczyk, C. Keul, M. Eichberger, D. Figge, D. Edelhoff, N. Lümkemann, Three generations of zirconia: From veneered to monolithic. Part I., Quintessence Int. (Berl). 48 (2017) 369–380.

[44] Y. Zhang, B.R. Lawn, Novel Zirconia Materials in Dentistry, J. Dent. Res. 97 (2018) 140–147.

[45] S.O. Koutayas, T. Vagkopoulou, S. Pelekanos, P. Koidis, J.R. Strub, Zirconia in Dentistry: Part 2. Evidence-based clinical breakthrough, Eur. J. Esthet. Dent. 4 (2009) 348–380.

[46] J. Abduo, K. Lyons, M. Swain, Fit of zirconia fixed partial denture: A systematic review, J. Oral Rehabil. 37 (2010) 866–876.

[47] T. Miyazaki, T. Nakamura, H. Matsumura, S. Ban, T. Kobayashi, Current status of zirconia restoration, J. Prosthodont. Res. 57 (2013) 236–261.

[48] J. Zhao, X. Wang, Dental Prostheses, in: J. Zhijian Shen, T. Kosmač (Eds.), Adv. Ceram. Dent., Elsevier Inc., 2014: pp. 23–49.

[49] B. Reinhardt, T. Beikler, Dental Implants, in: J. Zhijian Shen, T. Kosmač (Eds.), Adv. Ceram. Dent., Elsevier Inc., 2014: pp. 51–75.

[50] D. Weingart, S. Steinemann, W. Schilli, J.R. Strub, U. Hellerich, J. Assenmacher, J. Simpson, Titanium deposition in regional lymph nodes after insertion of titanium screw implants in maxillofacial region, Int. J. Oral Maxillofac. Surg. 23 (1994) 450–452.

[51] K. Dear, A.E. Boyce, A. Lee, Allergic contact dermatitis due to titanium in a total knee replacement, Contact Dermatitis 83 (2020) 161–162.

[52] G. Heydecke, R. Kohal, R. Gläser, Optimal esthetics in single-tooth replacement with the Re-Implant system: a case report., Int. J. Prosthodont. 12 (1999) 184–189.

[53] M. Dental Solutions, Post and core. Available at:http://medellindentalsolutions.com/post-and-core/ (accessed May 1, 2020).

[54] N. Biocare, NobelPearl™ – a unique 100% metal-free two-piece ceramic implant solution. Available at:https://www.sdmag.co.uk/2018/10/03/nobelpearl-a-unique-100-metal-free-two-piece-ceramic-implant-solution/ (accessed May 1, 2020).

[55] R.A. Gittens, R. Olivares-Navarrete, Z. Schwartz, B.D. Boyan, Implant osseointegration and the role of microroughness and nanostructures: Lessons for spine implants, Acta Biomater. 10 (2014) 3363–3371.

[56] Y. Chandorkar, K. Ravikumar, B. Basu, The Foreign Body Response Demystified, ACS

Biomater. Sci. Eng. 5 (2019) 19–44.

[57] J.H. Lee, G. Khang, J.W. Lee, H.B. Lee, Platelet adhesion onto chargeable functional group gradient surfaces, J. Biomed. Mater. Res. 40 (1998) 180–186.

[58] J.Y. Lim, X. Liu, E.A. Vogler, H.J. Donahue, Systematic variation in osteoblast adhesion and phenotype with substratum surface characteristics, J. Biomed. Mater. Res. - Part A 68 (2004) 504–512.

[59] C.J. Wilson, R.E. Clegg, D.I. Leavesley, M.J. Pearcy, Mediation of Biomaterial–Cell Interactions by Adsorbed Proteins: A Review, Tissue Eng. 11 (2005) 1–18.

[60] K. Anselme, L. Ploux, A. Ponche, Cell/material interfaces: Influence of surface chemistry and surface topography on cell adhesion, J. Adhes. Sci. Technol. 24 (2010) 831–852.

[61] E. Ruoslahti, RGD and other recognition sequences for integrins, Annu. Rev. Cell Dev. Biol. 12 (1996) 697–715.

[62] M.M. Martino, J.A. Hubbell, The 12th–14th type III repeats of fibronectin function as a highly promiscuous growth factor-binding domain, FASEB J. 24 (2010) 4711–4721.

[63] P. Kanchanawong, G. Shtengel, A.M. Pasapera, E.B. Ramko, M.W. Davidson, H.F. Hess, C.M. Waterman, Nanoscale architecture of integrin-based cell adhesions, Nature 468 (2010) 580–584.

[64] B. Ann Dalton, X. Frank Walboomers, M. Dziegielewski, M.D.M. Evans, S. Taylor, J.A. Jansen, J.G. Steele, Modulation of epithelial tissue and cell migration by microgrooves, J. Biomed. Mater. Res. 56 (2001) 195–207.

[65] E. Eisenbarth, P. Linez, V. Biehl, D. Velten, J. Breme, H.F. Hildebrand, Cell orientation and cytoskeleton organisation on ground titanium surfaces, in: Biomol. Eng., 2002: pp. 233–237.

[66] M.J. Dalby, M.O. Riehle, S.J. Yarwood, C.D.W. Wilkinson, A.S.G. Curtis, Nucleus alignment and cell signaling in fibroblasts: Response to a micro-grooved topography, Exp. Cell Res. 284 (2003) 274–282.

[67] P.M. Brett, J. Harle, V. Salih, R. Mihoc, I. Olsen, F.H. Jones, M. Tonetti, Roughness response genes in osteoblasts, Bone 35 (2004) 124–133.

[68] M.J. Dalby, N. Gadegaard, R. Tare, A. Andar, M.O. Riehle, P. Herzyk, C.D.W. Wilkinson, R.O.C. Oreffo, The control of human mesenchymal cell differentiation using nanoscale symmetry and disorder, Nat. Mater. 6 (2007) 997–1003.

[69] F.F.B. Hulshof, B. Papenburg, A. Vasilevich, M. Hulsman, Y. Zhao, M. Levers, N. Fekete, M. de Boer, H. Yuan, S. Singh, N. Beijer, M.A. Bray, D.J. Logan, M. Reinders, A.E. Carpenter, C. van Blitterswijk, D. Stamatialis, J. de Boer, Mining for osteogenic surface topographies: In silico design to in vivo osseo-integration, Biomaterials 137 (2017) 49–60.

[70] P.G. Coelho, R. Jimbo, N. Tovar, E.A. Bonfante, Osseointegration: Hierarchical designing encompassing the macrometer, micrometer, and nanometer length scales, Dent. Mater. 31 (2015) 37–52.

[71] A. Wennerberg, T. Albrektsson, J. Lausmaa, Torque and histomorphometric evaluation of c.p. titanium screws blasted with 25- and 75-µm-sized particles of Al2O3, J. Biomed.

Mater. Res. 30 (1996) 251–260.

[72] A. Wennerberg, T. Albrektsson, Effects of titanium surface topography on bone integration: A systematic review, Clin. Oral Implants Res. 20 (2009) 172–184.

[73] S. Hansson, M. Norton, The relation between surface roughness and interfacial shear strength for bone-anchored implants. A mathematical model, J. Biomech. 32 (1999) 829–836.

[74] J.Y. Park, C.H. Gemmell, J.E. Davies, Platelet interactions with titanium: Modulation of platelet activity by surface topography, Biomaterials 22 (2001) 2671–2682.

[75] J.E. Davies, Understanding peri-implant endosseous healing., J. Dent. Educ. 67 (2003) 932–949.

[76] M.-J. Kim, C.-W. Kim, Y.-J. Lim, S.-J. Heo, Microrough titanium surface affects biologic response in MG63 osteoblast-like cells, J. Biomed. Mater. Res. Part A 79 (2006) 1023–1032.

[77] Z. Schwartz, P. Raz, G. Zhao, Y. Barak, M. Tauber, H. Yao, B.D. Boyan, Effect of micrometer-scale roughness of the surface of Ti6Al4V pedicle screws in vitro and in vivo, J. Bone Jt. Surg. - Ser. A 90 (2008) 2485–2498.

[78] M.J. Dalby, N. Gadegaard, R.O.C. Oreffo, Harnessing nanotopography and integrin–matrix interactions to influence stem cell fate, Nat. Mater. 13 (2014) 558–569.

[79] M.J.P. Biggs, R.G. Richards, N. Gadegaard, C.D.W. Wilkinson, M.J. Dalby, The effects of nanoscale pits on primary human osteoblast adhesion formation and cellular spreading, J. Mater. Sci. Mater. Med. 18 (2007) 399–404.

[80] D. Khang, J. Lu, C. Yao, K.M. Haberstroh, T.J. Webster, The role of nanometer and sub-micron surface features on vascular and bone cell adhesion on titanium, Biomaterials 29 (2008) 970–983.

[81] P. Tambasco De Oliveira, A. Nanci, Nanotexturing of titanium-based surfaces upregulates expression of bone sialoprotein and osteopontin by cultured osteogenic cells, Biomaterials 25 (2004) 403–413.

[82] M.J. Dalby, D. McCloy, M. Robertson, C.D.W. Wilkinson, R.O.C. Oreffo, Osteoprogenitor response to defined topographies with nanoscale depths, Biomaterials 27 (2006) 1306–1315.

[83] G. Mendonça, D.B.S. Mendonça, L.G.P. Simões, A.L. Araújo, E.R. Leite, W.R. Duarte, F.J.L. Aragão, L.F. Cooper, The effects of implant surface nanoscale features on osteoblast-specific gene expression, Biomaterials 30 (2009) 4053–4062.

[84] R.A. Gittens, T. McLachlan, R. Olivares-Navarrete, Y. Cai, S. Berner, R. Tannenbaum, Z. Schwartz, K.H. Sandhage, B.D. Boyan, The effects of combined micron-/submicron-scale surface roughness and nanoscale features on cell proliferation and differentiation, Biomaterials 32 (2011) 3395–3403.

[85] D.E. Discher, P. Janmey, Y.L. Wang, Tissue cells feel and respond to the stiffness of their substrate, Science (80-.). 310 (2005) 1139–1143.

[86] A.J. Engler, S. Sen, H.L. Sweeney, D.E. Discher, Matrix Elasticity Directs Stem Cell Lineage

Specification, Cell 126 (2006) 677–689.

[87] R. Huiskes, H. Weinans, B. Van Rietbergen, The relationship between stress shielding and bone resorption around total hip stems and the effects of flexible materials, Clin. Orthop. Relat. Res. 274 (1992) 124–134.

[88] R. Korabi, K. Shemtov-Yona, D. Rittel, On stress/strain shielding and the material stiffness paradigm for dental implants, Clin. Implant Dent. Relat. Res. 19 (2017) 935–943.

[89] G. Soon, B. Pingguan-murphy, K. Wee Lai, S. Ali Akbar, Review of zirconia-based bioceramic : Surface modification and cellular response, Ceram. Int. 42 (2016) 12543–12555.

[90] F.H. Schünemann, M.E. Galárraga-Vinueza, R. Magini, M. Fredel, F. Silva, J.C.M. Souza, Y. Zhang, B. Henriques, Zirconia surface modifications for implant dentistry, Mater. Sci. Eng. C 98 (2019) 1294–1305.

[91] R.A. Delgado-Ruíz, J.L. Calvo-Guirado, P. Moreno, J. Guardia, G. Gomez-Moreno, J.E. Mate-Sánchez, P. Ramirez-Fernández, F. Chiva, Femtosecond laser microstructuring of zirconia dental implants, J. Biomed. Mater. Res. - Part B Appl. Biomater. 96 B (2011) 91–100.

[92] E. Roitero, F. Lasserre, M. Anglada, F. Mücklich, E. Jiménez-Piqué, A parametric study of laser interference surface patterning of dental zirconia: Effects of laser parameters on topography and surface quality, Dent. Mater. 33 (2017) e28–e38.

[93] T. Kosmač, Č. Oblak, L. Marion, The effects of dental grinding and sandblasting on ageing and fatigue behavior of dental zirconia (Y-TZP) ceramics, J. Eur. Ceram. Soc. 28 (2008) 1085–1090.

[94] E. Roitero, M. Ochoa, M. Anglada, F. Mücklich, E. Jiménez-Piqué, Low temperature degradation of laser patterned 3Y-TZP: Enhancement of resistance after thermal treatment, J. Eur. Ceram. Soc. 38 (2018) 1742–1749.

[95] D.B. Marshall, A.G. Evans, B.T.K. Yakub, J.W. Tien, G.S. Kino, The Nature of Machining Damage in Brittle Materials, Proc. R. Soc. A Math. Phys. Eng. Sci. 385 (1983) 461–475.

[96] T.G. Bifano, T.A. Dow, R.O. Scattergood, Ductile-Regime Grinding: A New Technology for Machining Brittle Materials, J. Eng. Ind. 113 (1991) 184–189.

[97] A.R. Alao, R. Stoll, X.F. Song, J.R. Abbott, Y. Zhang, J. Abduo, L. Yin, Fracture, roughness and phase transformation in CAD/CAM milling and subsequent surface treatments of lithium metasilicate/disilicate glass-ceramics, J. Mech. Behav. Biomed. Mater. 74 (2017) 251–260.

[98] L. Le Guéhennec, A. Soueidan, P. Layrolle, Y. Amouriq, Surface treatments of titanium dental implants for rapid osseointegration, Dent. Mater. 23 (2007) 844–854.

[99] M. Kern, S.M. Wegner, Bonding to zirconia ceramic: adhesion methods and their durability, Dent. Mater. 14 (1998) 64–71.

[100] J. Fischer, P. Grohmann, B. Stawarczyk, Effect of zirconia surface treatments on the shear strength of zirconia/veneering ceramic composites., Dent. Mater. J. 27 (2008) 448–454.

[101] P.J. Slikkerveer, P.C.P. Bouten, F.C.M. De Haas, High quality mechanical etching of brittle materials by powder blasting, Sensors Actuators, A Phys. 85 (2000) 296–303.

[102] R. Gruber, E. Hedbom, D. D. Bosshardt, R. Heuberger, D. Buser, Acid and alkali etching of

grit blasted zirconia: Impact on adhesion and osteogenic differentiation of MG63 cells in vitro, Dent. Mater. J. 31 (2012) 1097–1102.

[103] Q. Flamant, F. García Marro, J.J. Roa Rovira, M. Anglada, Hydrofluoric acid etching of dental zirconia. Part 1: Etching mechanism and surface characterization, J. Eur. Ceram. Soc. 36 (2016) 121–134.

[104] Q. Flamant, M. Anglada, Hydrofluoric acid etching of dental zirconia. Part 2: Effect on flexural strength and ageing behavior, J. Eur. Ceram. Soc. 36 (2016) 135–145.

[105] N. Saulacic, R. Erdösi, D.D. Bosshardt, R. Gruber, D. Buser, Acid and Alkaline Etching of Sandblasted Zirconia Implants: A Histomorphometric Study in Miniature Pigs, Clin. Implant Dent. Relat. Res. 16 (2014) 313–322.

[106] A.N. Samant, N.B. Dahotre, Laser machining of structural ceramics—A review, J. Eur. Ceram. Soc. 29 (2009) 969–993.

[107] Y.L. Yao, H. Chen, W. Zhang, Time scale effects in laser material removal: a review, Int. J. Adv. Manuf. Technol. 26 (2005) 598–608.

[108] V. Dumas, A. Guignandon, L. Vico, C. Mauclair, X. Zapata, M.T. Linossier, W. Bouleftour, J. Granier, S. Peyroche, J.C. Dumas, H. Zahouani, A. Rattner, Femtosecond laser nano/micro patterning of titanium influences mesenchymal stem cell adhesion and commitment, Biomed. Mater. 10 (2015) 055002.

[109] J.A. Muñoz-Tabares, E. Jiménez-Piqué, J. Reyes-Gasga, M. Anglada, Microstructural changes in ground 3Y-TZP and their effect on mechanical properties, Acta Mater. 59 (2011) 6670–6683.

[110] H. Hasegawa, Rhombohedral phase produced in abraded surfaces of partially stabilized zirconia (PSZ), J. Mater. Sci. Lett. 2 (1983) 91–93.

[111] Y. Kitano, Y. Mori, A. Ishitani, T. Masaki, Rhombohedral Phase in Y2O3-Partially-Stabilized ZrO2, J. Am. Ceram. Soc. 71 (1988) C-34-C–36.

[112] D.J. Kim, H.J. Jung, H.J. Kim, t→r phase transformation of tetragonal zirconia alloys by grinding, J. Mater. Sci. Lett. 14 (1995) 285–288.

[113] J. Kondoh, Origin of the hump on the left shoulder of the X-ray diffraction peaks observed in Y2O3-fully and partially stabilized ZrO2, J. Alloys Compd. 375 (2004) 270–282.

[114] A. V. Virkar, R.L.K. Matsumoto, Ferroelastic Domain Switching as a Toughening Mechanism in Tetragonal Zirconia, J. Am. Ceram. Soc. 69 (1986) C-224-C-226.

[115] K. Mehta, J.F. Jue, A. V Virkar, Grinding-Induced Texture in Ferroelastic Tetragonal Zirconia, J. Am. Ceram. Soc. 73 (1990) 1777–1779.

[116] J.J. Roa, M. Turon-Vinas, M. Anglada, Surface grain size and texture after annealing ground zirconia, J. Eur. Ceram. Soc. 36 (2016) 1519–1525.

[117] T. Kosmač, Č. Oblak, P. Jevnikar, N. Funduk, L. Marion, The effect of surface grinding and sandblasting on flexural strength and reliability of Y-TZP zirconia ceramic, Dent. Mater. 15 (1999) 426–433.

[118] C.J. Ho, H.C. Liu, W.H. Tuan, Effect of abrasive grinding on the strength of Y-TZP, J. Eur. Ceram. Soc. 29 (2009) 2665–2669.

[119] G.K.R. Pereira, M. Amaral, R. Simoneti, G.C. Rocha, P.F. Cesar, L.F. Valandro, Effect of grinding with diamond-disc and -bur on the mechanical behavior of a Y-TZP ceramic, J. Mech. Behav. Biomed. Mater. 37 (2014) 133–140.

[120] G.K.R. Pereira, S. Fraga, A.F. Montagner, F.Z.M. Soares, C.J. Kleverlaan, L.F. Valandro, The effect of grinding on the mechanical behavior of Y-TZP ceramics: A systematic review and meta-analyses, J. Mech. Behav. Biomed. Mater. 63 (2016) 417–442.

[121] T.K. Gupta, Strengthening by Surface Damage in Metastable Tetragonal Zirconia, J. Am. Ceram. Soc. 63 (1980) 117.

[122] P.J. Whalen, F. Reidinger, R.F. Antrim, Prevention of low-temperature surface transformation by surface recrystallization in yttria-doped tetragonal zirconia, J. Am. Ceram. Soc. 72 (1989) 319–321.

[123] J.A. Muñoz-Tabares, M. Anglada, Hydrothermal degradation of ground 3Y-TZP, J. Eur. Ceram. Soc. 32 (2012) 325–333.

[124] M. Inokoshi, K. Vanmeensel, F. Zhang, J. De Munck, G. Eliades, S. Minakuchi, I. Naert, B. Van Meerbeek, J. Vleugels, Aging resistance of surface-treated dental zirconia, Dent. Mater. 31 (2015) 182–194.

[125] P.F. Becher, M. V. Swain, Grain-size-dependent transformation behavior in polycrystalline tetragonal zirconia, J. Am. Ceram. Soc. 75 (1992) 493–502.

[126] J.F. Jue, J. Chen, A. V Virkar, Low-Temperature Aging of T'-Zirconia: the Role of Microstructure on Phase-Stability, J. Am. Ceram. Soc. 74 (1991) 1811–1820.

[127] M. Cattani-Lorente, S.S. Scherrer, S. Durual, C. Sanon, T. Douillard, L. Gremillard, J. Chevalier, A. Wiskott, Effect of different surface treatments on the hydrothermal degradation of a 3Y-TZP ceramic for dental implants, Dent. Mater. 30 (2014) 1136–1146.

[128] D. Deligianni, N. Katsala, S. Ladas, D. Sotiropoulou, J. Amedee, Y. Missirlis, Effect of surface roughness of the titanium alloy Ti-6Al-4V on human bone marrow cell response and on protein adsorption, Biomaterials 22 (2001) 1241–1251.

[129] K. Anselme, P. Linez, M. Bigerelle, D. Le Maguer, A. Le Maguer, P. Hardouin, H.F. Hildebrand, A. Iost, J.M. Leroy, The relative influence of the topography and chemistry of TiAl6V4 surfaces on osteoblastic cell behaviour, Biomaterials 21 (2000) 1567–1577.

[130] K. Anselme, M. Bigerelle, B. Noel, E. Dufresne, D. Judas, A. Iost, P. Hardouin, Qualitative and quantitative study of human osteoblast adhesion on materials with various surface roughnesses, J. Biomed. Mater. Res. 49 (2000) 155–166.

[131] J. Lincks, B.D. Boyan, C.R. Blanchard, C.H. Lohmann, Y. Liu, D.L. Cochran, D. Dean, Z. Schwartz, Response of MG63 osteoblast-like cells to titanium and titanium alloy is dependent on surface roughness and composition, Biomaterials 19 (1998) 2219–2232.

[132] J.L. Ong, D.L. Carnes, H.L. Cardenas, R. Cavin, Surface roughness of titanium on bone morphogenetic protein-2 treated osteoblast cells in vitro, Implant Dent. 6 (1997) 19–24.

[133] H. Huang, C. Ho, T. Lee, T. Lee, K. Liao, F. Chen, Effect of surface roughness of ground titanium on initial cell adhesion, Biomol. Eng. 21 (2004) 93–97.

[134] M. Irving, M.F. Murphy, M.N. Morgan, F. Lilley, P. French, D.R. Burton, P. Moran, Machine

grinding as an alternative method for creating functional surfaces for controlling cell behaviour, Int. J. Adv. Manuf. Technol. 87 (2016) 1023–1031.

[135] Y. Li, G. Huang, X. Zhang, L. Wang, Y. Du, T.J. Lu, F. Xu, Engineering cell alignment in vitro, Biotechnol. Adv. 32 (2014) 347–365.

[136] D. Bäuerle, Laser Processing and Chemistry, 4th ed., Springer, 2011.

[137] C. Zwahr, D. Günther, T. Brinkmann, N. Gulow, S. Oswald, M. Grosse Holthaus, A.F. Lasagni, Laser Surface Pattering of Titanium for Improving the Biological Performance of Dental Implants, Adv. Healthc. Mater. 6 (2017) 1600858.

[138] J. Krüger, W. Kautek, Ultrashort pulse laser interaction with dielectrics and polymers, Adv. Polym. Sci. 168 (2004) 247–289.

[139] F. Mücklich, A. Lasagni, C. Daniel, Laser interference metallurgy - Using interference as a tool for micro/nano structuring, Int. J. Mater. Res. 97 (2006) 1337–1344.

[140] A.F. Lasagni, Laser interference patterning methods: Possibilities for high-throughput fabrication of periodic surface patterns, Adv. Opt. Technol. 6 (2017) 1–11.

[141] J. Valle, S. Burgui, D. Langheinrich, C. Gil, C. Solano, A. Toledo-Arana, R. Helbig, A. Lasagni, I. Lasa, Evaluation of Surface Microtopography Engineered by Direct Laser Interference for Bacterial Anti-Biofouling, Macromol. Biosci. 15 (2015) 1060–1069.

[142] A. Rosenkranz, M. Hans, C. Gachot, A. Thome, S. Bonk, F. Mücklich, Direct laser interference patterning : Tailoring of contact area for frictional and antibacterial properties, Lubricants 4 (2016) 2–15.

[143] D.W. Müller, T. Fox, P.G. Grützmacher, S. Suarez, F. Mücklich, Applying ultrashort pulsed direct laser interference patterning for functional surfaces, Sci. Rep. 10 (2020) 3647.

[144] A. Peter, A.H.A. Lutey, S. Faas, L. Romoli, V. Onuseit, T. Graf, Direct laser interference patterning of stainless steel by ultrashort pulses for antibacterial surfaces, Opt. Laser Technol. 123 (2020) 105954.

[145] N. Bärsch, K. Werelius, S. Barcikowski, F. Liebana, U. Stute, A. Ostendorf, Femtosecond laser microstructuring of hot-isostatically pressed zirconia ceramic, J. Laser Appl. 19 (2007) 107–115.

[146] C. Daniel, B.L. Armstrong, J.Y. Howe, N.B. Dahotre, Controlled evolution of morphology and microstructure in laser interference-structured zirconia, J. Am. Ceram. Soc. 91 (2008) 2138–2142.

[147] J. Li, L. Ji, Y. Hu, Y. Bao, Precise micromachining of yttria-tetragonal zirconia polycrystal ceramic using 532 nm nanosecond laser, Ceram. Int. 42 (2016) 4377–4385.

[148] A.M. Stanciuc, Q. Flamant, C.M. Sprecher, M. Alini, M. Anglada, M. Peroglio, Femtosecond laser multi-patterning of zirconia for screening of cell-surface interactions, J. Eur. Ceram. Soc. 38 (2018) 939–948.

[149] A. Carvalho, L. Cangueiro, V. Oliveira, R. Vilar, M.H. Fernandes, F.J. Monteiro, Femtosecond laser microstructured alumina toughened zirconia: A new strategy to improve osteogenic differentiation of hMSCs, Appl. Surf. Sci. 435 (2018) 1237–1245.

[150] L. Goyos-Ball, C. Prado, R. Díaz, E. Fernández, A. Ismailov, T. Kumpulainen, E. Levänen, R.

Torrecillas, A. Fernández, The effects of laser patterning 10CeTZP-Al_2O_3 nanocomposite disc surfaces: Osseous differentiation and cellular arrangement in vitro, Ceram. Int. 44 (2018) 9472–9478.

[151] A. Carvalho, L. Grenho, M.H. Fernandes, A. Daskalova, A. Trifonov, I. Buchvarov, F.J. Monteiro, Femtosecond laser microstructuring of alumina toughened zirconia for surface functionalization of dental implants, Ceram. Int. 46 (2020) 1383–1389.

[152] R.S.F. Pereira, C.G. Moura, B. Henriques, J. Chevalier, F.S. Silva, M.C. Fredel, Influence of laser texturing on surface features, mechanical properties and low-temperature degradation behavior of 3Y-TZP, Ceram. Int. 46 (2020) 3502–3512.

[153] E.G. Gamaly, A. V. Rode, Physics of ultra-short laser interaction with matter: From phonon excitation to ultimate transformations, Prog. Quantum Electron. 37 (2013) 215–323.

[154] F. Zandiehnadem, R.A. Murray, W.Y. Ching, Electronic structures of three phases of zirconium oxide, Phys. B+C 150 (1988) 19–24.

[155] V.R. Paiverneker, A.N. Petelin, F.J. Crowne, D.C. Nagle, Color-center-induced band-gap shift in yttria-stabilized zirconia, Phys. Rev. B 40 (1989) 8555–8557.

[156] E. Roitero, F. Lasserre, J.J. Roa, M. Anglada, F. Mücklich, E. Jiménez-Piqué, Nanosecond-laser patterning of 3Y-TZP: Damage and microstructural changes, J. Eur. Ceram. Soc. 37 (2017) 4876–4887.

[157] R. Wagner, J. Gottmann, A. Horn, E.W. Kreutz, Subwavelength ripple formation induced by tightly focused femtosecond laser radiation, Appl. Surf. Sci. 252 (2006) 8576–8579.

[158] C. Daniel, J. Drummond, R.A. Giordano, Improving flexural strength of dental restorative ceramics using laser interference direct structuring, J. Am. Ceram. Soc. 91 (2008) 3455–3457.

[159] E. Roitero, M. Anglada, F. Mücklich, E. Jiménez-Piqué, Mechanical reliability of dental grade zirconia after laser patterning, J. Mech. Behav. Biomed. Mater. 86 (2018) 257–263.

[160] R.A. Delgado-Ruíz, G. Gomez Moreno, A. Aguilar-Salvatierra, A. Markovic, J.E. Mate-Sánchez, J.L. Calvo-Guirado, Human fetal osteoblast behavior on zirconia dental implants and zirconia disks with microstructured surfaces. An experimental in vitro study, Clin. Oral Implants Res. 27 (2016) e144–e153.

[161] Y. Taniguchi, K. Kakura, K. Yamamoto, H. Kido, J. Yamazaki, Accelerated osteogenic differentiation and bone formation on zirconia with surface grooves created with fiber laser irradiation, Clin. Implant Dent. Relat. Res. 18 (2016) 883–894.

[162] G. Abagnale, M. Steger, V.H. Nguyen, N. Hersch, A. Sechi, S. Joussen, B. Denecke, R. Merkel, B. Hoffmann, A. Dreser, U. Schnakenberg, A. Gillner, W. Wagner, Surface topography enhances differentiation of mesenchymal stem cells towards osteogenic and adipogenic lineages, Biomaterials 61 (2015) 316–326.

[163] M. Nevins, M. Camelo, M.L. Nevins, P. Schupbach, D.M. Kim, Connective tissue attachment to laser-microgrooved abutments: a human histologic case report, Int. J. Periodontics Restor. Dent 32 (2012) 385–92.

[164] S. Weiner, J. Simon, D.S. Ehrenberg, B. Zweig, J.L. Ricci, The effects of laser microtextured

collars upon crestal bone levels of dental implants, Implant Dent. 17 (2008) 217–228.

[165] H. Minamikawa, T. Ikeda, W. Att, Y. Hagiwara, M. Hirota, M. Tabuchi, H. Aita, W. Park, T. Ogawa, Photofunctionalization increases the bioactivity and osteoconductivity of the titanium alloy Ti6Al4V, J. Biomed. Mater. Res. - Part A 102 (2014) 3618–3630.

[166] S.B. Goodman, Z. Yao, M. Keeney, F. Yang, The future of biologic coatings for orthopaedic implants, Biomaterials 34 (2013) 3174–3183.

[167] A. Civantos, E. Martínez-Campos, V. Ramos, C. Elvira, A. Gallardo, A. Abarrategi, Titanium coatings and surface modifications: toward clinically useful bioactive implants, ACS Biomater. Sci. Eng. 3 (2017) 1245–1261.

[168] S. V Dorozhkin, Calcium orthophosphate coatings, films and layers, Prog. Biomater. 1 (2012) 1–40.

[169] A. Sola, D. Bellucci, V. Cannillo, A. Cattini, Bioactive glass coatings: A review, Surf. Eng. 27 (2011) 560–572.

[170] R.A. Surmenev, M.A. Surmeneva, A.A. Ivanova, Significance of calcium phosphate coatings for the enhancement of new bone osteogenesis - A review, Acta Biomater. 10 (2014) 557–579.

[171] L.L. Hench, J.M. Polak, I.D. Xynos, L.D.K. Buttery, Bioactive materials to control cell cycle, Mater. Res. Innov. 3 (2000) 313–323.

[172] H.W. Kim, G. Georgiou, J.C. Knowles, Y.H. Koh, H.E. Kim, Calcium phosphates and glass composite coatings on zirconia for enhanced biocompatibility, Biomaterials 25 (2004) 4203–4213.

[173] J. Mesquita-Guimarães, R. Detsch, A.C. Souza, B. Henriques, F.S. Silva, A.R. Boccaccini, O. Carvalho, Cell adhesion evaluation of laser-sintered HAp and 45S5 bioactive glass coatings on micro-textured zirconia surfaces using MC3T3-E1 osteoblast-like cells, Mater. Sci. Eng. C 109 (2020) 110492.

[174] P. Ducheyne, W. Van Raemdonck, J.C. Heughebaert, M. Heughebaert, Structural analysis of hydroxyapatite coatings on titanium, Biomaterials 7 (1986) 97–103.

[175] K.A. Gross, C.C. Berndt, In vitro testing of plasma-sprayed hydroxyapatite coatings, J. Mater. Sci. Mater. Med. 5 (1994) 219–224.

[176] T. Kokubo, F. Miyaji, H.-M. Kim, Spontaneous formation of bonelike apatite layer on chemically treated titanium metals, J. Am. Ceram. Soc. 79 (1996) 1127–1129.

[177] T. Kokubo, S. Yamaguchi, Bioactive Ti metal and its alloys prepared by chemical treatments: State-of-the-art and future trends, Adv. Eng. Mater. 12 (2010) B579–B591.

[178] M. Uchida, H. Kim, T. Kokubo, M. Nawa, T. Asano, K. Tanaka, T. Nakamura, Apatite-forming ability of a zirconia / alumina nano-composite induced by chemical treatment, J. Biomed. Mater. Res. 60 (2002) 277–282.

[179] T. Wang, Z. Weng, X. Liu, K.W.K. Yeung, H. Pan, S. Wu, Controlled release and biocompatibility of polymer/titania nanotube array system on titanium implants, Bioact. Mater. 2 (2017) 44–50.

[180] A.J. Niehaus, D.E. Anderson, V.F. Samii, S.E. Weisbrode, J.K. Johnson, M.S. Noon, D.L.

Tomasko, J.J. Lannutti, Effects of orthopedic implants with a polycaprolactone polymer coating containing bone morphogenetic protein-2 on osseointegration in bones of sheep, Am. J. Vet. Res. 70 (2009) 1416–1425.

[181] A.M. Peterson, C. Pilz-Allen, T. Kolesnikova, H. Möhwald, D. Shchukin, Growth factor release from polyelectrolyte-coated titanium for implant applications, ACS Appl. Mater. Interfaces 6 (2014) 1866–1871.

[182] J. Buxadera-Palomero, C. Canal, S. Torrent-Camarero, B. Garrido, F. Javier Gil, D. Rodríguez, Antifouling coatings for dental implants: Polyethylene glycol-like coatings on titanium by plasma polymerization., Biointerphases 10 (2015) 029505.

[183] J.D. Bumgardner, R. Wiser, P.D. Gerard, P. Bergin, B. Chestnutt, M. Marini, V. Ramsey, S.H. Elder, J.A. Gilbert, Chitosan: Potential use as a bioactive coating for orthopaedic and craniofacial/dental implants, J. Biomater. Sci. Polym. Ed. 14 (2003) 423–438.

[184] C. Peng, Q. Zhao, C. Gao, Sustained delivery of doxorubicin by porous CaCO3 and chitosan/alginate multilayers-coated CaCO3 microparticles, Colloids Surfaces A Physicochem. Eng. Asp. 353 (2010) 132–139.

[185] F. Munarin, S.G. Guerreiro, M.A. Grellier, M.C. Tanzi, M.A. Barbosa, P. Petrini, P.L. Granja, Pectin-based injectable biomaterials for bone tissue engineering, Biomacromolecules 12 (2011) 568–577.

[186] R.A.A. Muzzarelli, F. Greco, A. Busilacchi, V. Sollazzo, A. Gigante, Chitosan, hyaluronan and chondroitin sulfate in tissue engineering for cartilage regeneration: A review, Carbohydr. Polym. 89 (2012) 723–739.

[187] U. Geißler, U. Hempel, C. Wolf, D. Scharnweber, H. Worch, K.W. Wenzel, Collagen type I-coating of Ti6A14V promotes adhesion of osteoblasts, J. Biomed. Mater. Res. 51 (2000) 752–760.

[188] T.H. Barker, The role of ECM proteins and protein fragments in guiding cell behavior in regenerative medicine, Biomaterials 32 (2011) 4211–4214.

[189] S. Gomes, I.B. Leonor, J.F. Mano, R.L. Reis, D.L. Kaplan, Natural and genetically engineered proteins for tissue engineering, Prog. Polym. Sci. 37 (2012) 1–17.

[190] N.H. Romano, D. Sengupta, C. Chung, S.C. Heilshorn, Protein-engineered biomaterials: Nanoscale mimics of the extracellular matrix, Biochim. Biophys. Acta - Gen. Subj. 1810 (2011) 339–349.

[191] S.L. Bellis, Advantages of RGD peptides for directing cell association with biomaterials, Biomaterials 32 (2011) 4205–4210.

[192] M. Sinha, S. Kaushik, P. Kaur, S. Sharma, T.P. Singh, Antimicrobial Lactoferrin Peptides: The Hidden Players in the Protective Function of a Multifunctional Protein, Int. J. Pept. 390230 (2013) 1–12.

[193] R. Visser, G.A. Rico-Llanos, H. Pulkkinen, J. Becerra, Peptides for bone tissue engineering, J. Control. Release 244 (2016) 122–135.

[194] C. Mas-Moruno, R. Fraioli, F. Albericio, J.M. Manero, F.J. Gil, Novel peptide-based platform for the dual presentation of biologically active peptide motifs on biomaterials, ACS Appl.

Mater. Interfaces 6 (2014) 6525–6536.

[195] R. Fraioli, K. Dashnyam, J.H. Kim, R.A. Perez, H.W. Kim, J. Gil, M.P. Ginebra, J.M. Manero, C. Mas-Moruno, Surface guidance of stem cell behavior: Chemically tailored co-presentation of integrin-binding peptides stimulates osteogenic differentiation in vitro and bone formation in vivo, Acta Biomater. 43 (2016) 269–281.

[196] M. Hoyos-Nogués, F. Velasco, M.P. Ginebra, J.M. Manero, F.J. Gil, C. Mas-Moruno, Regenerating Bone via Multifunctional Coatings: The Blending of Cell Integration and Bacterial Inhibition Properties on the Surface of Biomaterials, ACS Appl. Mater. Interfaces 9 (2017) 21618–21630.

[197] Y.T. Liu, T.M. Lee, T.S. Lui, Enhanced osteoblastic cell response on zirconia by bio-inspired surface modification, Colloids Surfaces B Biointerfaces 106 (2013) 37–45.

[198] M. Liu, J. Zhou, Y. Yang, M. Zheng, J. Yang, J. Tan, Surface modification of zirconia with polydopamine to enhance fibroblast response and decrease bacterial activity in vitro: A potential technique for soft tissue engineering applications, Colloids Surfaces B Biointerfaces 136 (2015) 74–83.

[199] D. Ito, T. Kado, F. Nagano-Takebe, T. Hidaka, K. Endo, Y. Furuichi, Biological activation of zirconia surfaces by chemical modification with IGF-1, J. Biomed. Mater. Res. - Part A 103 (2015) 3659–3665.

[200] S.K. Hsu, H.C. Hsu, W.F. Ho, C.H. Yao, P.L. Chang, S.C. Wu, Biomolecular modification of zirconia surfaces for enhanced biocompatibility, Thin Solid Films 572 (2014) 91–98.

[201] E. Fernandez-Garcia, X. Chen, C.F. Gutierrez-Gonzalez, A. Fernandez, S. Lopez-Esteban, C. Aparicio, Peptide-functionalized zirconia and new zirconia / titanium biocermets for dental applications, J. Dent. 43 (2015) 1162–1174.

[202] Z. Yang, M. Liu, Y. Yang, M. Zheng, Y. Yang, X. Liu, J. Tan, Biofunctionalization of zirconia with cell-adhesion peptides via polydopamine crosslinking for soft tissue engineering: Effects on the biological behaviors of human gingival fibroblasts and oral bacteria, RSC Adv. 10 (2020) 6200–6212.

[203] K. Burridge, M. Chrzanowska-Wodnicka, Focal Adhesions, Contractility, and Signaling, Annu. Rev. Cell Dev. Biol. 12 (1996) 463–519.

[204] V. Rosen, BMP2 signaling in bone development and repair, Cytokine Growth Factor Rev. 20 (2009) 475–480.

[205] P.J. Marie, F. Debiais, E. Haÿ, Regulation of human cranial osteoblast phenotype by FGF-2, FGFR-2 and BMP-2 signaling, Histol. Histopathol. 17 (2002) 877–885.

[206] D.A. Wong, A. Kumar, S. Jatana, G. Ghiselli, K. Wong, Neurologic impairment from ectopic bone in the lumbar canal: a potential complication of off-label PLIF/TLIF use of bone morphogenetic protein-2 (BMP-2), Spine J. 8 (2008) 1011–1018.

[207] E.J. Carragee, E.L. Hurwitz, B.K. Weiner, A critical review of recombinant human bone morphogenetic protein-2 trials in spinal surgery: Emerging safety concerns and lessons learned, Spine J. 11 (2011) 471–491.

[208] Y.-J. Seol, Y.-J. Park, S.-C. Lee, K.-H. Kim, J.-Y. Lee, T.-I. Kim, Y.-M. Lee, Y. Ku, I.-C. Rhyu, S.-B.

Han, C.-P. Chung, Enhanced osteogenic promotion around dental implants with synthetic binding motif mimicking bone morphogenetic protein (BMP)-2, J. Biomed. Mater. Res. Part A 77A (2006) 599–607.

[209] J.-B. Park, J.-Y. Lee, H.-N. Park, Y.-J. Seol, Y.-J. Park, S.-H. Rhee, S.-C. Lee, K.-H. Kim, T.-I. Kim, Y.-M. Lee, Y. Ku, I.-C. Rhyu, S.-B. Han, C.-P. Chung, Osteopromotion With Synthetic Oligopeptide–Coated Bovine Bone Mineral In Vivo, J. Periodontol. 78 (2007) 157–163.

[210] J.Y. Lee, J.E. Choo, Y.S. Choi, J.S. Suh, S.J. Lee, C.P. Chung, Y.J. Park, Osteoblastic differentiation of human bone marrow stromal cells in self-assembled BMP-2 receptor-binding peptide-amphiphiles, Biomaterials 30 (2009) 3532–3541.

[211] L. Falcigno, G. D'Auria, L. Calvanese, D. Marasco, R. Iacobelli, P.L. Scognamiglio, P. Brun, R. Danesin, M. Pasqualin, I. Castagliuolo, M. Dettin, Osteogenic properties of a short BMP-2 chimera peptide, J. Pept. Sci. 21 (2015) 700–709.

[212] Y. Oki, K. Kirita, S. Ohta, S. Ohba, I. Horiguchi, Y. Sakai, T. Ito, Switching of Cell Proliferation/Differentiation in Thiol-Maleimide Clickable Microcapsules Triggered by in Situ Conjugation of Biomimetic Peptides, Biomacromolecules 20 (2019) 2350–2359.

[213] L. Oliver-Cervelló, H. Martin-Gómez, L. Reyes, F. Noureddine, E.A. Cavalcanti-Adam, M.-P. Ginebra, C. Mas-Moruno, An engineered biomimetic peptide regulates cell behavior by synergistic integrin and growth factor signaling, Adv. Healthc. Mater. (2020).

[214] S. Mallakpour, M. Madani, A review of current coupling agents for modification of metal oxide nanoparticles, Prog. Org. Coatings 86 (2015) 194–207.

[215] S.J. Xiao, M. Textor, N.D. Spencer, M. Wieland, B. Keller, H. Sigrist, Immobilization of the cell-adhesive peptide Arg-Gly-Asp-Cys (RGDC) on titanium surfaces by covalent chemical attachment, J. Mater. Sci. Mater. Med. 8 (1997) 867–872.

[216] M. Godoy-Gallardo, C. Mas-Moruno, M.C. Fernández-Calderón, C. Pérez-Giraldo, J.M. Manero, F. Albericio, F.J. Gil, D. Rodríguez, Covalent immobilization of hLf1-11 peptide on a titanium surface reduces bacterial adhesion and biofilm formation, Acta Biomater. 10 (2014) 3522–3534.

[217] J.H. Waite, M.L. Tanzer, Polyphenolic substance of Mytilus edulis: Novel adhesive containing L-dopa and hydroxyproline, Science (80-.). 212 (1981) 1038–1040.

[218] H. Lee, N.F. Scherer, P.B. Messersmith, Single-molecule mechanics of mussel adhesion, Proc. Natl. Acad. Sci. 103 (2006) 12999–13003.

[219] P. Kord Forooshani, B.P. Lee, Recent approaches in designing bioadhesive materials inspired by mussel adhesive protein, J. Polym. Sci. Part A Polym. Chem. 55 (2017) 9–33.

[220] X. Miao, Y. Hu, J. Liu, X. Huang, Hydroxyapatite coating on porous zirconia, Mater. Sci. Eng. C 27 (2007) 257–261.

[221] Y. Cho, J. Hong, H. Ryoo, D. Kim, J. Park, J. Han, Osteogenic responses to zirconia with hydroxyapatite coating by aerosol deposition, J. Dent. Res. 94 (2015) 491–499.

[222] P.I. Brånemark, B.O. Hansson, R. Adell, U. Breine, J. Lindström, O. Hallén, A. Ohman, Osseointegrated implants in the treatment of the edentulous jaw. Experience from a 10-year period., Scand. J. Plast. Reconstr. Surg. Suppl. 16 (1977) 1–132.

[223] C.M. Abraham, A brief historical perspective on dental implants, their surface coatings and treatments, Open Dent. J. 8 (2014) 50–55.

Annex A
Selection of an optimal surface modification technique

Introduction

In this Ph.D. Thesis, two surface-modifying treatments were employed to modify 3Y-TZP topography: grinding/polishing and laser micro-patterning. Between them, the one with better properties had to be selected for the study combining topography and a biomolecule.

Regarding grinding/polishing, four different treatments of increasing severity were used (1 to 4), and two different directionalities were explored: multidirectional (M) and unidirectional (U) grooves. Results can be found in *Papers I* and *II.* It was concluded that grades 2-M/U and 3-M/U could totally protect the surface from LTD. In addition, just cells growing on 3-U and 4-U displayed contact guidance. Thus, 3-M/U were selected among the grinding/polishing samples as the ones with better properties as could both protect the surface from LTD and promote contact guidance in the U grooved specimens.

Regarding laser micro-patterning, two different periodicities were explored: 3 μm (3L) and 10 μm (10L). Results can be found in the first part of *Paper III.* Both periodicities displayed just traces of *m*-phase after laser treatment. Very low amounts of surface damage were detected and the LTD behavior was not decreased as compared to the mirror-like polished (also known as control, CTRL) specimens, if a post-thermal treatment was applied. Both surfaces presented contact guidance. Thus, the two periodicities were kept as representative for the laser micro-patterning treatment.

In order to choose between grinding/polishing and laser-treated samples for further surface functionalization, a cell-adhesion experiment was carried out. This experiment was employed as the cell-adhesive properties and cell morphology can give a clue on the degree and type of cell-material interaction. The samples compared were 3-M and 3-U (ground) and 3L and 10L (laser-treated).

Experimental procedure

The samples used in this experiment are listed in ***Table A.***

Table A *Label and description of the specimens employed in the cell-adhesion experiment.*

Sample label	**Description**	
CTRL	Non- functionalized	Mirror-like polished specimen, employed as a flat topography reference
3-M		Specimen multidirectionally ground
3-U		Specimen unidirectionally ground
3L		Laser-patterned specimen with a linear pattern of 3 μm periodicity
10L		Laser-patterned specimen with a linear pattern of 10 μm periodicity
CTRL-P	Functionalized	CTRL specimen functionalized with the peptidic platform
3-M-P		3-M specimen functionalized with the peptidic platform
3-U-P		3-U specimen functionalized with the peptidic platform
3L-P		3L specimen functionalized with the peptidic platform
10L-P		10L specimen functionalized with the peptidic platform

The method to produce CTRL, 3-M and 3-U specimens can be found in *Paper I* (in this paper CTRL specimens are labeled as MP). The method to produce 3L and 10L surfaces, the surface functionalization protocol, as well as details about the chemical structure of the peptidic platform can be found in *Paper III*.

For the cell-adhesion assay, hMSCs at passage 6 were seeded at a concentration of 5000 cells/well in serum-free medium and incubated at 37 °C and 5% (v/v) CO_2 containing atmosphere. After 6 hours, medium was aspired and non-adherent cells were removed by carefully washing with PBS. Cells were fixed with paraformaldehyde (PFA, 4 % w/v in PBS) for 30 min and permeabilized

with 0.05% (w/v) Triton X-100 in PBS for 20 min. Actin fibers were stained by incubating with TRITC-conjugated phalloidin (1:300, in permeabilizing buffer) for 1 h and nuclei were stained using 4′,6-diamidino-2-phenylindole (DAPI) (1:1000, in PBS-glycine 20 mM) for 2 min, both in the dark. Between all steps, samples were rinsed three times with PBS-glycine for 5 min. Specimens were mounted in Mowiol 4-88, examined under a fluorescence CLSM (Carl Zeiss LSM 800) and images were processed using Fiji/Image-J package to calculate cell-shape parameters.

Values in graphs are displayed as mean ± standard deviation. Statistical differences were assessed by ANOVA using Tukey's test for pair-wise comparisons ($p < 0.05$). Differences were further analyzed and confirmed with the non-parametric Mann-Whitney test. The software employed was Minitab® 18.1.

Results and discussion

As it can be observed in **Figures A.1** and **A.2**, ground specimens behaved very similarly to CTRL specimens, both functionalized and non-functionalized. Cell morphology was similar, and the changes after functionalization, such as the increase in cell area, followed the same trend. This can be observed by comparing **Figures A.1a**, **c** and **e** (CTRL, 3-M and 3-U, respectively) that are practically identical. After functionalization with the biomolecule, cells increased their area and changed their shape, but still looked similar when comparing ground and CTRL specimens in **Figures A.1b**, **d** and **f** (CTRL-P, 3-M-P and 3-U-P, respectively). Just a slight cell alignment and increase in aspect ratio (cell elongation) could be observed in 3-U specimens (**Figure A.2c** and **d**), especially in the functionalized specimens 3-U-P (**Figure A.1f**).

Paper II showed a clear cell alignment and elongation after culturing human sarcoma osteogenic (SaOS-2) cells in unidirectionally grooved 3-U specimens. The lack of significant morphological changes in this experiment, even after functionalization, can be related to the different cell size. MSCs are much larger than SaOS-2, and while SaOS-2 can be well guided by this topography; the size of the topographical features (average roughness, peak-to-valley height, etc.) may not be enough to affect MSCs to the same degree.

However, cells grown on laser micro-patterned surfaces were significantly affected by the topography (**Figures A.1 g, h, i and j**), displaying a very evident cell elongation and alignment in both functionalized and non-functionalized surfaces (**Figures A.2c** and **d**). Yet, just in terms of cell adhesion, the peptide seemed to have a stronger effect on CTRL and ground specimens as compared to laser patterned samples, where topography had a leading role in guiding cell shape.

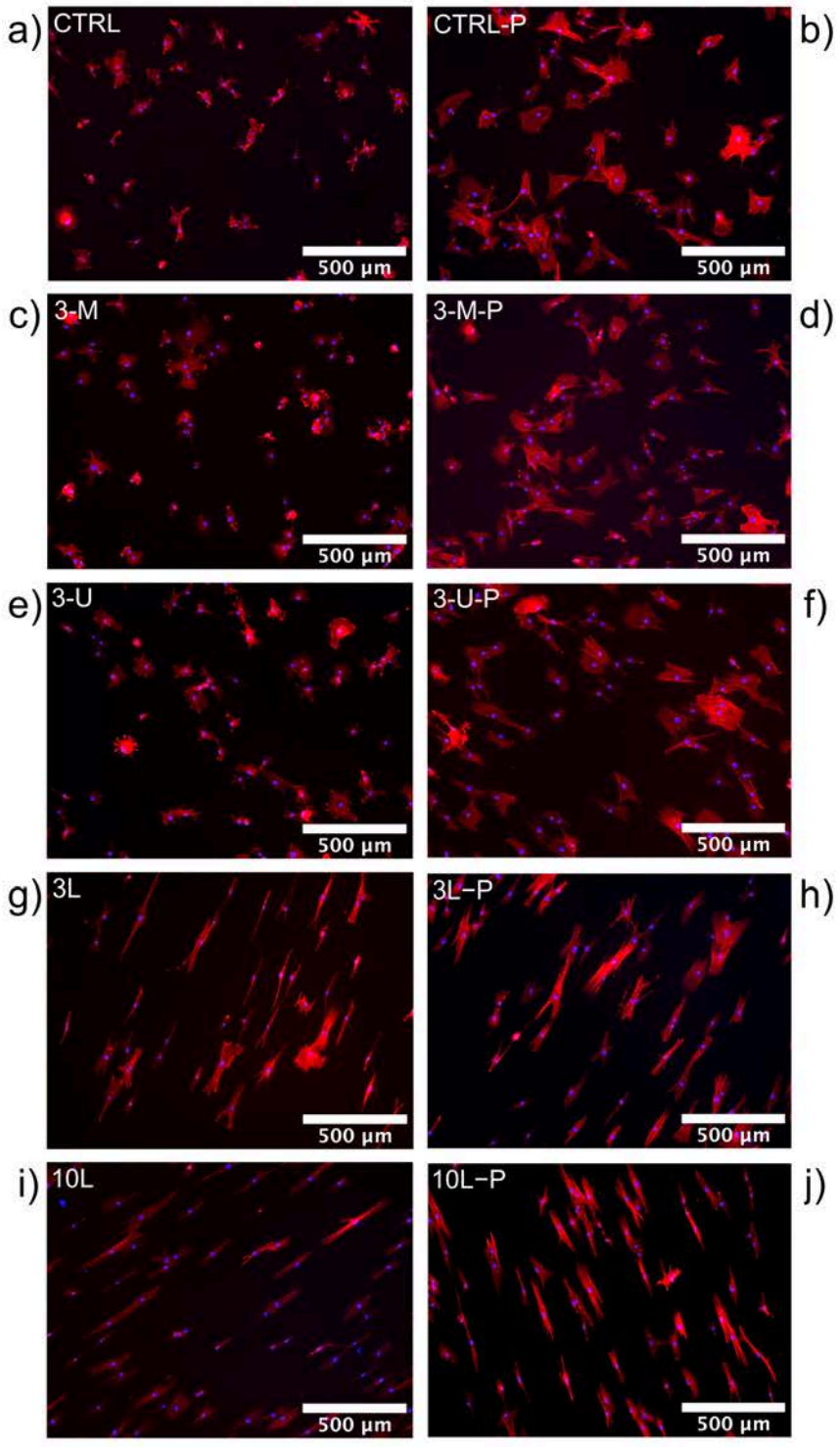

Figure A.1 Human MSCs adhesion results after 6h in serum free medium. Representative images of the studied specimens under fluorescence confocal laser scanning microscopy. Actin filaments were stained with TRITC-conjugated phalloidin (red), and cell nuclei with DAPI (blue).

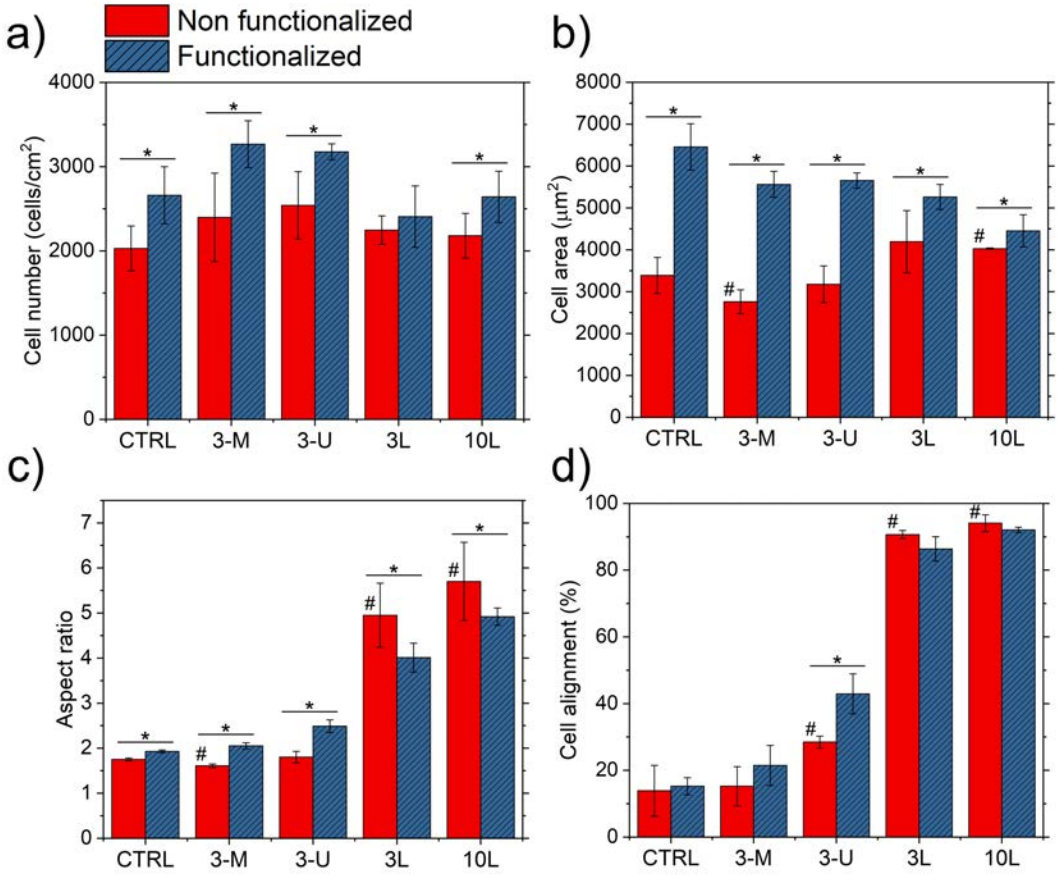

Figure A.2 *Cell parameters extracted from the cell-adhesion assay. a) Cell number (cells/cm²), b) cell area (µm²), c) cell aspect ratio and d) cell alignment (%). Cell alignment was defined as the percentage of cells aligned along a direction ±15° respect to the pattern direction. Red bars correspond to the non-functionalized specimens while blue bars represent specimens functionalized with the peptidic platform. * indicates statistical differences between functionalized and non-functionalized specimens with the same topography (e.g. 10L vs. 10L-P). # indicates statistical differences between 3-M, 3-U, 3L or 10L with respect to CTRL, analyzing only the effect of topography, without functionalization (p<0.05).*

Conclusions

One of the main goals of this Ph.D. Thesis is to combine the effects of surface topography and a biomolecule to improve the tissue integration properties of 3Y-TZP implant surfaces. However, the effect of topography was shown to be highly reduced in the ground surfaces tested (3-M and 3-U) when employing large cells such as MSCs. For this reason, **the laser micro-patterned samples were the ones selected** for further functionalization with a peptidic molecule, in *Paper III*.

From the material point of view, laser patterning allows creating homogeneous and well-defined patterns with different periodicities and depths, with a limited surface damage. In the case of grinding/polishing, however, producing rougher surfaces with higher pattern depths is always associated with increased surface damage.